Experimental and numerical investigation of mechanical properties of irradiated ferritic/martensitic steel-T91 with microstructure evaluation

By

N. Naveen Kumar
(ENGG01200704035)

Bhabha Atomic Research Centre,
Mumbai 400085, India

A thesis submitted to the
Board of Studies in Engineering Sciences
In partial fulfillment of requirements
For the Degree of

Doctor of Philosophy

of

HOMI BHABHA NATIONAL INSTITUTE

July, 2013

Homi Bhabha National Institute

Recommendations of the Viva Voce Board

As members of the Viva Voce Board, we certify that we have read the dissertation prepared by Naveen Kumar N., entitled "Experimental and numerical investigation of mechanical properties of irradiated ferritic/martensitic steel-T91 with microstructure evaluation" and recommend that it may be accepted as fulfilling the dissertation requirement for the Degree of Doctor of Philosophy.

_____Date:

Chairman: Dr. V. K. Suri

_____Date:

Guide: Dr. B.K. Dutta

_____Date:

Co-guide: Dr. G. K. Dey

_____ _____Date:

Member 1: Dr. P. Chellapandi

_____Date:

Member 2: Dr. G. R. Reddy

_____Date:

Member 3: Dr. J. Chattopadhyay

Final approval and acceptance of this dissertation is contingent upon the candidate's submission of the final copies of the dissertation to HBNI.

I hereby certify that I have read this dissertation prepared under my direction and recommend that it may be accepted as fulfilling the dissertation requirement.

Guide: Date:

Co-guide: Date:

STATEMENT BY AUTHOR

This dissertation has been submitted in partial fulfillment of requirements for an advanced degree at Homi Bhabha National Institute (HBNI) and is deposited in the Library to be made available to borrowers under rules of the HBNI.

Brief quotations from this dissertation are allowable without special permission, provided that accurate acknowledgement of source is made. Requests for permission for extended quotation from or reproduction of this manuscript in whole or in part may be granted by the Competent Authority of HBNI when in his or her judgment the proposed use of the material is in the interests of scholarship. In all other instances, however, permission must be obtained from the author.

(N. Naveen Kumar)

DECLARATION

I, hereby, declare that the investigations presented in this thesis have been carried out by me. The work is original and has not been submitted earlier in whole or part for a degree / diploma to this or any other Institution / University.

(N. Naveen Kumar)

ACKNOWLEDGMENTS

I wish to express my sincere gratitude to my research guides Prof. B.K. Dutta and Prof. G. K. Dey for their valuable guidance and constant encouragement throughout the work. I am also very thankful to them for helping me out of the difficulties found during research journey.

It is my great privilege to thank Mr. P. V. Durgaprasad, Prof. R. Tewari, Dr. P. Mukharjee (VECC-Kolkata), Shri. C. S. Vishwanadham and Mr. A. K. Pawar for their keen interest in my work and giving me valuable suggestions and encouraging me to learn the subject more deeply. The Chairman (Dr. V. K. Suri) and members of doctoral committee are deeply acknowledged for their critical analysis and valuable suggestions provided during the review presentations and pre-synopsis viva-voce.

I am grateful to Prof. I. Samajdar (IIT, Mumbai), Prof. Pritha Pant (IIT, Mumbai) for allowing me to carry out the experiments in their labs. It is my pleasure to thank Mr. B. Viswanadh, Mr. K. V. Manikrishna, Dr. D. Srivastava, Dr. Gayatri Banerjee (VECC-Kolkata) for their encouraging discussions during the course of my doctoral research. Also, I thank Dr. L. Malerba (SCK-CEN, Belgium) for providing the T91 material. Dr. J. A Caro (LANL, USA), Dr. E. S. Martinez (LANL, USA), Dr. Q. Sylvian (LLNL, USA), Dr. B. Devincre (CNRS/ONERA, France), Dr. A. Stukowski (TUD, Germany) for helping me while learning different simulation tools used in the present work.

I would like to acknowledge my sincere gratitude to my friends Ajay (IIT, Mumbai), Ankit, Govind, Somesh, Ritesh, Rohit Singh, Pankaj, Urvashi, Debes roy, Nazir, Arvind, Gambhir, Vijay, Ameya, Sunil Rawat, Sunil Kumar, Nitendra Singh and friends from 51st batch training school for their support and help, also I thank Dr. K. S. Shambhulingaiah for his encouragement and support.

Finally, I wish to acknowledge my parents, my brother and family for their love and support during the research work and making me successful in achieving my dream.

July, 2013 N. Naveen Kumar

CONTENTS

"Experimental and numerical investigation of mechanical properties of irradiated ferritic/martensitic steel-T91 with microstructure evaluation"

Nuclear reactors are the promising energy sources for the fulfillment of energy needs of human being in the present time as well as in future. Life of a nuclear reactor completely depends upon the degradation of properties of structural materials. Understanding property degradation of structural materials used in nuclear reactors due to irradiation is one of the major challenges faced by the nuclear community. The next generation fission (Gen-IV) and fusion reactors are planned to operate between 500-1000 ^{0}C temperature in a severe irradiation environment (with cumulative dose of 100-200 dpa) [1]; a dose which is not seen by a material in the past or present reactors. There is no single material which can satisfy all the design requirements of Gen-IV and fusion reactors. All these materials have a common problem of irradiation hardening and embrittlement [2-3]. In the presence of their own advantages and disadvantages of different materials, after four decades of research the nuclear reactor community came up with reduced or low activation FM steels (R/LAMS) as the candidate structural materials for future high temperature fission and fusion reactors. The main attractive properties of these materials are very low volumetric swelling, high radiation and high temperature tolerant and reduced activity in comparison to other family of materials [4]. The radioactivity levels of these materials are expected to reach low enough in about 100 years as compared with the thousands of conventional structural steels [5].

Degradation in macroscopic properties of the materials components upon irradiation (of dimensions in meter scale) depend on their microstructures (in nanometer and micrometer scale). Microstructure of the materials typically comprises crystalline defects and precipitates prior to

irradiation, defects generated by irradiation (few nanometers to micrometers size), alloying/impurity elements, etc, in the grains of few micrometers of the matrix phase. Apart from degradation of properties induced by defects generated in the microstructure by irradiation, property degradation in the structural materials could also be introduced by the production of transmutation helium due to high energy neutron bombardments. The amount of He produced in fusion reactors is found to be 10-15appm/dpa [6] and in Gen-IV reactors it is 3-10appm [5] in their life time of operation.

A number of experimental techniques exist to determine the mechanical properties of the materials (e.g. tensile testing, creep testing, fracture testing etc) using standard sized samples. The limited availability of the irradiated material volume in reactors and in accelerators and radioactivity of the samples after neutron irradiation limits the standard size sample testing. Explicit evaluation of micro-structural changes and the related phenomena are difficult to elaborate using only experiments, since, the process of property changes due to material damage occurring from the interaction of energetic particles, defect production, diffusion, agglomeration, mutual interaction and their manifestation at macro scale covers a wide range of length and time scale phenomena [7-8].

To overcome limitations of irradiation experiments and to understand the phenomenon occurring at different length and time scales, a new methodology has been developed by the coordination of nuclear materials community all over the world. This methodology comprises all the length and time scales and based on passing key information obtained from a lower scale to successive higher length and time scales and is known as Multi-scale Material Modeling (MMM)

approach [9]. Material modeling is important as; a) it helps in better understanding of the different deformation and hardening mechanisms involved, b) optimization of material parameters with less human efforts and, c) the virtual material testing can be done with less experimental trials.

In the present study a combination of experimental and MMM methodology has been used to investigate the change in mechanical property, defects present in the microstructure and their effect on the mechanical properties of the material. In this work, we consider macroscopic mechanical properties such as yield/ultimate strength, ductility and deformation behavior of the materials. The effect of irradiation induced defects has been theoretically estimated. In order to have understanding of irradiation effects on the structural material, T91 FM steel is used. In view of these, the objective of the present work has been divided in to two parts and could be summarized as follows;

In the first part, irradiation experiments are conducted under controlled conditions to determine the mechanical properties (in particular hardness and yield strength) and investigation of microstructural changes of samples irradiated to different doses. One of the candidate materials, FM steel (T91) has been irradiated by argon ion irradiation. Nanoindentation experiments are carried out to determine the change in mechanical property (yield strength) of the material. Using microstructure characterization techniques, such as, transmission electron microscopy (TEM) and grazing incidence X-ray diffraction (GIXRD) to examine the irradiation damage localized at surface.

In the second part, numerical simulations are carried using MMM methodology comprising atomistic and dislocation dynamics simulations by systematically introducing the

irradiation induced defects (particular voids or bubbles and loops) as observed in microstructural (TEM) investigation of irradiated samples. In this part, model Fe and Fe-10%Cr systems are considered for atomistic and dislocation dynamics study due to complex nature of microstructure and absence of suitable multi component potentials.

Keeping the above objectives in mind, the present thesis is organized in the following chapters,

CHAPTER 1: INTRODUCTION

In this chapter, general introduction to operating conditions of next generation reactor, materials proposed and irradiation effects are highlighted. This chapter also describes the hierarchical multi-scale modeling methodology to correlate irradiated micro-structure to macroscopic material behavior. Challenges faced by the reactor material community for safe operation of next generation reactors are highlighted. At the end of this chapter, motivation and objective for the present work has been described.

CHAPTER 2: LIERATURE REVIEW

This chapter consists of a detailed literature review of current status of experimental, characterization and numerical techniques used in the present work. Initially, desirable properties of the nuclear materials are listed and effect of unirradiated microstructure is explained. Subsequently, an overview of basic radiation damage process and effect of irradiation induced defects on mechanical properties are given. A brief introduction to small specimen testing techniques is given and one of the techniques nanoindentation is elaborated. A brief introduction to MD and DD simulations, force evaluation in each method and highlights the previous effort made to study the interaction of dislocation with irradiation induced defects as found in the literature. The application of characterization techniques transmission electron microscopy

(TEM) and grazing incidence X-ray diffraction (GIXRD) for irradiated microstructure analysis is also reviewed in the light of available literature.

CHAPTER 3: EXPERIMENTAL TECHNIQUES

This chapter briefly provides the various experimental techniques, sample preparation and experimental conditions used in the present study. A brief description of irradiation studies and the methodology adopted for Ar ion irradiation experiments has been explained. In addition optimization of parameters and short description of various line profile techniques has been provided. Details about dpa calculation and calculation of fluence of ion irradiation have also been included.

CHAPTER 4: NANOINDENTATION EXPERIMENT AND MICROSTRUCTURE CHARACTERIZATION OF IRRADIATED MATERIAL USING TEM AND GIXRD

In order to study the response of material to irradiation, T91 FM steel samples were irradiated to 5, 10 and 20dpa using Ar^{9+} ions and subsequently each sample was characterized using X-ray line profile, nanoindentation and TEM. This chapter provides results obtained from nanoindentation testing of irradiated samples and irradiation induced defects present in the microstrcutre. X-ray line profile experiments provided a global view of the changes in microstructure and accumulation of strain in the matrix as function of irradiation. TEM observations provided direct evidence of radiation induced defects in localized regions. Nanoindentation experiments were carried out to obtain change in the hardness and other mechanical properties as a function of irradiation.

A comparison of mechanical properties obtained by nanoindentation of the unirradiated and irradiated samples could successfully show changes in yield strength of the materials upon irradiation. Load vs. depth of indentation curves (Figure 1a) obtained on unirradiated as well as irradiated material showed the hardening effect as an increase in the load for a given depth of indentation. The change in hardness (ΔH_{NANO}) and yield strength ($\Delta\sigma_{YS}$) [10] were found to have similar dependence on the irradiation dose at a temperature < 60^0C (Figure 1b). The inset Figure (Figure 1b) shows the $\Delta\sigma_{YS}$ from lietarture [10] and ΔH_{NANO} as a function of dose in logarithmic scale with slope of both the linear fits near to ~0.25. Due to this similarity between variation of ΔH_{NANO} and $\Delta\sigma_{YS}$ due to irradiation a correlation of the form $\Delta\sigma_{YS}=\boldsymbol{K}\Delta H_{NANO}$ can be proposed. The value of $\boldsymbol{K}$ from the present work (~$324x10^{-3}$) was found to be in reasonable agreement with the literature value (~$274\ x10^{-3}$) (Figure 1b).

TEM observations of unirradiated material showed typical two phase microstructure having martensite laths along with ferrite grains in the microstructure (Figure 2a). The microstructure also revealed the presence of carbide which was captured by diffraction as well as chemical analysis in the unirradiated conditions as black spots in the TEM micrograph shown in Figure 2b. TEM investigations of irradiated samples showed also reduction in the size of the precipitates. In addition, upon irradiation presence of dislocation loops and cavity/bubble were observed in irradiated microstruture (Figure 3 (a) and (b)).

The grazing incidence X-ray diffraction line profile analysis by single peak analysis, sherrer's equation and Williamson-hall technique have provided information about the domain size as well as strain accumulation with irradiation. All the methods qualitatively predicted the

irradiation effect near the peak damage region. The X-ray diffraction line profile analysis showed that the irradiation decreases the coherent domain size formed due to self alignment of irradiation induced defect such as loops forming coherent domain boundaries. At the end of the chapter comparison of the results obtained from different characterization techniques was made. This is followed by closure of the chapter highlighting the outcome of the nanoindentation, TEM and GIXRD techniques. Also, the important microstructural features which are used in the numerical simulations are highlighted.

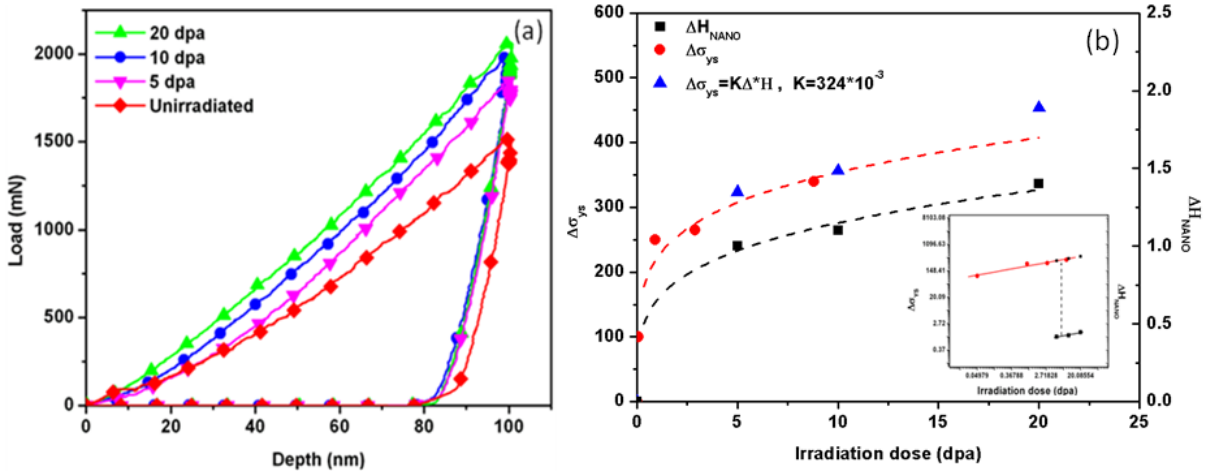

Figure 1: a) Nanoindentation load vs. depth of indentation curves for unirradiated and irradiated material and b) Estimated change in yield stress of T91 steel after irradiation

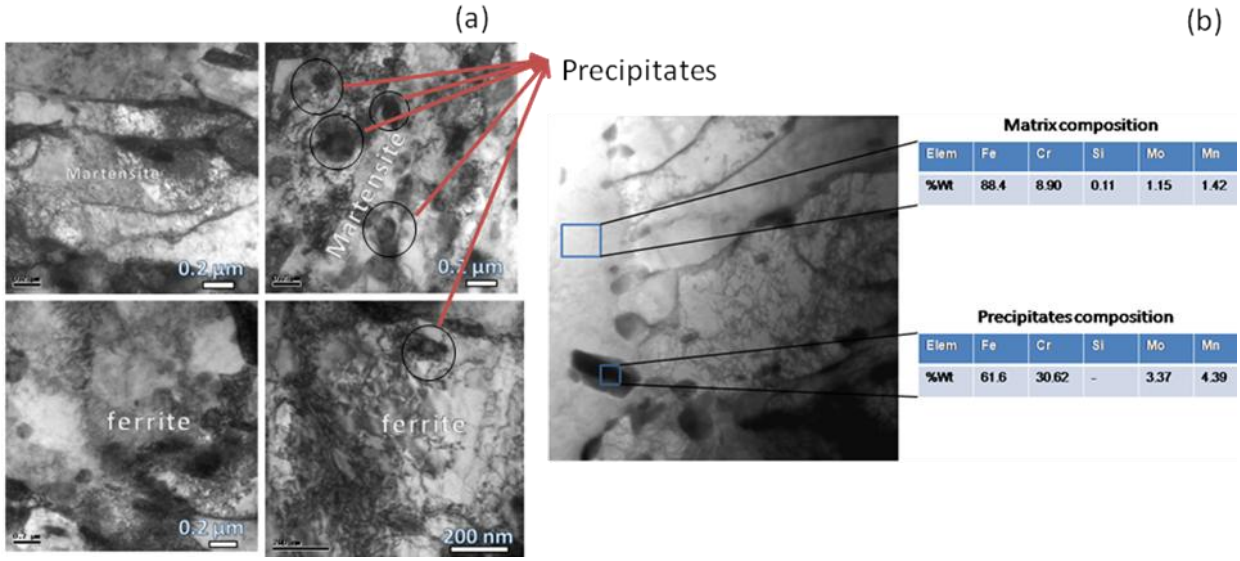

Figure 2: TEM micrographs showing a) the unirradiated microstructure and b) matrix and precipitates typical composition.

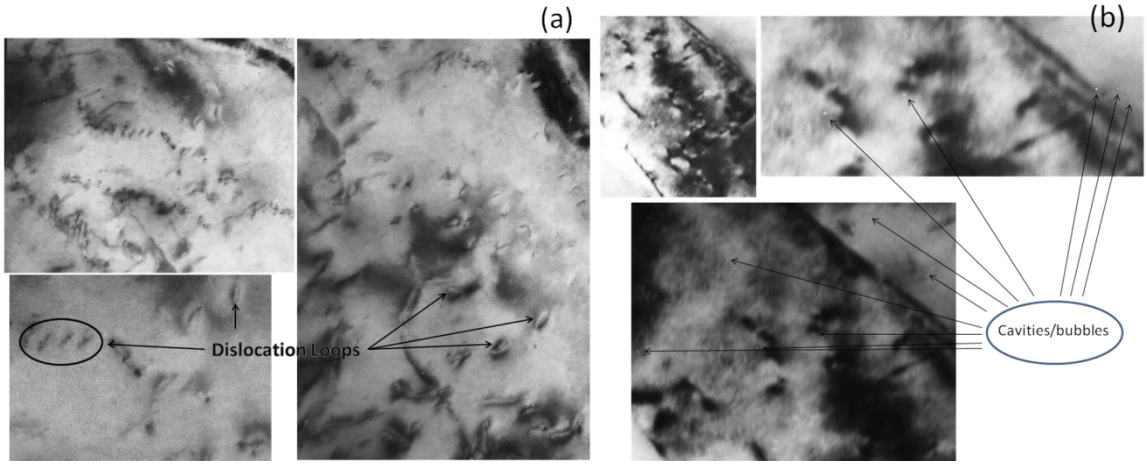

Figure 3: TEM micrographs showing a) dislocation loops and b) cavity/bubbles in T91 sample irradiated to a dose of 10 dpa.

CHAPTER 5: MOLECULAR DYNAMICS SIMULATION OF IRRADIATED MATERIAL

In this chapter introduction to molecular dynamics simulation methodology has been introduced which is followed by the computational details adopted comprising interatomic potential used, problem specific simulation domain size and their orientation are presented. The experimentally observed defect structures such as voids or bubbles or loops are systematically introduced to study the effect of irradiation on flow stress of the materials at atomic scale. Different simulations were carried out and their results at this length scale are as follows:

- Study of dislocation motion in pure iron (Fe) system, in binary Fe with 10%Cr and in ternary Fe-10%Cr containing different concentrations of helium (He) content in interstitial or substitutional position were conducted. Important output of the simulations was friction stress experienced by the dislocation during motion in pure Fe and Fe based alloy system as shown in Figure 4a & b. The study has shown that the combination of alloying element Cr and He acts as stronger obstacles to dislocation motion in comparison to binary Fe-Cr resulting in the hardening of the materials. Also the effect of substitutional or interstitial He concentration and temperature

dependence of the friction stress were studied. These results are summarized in Figure 5a-b respectively. A typical dislocation configuration in Fe-10%Cr-1%He system is as shown in Figure 6a. From Figure 6a it can be observed that the dislocation has a curvilinear shape due to solute and impurity atom interaction.

- Study of interaction of an edge dislocation with irradiation induced defects such as voids/ He bubbles/loops were carried out. An important outcome of the above simulations was the critical resolved shear stress required for the edge dislocation to overcome the periodic array of obstacles (void/bubble). Figure 6a & b shows the typical representative shear stress strain curve for the edge dislocations interacting with void and bubbles in pure Fe respectively. The alloy system also showed the similar behavior and dependence of CRSS on the different size of the obstacles. The interaction of edge dislocation with 1.6 and 2.0nm diameter dislocation loops with Berger's vector ½<111> are studied in Fe-10%Cr system only. Loops were found to be pinned by Cr atoms and its interaction with the dislocation resulted in the partial loop absorption forming a jog on the straight edge dislocation. The increases in loop size shown increase in stress to overcome the loops by dislocations.

- Irradiation induced defects present at the grains also has a significant influence on the material properties, so, effect of He bubbles on the grain boundary sliding behavior is studied in this section. It has been established and experimentally found that the dislocation intersection nodes at the low angle twist grain boundaries act as the sink and traps for the He atoms forming bubbles. Keeping this in view, molecular dynamics simulations were carried out to study the effect of these bubbles with varying diameter on the sliding behavior or shear deformation

behavior of the material. Initially the effect of strain rate and loading direction on the sliding behavior was studied. The decrease in strain rate by an order showed no significant difference in the shear stress strain curve but stress strain curve showed strong direction dependence (Figure 7a). Critical stress obtained from molecular dynamics simulations for grain boundary sliding is shown in Figure 7b as a function of interface bubble diameter. It was found that bubbles formed at GBs act as strong grain boundary sliding inhibiters if the bubble diameter is lesser than the inter-node distance of the dislocation network.

Based on these molecular dynamics simulations some of the output generated could be passed to higher length scale. A short description has been provided at the end of the chapter related to key information passed on to higher length scale. This is followed with closure of the chapter highlighting the outcome of the above three simulation categories.

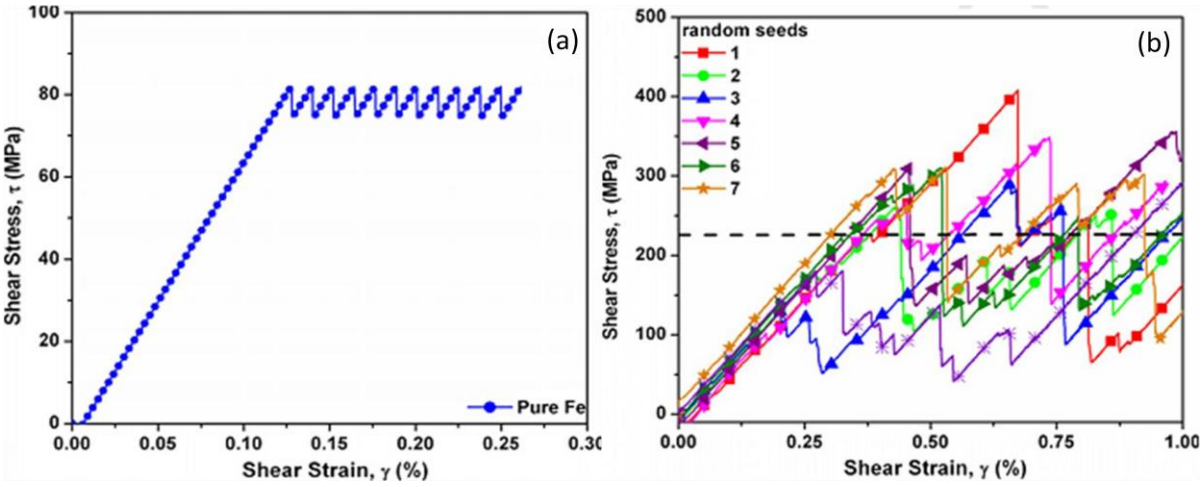

Figure 4: Shear stress strain curve for edge dislocation in a) pure Fe and b) Fe-10%Cr-1%He system

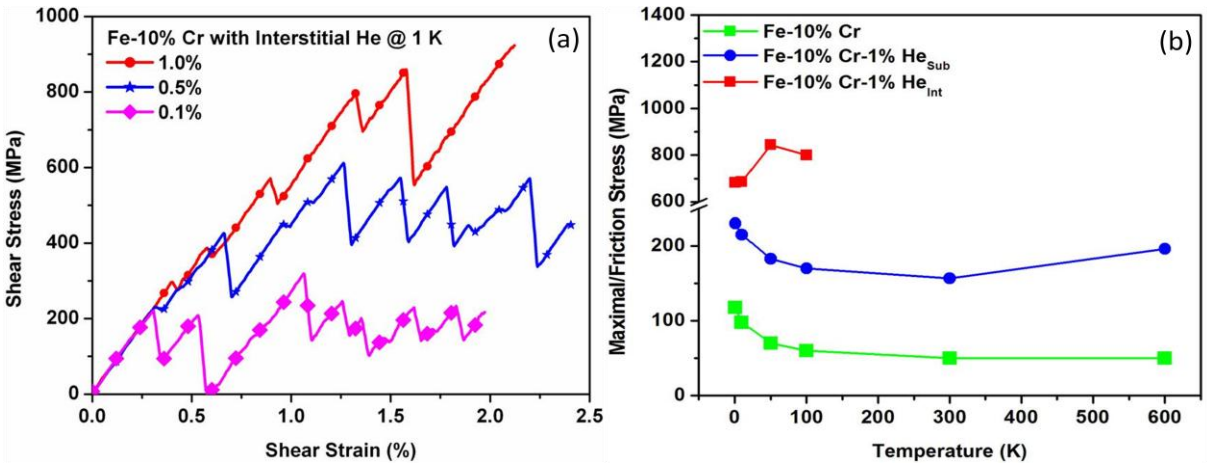

Figure 5: Variation of friction stress a) in Fe-10%Cr with varrying interastial He concentrations and b) in Fe-10%Cr with/with out He as function of temperature.

The initial linear region in Figure 4a shows the elastic behavior of pure Fe. This linear portion is followed by a region where plastic deformation of the Fe-crystal occurs by the mobility of the dislocation. The periodic drop in the values of stress, as shown in Figure 4a, is due to dislocation core movement by a distance of b/3 along x-direction, where b is the magnitude of Burger's vector. The periodic maximum and minimum values of stress on the curve are due to breaking and making of the bonds between atoms near the dislocation core. Similarly, in case of Fe with 10%Cr (Figure 4b) or 0.1-1.0%He (Figure 5a), the oscillations in the shear stress strain curves is found to be larger than that of pure Fe. This is due to the increase in the Pierel's barrier energy of the Fe system by the addition of Cr and He atoms. Cr is being slightly oversize solute atom in Fe and He is the undersized impurity atom resulting in a compressive and tensile stress field around them which is randomly distributed in the Fe matrix. These stress fields interact strongly with the dislocation stress fields resulting in the oscillations in the shear stress curves.

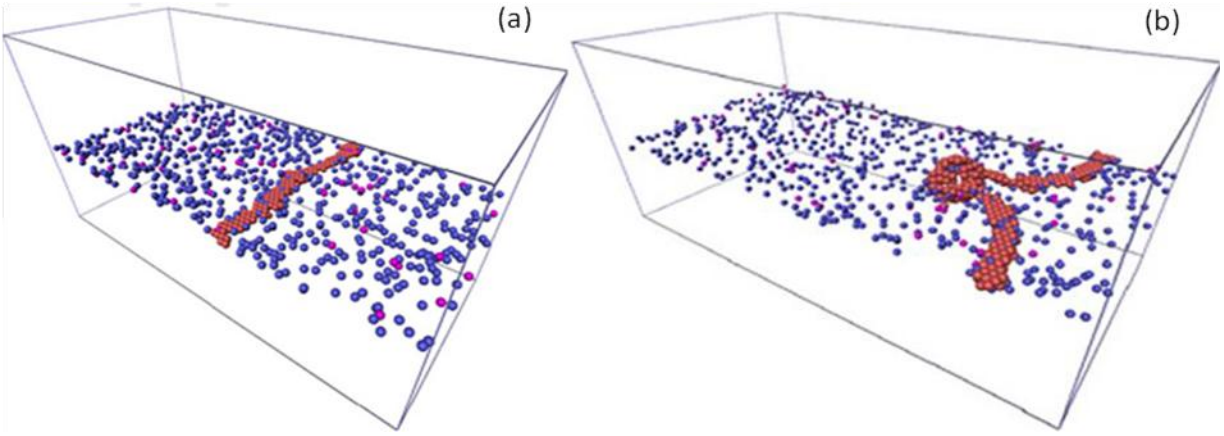

Figure 6: Typical dislocation configurations in Fe-10%Cr a) without and b) with irradiation induced defect (void)

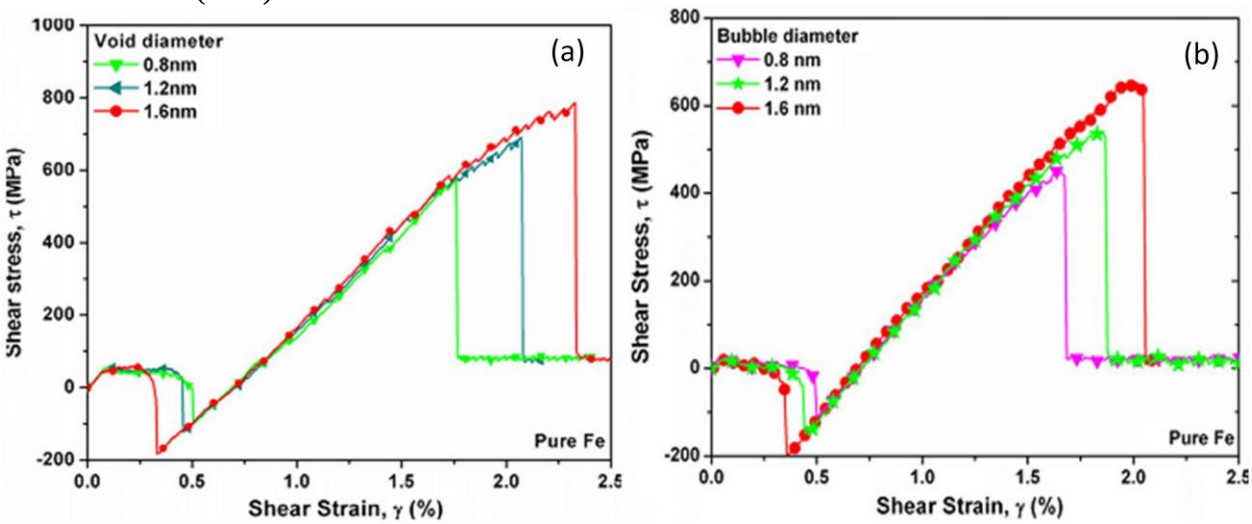

Figure 7: Typical shear stress strain curves for the edge dislocation interacting with a) voids and b) bubbles of different diameter in pure Fe

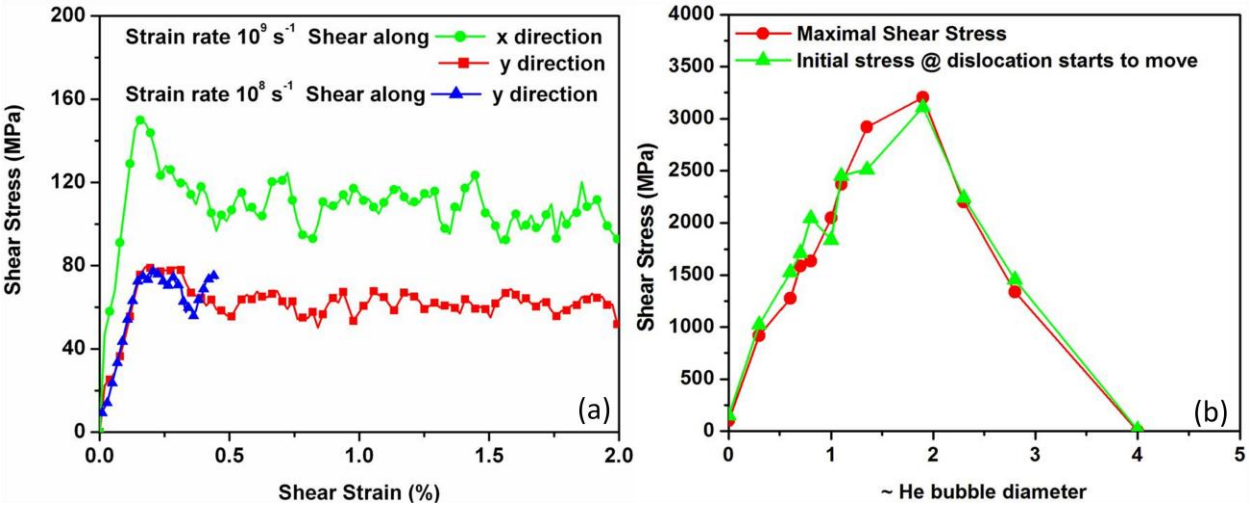

Figure 8: a) Typical shear stress strain curves for grain boundary sliding without helium bubbles and b) variation of sliding resistance as a function of helium bubble diameter.

The directional dependence of shear stress during shear deformation of low angle twist grain boundaries (GB) can be attributed to the presence of triple point junctions (point of intersection of three dislocation segments) [11] and the <100> junction segments. In case of loading along X-direction (Figure 8a), the GB dislocation network experience a friction stress for both <111> (red color) and <100> (blue color) screw segments. In case of loading along Y-direction, the GB dislocation network only experience the friction stress due for <111> (red color) screw segments and the <100> segment moves along their line direction with one dimensional motion of junction points which reduces the overall friction stress required for the dislocation network motion. Oscillations in the shear stress strain curves can be attributed to the dislocation network motion by the temperature assisted formation and disappearance of kinks and their propagation across the length of dislocation segments which assist in the dislocation motion under loading conditions

CHAPTER 6: MOLECULAR DYNAMICS SIMULATION OF NANOINDENTATION

After addressing issues related with interaction of dislocation with solute atoms, voids, bubbles, loops and GBs, attention was diverted towards generation of dislocations under the influence of external parameters and internal parameters. The external parameters like indentation load, temperature and internal parameters like irradiation induced defects (voids/bubble/loops) and their interaction. In this chapter, computational details and results obtained from explicit simulation of nanoindentation at atomic scale using Berkovich and spherical indenter were presented. Nanoindentation with Berkovich indenter was carried out to study the effect of systematically introduced irradiation defects (vacancies and loops) on load versus depth of indentation curves in Fe and Fe-10%Cr system. Figure 9a shows the typical MD setup of nanoindentation with Berkovich indenter (red color atoms) and Fe (Blue color atoms)

sample with 10% Cr (distributed green color atoms). The load displacement curves obtained from the MD simulations of nanoindentation showed remarkable similarity with that of experimentally obtained (Figure 9b). Domains with preexisting loops were generated. Such a domain represents irradiated microstructure. These domains were subjected to nanoindentation. It was found that the preexisting loops interact nearby loops forming <100> dislocation segments. The other dislocation segments nucleated and while propagating interacted with dislocation loops forming dislocation junction which are responsible for hardening of the material during deformation. Also, the dislocation microstructure generated due to indentation was analyzed in Fe and Fe-10%Cr systems to study the dislocation nucleation and different slip system activity. Simulations were carried out using two differently sized domains to study the effect of system size on the slip system activity.

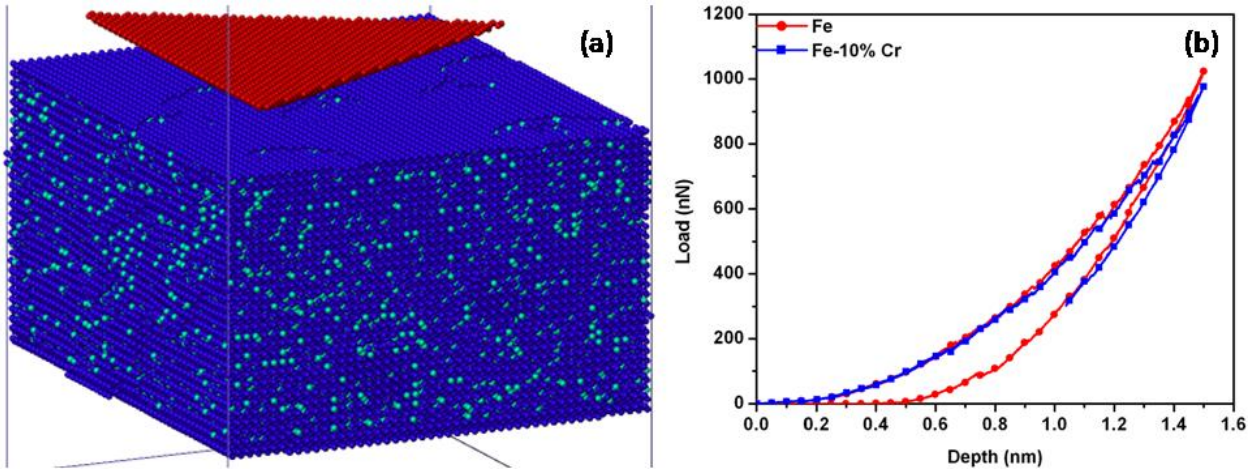

Figure 9: a) Typical MD setup of nanoindenter (red color) and sample (blue) and, b) Typical load vs. depth of indentation curves

Berkovich and spherical indenters were used to study the effect of indenter shape on the dislocation nucleation and slip system activity and dislocation density evolution in (110), (112), (123) and (100) slip planes. It was found that a significant portion of dislocation density during indentation corresponds to the (123) slip planes along with (110). The (112) and (100) slip planes had significantly lower dislocation density in comparison to other two slip planes.

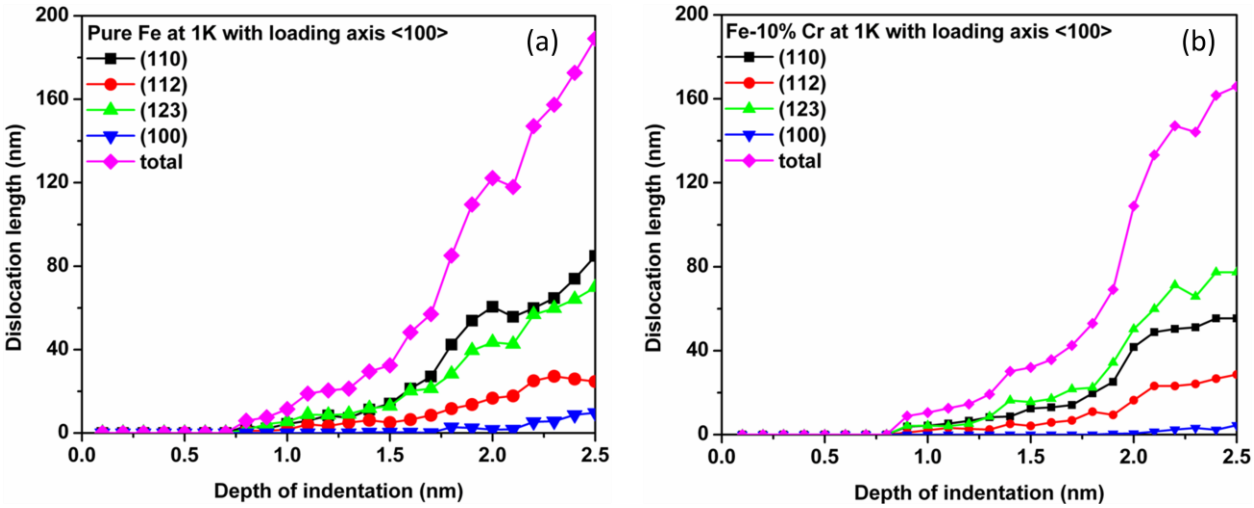

Figure 10: Dislocation evolution on different slip planes during nanoindentation using Berkovich indenter in a) Pure Fe and b) Fe-10%Cr system at 1 K temperature.

A typical dislocation density evolution curves in Fe and Fe-10%Cr system indented with Berkovich indenter with loading axis <001> is shown in Figure 10 (a) and (b) respectively. The effect of domain size, indenter shape and loading rate effects on the slip system activity were found to be negligible. Also, the dislocation line character analysis of selected case had shown no preferential presence of edge or screw dislocation at low temperature deformation,

Simulations were also carried out on the samples at room temperature (300K). At room temperature the dislocation density was reduced but the trend of the slip plane activity remained same as that of 1K simulations. The above results shows the importance of the slip systems other than (110) taking part in the deformation mechanism. Subsequently, the limitation of the simulations and important findings are discussed. Also, important findings of MD simulation of nanoindentation, which can be used in higher length scale are described and ends with a closure section highlighting the outcome of the nanoindentation simulations.

CHAPTER 7: DISCRETE DISLOCATION DYNAMICS SIMULATION OF IRRADIATED MATERIAL

After obtaining necessary parameters from MD simulations, these parameters were passed to the higher length scale. This chapter elaborates the higher length scale dislocation dynamics simulations. A short introduction to the dislocation dynamics simulations is given in the starting paragraphs, which is followed by problem specific computational details along with the inputs taken from molecular dynamics simulations have been presented along with suitable discussions to address specific issues. The dose dependence of flow stress as obtained from dislocation dynamics simulation of Fe matrix with irradiation induced He bubbles shown in Figure 11. In the absence of detailed irradiated microstructural details such as defect size distributaion, an attempt has been made to estimate the flow stress of the T91 materials based on the microstructural details available in the literature. The results are found to be in qualitative agreement with the experimental hardening behavior of irradiated materials. The quantitative prediction is found to be not possible due to the limitations such as difficulty in accounting polycrystalline nature of the materials, difficulty in accounting different defects in a single simulation, etc,. The reasons and limitations of the approach used in the present study were discussed in the succeeding section. The important outcome of the dislocation dynamics simulations was the qualitative prediction of the irradiation hardening of the material considered in the present study. This section is followed by closure of the chapter highlighting the outcome of the dislocation dynamics simulation technique.

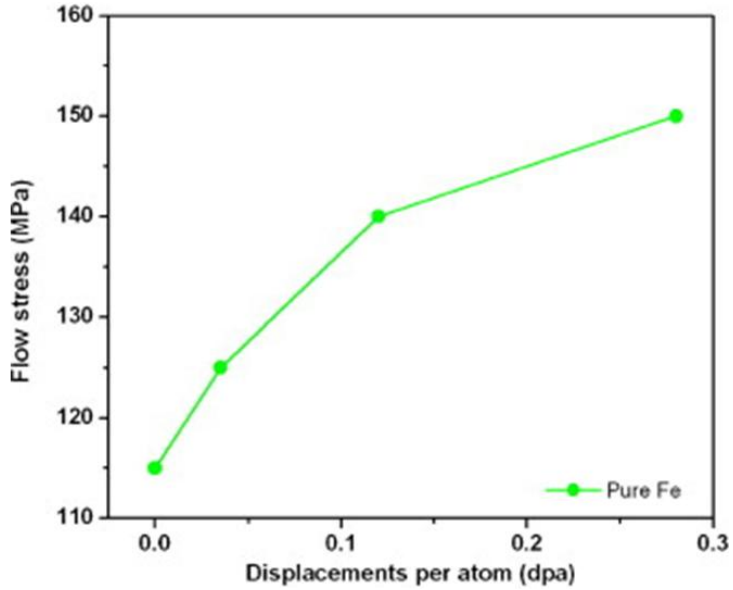

Figure 11: Flow stress variation with respect to displacements per atom (dpa) in Fe

CHAPTER 8: CONCLUSIONS & FUTURE PERSPECTIVE

The present research work deals with the mechanistic understanding of interaction of dislocation with irradiation induced defects and their effect on mechanical properties. Change in the hardness (yield strength) of the irradiated ferritic martensitic steel T91 was determined using nanoindentation. An empirical correlation of the form $\Delta\sigma_{YS}=\boldsymbol{K}\Delta H_{NANO}$ has been proposed to estimate the $\Delta\sigma_{YS}$, where $\boldsymbol{K}$ is the proportionality constant found to be in reasonable agreement with the literature data. Irradiation induced microstructural defects responsible for the property change of T91 FM steel was investigated using TEM along with different GIXRD line profile analysis techniques. TEM investigation provided the local information of defect structure whereas the line profile analysis given the global effect of irradiation induced defects in terms of micro strain of the samples and size of the coherent domain size. Microstructural details such as defect types and their size for voids, bubbles and loops are used in MD simulations to study the interaction of mobile dislocation with irradiation induced defects. The microstructural defects observed in irradiated samples using TEM has been successfully generated in atomistic

simulations. Also, the effect of irradiation induced He bubbles shown strong impedance for the GB sliding behavior. The numerical simulations of the interaction of dislocation and irradiation induced void, bubbles and loops are shown the hardening effect due to irradiation. The bridging of atomic length scale and mesoscale has been successively demonstrated. This was achieved by passing key parameters from MD to DD simulations. The DD simulations qualitatively predicted the irradiation hardening of the iron which is base material for FM steels. The existence of dislocation activity on (112) and (123) slip planes along with (110) planes have been found during MD simulations of nanoindentation on Fe and Fe-10%Cr samples which needs to be considered in the higher length scale material models. It also suggests studying the dislocation mobility on the different slip systems present and their interactions in bcc iron. Bridging the experimental and simulation part has been successfully demonstrated. All the major findings of the present work have been highlighted.

References:

1. Zinkle, S.J. and J.T. Busby, *Structural materials for fission & fusion energy.* Materials Today, 2009. 12(11): p. 12-19.
2. Was, G.S., *Fundamentals of radiation materials science-Metals and alloys*. 2007: Springer publications.
3. L. I. Ivanov, Y.M.P., *Radiation physics of metals and its applications*. 2004: Cambridge interanational science publisher.
4. Klueh, *Elevated temperature-ferritic/martensitic steels and their application to future nuclear reactors*, in *ORNL/TM-2004/176*2004, ORNL.
5. Bloom, E.E., *The challenge of developing structural materials for fusion power systems.* Journal of Nuclear Materials, 1998. 258–263, Part 1(0): p. 7-17.
6. Schäublin, R., J. Henry, and Y. Dai, *Helium and point defect accumulation: (i) microstructure and mechanical behaviour.* Comptes Rendus Physique, 2008. 9(3–4): p. 389-400.
7. Wirth, B.D., et al., *Mechanical property degradation in irradiated materials: A multiscale modeling approach.* Nuclear Instruments and Methods in Physics Research Section B: Beam Interactions with Materials and Atoms, 2001. 180(1–4): p. 23-31.
8. Bacon, D.J. and Y.N. Osetsky, *Multiscale modelling of radiation damage in metals: from defect generation to material properties.* Materials Science and Engineering: A, 2004. 365(1–2): p. 46-56.
9. Samaras, M., M. Victoria, and W. Hoffelner, *Advanced materials modelling – E.U. perspectives.* Journal of Nuclear Materials, 2009. 392(2): p. 286-291.
10. S.A. Maloy, M.R. James, G. Willcutt, W.F. Sommer, M. Sokolov, L.L. Snead, M.L. Hamilton, F. Garner, Journal of Nuclear Materials, 296 (2001) p. 119.
11. V. V. Bulatov and Wei Cai, *Physical review letters*, Vol. 89, Num. 11. (2002) 115501.

LIST OF FIGURES

Figure 4.17: Change in hardness (GPa) and change in yield strength versus irradiation dose.(inset figure log ($\Delta\sigma_{YS}$) vs. log (dpa) for change in experimental change in YS (MPa) [51] and log (ΔH_{nano}) vs. log (dpa) for change in hardness determined present work).

Figure 5.1: Schematic diagram showing the upper half crystal (filled circles) with N (=16) and lower half crystal (open circles) with N-1(=15) planes.

Figure 5.2: (a) Schematic diagram showing the two crystals rotated about $< 110 >$ direction to form the twist GB and (b) Hexagonal dislocation structure formed by low angle (θ=±2) twist GB.

Figure 5.3: Shear stress strain curve corresponding to edge dislocation motion in pure Fe system (region A and B corresponding to elastic and plastic deformation).

Figure 5.4: Initial edge dislocation configuration in pure Fe system (red and blue color atoms corresponding to dislocation core region and perfect lattice).

Figure 5.5: Shear stress strain curve corresponding to edge dislocation motion in Fe-10%Cr system with different random seed (different color curves corresponds to different random number seeds used for Cr distribution).

Figure 5.6: Initial edge dislocation configuration in Fe-10%Cr system (blue color atoms corresponds to Fe atoms near core region and red color atoms corresponding to Cr atoms present on the slip plane).

Figure 5.7: Shear stress strain curve corresponding to edge dislocation motion in Fe-10%Cr system at different temperatures.

Figure 5.8: Temperature dependence of maximal/friction stress in Fe-10%Cr system (saturation of friction stress to lower stress values as temperature increase).

Figure 5.9: Shear stress strain curve corresponding to edge dislocation motion in Fe-10%Cr-1%He system with different random seed.

Figure 5.10: Initial edge dislocation configuration in Fe-10%Cr-1%He system (red color atoms corresponds to Fe atoms near dislocation core region and blue/magenta color atoms corresponding to Cr/He atoms present on the slip plane).

Figure 5.11: Shear stress strain curve corresponding to edge dislocation motion in Fe-10%Cr system with different temperatures.

Figure 5.12: Dependence of maximal/friction stress of an edge dislocation on temperature in Fe-10% Cr system with 0.1, 0.5 and 1.0% He in substitutional position.

Figure 5.13: Dependence of maximal/friction stress of an edge dislocation on substitutional He content in Fe-10% Cr system at different temperatures.

Figure 5.14: Shear stress strain curves for edge dislocation motion in Fe-10%Cr with 0.1%,

0.5% and 0.5%He in interstitial position at 1K.

Figure 5.15: Dependence of maximal/friction stress of an edge dislocation on temperature in Fe-10% Cr system with 0.1, 0.5 and 1.0% He in interstitial position.

Figure 5.16: Dependence of maximal/friction stress of an edge dislocation on interstitial He content in Fe-10% Cr system at different temperatures.

Figure 5.17: Isolated interstitial atoms at (a) 1K and (b) 100K in Fe-10%Cr with 0.5% interstitial atoms (red color dots-Fe atoms at dislocation core region, blue color dots-Cr atoms and yellow color dots-interstitial He atoms).

Figure 5.18: Fraction of He atoms present on {110} slip plane at a distance in Fe-10%cr sample as a function of temperature for 0.5% interstiatial He atoms (He atoms are more attracted toward the tensile region of dislocation core than that of compression region).

Figure 5.19: Curvilinear shape of the edge dislocation (red color curve) and interstitial He (beed like structure) in Fe-10%Cr as extracted using DXA tool.

Figure 5.20: Comparison of variation of maximal/friction stress for an edge dislocation in Fe-10%cr with 1% substitutional and interstitial helium with respect to temperature.

Figure 5.21: Shear stress strain curve for edge dislocation interacting with irradiation induced/produced voids of diameter 0.8, 1.2 and 1.6 nm in pure Fe (region A-initial dislocation motion, region B-attraction of dislocation by void and region C-increase in stress due to pinning of ED by void and sudden drop in stress due to unpinning from void).

Figure 5.22: Dependence of critical resolved shear strength of edged dislocation on void diameter in pure Fe.

Figure 5.23: (a) Initial and (b) bowed out dislocation configuration of edge dislocation in pure Fe (red color and blue color corresponds to dislocation core region and perfect lattice atoms).

Figure 5.24: The snapshots showing the jog formation on edge dislocation while releasing from the void. (a) (b) initial, (c) (d) before release and (d) (e) after release (blue color line-dislocation, yellow color sphere-void, yellow color small sphere vacancy).

Figure 5.25: Shear stress strain curve for edge dislocation interacting with irradiation induced/produced voids of diameter 0.8, 1.2 and 1.6 nm in Fe-10%Cr.

Figure 5.26: Dislocation configuration before release from the void of diameter (a) (b) 0.8nm in Fe (blue), Fe-10%Cr (green) and (c) (d) 1.6nm in Fe (green), Fe-10%Cr (brown).

Figure 5.27: Shear stress strain curve for edge dislocation interacting with irradiation induced/produced voids of diameter 0.8, 1.2 and 1.6 nm in Fe-10%Cr-1%He.

Figure 5.28: (a) Initial and (b) bowed out dislocation configuration of edge dislocation interacting with a void of 1.6 nm diameters in Fe-10%Cr-1%He (red, blue and magenta color

LIST OF TABLES

CHAPTER 1: INTRODUCTION

1.1 Background

The proposed Generation-IV (Gen-IV) and fusion reactor concepts have common features like high operating temperatures (500-1000^{o} C) and high level of irradiation doses (~100 dpa) [1–7]. Figure 1.1 compares these features in the proposed Gen-IV reactors like Very High Temperature Reactor (VHTR), Super Critical Water Reactor (SCWR), Gas cooled Fast Reactor (GFR), Lead Cooled Fast Reactor (LFR), Molten Salt Reactor (MSR), Sodium Cooled Fast Reactor (SFR) and the fusion reactors [6]. High levels of irradiation doses are largely due to the fast neutrons produced during fission or fusion reactions in the respective reactors. High energy neutrons produced due to nuclear reactions interact with the materials used in the reactor core and degrade their properties. The degradation in the properties of these materials is due to the changes in the microstructure of the material caused by the formation of point defects, point defect clusters (voids, loops and stacking fault tetrahedra-SFT), helium bubbles and segregation of alloying/impurity elements (precipitates and secondary phases) [8, 9]. These changes in microstructure due to irradiation lead to hardening, embrittlement, an increase in the ductile to brittle transition temperature (DBTT) and a decrease in fracture toughness [10]. Materials used in nuclear reactors also undergo transmutation reactions, producing insoluble gaseous atoms such as hydrogen (H) and helium (He) [8]. These gases have limited or no solubility in the structural materials leading to the formation of bubbles. The formation of bubbles is a temperature dependent phenomenon. At elevated temperatures, fission/fusion generated atoms of gases segregate at grain boundaries (GBs) and form bubbles which reduce the GB strength and induce high temperature embrittlement [2, 8, 10]. At low temperatures, most of the bubbles form within grains causing low temperature hardening. The amount of He produced in the fusion reactors is

found to be 10-15 appm/dpa [11] and in Gen IV reactors it is 3-10 appm [2]. In short, the basic microstructural features involved in the changes of the property of materials are dislocations, irradiation induced defect structure, grain boundaries and their mutual interaction.

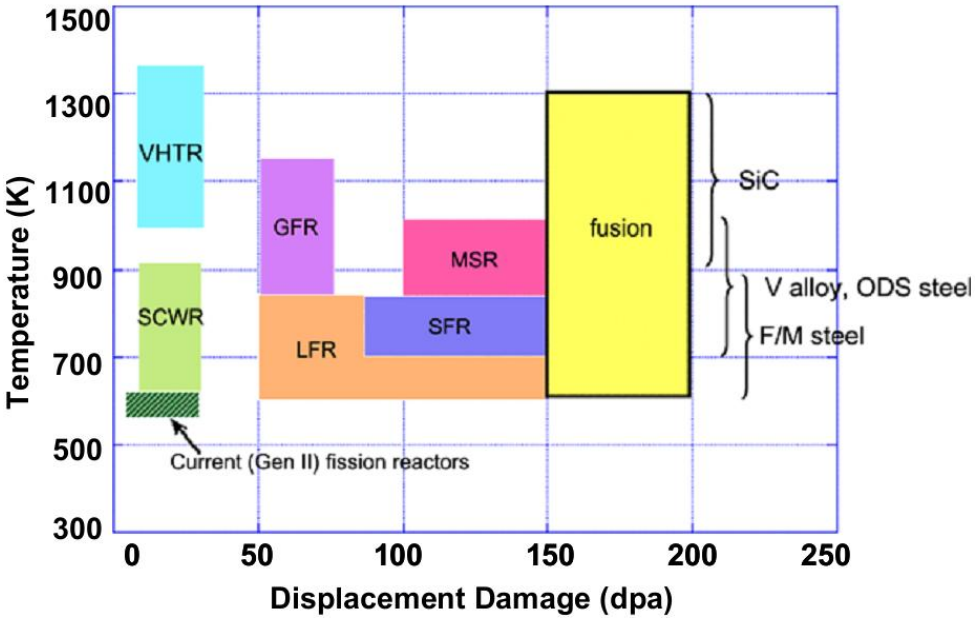

Figure 1.1: Operating conditions for core structural materials in different power reactors (Very High Temperature Reactor (VHTR), Super Critical Water Reactor (SCWR), Gas cooled Fast Reactor (GFR), Lead Cooled Fast Reactor (LFR), Molten Salt Reactor (MSR), Sodium Cooled Fast Reactor (SFR) and the fusion reactors) [6].

The safety considerations of the Gen-IV reactors require a complete understanding of materials behavior for the entire range of operating conditions. Even though a considerable amount of experimental work has been carried out in the last four decades, the basic mechanisms of radiation damage, the associated microstructural changes and their effect on mechanical properties are not completely understood. This is mainly due to the following two reasons; (i) the evolution of radiation damage covers a wide range of length and time scale phenomena, which are amenable to observation during experiments, and (ii) the limited availability of irradiated material volume along with the difficulties associated with handling radioactive samples. Even

though a number of experimental techniques exist to determine the mechanical properties of the materials (e.g. Tensile tests, creep tests, fracture tests etc.) using standard samples, due to the limitation imposed by radioactivity, experimental data from standard size samples covering diversified irradiation conditions (irradiation temperature, irradiation particles, particles energy, flux, fluence, etc,.) and experimental conditions (test temperatures, loading rate etc,) are scattered in nature. To overcome this difficulty, the reactor materials community developed new testing techniques using the available small amount of irradiated material which are known as small specimen testing techniques [12–16].

Essentially the idea behind using all these experimental techniques is that the changes in the properties of the materials due to irradiation can be estimated by studying defect properties, type of defects, their sizes, distribution and their mutual interactions under different irradiation and loading conditions. However, an explicit evaluation of the irradiation induced defects and micro-structural phenomena are difficult to achieve using only (conventional and non-standard or small-scale) experiments. This is because the process of property change due to material damage occurring from the interaction of energetic particles, defect production, diffusion, agglomeration, mutual interaction and its manifestation at the macro scale covers a wide range of length and time scale phenomena [17, 18].

To overcome the limitations of experiments and to understand the phenomena occurring in the different length and time scales a new methodology has been developed by the nuclear community. In this methodology, the fundamental scale is ab-initio or electronic structure calculations where Schrödinger wave equations describing the motion of electrons around an atom are solved to get the point defect properties, elastic constants and potential energy function.

These ab-initio calculations are computationally intensive, need a lot of computational time and few hundreds to few thousands of atoms can only be modeled at a time. Due to these limitations, ab-initio calculations are not suitable tools to model the real test samples, which consist of Avogadro number of ($\sim 10^{23}$) atoms. The output of these ab-initio calculations, in particular the potential energy function, is used as input for molecular dynamics (MD). The molecular dynamics method is relatively less accurate than ab-initio calculations since electronic interactions are replaced by approximate radially isotropic potential energy functions. At MD scale, the atoms are treated as point particles governed by Newton's equation of motion neglecting the presence of electrons. The force on each atom having certain mass is evaluated by considering the force exerted by the neighboring atoms, which are at a distance less than that of some specified cutoff radius from a considered atom. The number of atoms used in this scale till date is $\sim 10^{9}$ which is still far lower than the Avogadro number. This length scale, however, is found to be suitable for the study of isolated defect properties or a pair of defects interacting with each other. The output from MD scale such as dislocation mobility, friction stress etc., are used as input to a higher length scale such as dislocation dynamics (DD) scale. In DD calculations, the collective behavior of defects and their mutual interactions are studied. Here dislocations are modeled explicitly based on the elasticity theory without considering the intrinsic atomistic nature surrounding the defect core. This scale can handle few grains of micron size in a time scale of nanoseconds to microseconds. Single crystal deformation properties such as slip system hardening, flow stress, dislocation evolution etc., can be evaluated at this scale. The output of DD scale is used in crystal plasticity or finite element based crystal plasticity formulations, which can handle testing of polycrystalline samples, used in conventional testing procedure. It can cover a length scale of microns to millimeter and a time scale of few seconds to years. The

properties usually found to be extracted are load displacement curves, stress strain curves etc. The stress strain curves thus obtained act as input to continuum scale component level analysis, fracture studies and structural integrity analysis extending over a time scale of years. This methodology of using different length scales is known as Multi-scale Material Modeling (MMM) approach [19] comprising all the length and time scales as shown in Figure 1.2. MMM is a hierarchical modeling technique dependent on passing key parameters involved in the radiation damage process and considered deformation mechanism to connect the two successive or overlapping length and time scales (Figure 1.2). MMM is a developing field where the effect of microstructure and its evolution on macroscopic material properties can be determined reliably. The various steps of collision-recombination-relaxation-defect migration-clustering-nucleation-growth-interaction, etc., start to occur from picoseconds and extend over the years [17]. Experimentally it is not possible to observe these competing processes in real-time and only inferences could be drawn by examining the post irradiation resultant static microstructures. In this regard MMM technique helps us to look inside the materials at small scale as low as fraction of a micron.

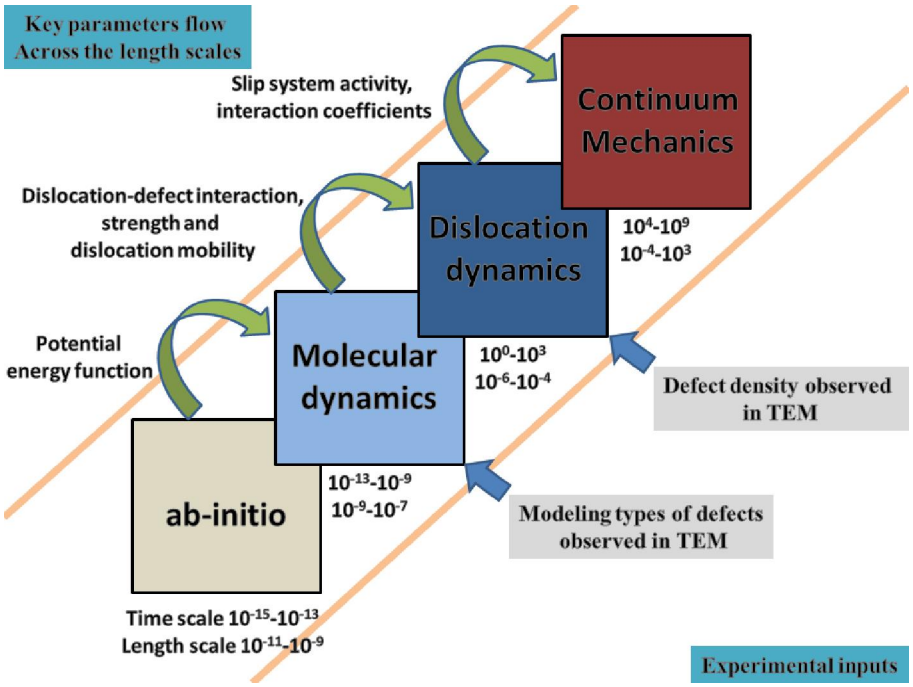

Figure 1.2: Schematic diagram showing multi-scale material modeling stages with key parameters taken as input/output in different stages.

There is a lack of studies coordinating experiments and characterization techniques with numerical simulations. Such a coordinated research work will help in better understanding, developing and validating, the material models, which subsequently can be used to predict the behavior of materials under irradiation conditions where the generation of experimental data is extremely difficult. MMM provides a solution where by analyzing the data from MMM methodology gives the understanding of the underlying mechanisms. The final validations of the estimated or predicted results can be done by experiments designed by "numerical simulations".

Ferritic martensitic (FM) steels are the candidate structural materials in the future fusion and next generation fission reactors [20–22]. The main attractive properties of these materials are very low volumetric swelling, high radiation & high temperature tolerance and low DBTT shift [10, 20] in comparison to other family of steels and materials. Change in the properties of these

materials is found to be within the acceptable limits even at operating temperature of 500 ^{0}C and a dose level > 100 dpa. The newly developed FM steels, also called Reduced or Low activation FM steels (R/LAFMS) due to the absence of long lived radionuclide's formed under transmutation reactions, contain such alloying elements which reduce the activity of these steels to an acceptable level within about 100 years as compared to the thousands of conventional structural steels [23]. Calculations have shown that V, W and Ta presented much better radiological properties in comparison to some alloying elements like Co, Cu, N, Ni. Hence these elements have been excluded from the steel composition while Nb and Mo are replaced by W, V and Ta [24]. FM steels have emerged as promising structural materials for next Gen-IV and fusion reactors due to their lower cost compared to other materials and the technical maturity achieved in all aspects of their fabrication and processing. Even though the FM steels are radiation swelling resistant and possess good fracture toughness up to a temperature of 550^{0}C, they suffer from loss of ductility during low temperature irradiation (<300^{0}C).

1.2 Motivation

The estimation of mechanical strength of a material and its degradation from fundamental levels, atomistic to meso to macro scale, is a long-standing challenge for the nuclear materials community. The inherently complex microstructures of FM steels and their evolution during irradiation restrict the detailed analysis of the microscopic deformation phenomena from experimental as well as from simulation point of view. Development of radiation tolerant FM steels and prediction of their degradation is only possible if an improved understanding of the defects generated due to high radiation doses, their relative concentrations at different fluences and the effect of temperature on the irradiated microstructures as well as the changes in the properties of these materials could be attained. Till date, though many efforts have been made to

understand the effect of irradiation on the properties of materials, most of these efforts have been confined either to experiments and characterization or to simulation techniques leaving a gap between the predicted and observed behavior of FM steels. Also, the data available on irradiated FM steels in each category is scattered in nature due to different experimental and simulation conditions used by different scientists [25]. In addition, several attempts have been made to predict neutron damage of FM steels by using ion irradiation. This makes simulation-based predictions of neutron damage of FM steels deviate even more from the observed behavior.

It is, therefore, necessary to examine the ion irradiation comprehensively. Such an examination would require complementary approaches: MMM simulations accompanied by experimental irradiations, followed by characterization of the damaged zone using multiple techniques. Ions of inert gases like helium and argon are most suitable for the irradiation as they do not lead to any chemical interactions. However, the damage generated by these ions is localized to surface and near surface regions. The characterization techniques used for evaluating the damaged material should complement each other in producing reliable information on such localized regions. Calibration of the MMM models using such information would ultimately lead to models and their inputs being reliable enough to predict material properties for radiation doses beyond the domain of available data.

1.3 Objectives

The objectives of the present work are as follows:

1. One of the major aims of the present study is to generate irradiated microstructures by irradiation using Argon ions under controlled conditions on FM steel (T91).

2. The irradiated material volume being highly localized, a combination of novel characterization tools suitable to examine such small volumes is required. For this purpose three techniques, namely, grazing incidence X-ray diffraction, nanoindentation and transmission electron microscopy have been selected. The main aim of combining these experimental tools is to obtain depth sensitive global information, to observe the irradiation defects directly and to evaluate the variation in the mechanical response of the material due to irradiation-induced damage. The information provided by these techniques has been simulated by multi-scale modeling.

3. In order to simulate defects generated by argon ion irradiation, two length scales, namely, molecular dynamics and dislocation dynamics of MMM methodology have been selected. The essential aim of selecting these simulations is that they provide suitable length scale to study the irradiated volume generated by argon ions. In order to carry out detailed MD simulations the first set simulations have been done to demonstrate the effect of alloying addition in bcc iron. Subsequently these simulations have been attempted on a combination of alloying additions and impurities. The aim of such a study is to demonstrate the effect of Cr, the main alloying element in T91 FM steel and transmutation produced impurity like He and obtain necessary friction stress required to simulate dislocation motion.

4. After obtaining the information about the dislocation motion and their interaction with impurities of unirradiated materials, MD simulations have been carried out by systematically introducing observable irradiation induced defects. In order to complete the study of irradiation-induced defects, the sliding behavior of grain boundaries in the presence of irradiation induced He bubbles has been studied. The main aim of this study is to determine

the increase in critical resolved shear stresses (CRSS) due to the presence of irradiation induced defects in the matrix as well as at grain boundaries.

5. The value of friction stress and CRSS obtained from MD simulations has been used as input for dislocation dynamics simulations: a higher length scale model. DD simulations have been used to study the collective behavior of dislocations with randomly distributed defects and to determine the increase in flow stress of the material due to Ar ion irradiation.

6. In order to simulate the behavior of irradiation-induced defects on the load versus depth of indentation curves, MD simulations of nanoindentation have been carried out on domains with systematically introducing irradiation-induced defects. In order to study the nucleation and evolution of dislocations, dislocation density and slip plane activity during nanoindentation, nanometer scale analysis of numerically simulated microstructure has been carried out. The main aim of this study is to isolate irradiation-induced defects and study their effect on the load versus depth of indentation curves.

1.4 Organization of the thesis

This thesis is organized into eight chapters. In chapter 2, a review of the current status of the subject area comprising irradiation damage, variation in properties and degradation of properties along with the MD and DD simulations as found in the literature is presented. Chapter 3 describes the experimental and characterization techniques used in the present study and optimization of experimental parameters for nanoindentation and GIXRD measurements. In chapter 4, the results obtained from nanoindentation, TEM and GIXRD techniques have been presented. In chapter 5, the computational details and input parameters adopted for MD simulation along with the results obtained from these simulations on dislocation motion,

dislocation-obstacle interactions in Fe and Fe-Cr with or without He (He present at substitutional and interstitial positions) are presented. This chapter also includes results obtained from the study of deformation behavior of the low angle twist grain boundary with and without irradiation induced He bubbles at the interface. Chapter 6 describes the computational details and results obtained from MD simulation of nanoindentation, Chapter 7 describes the computational method and details adopted and results obtained from dislocation dynamics simulations of collective behavior of dislocations in Fe, Fe-Cr and Fe-Cr-He systems with and without irradiation-induced obstacles. Finally, Chapter 8 provides summary and conclusions of the present study. In addition, future scopes for further studies are also listed in this chapter.

CHAPTER 2: LITERATURE REVIEW

2.1 Introduction

The response of a material to irradiation damage depends on both material as well as irradiation parameters. Material parameters are crystal structure, grain size, alloying elements present, defect structures introduced by irradiation, nature of bond etc. Irradiation parameters comprise type of irradiation, energy of the particles, irradiation fluence or flux and irradiation temperature at which material is irradiated. In literature, many irradiation studies have been reported for neutrons, protons, heavy ions and electrons. Ideally, all irradiation studies should involve neutrons only. However, experiments involving neutrons are very time consuming. Due to space constraints in a research reactor, it is difficult to irradiate full length standard samples. In addition, handling of radioactive samples needs special arrangements. It is, therefore, attempted to simulate neutron damage by ion irradiation. The high energy particle irradiation in accelerators allows the easy variation of irradiation parameters (volume of irradiation, depth of damage, energy of the particles, dose required etc.). The damage induced by the particle accelerators using heavy or light ions (electrons and protons) results in no activation of the materials for a given temperature and fluence. In addition, it is easy in an ion irradiation experiment to isolate a variable and preferentially induce one kind of defect. Therefore, irradiation in an accelerator is a good substitute to study the behavior of materials by simulating the operating conditions of a nuclear reactor [26].

2.2 Material properties, microstructure and irradiation effects

2.2.1 General desirable properties of the reactor materials

The *table 2.1* summarizes some of the important properties required by materials used in the future nuclear reactors. Intrinsically all the materials have their own advantages and disadvantages, like materials having fcc crystal structure are highly ductile in nature, materials with hcp crystal structure are relatively less ductile and highly anisotropic in nature. Properties of the materials having a bcc crystal structure fall in between these two cases. In the presence of high flux irradiation, the high temperature mechanical properties of materials are altered considerably. For example, in materials with bcc crystal structure it has been found that the irradiation increases the ductile to brittle transition temperature (DBTT), reduces creep resistance at high temperature and induces hardening and embrittlement. In materials having fcc or hcp crystal structure variations in these properties due to high irradiation doses are relatively moderate. However, in these alloys high irradiation doses induce unacceptable swelling and growth. In short, all the above materials have common features, like an increase in yield strength, ultimate strength, and decrease in ductility.

Table 2.1: Desirable properties of nuclear structural materials [27].

Physical	High melting point, low density, dimensional stability, adequate thermal conductivity and low coefficient of thermal expansion
Mechanical	Adequate high temperature tensile strength, impact strength, fatigue strength and ductility, low ductile- brittle transition temperature, good creep resistance at reactor operating temperature, resistance to thermal shock and thermal fatigue.
Chemical	Good corrosion resistance for cooling medium at reactor operating temperature and low pick up for transmuted gaseous atoms.
Nuclear	Resistance to irradiation creep, growth and swelling, resistance to irradiation hardening and embrittlement, no harmful transmutation of atoms by radiation.
Metallurgical	Thermal and irradiation stability of the microstructure against irradiation-enhanced creep, irradiation growth and swelling, no irradiation induced phase transformation.

2.2.2 *Irradiation damage*

High energy particles generated due to fission and fusion reactions collide with the lattice atoms of the core and structural materials of a nuclear reactor. In this process they lose their kinetic energies partially or fully to lattice atoms until they come to rest by losing all their energy or escape from the materials. The first atom, which is displaced from its lattice position by these high energy particles, is commonly addressed as *Primary Knock-on Atom* (PKA). In this process, a pair of self-interstitial atom and a lattice vacancy known as Frenkel pairs are produced. PKAs with appreciable kinetic energy subsequently displace other neighboring atoms which are known as Secondary Knock-on Atom (SKA), Tertiary Knock-on Atom (TKA), etc. Figure 2.1 shows the different level knock on atoms based on binary collision approximation. This process continues until all the knock-on atoms come to rest. This process of energy transfer from one atom to another generates cascades.

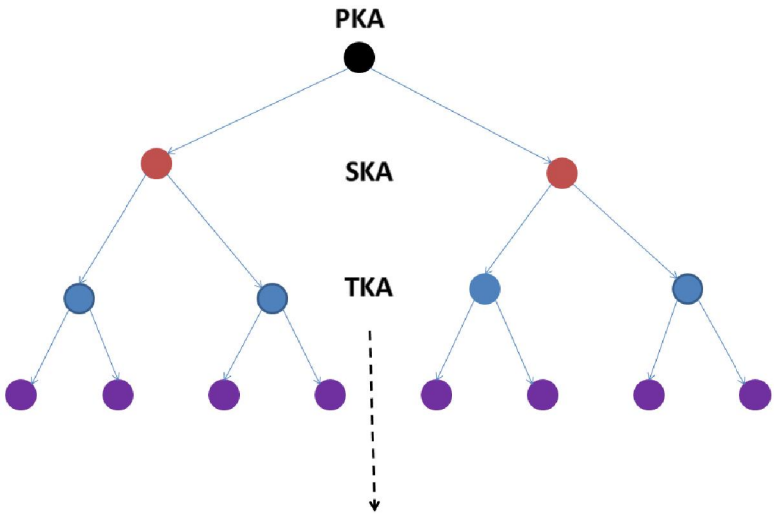

Figure 2.1: Schematic representation of different levels of atomic displacements during a cascade.

The energy transfer to lattice atoms is a function of type of particles, energy of the particles and the nature of target materials. The effect of this cascade results in displaced atoms

which reside at interstitial positions (self interstitials) and empty lattice positions (vacancies). This process completes in a time scale of few femtoseconds and defects generated in a cascade require a few picoseconds to stabilize. At the end of this process a vacancy rich central and an interstitial rich shell regions are formed [18]. These defects take a few nanoseconds (~10^{-9}s) to a few months (~10^{6}s) to escape from the cascade regions and become bulk mobile defects. These bulk mobile defects during diffusion may interact with the other alloying or impurity elements present in the materials resulting in a change of the initial microstructures. Changes in the microstructures during the lifetime of a nuclear reactor (~10^{8} s) become substantial [18]. These events on a time-scale are schematically shown in Figure 2.2. Broadly, these diffusing defects are divided into two categories. First type are the isolated point defects like, vacancies, interstitials which have high mobility in the matrix and second type are defect-clusters which may or may not be mobile in nature. Interaction of these defect-clusters or isolated defects with other preexisting second phase particles, dislocation network, grain boundaries or with themselves form extended defects such as voids, bubbles, loops or precipitates [28]. Figure 2.3 shows the schematic representation of defects observed in the irradiated materials.

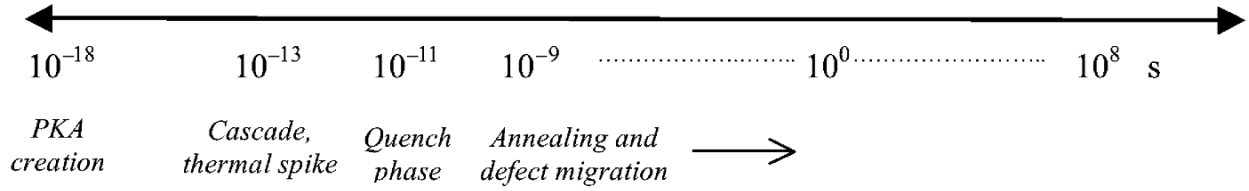

Figure 2.2: Schematic diagram showing the time scales involved in the radiation damage [28].

Clustering of point defects forms extended defects such as loops (two dimensional defects), voids or SFT (three dimensional defects). Vacancies and interstitials cluster in configurations which are decided by minimum energy criterion. The formation of voids occurs if the number of vacancies in a cluster is lower than a threshold value whereas loops are favored

when the number of vacancies is higher than the threshold value. It has been found that in materials with bcc and fcc crystal structures, voids are favored over loops due to lower formation energy needed for the former defect [29]. Loops are found to be metastable defect clusters with respect to voids and have a tendency to transform into voids with the absorption of additional vacancies with time. The tendency of transformation of loops into void increases with increase in temperature. In the case of hcp materials, SFTs are more stable defects in comparison to voids and loops. Loops are formed by the condensation of vacancies or interstitial on densely packed planes (i.e., on {110} planes of bcc, on {111} planes of fcc materials). Imperfect or frank or faulted loops form by condensation of interstitials or vacancies in form of platelets. These faulted loops are found unstable as they absorb or emit point defects to achieve more stable configurations. For example, a perfect glissile dislocation loop configuration can be achieved by the rotation of imperfect loops to <111> loops in the case of bcc structures and <110> in the case of fcc structures [29].

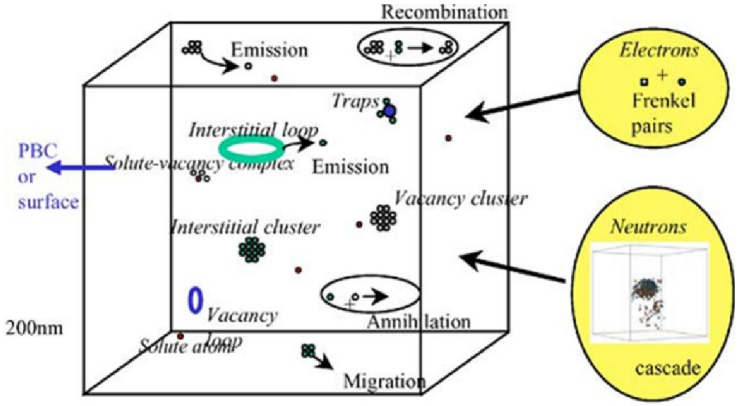

Figure 2.3: Schematic representation of defects observed in the irradiated materials [30].

In general, it has been found that at lower irradiation temperatures (<350^{0}C) maximum fraction of defects observed were dislocation loops. In this temperature range the size and density of the dislocation loops increase with increase in irradiation dose and irradiation

temperature [31-33]. Dai et al. [32] found that the density and size of the defect clusters increases with irradiation dose in three FM steels namely DIN1.4926, F82H and Optimax-A irradiated at temperature < 230^0C using 800MeV protons up to 6dpa. At higher temperature (693-743K) the size and number density of dislocation loops has been found to decrease with increasing irradiation temperature for Japanese low activation FM steel for 60 dpa dose [33]. The density of dislocation loops was reported to saturate above a dose level of 10 dpa in cold worked 316 steel for a given dose rate and irradiation temperature. The density of loops was found to vary from 10^{20} to 10^{23} per m^3 in a dose range of 1 to 10 dpa. It has been also found that the presence of alloying elements effect the formation of loops. For example, metallic materials have shown that the density of loops increases and diameter decreases with increase in solute atoms like chromium [23].

Void formation is an interesting phenomenon since, maximum void swelling is observed in intermediate temperature range. This temperature range generally falls between $0.3T_m < T < 0.5T_m$, where T_m is melting temperature in K and most of the reactors operate at this temperature. In the case of voids, it has been found that the number density of voids decreases with increase in irradiation temperature whereas diameter of the void increases with temperature [28]. At low temperatures, vacancy defects are not sufficiently mobile to diffuse and they cluster together to form cavities. At higher temperatures ($T \geq 0.5T_m$), the density of voids remains low as thermodynamically the material can accommodate higher concentration of vacancies. In this temperature range voids anneal out by the process of vacancy emission. The typical dose dependence of swelling is shown in Figure 2.4.

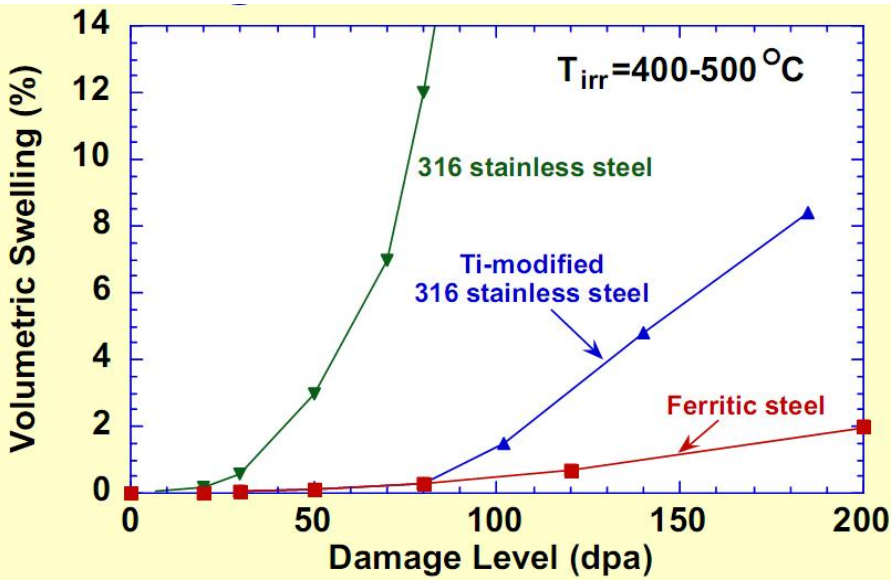

Figure 2.4: Dose dependence of volumetric swelling in austenitic and ferritic steels[34]. Ferritic steels are found to have good swelling resistance as compared to austenitic stainless steels irradiated at 400-500^{0}C.

Swelling behavior by a material typically shows two distinct regions. Initially, swelling rates increase slowly with the increase of irradiation dose. This region is commonly referred to as incubation period. Beyond the incubation period, swelling rate increases with a moderate rate rapidly reaching a terminal swelling rate. The terminal swelling rate attained in austenitic stainless steels is roughly 1%/dpa. For ferritic martensitic steels, the terminal swelling rates are roughly 0.2%/dpa [35]. For example, irradiation induced swelling in 20% cold worked austenitic stainless steel (316) is shown in Figure 2.5. The void swelling is also affected by the presence of alloying elements Cr, B, Ti, etc. For example, the addition of Boron enhances the void selling, where as the addition of Ti suppresses. It has been also found that the decrease in Cr concentration also decrease the void swelling [11, 38]. Swelling is highest for a particular material at a specific dose when the transient period is shortest. Transient period is the time after incubation period, which is dominated by void nucleation of critical size required for the stable

void growth. The developments of swelling resistant materials therefore, aim for increasing this transient period. Swelling is also influenced by the rate with which the radiation damage occurs [28]. Those samples irradiated at a lower irradiation rate exhibited short-term transient time and thus higher swelling at any specific dose. The terminal swelling rate for ferritic-martensitic steels is, in general, smaller than for austenitic stainless steels. The increased number of point defect sinks reduces the point defects available to an individual void and thus reduce swelling. For this reason, ferritic-martensitic steels are now the principal choice for high dose components.

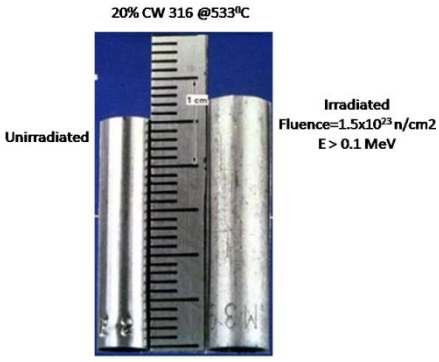

Figure 2.5: Irradiation void swelling of 20% cold worked (CW) austenitic stainless steel 316 [34].

Helium is produced in the structural materials of nuclear reactors by transmutation reaction caused by neutron interactions. Due to their insolubility He atoms cluster together to form bubbles. It is found that even two He atoms sharing a vacancy is a stable configuration and may act as a nucleation site for bubbles [28]. The kinetics of He bubble formation is high due to the high mobility of He through interstitial diffusion. At low temperatures ($< 0.3T_m$), He atoms have been found to form high density of small bubbles (> 1nm) in the presence of ~500 appm He concentration [31]. With increase in the temperature, the smaller size bubbles are consumed and the average size of He bubbles increases with reduction in bubble density. Also at intermediate and at elevated temperatures, segregation of He at GBs may stabilize cavities or voids present at GBs. Growth of He stabilized cavities results in swelling or void induced growth in materials

[36]. In a FM steel - F82H- it has been also found that the increase in the He content increases the swelling from 0.1% (10appm) to 1.1% (330appm) at 400^0C [37]. He bubbles with He to vacancy ratio ≥ 2 are found to plastically deform the surrounding matrix and emit a plane of self-interstitial atoms forming a dislocation loop which is known as loop punching. This mechanism of loop punching was proposed by Greenwood et al. [38], Evans et al. [39], Trinkaus et al. [40] for noble gases in metals. Recently, this loop punching process has been simulated by Hafez et al. [41] using MD simulations.

Degradation of the properties is found to be even more severe when insoluble gaseous atoms of hydrogen and helium generated by transmutation reaction are present along with other irradiation-induced defects [7, 46-48]. It has been observed that the presence of a small amount of He stabilizes very small size of point defect clusters and otherwise energetically unfavorable bubbles at low irradiation temperatures [36]. This induces low temperature hardening in structural materials. At elevated temperatures, segregation of He at GBs reduces GB strength resulting in the high temperature grain boundary embrittlement [42][49-51]. Irradiation hardening, therefore, has a strong temperature dependence and it is more severe at low temperatures [25].

Precipitates or secondary phase particles form under normal thermo-mechanical processing conditions. Some of the precipitates are purposefully introduced to increase the strength of the material without or slightly reducing its ductility (for example, chromium carbide particles in steels). However, other secondary particles like sigma phase, χ phase, laves phase etc., have been found to be detrimental to mechanical properties [52, 53]. Under irradiation conditions, increased concentration of point defects and their preferential motion with solute or

impurity elements results in the segregation of the respective atoms at sinks such as GBs or dislocations [54, 55]. In general, if the sink density is greater than the recombination site density, segregation of solute atoms occurs. The segregation is also affected by the solute solubility at the given irradiation temperature. In case the bulk concentration is lower than the solute solubility limit, no segregation occurs in that irradiation temperature [23]. The presence of the other solute elements also affects the precipitate by stabilization or destabilization of the precipitates [43]. TEM observations have shown that the dislocations and GBs act as nucleation sites for precipitates. It is also reported that irradiation affects the pre-existing precipitates and phases in one of the following ways; i) by changing the chemical composition of the precipitates, ii) by coarsening of the precipitates or iii) by amorphization of the precipitates [34, 55, 57]. The continued irradiation also affects the precipitates or phases formed during irradiation depending on the irradiation dose, dose rate, temperature and particle type and its energy [45]. The effects of these phases and/or precipitates and their composition on the mechanical properties of the materials are still unknown [23].

2.2.3 Effect of irradiation temperature on mechanical properties of the materials

Effect of irradiation can be grouped into three temperature regimes (*Table 2.2*), in which different microstructural features and mechanisms play the dominant role in material property degradation.

Table 2.2: Different irradiation temperature regimes

Temperature regime	Temperature Range	Dominant Irradiation effects	Microstructural features
Low	$T \leq 0.3$ Tm ($T < 300\ ^0$C)	Hardening and embrittlement.	Pinning of mobile dislocations by in cascade point defect clusters (loops/cavities).
Intermediate	0.3 Tm $< T \leq 0.5$ Tm ($300\ ^0$C $< T \leq 600^0$ C)	Swelling, irradiation induced phase transformation.	Increased concentration of point defects and their diffusivity results in segregation/precipitation of alloying/impurity elements and point defects near sinks. Growth of gaseous atom stabilized voids.
High	$T > 0.5$ Tm ($T > 600\ ^0$C)	Increased creep deformation and He induced GB embrittlement.	Increased dislocation climb probability, Stabilization of cavities by helium and formation of array of bubbles at GBs.

At low irradiation temperatures ($T < 300^0$C) the maximum fraction of the defects produced comprises dislocation loops along with small point defect clusters which appear as black dots under TEM [11, 20, 34, 52, 55, 59–61]. The loops were found to be with Burgers vector 1/2<111>. Some of the irradiation studies have shown the presence of <100> loops [35, 52]. The 1/2<111> dislocation loops are found to interact with each other forming the <100> type loops which are usually observed in steels with low Cr content [50]. Dislocation loops and point defect clusters lying on the slip plane of mobile dislocations act as obstacles to dislocation motion. The mobile dislocations are pinned to these defects and need higher stresses to continue their motion on their slip planes. This increase in stress for dislocations to overcome irradiation-induced defects appears as an increase in the YS of the materials. Some of the irradiation studies carried out in spallation sources have shown the presence of small He bubbles of size < 1.5nm with high number density which have been found to be responsible for the low temperature

hardening [20]. Figure 2.6 shows typical tensile stress strain curves of irradiated austenitic stainless steel (316L) and ferritic martensitic steel (T91).

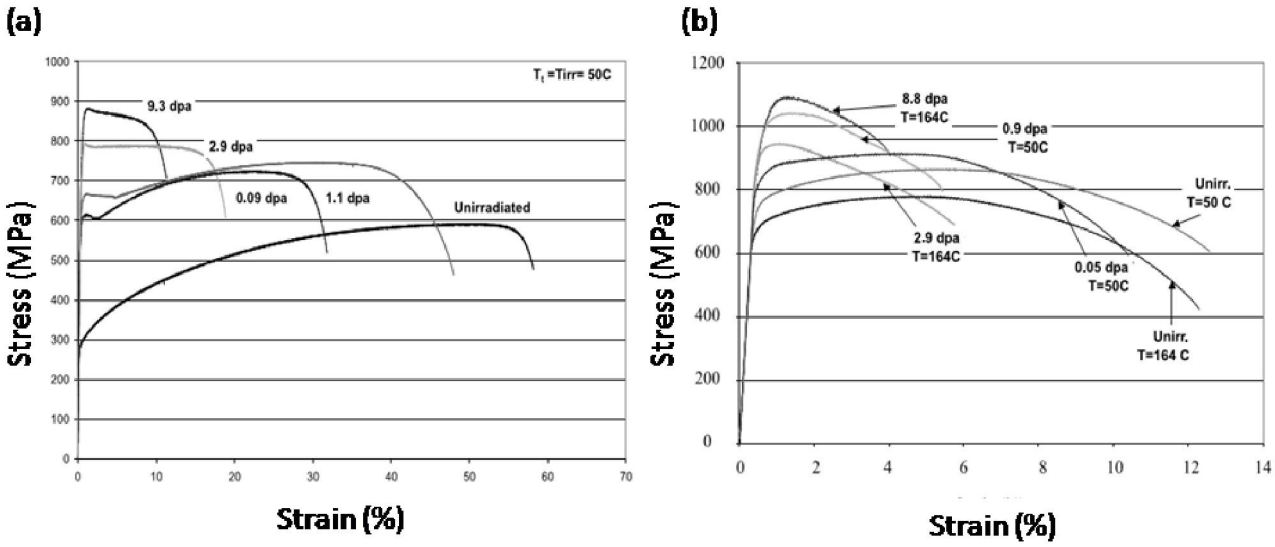

Figure 2.6: Typical stress strain curves of a) fcc and b) bcc materials before and after irradiation [51]. Increase in yield stress and changes in other stress strain curve properties due to irradiation in a typical fcc and bcc materials can be observed from the figure.

In this temperature region, at higher irradiation doses, YS reaches closer to ultimate tensile stress (UTS) with or without appreciable elongation [32]. This effect is essentially due to strain localization by the formation of dislocation channels [55, 64]. In dislocation channel deformation, defect free bands form due to absorption or shearing of defects by dislocations. Hardening (in terms of increase in YS) due to irradiation was found to saturate depending on the irradiation temperature (T_{irr}), testing temperature (T_{test}) and prior heat treatment conditions [25, 28, 33,65, 66]. In addition, when irradiation and testing temperatures are same, highest hardening is observed in this temperature region. For the condition $T_{test} > T_{irr}$ hardening decreases in the low temperature regime [49].

At intermediate temperatures ($300\ ^0C < T \leq 600^0$ C) irradiation hardening reduces considerably [25, 67]. In this temperature range density of dislocation loops is found to be lower

than the density of loops observed in the low temperature region. But most of dislocation loops in the intermediate temperature region are accompanied by the radiation induced segregation of small secondary phase particles which also take part in the hardening of the materials [33]. The presence of He has been found to enhance the irradiation hardening in this temperature region [9, 35, 65, 68]. Helium bubbles have been found to prefer pre-existing dislocations [56] and pin these dislocations and thereby increase the hardening effect in this temperature range. Irradiation studies at intermediate temperature region have shown that the defect density decreases and size of defects increases resulting in overall decrease in yield stress and increase in ductility.

In the high temperature region (T > 600 ^{0}C), due to high mobility of dislocations and higher probability for dislocation climb the effect of irradiation hardening is nearly neutralized. With increased diffusivity of point defects, chances of recombination increases resulting in reduction of the density of the irradiation induced defects. In this temperature region, cavities are stabilized because of absorption of helium by cavities. Formation of array of bubbles at GBs has been observed in samples irradiated in this temperature range. Due to this effect, high temperature grain boundary embrittlement has been observed.

Different hardening models were used in the literature to estimate the increase in YS due to dislocation obstacle interaction. The two barrier hardening models which are extensively used to estimate the irradiation hardening in materials with bcc or fcc crystal structure are, Dispersed Barrier Hardening (DBH) [57] model and Fridel-Kroupa-Hirsch (FKH) hardening model [71, 72]. DBH and FKH models are mainly used to estimate the hardening due to strong and weak obstacle respectively. These models relate the change in yield strength due to the presence of

defect clusters to their size (d), density (ρ), Burgers vector magnitude (b) and shear modulus (μ) of the given material by following Eqs. (2.1a) and (2.1b);

$$\Delta\sigma = M\alpha\mu b\sqrt{d\rho} \tag{2.1a}$$

$$\Delta\sigma = \frac{1}{8}M\mu b\left(d\rho\right)^{\frac{2}{3}} \tag{2.1b}$$

where M is Taylor factor and α is characteristic strength for the given obstacle type at a given temperature. Empirically the Taylor factor is determined to be 3.06 for materials having fcc and bcc crystal structures [59]. The strength coefficient α depending on the obstacle type can take the value from 0 to 1. The value of α with < 0.25 suitably represents the small irradiation induced defects which are intrinsically weak. Earlier experiments [60] have shown that the hardening due to these weak obstacles can be adequately represented by FKH model. The obstacles with α between 0.25 to 1.0 represent strong obstacles in the materials. The hardening due to these strong obstacles is estimated by DBH model [61].

In literature DBH model has been extensively used to estimate the increase in irradiation hardening of RAFM steels due to irradiation induced defects such as loops, cavities, bubbles and precipitates [28, 35, 54, 55, 58, 76]. Chaouadi et al. [55] have made an attempt to correlate the change in yield stress as a function of dpa considering the presence of He. It has been shown that the hardening due to neutrons, protons and implantation studies are different. Garner et al. [63] have estimated the YS of AISI 316 steel using detailed microstructural data before and after irradiation and substituting the relevant parameters in Eq.(2.1a-b). The equation is used for the calculation of changes in YS due to long and short range interaction of dislocations and irradiation induced defects respectively. It was concluded that the saturation behavior of the YS is the reflection of saturation of all the microstructural components (irradiation-induced defects).

Some of the irradiation studies on RAFM steels have shown that DBH model underestimated the change in YS due to the absence of complete microstructural details [52, 55, 58, 76].

The shift in the DBTT of FM steels after irradiation is another important concern. Ferritic martensitic and RAFM steels suffer more severely from increased DBTT shift upon irradiation as compared to other materials. It was found that the RAFM steels with 9-10% Cr have minimum DBTT shift as compared to steels containing Cr out of 9-10% composition range (Figure 2.7) [64]. Therefore, most of the irradiation studies of FM steels are confined to 9-10% Cr steels. Other than the Cr, the replacement of Mo by W and Nb by Ta also found to reduce the DBTT shift of RAFM steels [65]. Similar to YS, shift in DBTT has also shown saturation behavior [53] and this shift can be correlated with decrease in ductility and increase in YS [66]. The shift in DBTT of RAFM steel is maximum when steel is irradiated in the low temperature regime and is negligible in intermediate temperature regime [67]. Therefore, shift in DBTT is inversely proportional to irradiation temperature. It was observed that the shift in DBTT is also affected by initial heat treatment conditions during fabrication process [9]. The pre-existing and radiation induced inter-metallic brittle phases such as sigma, chi, Laves etc., and their coarsening at GBs are also found responsible for the increased DBTT shift with brittle fracture in RAFM or 9%Cr steels [68]. At higher temperature regime some of the studies have shown the presence of He bubbles at GBs in the form of array and preferential association of bubbles with precipitates or dislocations [69]. The presence of He in RAFM steels showed a significant increase in DBTT [68]. Also, presence of He in RAFM steel showed inter-granular fracture with GB weakening [11]. All of these results related to He effects on mechanical properties indicate the possible He effects but not the exact phenomena which will occur in a fusion neutron irradiation environment.

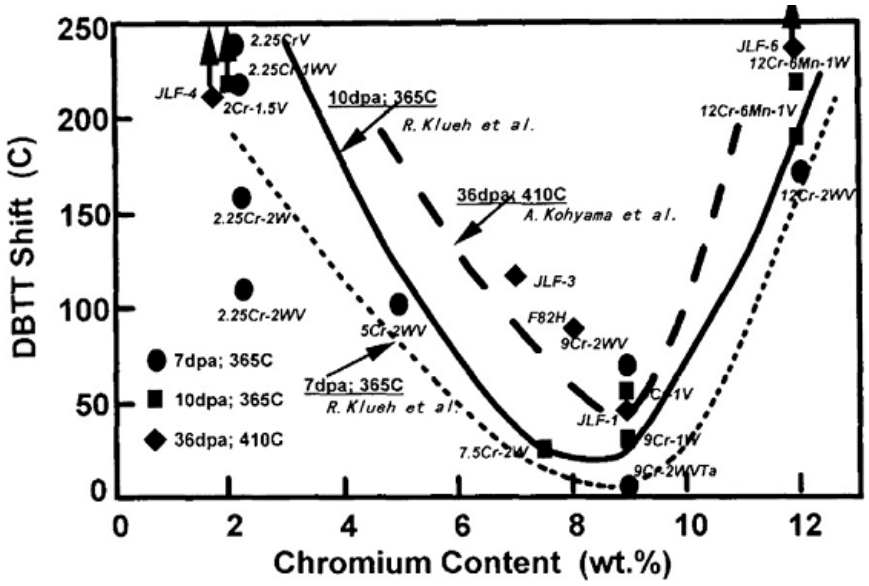

Figure 2.7: Effect of Cr concentration on DBTT shift [64]. Steels containing 8-10 wt% Cr showed least shift in DBTT.

2.3 Ion irradiation

Main objective of ion irradiation in accelerators is to provide an alternate route to study radiation damage process. If damage created by ions has similarities with the neutron damage, it can be used to study materials behavior under reactor operating conditions. This will help in determining changes in mechanical properties of the materials under extreme operating as well as accidental conditions to evaluate the integrity and safety operation of the reactors. Main advantages of ion irradiation are that irradiation experiments can be conducted under controlled temperature, dose rate and total dose. These conditions are difficult to achieve in nuclear reactors due to fluctuations in the operating conditions. Ion irradiated samples are nearly non-radioactive and can be handled easily. In an ion irradiation experiment, experimental variables can be isolated and their effect on microstructure and mechanical properties can be studied.

The ion irradiation could be broadly classified as, heavy ion and light ion irradiations. Heavy ions usually used are Ni, Fe, O, Ar etc., and light ions are H, He, electrons. The main

challenge of the ion irradiations is to imitate the neutron damage. For this reason specific condition of ion irradiations in the accelerator is to be experimentally determined [28]. Each type of ion irradiation has its own advantages and disadvantages with respect to neutrons as given in Table 2.3.

Table 2.3: Different irradiating particles, their advantages and disadvantages over neutrons [28].

Particles	Advantages	Disadvantages
Protons	Accelerated dose rate – moderate irradiation times Modest ΔT required Good depth of penetration Flat damage profile over tens of μ m	Minor sample activation Smaller, widely separated cascades No transmutation
Electrons	Relatively "simple" source – TEM Uses standard TEM sample High dose rate – short irradiation times	Energy limited to ~1 MeV No cascades Very high beam current (high dpa rate) requires high temperature Poor control of sample temperature Strong "Gaussian" shape (non uniform intensity profile) of beam No transmutation
Heavy ions	High dose rate – short irradiation times High T_{avg} Cascade production	Very limited depth of penetration Strongly peaked damage profile Very high beam current (high dpa rate) Requires high temperature No transmutation Potential for composition changes at high dose via implanted ion

Protons being equivalent in mass to neutrons carry many advantages. Protons of few MeV energy can achieve the high depth of penetration and flat damage profile up to few tens of microns. The dose rate is found to be 2 to 3 orders of magnitude lower than that for electrons or ions. This requires a modest shift in irradiation temperature to get a modest dose in a short irradiation time. The cascade regions produced by protons are found to be widely spaced & less dense than that of neutrons. One of the major limitations of using protons is that with energy above 5 or 6 MeV they can easily cross the coulomb barrier of target material atoms resulting in sample activation.

The electron irradiation experiments, on the other hand, are easy to conduct as these experiments can be carried out in a high voltage TEM and the same can be used to investigate the irradiation damage. Also high energy electron accelerators can be used for the irradiation experiments. High dose rates can be achieved during a short irradiation time with increased irradiation temperature shift. Main limitation of the high voltage electron irradiation using TEM is that the electrons with energy exceeding 1MeV will result in widely spaced Frenkel pair than cascades in transition metals. Controlling of temperature is difficult during high dose irradiations in a typical TEM sample stage [28]. The irradiations are often conducted on thin foils and therefore, defects created in close proximity to the surface may anneal out to the surface. Also the Gaussian shape of electron beam can give rise to strong dose rate gradients across the irradiated region.

Heavy ions can be used for high doses with high dose rates in a short irradiation time. Heavy ions are limited by short depth of penetration and the damage varies continuously across the depth of penetration. In addition, the low diffusivity of the heavy ions causes them to remain concentrated within a narrow range from the irradiated surface. Heavy ions have a potential to create higher damage than the light ions and thereby reduces the experimental time requirement for a given dose. An extensive study of irradiation damage caused by heavy ions has been reported in literature [45]. Majority of the defects produced by heavy ions are similar to the defects produced by neutrons, these simulation studies provide important insight into the nature of the displacement damage produced [28]. The individual irradiation parameter that affects the microstructure can be studied by controlled heavy ion irradiations. For example, defects induced by neutron irradiation, such as voids, swelling, dislocations loops, etc., can be selectively

induced by selecting the appropriate ions for irradiation [70]. Plenty of work has been reported in literature using He, Ar and Fe ion irradiation [45]. In the present study Ar ions are used for irradiation of FM steels due to the following reasons; i) Ar being a noble gas it is insoluble in Fe (similar to He) ii) shorter time of experiment required for the target damage as compared to protons or He ions and also mimics the He production due to transmutation reactions in next generation nuclear reactors and iii) availability of stable beam of Ar ions. In the present study, effect of Ar ion irradiation on microstructural changes and hardening behavior of FM steels is examined.

In short, a major drawback of ion irradiation is the low depth of penetration leading to the exposure of small volume of irradiation as compared to the volume generated by neutron irradiation in reactors. Many times, the defects generated by ions are not of similar nature as those generated by neutrons making interpretation difficult [28, 47].

2.4 Experimental technique: Nanoindentation (NI)

Nanoindentation is an indispensible tool for mechanical property measurements at small length scale with advanced analysis methods [71]. In nanoindentation, load and depth are continuously measured during the loading and unloading of the indenter. This overcomes the requirement to image the impression to extract the hardness from the indentation load and depth. The other properties such as the elastic modulus can also be extracted from the load versus depth of indentation data. A typical load versus depth of indentation curve is shown in Figure 2.8 for a complete cycle of loading and unloading. In order to analyze the indentation data the most commonly used methods are based on the problem of a rigid punch indenting an elastic half space. Sneddon [72] established an analytical procedure to show that for any axi-symmetric

indenter geometry, the relationship between the applied load P and the elastic displacement *h* may be expressed as

$$P = \alpha h^m \tag{2.2}$$

Where α is a constant and m is an exponent that was found to be m = 1 for flat cylinders, m = 1.5 for paraboloids and m = 2 for cones.

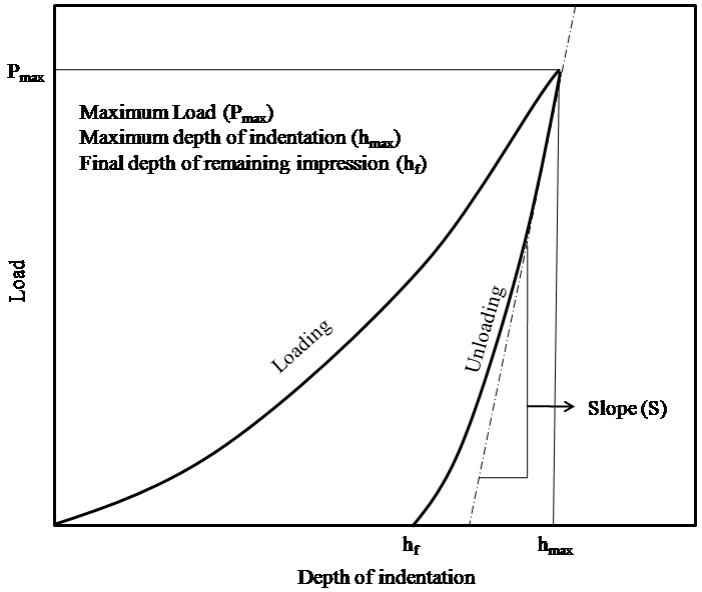

Figure 2.8: Schematic Nanoindentation load versus depth of indentation curve showing loading and unloading part along with stiffness estimation using slope of initial unloading part.

According to the elastic contact theory [73], from the unloading stiffness, *S*, and the projected contact area, *A*, obtained from load vs. depth of indentation curves can be used to calculate the elastic modulus of a material indented by a conical indenter through the equation

$$S = \frac{dp}{dh} = \frac{2}{\sqrt{\pi}} \beta E_r \sqrt{A} \tag{2.3}$$

with β=1. The reduced modulus E_r accounts for the finite stiffness of the indenter according to

$$\frac{1}{E_r} = \frac{\left(1-\nu^2\right)}{E} + \frac{\left(1-\nu_i^{\,2}\right)}{E_i} \tag{2.4}$$

where E and v are the elastic modulus and the Poisson's ratio of the material, respectively, and E_i and v_i are the same parameters for the indenter. While Eq. (2.3) was originally derived for a conical indenter, it has been established that it holds equally well with $\beta = 1$ for indenter tip geometry generated by revolution of any smooth function. The Berkovich indenter is the most commonly used indenter shape for nanoindentation, which is having a pyramidal shape (three-sided) with a total included angle of 142.3°. In order to extract the hardness and elastic modulus from nanoindentation load vs. depth of indentation curve a comprehensive method has been developed by Doerner and Nix [74]. In their method, initial part of the unloading curve is assumed linear based on the observations made on selected metals during nanoindentation. This implies a constant contact area during unloading, as would be the case for a flat-ended punch. Fitting a straight line to the upper portion of the unloading curve, the unloading stiffness (S) can be easily calculated. Nanoindentation carried out by Oliver and Pharr [71] on materials having different hardness showed that the initial unloading behavior for Berkovich indenters is adequately described by a power-law relationship analogous to Eq. (2.2):

$$P = \alpha(h - h_f)^m \tag{2.5}$$

where h_f is the final depth of the remaining impression and the parameters α, h_f and m are obtained by fitting to the entire unloading curve. The variation in the exponent m was found in the range of 1.25 to 1.51 for different materials. The derivative of Eq. (2.5) evaluated at $h = h_{max}$ gives the unloading stiffness S at peak load. Eq. (2.3) subsequently relates the elastic modulus E_r to this stiffness and the projected contact area A at peak load.

Area function $A(h)$ relates the indenter cross-sectional area with that of distance from indenter tip end h, which is required in order to calculate the projected contact area. An ideal

Berkovich indenter has a square area function of $A(h) = 24.5xh^2$. In practice blunting of tip due to repeated usage leads to smaller deviations in the ideal area function, which is usually accounted by the following approximation:

$$A(h) = a^0 h_2 + a^1 h_1 + a^2 h^{\frac{1}{2}} + a^3 h^{\frac{1}{4}} + a^4 h^{\frac{1}{8}} + \cdots\cdots \quad (2.6)$$

In order to evaluate the coefficients a^n through calibration isotropic material with known mechanical properties are used. From the calibrated area function, the effective end radius of the tip may be estimated by defining the equivalent radius $r = \sqrt{\frac{A}{\pi}}$, writing $h(r)$ as a function of r and numerically evaluating d^2h/dr^2 at r=0.

Figure 2.9 shows a cross section of an indented surface under load and after load removal, illustrating that elastic recovery takes place only in the depth direction of the applied load and the radius of the impression remains constant as mentioned before. The total displacement that any time during the indentation cycle can be written as $h = h_c + h_s$, where h_c is the depth along which contact is made (the contact depth) and h_s is the displacement of the surface at the perimeter of the contact. Using Sneddon's expression [72] for the surface profile outside the area of contact, Oliver and Pharr [71] obtained the following expression for the contact depth h_c at peak load P_{max}:

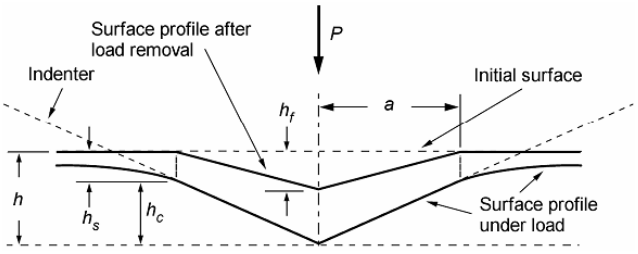

Figure 2.9: Schematically represented indented surface geometry of sample at peak load and after removal of the load.

$$h_c = h_{\max} - \varepsilon \frac{P_{\max}}{S} \tag{2.7}$$

where ε is a parameter that depends on the indenter geometry, ε assumes a value of 0.75 for a Berkovich indenter. Once the contact depth is known, the contact area $A(h_c)$ can be evaluated according to Eq. (2.6), and together with the unloading stiffness determined using Eq. (2.3), the elastic modulus is readily obtained following Eq. (2.4). Furthermore, the hardness, H, defined as the mean pressure of the material under load, can be determined using

$$H = \frac{P_{\max}}{A(h_c)} \tag{2.8}$$

Oliver and Pharr's methodology, as described above, has been validated for various elastically isotropic materials to give results for hardness and elastic modulus within 4% of reported values [71]. There are, however, materials for which the assumption of elastic contact on which the method is based leads to a systematic underestimation of the contact area, resulting in an overestimation of the hardness and the elastic modulus. This occurs when a relatively large amount of material piles up around the perimeter of the contact, as is the case for many soft materials [75]. The pile-up results in a significantly larger contact area than predicted by Eq. (2.6). Finite-element analyses [76] have established that the amount of pile-up is well characterized by two parameters, namely the ratio of the final to maximum indentation depth h_f/h_{max} and the work hardening rate η. For indentations with $h_f/h_{max} < 0.7$, very little pile-up occurs, however, as h_f/h_{max} approaches 1. The amount of pile-up becomes significant if the material shows little work hardening, i.e. $\eta << \sigma_y$.

Berkovich indenter has been extensively used for nanoindentation tests to determine the mechanical properties. The main advantage of the Berkovich type (sharp) indenters over spherical (blunt) indenters is as given in the following *Table 2.4*;

Table 2.4: Advantages and disadvantages of Berkovich and spherical indenter

	Berkovich indenter	**Spherical Indenter**
Advantage	Sharp and well-defined tip geometry. Well defined plastic deformation into the surface. Good for measuring modulus and hardness values.	Extended elastic-plastic deformation Load displacement results can be converted to indentation stress-strain curve. Useful in determination of yield point.
Disadvantage	Elastic-plastic transition is not clear.	Tip geometry is not very sharp and the spherical surface is not always perfect.

Even though a considerable amount of work has been carried out on unirradiated samples there is no standard method available to extract the mechanical properties of the materials other than the empirical correlation between the hardness and yield strength. Some of the authors carried out numerical studies using finite element method to simulate the load vs. depth of indentation curves and found good agreement with the experimental data [77]. There are attempts to estimate the yield strength and hardening coefficient of the unirradiated material using forward and reverse algorithms, as could be found in references [78–85]. Dao et al. [78] discussed the fundamental issues related to pileup/sink in effects, requirement of closed form solution to uniquely determine the material's plastic properties, and highlighted the importance of large deformation analytical formulation required to address these issues.

The determination of mechanical properties of irradiated materials using nanoindentation has also been carried out by some of the authors. Hosemann et al. [86] have carried out nanoindentation tests on He and proton irradiated HT9 martensitic and tempered martensitic steels at a temperature less than 550 ^{o}C up to a dose of 2dpa and reported significant increase in hardness. It has also been reported that hardness increases with increase in irradiation dose rate. Samples irradiated at higher temperatures showed hardness lower than the hardness at room temperature and upto 550C the variation in the hardness remained within error bars of the

unirradiated hardness. Ryuta et al. [87] have carried out irradiation at 290^0C with Fe^{3+} with 6.4MeV energy on Fe-Cu and Fe-Mn model alloys and reported that the load-displacement data and hardness data obtained from depth within the range of 100nm to 500nm can be used to estimate the Nix-Gao model parameters and hardness. Heintze et al. [88] carried out nanoindentation on Fe ion irradiated SS304SA, Eurofer'97 and Fe-9%Cr model alloy at a temperature of 300^0C from 1 to 10dpa. It was found that the irradiation increases the hardness in the investigated dose range and the change in hardness of ferritic martensitic steel (Eurofer'97) has shown a square root dependence on the dose (dpa). Yabuuchi et al. [89] have investigated the irradiation hardening in model binary ferritic alloys using Fe^{3+} ion irradiation. The change in hardness was reported up to 1dpa for the samples irradiated at 290^0C. It was found that the small matrix defects were mainly responsible for the hardening behavior in the given dose range. Takayama et al. [90] have carried out 6.4 MeV Fe^{3+} irradiation of F82H material with 1 and 2 at. % Ni up to 10 dpa. These studies have shown that the hardness increases with Ni content. In spite of substantial amount of work has been carried out on the irradiated ferritic martensitic steels, no universal or standardized correlation is found to correlate the indentation properties with the macroscopic mechanical properties such as yield strength. Hosemann et al. [86] have discussed the effect of dose profile, indentation size effect and implantation surface effect on the hardness data extracted from the nano-indentation. When the indentation was carried out on the irradiated surface along the direction at which beam had scanned the surface of the sample the material volumes irradiated with different dose it was observed that misleading data is obtained if one tries an attempt to correlate to macroscopic measurements with the hardness measured in the same direction as the beam direction. Xin et al. [91] have carried out indentation tests to find variation in hardness as a function of irradiation temperature. It was found that the hardness

increases initially and subsequently decreases due to the annihilation of defects at high temperatures. Shin et al. [92] have carried out nanoindentation experiments on ion irradiated Fe-Cr model alloy and FE simulation of the same to find the dose dependence changes in yield strength. They also compared these changes in yield strength from FE simulation with that of empirical equation given by Rice and Stoller [93]. Jin et al. [94] have carried out the nanoindentation experiments on Fe with 5% and 15% Cr to study the effect of 8 MeV Fe ion irradiation to different fluences. It was found that the increase in Cr content and irradiation fluence increases the hardness of the material. The irradiated microstructure was shown to be mainly having interstitial dislocation loops with a density of the order 10^{22} m^{-3}. These results also show that as the Cr content increases the density of loops decreases but the average diameter increases from 2.5 nm to 3.5 nm upon irradiating. These dislocation loops were of the character <111> and <100> type. Recently, Rice and Stoller [93] have correlated the change in the nanohardness of steels with the change in their yield strength. They considered different aged high copper alloy steels, pressure vessel steel (533B) and ferritic martensitic steel (HT-9) for the study. They conducted a systematic study of Vickers hardness testing, nanoindentation and standard tensile testing on different steels. Correlations have been developed between change in nanohardness (ΔH_{NH}) and Yield strength ($\Delta\sigma_{YS}$) through change in Vickers hardness (ΔH_{VH}) measurement using the equations as given below.

$$\left.\begin{aligned}\Delta\sigma_{YS} &= C_1\Delta H_{VH}\\ \Delta H_{VH} &= C_2\Delta H_{NH}\end{aligned}\right\} \Rightarrow \Delta\sigma_{YS} = C_3\Delta H_{NH} \tag{2.9}$$

where C_1, C_2 and C_3 are proportionality constants. The correlation (Eq. 2.9) predicted the yield strength values reasonably in agreement with the experimental results [92].

2.5 Microstructure characterization

2.5.1 Transmission electron microscopy

TEM has been extensively used to characterize the microstructure of material before and after irradiation. The irradiation induced defects such as loops, stalking fault tetrahedral, voids, gas bubbles, precipitates, tangled dislocation substructures have been directly observed under TEM. This is possible due to the nanometer level spatial resolution of TEM. In addition, strong contrast variations generated by irradiation-induced defects make it easy to examine them under TEM. In the case of ion irradiation, TEM investigation is especially useful as it provides information from local region of less than $1\mu m^3$. This volume matches very well with the defect regions created by heavy ions. Many efforts have been made to simulate the neutron damage by using protons and heavy ions and by observing microstructural differences which provide a good correlation for property change.

Many of the groups carried out irradiation studies on FM steels at different irradiation environment (reactors, accelerators, spallation sources) and conditions (irradiation temperature, testing temperatures, irradiation flux, fluence, dose and dose rate). Majority of TEM observations have shown the formation of defect clusters and loops in samples irradiated at different temperatures and doses [20,34,109–113]. In irradiated microstructures defect clusters appear as small black dots at lower temperatures ($\leq 300^0$c) [112,114]. With increase in irradiation temperature and dose, these irradiation-induced defects appear in form of loops. Reason for such a change in the morphology of irradiation induced defects with increasing irradiation temperature and dose is due to increase in the size of defect cluster at the cost of reduction in their density [96]. Helium bubbles were found to form when concentration of He exceeds beyond 500appm at irradiation temperature of 200^0C. At lower irradiation temperatures ($\leq 300^0$C), highly dense

distributions of small sized of He bubbles have been observed which are mainly responsible for low temperature hardening along with dislocation loops [96]. He bubbles have been found to coarsen with increase in irradiation temperature due to increased mobility of the He atoms. In the presence of the He, FM steels have shown increased swelling at high doses [113,115]. Changes in the structure and composition of pre existing precipitates such as $M_{23}C_6$ and M_6C carbides were observed in samples irradiated at low temperature and doses. Many of studies reported amorphization of the carbide particles and changes in their composition. It was concluded that the amorphization takes place when irradiation temperature remains below 250 ^{0}C [96][34, 109, 110, 114]. The radiation induced precipitation of M_6C carbides has been also reported in the literature [101].

2.5.2 Grazing incidence X-ray diffraction

X-Ray Diffraction Line Profile Analysis (XRDLPA) of the GIXRD data was carried out using two different techniques of line profile analysis; single peak analysis by integral Breadth Method [102] and the Modified Rietveld Technique as a function of dose of irradiation as well as with depth of irradiation and the above methods are discussed below:

2.5.2.1 Single peak analysis by Simplified Breadth method

According to Van de Hulst and Reesinck [103] a better approximation of X-ray line profiles would be a Voigt function which is a convolution of a Cauchy and a Gaussian function. Langford [104] derived an explicit equation for a Voigt function and showed that the breadth of Cauchy and Gaussian part can be obtained from the value of $2\omega/\beta$ (= φ , called the Shape Factor where ω is the Full Width at Half Maxima). For a Voigt function φ varies between the limits $0.63 \leq \varphi \leq 0.94$, where $\varphi = 0.63$ is the Cauchy limit and $\varphi = 0.94$ is the Gaussian limit.

In the absence of higher orders of a particular family of reflection the size-strain analysis based on a Voigt function requires the assumption of profile shapes for size and strain broadened profiles. It is generally assumed that the Cauchy component of the Voigt profile is solely due to small crystallite size and the Gaussian component is due to the microstrain.

The relation between D_v, ε, β_c and β_G is given by [104]:

$$D_v = \frac{\lambda}{\beta_c \cos(\theta)} \tag{3.4}$$

And

$$\varepsilon = \frac{\beta_G}{\tan(\theta)} \tag{3.5}$$

Here, D_v is the volume weighted domain size, ε is the upper microstrain, β_c and β_G represent the Cauchy and Gauss component of the integral breadth respectively.

2.5.2.2 Modified Rietveld Technique

In the modified Rietveld analysis, the diffraction profiles have been modeled by pseudoVoigt (pV) functions using the program LS1 [105]. The initial values of the lattice parameters were obtained from a least square fit of the powder diffraction peaks. The program includes the simultaneous refinement of structural and microstructural disorder of the polycrystalline material. It is based on the Rietveld method combined with the Fourier analysis of the broadened peaks. Crystallite size and the microstrain were regarded as fitting parameters. The instrumental broadening correction was done using a standard defect free Si sample. The lattice parameters, surface weighted average domain size (Ds) and microstrain $<\varepsilon_L^2>^{1/2}$ were

used as fitting parameters simultaneously to obtain the best fit in order to calculate the average values of the fitting parameters.

The conventional X-ray diffraction LPA of heavy ion and proton irradiated zirconium base alloys and austenitic steel (SS316L) has been carried out by Sarkar et al. [106], Paramita et al. [107] respectively. Other than the above studies, the XRDLPA has been used quantify the dislocation density, micro strain, coherent domain size and residual stresses present in the materials after cold working of the materials [108–111]. The XRDLPA studies on the irradiated materials show that the dislocation density and microstrain increases and the coherent domain size decreases with irradiation dose [126, 127].

2.6 Multi-scale Material Modeling (MMM) Techniques

The literature on the deformation studies using MMM techniques is described in this section. The material features at nano and mesoscale, such as defects loops, voids, precipitates, stalking fault-tetrahedra (SFT) interacting with isolated and collection of dislocations, govern the macroscopic mechanical properties and plastic deformation behavior of the material. In view of this, mainly the atomistic scale (molecular dynamics) and mesoscale (discrete dislocation dynamics) simulation methods are considered and described here. The atomistic scale simulation helps in understanding isolated defect-defect interaction. The mesoscale simulations help in studying the response of materials in the presence of randomly distributed defects and their mutual interaction.

2.6.1 *Molecular Dynamics Simulations*

In MD simulations, atoms are approximated as point mass particles with no internal structure and their motions are described by solving Newton's equation of motion. In this methodology, atomic forces are not calculated from electronic structures; instead these are calculated by taking the derivative of the radial isotropic potential function which is obtained from the electronic calculation i.e. by solving Schrödinger wave equation. The equation of force could be given as;

$$f_{ij} = -\frac{dU(r_{ij})}{dr} \tag{2.9}$$

Where, U is the potential energy functional as a function of position vectors of nearest neighboring atoms and f_{ij} force as negative derivative of the potential energy functional. There exist a number of different forms of potential energy functional, depending on the type of systems to be addressed. They are also termed as 'empirical interatomic potentials'. The potentials currently used are mainly of empirical in nature obtained by different realizations of the Embedded Atom Model (EAM) [113]. Their empirical parameters are based typically on the fitting to properties of the metal such as elastic constants, phonon spectra, cohesive energy, stacking fault energy, and surface and point defect energies, and, increasingly to *ab-initio* data [114]. In the present study only the potential energy functionals related to metallic pure/alloy systems which are extensively used in the literature have been considered. These potential energy functionals for the metallic systems were developed by Daw and Baskes [113] and other by Finnis and Sinclair [115]. Both are commonly known as embedded atom potentials due to their intrinsic form. Mathematically the potential energy functional of the system is written as follows:

$$U = \frac{1}{2}\sum_{i}\sum_{i\neq j} V\left(r_{ij}\right) + \sum_{i} \phi\left(\rho_i\right) \tag{2.10}$$

$$\rho_i = \sum_{i\neq j} \rho\left(r_{ij}\right) \tag{2.11}$$

Where the summation over the first term covers the neighboring atoms which are at a distance less than the certain cutoff radius of the atom of interest and it is known as pair potential. The second term is the embedding function depending on the effective local electron density due to neighboring atoms at the point of interest. The embedding function comes from the assumption that, the atoms/defects assumed as positively charged particles embedded in the negatively charged electron cloud.

The embedding energy of an atom in a solid is the energy of that atom in a uniform electron gas relative to the energy of the same atom separated from the electron gas. Stating simply embedding energy is the energy of the atom inside the solid versus the outside the solid. The atomistic simulations are divided into two categories,

1.Molecular statics or Zero Kelvin simulations

2.Molecular dynamics or Finite temperature simulations

In molecular statics, the atomic positions are calculated based on the minimum energy configuration of the system under consideration. To achieve the minimum energy configuration one of the two following methods can be used.

Metropolis Monte-Carlo method (MC), where the atoms are moved randomly in the system and the new configuration is accepted if the current configuration results in lower energy than the previous one with a certain probability measure [129, 131].

Conjugate gradient method (CG), where the specific rearrangement of atoms, which are conjugate to previous configurations, searched iteratively such that the energy follows the steepest descent direction on the global potential energy curve. In both the methods it is not guaranteed to achieve the global minimum energy positions [129, 131].

The finite temperature simulations are based on the energy and dynamics of the atoms according to classical dynamics which obeys the Newton's equation of motion. The equation of motion of each atom is coupled with the other atoms in the system. The Newton's equations of motion are integrated under different statistical ensembles, the new positions of the atoms are obtained and system is updated to the new configuration. The positions, velocities and accelerations of atoms are updated at each predetermined simulation time step by substituting the previous time step positions in the equation of motion in the presence of external loading/boundary conditions. This process is repeated for the required time by discretizing the continuous time into smaller time steps of the order of Femto to Pico seconds based on the problem at hand.

The term 'ensemble' corresponds to the collection of identical systems in a given state. Different ensembles give the idea of how the considered system is interacting with its surroundings. The important basic statistical ensembles are canonical, micro-canonical and grand-canonical ensemble. The micro-canonical ensemble represents an isolated system which does not interact with its surrounding either by energy or mass transfer. In canonical ensemble the energy transfer between the system and surrounding occurs and in the case of grand-canonical, both energy and mass transfer occurs between system and surroundings. The details of ensembles and their mathematical formulations are well documented in the literature [129, 131].

The embedded atom potentials which were initially developed and used to simulate the pure transition metals are now being developed for alloy systems. In general, the alloy system is the one which contains two or more species of metallic atoms soluble in each other at a given temperature. To account the secondary/alloying elements added to the host system, the basic EAM potential energy functional is modified to include the alloying element concentration. This potential is known as Concentration Dependent EAM (CD-EAM) potential which is originally developed by Caro et al. [117] (two site model) and later modified by Stukowski et al. [118] (one site model) to increase the computational efficiency. Since the potential developed based on this formulation is used in the present work, small description of the force evaluation using this formulation is given in the following lines as taken from Stukowski et al. [118]. The modification in the basic EAM formulation to account for the concentration dependence is given as follows:

$$E = \sum_{i}^{N} E_i = \sum_{i}^{N} \left[F_{\alpha_i}\left(\varrho_i\right) + \frac{1}{2} \sum_{j \neq i} V_{\alpha_i \beta_j}\left(r_{ij}\right) \right] \tag{2.12}$$

Where α and β denote the atom types and F_α is the embedding function for type α. The total electron density, ρ_i, at site i is calculated as

$$\varrho_i = \sum_{j \neq i} \rho_{\alpha_j}\left(r_{ij}\right) \tag{2.13}$$

The pair potentials V_{AA} and V_{BB} for the pure elements are the functions of the inter atomic distance r_{ij} only, whereas the cross potential V_{AB} depends on both the distance, r_{ij}, and the local concentration, x_{ij} , which could be expressed as

$$V_{AB}\left(r_{ij}\right) = h\left(x_{ij}\right)\phi\left(r_{ij}\right) \tag{2.17}$$

The function $h(x)$ is fitted to reproduce the concentration dependence of the heat of formation. If $h(x)$ =1 the conventional EAM format is recovered. In the original CD-EAM model the cross pair potential, Φ_{AB}, was simply chosen as

$$\phi_{AB}\left(r_{ij}\right)=\frac{1}{2}\left[V_{AA}\left(r_{ij}\right)+V_{BB}\left(r_{ij}\right)\right] \tag{2.18}$$

Although in principle this function can be fitted as well. The local concentration of B atoms, x_{ij}, is estimated from the partial 'B electron densities' at sites i and j

$$x_{ij}=\frac{1}{2}\left(x_i+x_j\right)=\frac{1}{2}\left(\frac{\varrho^{B}{}_{i}}{\varrho_i}+\frac{\varrho^{B}{}_{j}}{\varrho_j}\right) \tag{2.19}$$

With

$$\varrho_j^{\,B}=\sum_{j\neq i}\rho_{\alpha_j}\left(r_{ij}\right)\delta_{\alpha_j B} \tag{2.20}$$

The Kronecker symbol, $\delta_{\alpha jB,}$ in Eq. 2.20 equals 1 if atom j is of type B and equals 0 otherwise, i.e. the partial density, $\varrho_j^{\,B},$ includes contributions only from B atoms within the neighborhood of site i. Finally, the force acting on each atom is given by taking the derivative of Eq.2.12 which is similar to Eq.2.9.

The general steps involved in the atomic simulations are,

1. Initialization: defining atomic structure (atom coordinates), temperature, the interaction potential.
2. Applying boundary conditions: problem specific boundary conditions such as periodic or non periodic surfaces, traction forces on free surfaces.
3. Integration of Equation of motion: integration of coupled equations using different integration schemes. For example, Verlet or Velocity Verlet algorithm [129, 131].

4. Result output and post processing: The results obtained from the integration process such as new atomic positions, velocity, free energy, force acting on each atom are post processed to get derived parameters such as stress and strain, etc.

MD simulation is a tool used to study the atomic scale phenomena such as radiation cascades and isolated dislocation interacting with other defects such as voids or precipitates or bubbles. The MD simulations are also used to study the atomic diffusion processes, biological systems etc., which are not related to present work. In the present study simulation of metallic system is considered.

2.6.1.1 MD simulations of cascade

In the last two decades a considerable amount of work has been carried out on the radiation cascade simulation in different metallic systems. These simulations have provided physical insight into the radiation cascade formation and defect structure generated after cascade collapse which is observable from *in-situ/ex-situ* experiments. Bacon et al. [119–125] studied the cascade structure and defects fractions produced by different energy PKAs and the direction of PKA. The increase in PKA energy increases the number of frenkle pairs produced. In addition, the increase in temperature decreases the number of frenkle pairs produced during cascade and fraction of interstitials in the cluster form increases. In general it has been found that the atomic mixing, disordering in metallic compounds and vacancy agglomeration takes place within the cascade core. Roger et al. [141, 142] studied the effect of cascade overlapping and sub cascade formations in the alpha-iron system. Some of the authors performed the cascade simulations such as; effect of helium on cascade structure as a substitution/interstitial atom in alpha Fe [126], interaction of bubble with cascade [127], effect of temperature on He production [128] and

bubble stability during irradiation [129]. It has been found that if the He < 0.5% no significant change in the damage production was observed, however for He > 0.5%, increases the total number of Frenkel pairs during the cascade [130]. Wirth et al. [17], Kwon et al. [131], Yoshiie et al. [132] used MD and MC simulation to generate the microstructure with irradiation induced defect density and size distribution. The defects formed directly from cascade may be mobile or immobile point defects and clusters. The defects act as the obstacles to the plasticity carriers, i.e. mobile dislocations and resist their motion. The resistance to the dislocation motion appears as the increase in the flow strength of the materials. Therefore, the dislocation interaction with the defects is one of the important mechanisms to be studied with plastic deformation using MD simulations.

2.6.1.2 MD simulations of interaction of dislocation with defects

Dislocation defect interaction studies have been carried out by many authors. MD simulations of the interaction of dislocation with defects are performed to obtain the resistance of the obstacle to dislocation motion and their mutual interactions. At the atomic scale, the interaction of an edge dislocation (ED) with irradiation induced defects such as voids [133–138], loops [139–142], precipitates and helium bubbles are investigated using MD simulations. It is shown that defects lying on the dislocation slip plane offer resistance to dislocation motion resulting in the hardening of the materials. Kwon et al. [131] performed DD simulations by using MD and MC results to assess the irradiation embrittlement of reactor pressure vessel steel.

2.6.1.2.1 MD simulations of interaction of dislocation with voids

To highlight few important results, Osetsky et al. [149, 150,159, 160], Bacon et al. [144], Terentyev et al. [138], Hafez et al. [151, 162] carried out MD simulations of interaction of

dislocation with voids in Fe and Fe-Cr. Osetsky et al. [133] have given a method to construct an infinite edge dislocation in a domain with periodicity along line and Berger's vector direction. The authors carried out the above study by varying the simulation parameters such as domain size, Cr solute concentration, temperature, void diameter, perpendicular distance between the slip plane and void center.

In summary, the above simulations show that, a) Varying the domain size along line direction, slip plane normal and burgers vector direction, it was suggested that that domain size has to be chosen such that the boundary effects are negligible on the dislocation [133]. b) The increase in the obstacle size and increase in the solute concentration increases the critical stress required for the dislocation to overcome the obstacles. c) The increase in the simulation temperature and decrease in strain rate decreases the critical stress required for shearing the obstacles. d) under application of constant stress the dislocation overcomes the void with lesser stress value in comparison to constant strain rate simulations [144]. e) screw dislocation segments were formed and their length increase with further increase of void diameters (> 2.0 nm) in the investigated domain size and inter-particle spacing [134]. f) In Fe and Fe-12%Cr system dislocation interacting with the voids has shown increase in CRSS for Fe-Cr system in comparison to pure Fe [138]. f) Dislocations were found to absorb vacancies and shrink the voids in Fe [134] which is not observed in case of voids in copper [146]. g) It has been found that as the perpendicular distance between the slip plane and void center increases, the CRSS value decreases due to reduction in effective diameter of the void with which dislocation interacts on its slip plane [135].

Also the MD studies carried out by Terentyev et al. [137], Hafez et al. [145] using different potentials have shown different Peierl's stress values for the edge dislocation in Fe. It was found that the Dudarev-Derlet potential predicts stronger resistance to dislocation interacting with voids at a given temperature in comparison to that of Ackland et al. [147] and Mendelev et al. [148] potentials. Later in his work, Hafez et al. [135] did a comparison of resistance of voids for dislocation motion by MD and DD simulations. The MD simulations were carried out by varying the distance between the slip plane and the center of the void and found that the stress required to overcome the obstacle decreases with increase in the center to slip plane distance. The DD simulations with void internal surface image forces successfully reproduced the MD results. Recently, Dutta et al. [149] have carried out molecular static and dynamics simulations of dislocation interacting with void in Molybdenum crystal. It was shown that the presence of structural energy gradient facilitates the climb of the dislocation in contrast to previously believed diffusion controlled phenomenon.

2.6.1.2.2 MD simulations of interaction of dislocation with precipitate

Kohler et al. [150], Terentyev et al. [167, 168], Hafez et al. [152] carried out the MD simulations of dislocations interacting with precipitates (Cu/Ni/ordered, Cu-Ni, Cr) of different diameters and with different concentration of solute atoms (Cu/Ni) in the coherent precipitates. The dislocation precipitate interaction studies have shown that increase in diameter of the precipitates resulted in the increase of the CRSS [154, 166] and increase in temperature decreases the CRSS required for the dislocation similar to that of voids [152]. Cu-Ni precipitates have been found to be stronger obstacle than the pure Cu or Ni precipitates. Reduction in CRSS is sharper when Fe is present in the Cu/Ni precipitates as compared to Cu/Ni precipitates without Fe. CRSS is lower for shell structure precipitates in comparison to pure Cu/Ni precipitates. It

was also noticed that the Cu/Ni undergo bcc to fcc transformation inside the precipitates [150] resulting in the significant difference in the interaction mechanism and critical shear stress [149,150, 161]. Precipitates were found to be sheared by the dislocation and found that the precipitates offer less resistance for dislocation motion in comparison to voids [134]. The increase in the Cr content in the precipitate increases the required CRSS for the edge dislocation to overcome the precipitate [138] and no dislocation climb or jog formation is observed.

2.6.1.2.3 MD simulations of interaction of dislocation with bubble

Schaublin et al. [153] and Hafez et al. [154] have studied the interaction of edge dislocation with He bubbles with different He-vacancy ratio in pure Fe. They have reported that the CRSS increases with increasing bubble diameter and decreases with temperature for one helium and one vacancy configuration. It was also found that CRSS for the edge dislocation interacting with bubble of 1-2nm diameters containing 2 to 3 helium atoms and one vacancy configuration decreases but CRSS was found to increase for bubbles with more than 3 He atoms. The increase in the CRSS for high He content bubbles is attributed to the loop punching mechanism. Similarly, Hafez et al. [41] also reported the effect of different Fe potentials on the CRSS obtained for a dislocation interacting with He bubbles of different size at different temperatures and found similar behavior. Other than He bubbles, the effect of isolated He at interstitial or substitutional positions and Helium-vacancy pairs on the edge dislocation mobility has been studied by a few authors. Heinisch et al. [155] studied the interaction of edge and screw dislocation with He atoms in alpha iron. The results of these simulations indicated that interstitial He atoms are either repelled from or trapped at edge dislocations in α-Fe, depending on the direction of approach. Near the dislocation core on the tension side, He is strongly trapped as a crowdion with 1–2 eV greater binding energy than as an octahedral interstitial, and in this form,

He atoms can migrate along the dislocation with migration energy of 0.4–0.5 eV. Yang et al. [156] carried out the MD simulation at 0 K to determine the effect of He cluster on the edge dislocation mobility with different He/vacancy (V) ratio on slip plane. The results have shown that the He_n-V_m ($n \geq m$) clusters are trapped in the dislocation on the tension side, but the He_n-V_m ($n < m$) cluster are trapped within about 0.5 nm from the dislocation core on both the compression and tension sides. The binding energies of the He_n-V_m ($n \geq m$) clusters to the dislocation do not depend much on cluster size, but rather on the He/V ratio. The effects of dislocations on the formation of He–V clusters is very small for the distances more than about 1.3 nm from the dislocation core on the slip plane, and the binding energies of the clusters depends on only the He/V ratio at these positions. Wang et al. [157] carried out MD simulation to study the effect of dislocation on the interstitial He in α Fe.

2.6.1.2.4 MD simulations of interaction of dislocation with dislocation loops/SFTs

The interstitials formed during the radiation damage (cascading) process accumulate to form self interstitials (SI) perfect or faulted dislocation loops on {110} plane and act as obstacles to the gliding dislocation on the {110} planes. Rodney et al. [158], Osetsky et al. [177, 178], Rong et al. [142], Nogaret et al. [160] and Terentyev et al. [154, 180] have studied interaction of dislocations with dislocation loops in materials with fcc (Ni, Cu) or bcc (Fe, Fe-Cr) crystal structure at zero or finite temperatures. Similar studies on dislocation interacting with SFTs have been carried out by Osetsky et al. [162–164], Wirth et al. [17] and Rodney et al. [158].

The mentioned MD studies have shown that decrease in strain rate allows dislocation to remain in contact for longer duration, thereby increasing the probability of cross slip which may change the interaction mechanism itself. The mechanisms of interaction of dislocation with

interstitial dislocation loops are loop shearing, loop unfaulting and absorption in a glissile configuration and loop unfaulting and absorption in a sessile helical turn [160]. These mentioned interactions have been found to be temperature, strain rate dependent and sensitive to stacking fault energy. The probability of dislocation cross-slip decreases with decreasing temperature and stacking fault energy. The unpinning stress required for an edge dislocation was found to be lower than that needed for a screw dislocation. The interaction of screw dislocation with interstitial frank loops results in the jog/helical turn formation and helps in the climb of the dislocation and unfaulting of the loops [160]. The interaction of dislocation with loops/SFTs results in the formation of helical segments/super jogs with the absorption of interstitial loops/SFTs completely (temperature > 300K) or partially (temperature ~ 1K) resulting in microstructural changes which increase the stress required for further dislocation motion. When dislocations glide with low velocity near the small loops, it has been found that the loops in the vicinity of dislocation are captured and dragged by the dislocation [158, 176] and thereby loops are transferred over a relatively long distances. Formation of jogs and super jogs are observed due to the interaction of edge and screw dislocations with the perfect SFTs. It has been found that the climb mechanism is more pronounced for SFTs and loops in comparison to voids/precipitates. This shows that the interaction of dislocations with defects results in the removal/annihilation of a significant fraction of obstacles.

2.6.1.2.5 MD simulation of interaction of dislocation with solute atoms

Out of the two types of dislocations, edge dislocations are extensively studied in comparison to screw dislocations because of the simplicity in their construction. Other than the interaction of dislocation with defects, many authors also studied the mobility of isolated infinite length dislocations in pure and solid solutions/alloy systems. The MD simulations are extended

to binary alloys such as Al in Ni [184, 185], Mg in Al [166], Cu in Fe [167–169], Ni in Fe [169], C in Fe [169] and Cr in Fe [154, 170], where it is shown that the addition of alloying elements significantly increases the flow stress of the materials. The solute hardening behavior in all the alloys is found to be due to the short range interaction of solute atoms with mobile dislocations. A pair of solute atoms in nearest neighbor configuration lying on the adjacent planes of the geometric slip plane acts as a strong obstacle to gliding dislocation. Through MD studies it was possible to demonstrate that the flow stress increases with an increase in solute concentration and decreases with an increase in temperature due to thermally assisted motion.

2.6.1.3 MD simulations of GB in the presence irradiation induced defects

The aforementioned MD simulations were concerned about the dislocations interacting with defects in grain interior. The interaction and pinning of dislocations at defects and dislocations glide are more relevant deformation mechanisms in the low and intermediate temperature ranges. Planar defects such as grain boundaries also play a major role in the deformation resistance of the materials. GB sliding, for example is an important deformation mechanism in the high temperature regime. In general, interaction of lattice dislocation with a grain boundary is one of the fundamental strengthening mechanisms which play a major role at all temperature regimes. The grains slide with respect to each other at their common interface which may be tilt or twist or mixed (tilt and twist) character. GBs in general are of mixed type. For, tilt and twist character, if the misorientation angle between two grains is less than $\leq 10^0$ such GBS are called low angle GBs and if it is greater than 10^0 GBs are called high angle GBs [170]. In low angle GBs a well aligned dislocation arrays at the interface can be observed. In case of high angle GBs, due to overlapping of neighboring dislocations core, no distinction can be made between any two dislocations.

Significant amount of work has been carried out by many workers on the different types of GBs, in particular, tilt and twin boundaries. Till date, the experimental and computer simulation studies related to grain boundaries are mainly concerned with the tilt and twin GB atomic structure, their energetics and deformation behavior ([171] and references therein). A few authors reported on atomistic simulation of twist grain boundaries from energetics and structural points of view [172]. Sansoz et al. [173] have shown from MD simulations that, the low angle tilt GBs slide by stick and slip mechanism. This stick and slip mechanism is due to the absence of a well defined slip plane for the edge dislocations formed at an interface. In case of twist GBs, a misfit interface screw dislocation network is formed and they glide on the well defined slip plane [172]. Bulatov et al. [174] have studied the anomalous low temperature slip behavior and direction dependence of low angle twist GB sliding with conservative motion of interface screw dislocation network in molybdenum. It was shown that the screw dislocation network formed at the twist GB offers less resistance (2.4-2.6 GPa) for sliding in comparison to the isolated infinite length screw dislocation (2.7-3.2 GPa). Liu et al. [175] studied the tensile properties of a bi-crystal copper with twist grain boundaries. Recently, Terentyev et al. [176] studied the effect of Cr precipitates and He bubbles on the tensile strength of <110> tilt grain boundaries in BCC iron. MD simulations of growth of He bubbles at twist GBs have been reported by Hetherly et al. [177] in alpha iron and by Demkowicz et al. [178] in Cu-Nb and Cu-V samples. Metropolis Monte Carlo simulations show that, energetically, He prefers to nucleate heterogeneously at nodes. Zengfeng et al. [179] have investigated the helium bubble nucleation at low-angle twist boundaries in gold. It has been found that the helium bubbles preferentially nucleate at screw dislocation nodal points and result in helium bubble super lattice formation, which is completely isomorphic with the screw dislocation network along the twist-grain boundary. Molecular statics

calculations have revealed that defect formation/solution energies along the screw dislocations, especially at the nodal points, are lower than their bulk counterparts. It is believed that this driving force is responsible for the helium bubble super lattice formation. The study suggests that grain boundary engineering via adjustable twist angles in parallel boundaries to form tunable 3D bubble super lattices could afford a very promising approach for design of radiation tolerant materials. In addition to energetics, it is also necessary to understand the deformation behavior of the grain boundaries to the external applied loading and temperature.

A few authors performed experiments on GBs showing that nodes formed by the intersection of dislocations within the matrix and at the grain boundaries act as nucleation and sinks/annihilation sites for He bubbles [195, 196, 198] and point defects respectively. Transmission electron microscopic investigations on irradiated samples [198, 199] showed the formation of He bubbles as super-lattices at the misfit dislocation intersections. In spite of such studies, sparse or less information is available on the sliding behavior of twist grain boundaries in the literature.

2.6.1.4 MD simulations of nanoindentation

Nanoindentation simulations have also been carried out on the materials with fcc and bcc crystal structures. Much of the simulation studies are carried out using spherical indenters [182–187]. A few studies have been carried out using plane strain or wedge or pyramidal shaped indenters [206, 207] under MD and quasi continuum formulations [189]. All the simulations are carried out on perfect crystals in order to study the dislocation nucleation beneath the indenter. Also the effect of indentation on preexisting vacancies and voids in the samples has been studied [209, 210]. Some of the studies carried out on pure element systems in order to develop the

numerical techniques to extract the crystalline defects (dislocations, stalking faults. etc.,) generated during the indentation or plastic deformation at atomic scale [191].

The studies have shown that during nanoindentation using spherical indenter, the homogeneous nucleation of partial dislocation occurs below the surface inside the indenter contact area in fcc lattice materials Nickel [192], Silver [193] and Gold [194]. Simulations carried out on Ni single crystals have shown that the decrease in the sample thickness along indentation direction increases the force required for the same depth of indentation [185]. Indentation of low angle GBs, twin boundaries have shown that GBs act as dislocation sources under indentation. It has been also found that the GBs can absorb and ripple the dislocations, which are accompanied by atomic shuffling and free volume migration at GBs. Dislocation nucleation stress at GBs decreases with increase in the sample thickness along the indentation direction. GBs have been found to obstruct the incoming mobile dislocations during nanoindentation [182].

In summary MD simulations have high applicability to simulate interaction of dislocation with irradiation-induced defects to understand their different interaction mechanisms. Much of the work carried out shows a wide scatter in the simulation parameters. Based on the outcome of MD simulations, the phenomenological local rules for individual or collective behavior of defect-defect or defect-interfaces interaction can be derived. This qualitative or quantitative information can be passed on to higher length scales such as discrete dislocation dynamics or crystal plasticity models to predict realistic polycrystalline materials behavior. In this way, Martinez et al. [214, 215] made an attempt to include the stacking fault energies and partial

dislocations in DD simulations. Chang et al. [196] have used the atomistic dislocation nucleation mechanism during the nanoindentation of Cu crystal in DD simulation of nanoindentation.

2.6.2 Discrete Dislocation Dynamics (DDD) simulations

Dislocations are formed in materials during solidification as well as during plastic deformation under various fabrication processes. Based on the angular relationship between their Burgers vector direction and their line direction, dislocations are mainly categorized into edge, screw and mixed dislocations; as shown in Figure 2.10. A dislocation line segment with Burgers vector ***b***, which is perpendicular to its line direction l, is called as edge dislocation and it is denoted by the symbol (⊥). On the other hand, if the Burgers vector ***b*** is parallel to its line direction ***l*** it is called as screw dislocation. The dislocation line segments having a partial edge and screw characters is called as a mixed dislocation. Edge dislocations are in general confined to move on a well defined plane called as slip planes. These slip planes are represented by the normal vector perpendicular to its line and Burger's vector direction. On the other hand, screw dislocations are not confined to move in a predefined slip plane. Though, the dislocations are line defects, they form three-dimensional network in materials.

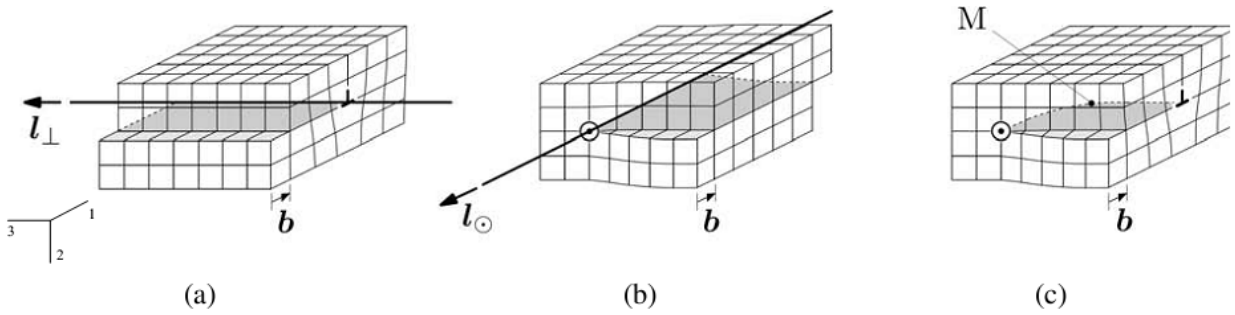

Figure 2.10: Schematic diagram showing the (a) edge, (b) screw and (c) mixed dislocation configurations in a cubic crystal with ***l*** representing dislocation line direction and **b** Burgers vector direction.

During plastic deformation, the glide of dislocations creates numerous steps on the surface of the sample, which are integral multiples of elementary Burger's vector magnitude $|\boldsymbol{b}|$. In general, the slip occurs on the plane of highest atomic density and in the closest packed directions. For example, in body centered cubic crystal structure materials, $\{110\}$ planes have highest atomic density and along $\langle 111 \rangle$ directions, the atoms are closely spaced. In the present study, only bcc slip systems are considered.

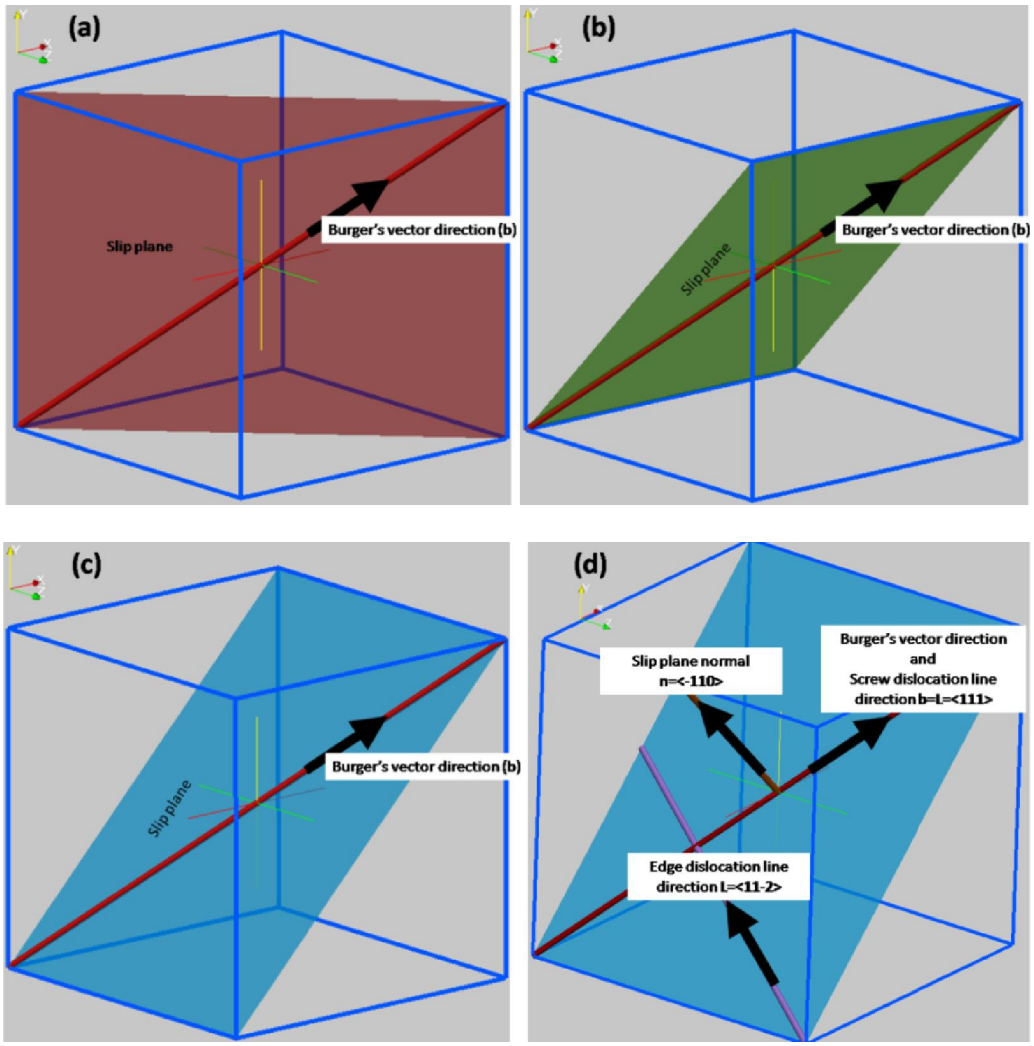

Figure 2.11: Schematic representation of the planes (a) $(\bar{1}01)$ (b) $(01\bar{1})$ (c) $(\bar{1}10)$ sharing $\frac{a_0}{2}\langle 111 \rangle$ Burgers vector direction (d) edge, screw dislocation line directions and plane normal.

A slip system is defined by a set of vectors representing the slip plane normal **n** and slip direction **m**. The bcc structure has 48 slip systems comprising the 12 slip system from each family of $\{110\}\frac{a_0}{2}\langle 111\rangle$ and $\{112\}\frac{a_0}{2}\langle 111\rangle$ and 24 slip systems of family $\{123\}\frac{a_0}{2}\langle 111\rangle$ where 'a' is lattice constant. Out of all the slip systems, only few are generally active during deformation at a given temperature. Single crystal experiments have shown that only the $\{110\}\frac{a_0}{2}\langle 111\rangle$ family slip systems are active at room temperature. Therefore, in the present study only $\{110\}\frac{a_0}{2}\langle 111\rangle$ family representing 12 slip systems are considered. A set of planes sharing $\frac{a_0}{2}\langle 111\rangle$ the Burgers vectors is as shown in Figure 2.11. The $\frac{a_0}{2}\langle 111\rangle$ direction shared by $(\bar{1}01)$, $(01\bar{1})$ and $(\bar{1}10)$ planes are shown in Figure 2.11 (a), (b), (c) respectively. Figure 2.11 (d) shows the edge and screw dislocation line direction on a $(\bar{1}10)$ plane.

There are mainly two methods in the DD formulations. It is based on how the continuous dislocation lines with infinite degree of freedom are discretized into finite degree of freedom system. The discretization helps in approximately representing the continuous lines and reducing the computational cost and time. Depending on the discretization of the dislocation segments, the following two dislocation dynamics models are found in the literature.

Model one: The discretization of dislocation into a finite number of edge, screw and mixed dislocation segments is known as Network model or Pure-Mixed model. The DD codes based on network model are microMegas (mM) [197] and TRIDIS [198].

Model two: The discretization of dislocation into a finite number of piecewise straight segments connected in series having mixed character and arbitrarily oriented is known as Nodal model. The DD codes based on Nodal framework are PARAllel DISlocation dynamics simulator (PARADIS) [199] and Micro3D [200].

The three dimensional 'microMegas' dislocation dynamics code which is based on network model is extensively used in the present work [197].

The general steps involved in DDD analysis are as follows,

- Initially appropriate size of the domain needs to be defined.
- The dislocations lines or frank read source has to be randomly distributed on the considered slip systems
- Boundary conditions have to be specified like, free surface, surface traction forces etc.
- Evaluation of forces acting on each segment's with linear elasticity approximation.
- Determination of velocity of the segments.
- Updating the position of each segment by searching for the obstacles and contact reactions in between the current and next time step.
- Post processing of results to obtain the required output parameters.

The velocity of each dislocation segment is determined by the effective resolved shear stress, $\tau_{eff,}$ acting on the segment which has contributions from a) external applied stress (σ_{app}), b) internal stress field (σ_{int}) due to other dislocation segments present in the simulation volume, c) lattice friction (τ_F) and finally, d) the dislocation line tension (T), which always tries to straighten the dislocation lines when they become curvilinear. The stress field due to alloying elements that

affects the dislocation motion at the atomic level is included in the lattice friction stress and is assumed to be homogeneous throughout the simulation volume.

Depending on the boundary conditions involved, the external stresses are applied in two different ways. In the first case (conventional DD simulations), in order to simulate the bulk crystalline nature a small simulation volume is considered which is a part of large crystal. It is assumed that the entire simulation volume is under a uniform external stress field. Each dislocation segment inside the simulation volume experiences the same external stress tensor applied and at each step of the simulation, components of applied stress tensor are updated. In the second case (hybrid simulations), due to the presence of heterogeneities such as internal free surfaces, secondary particles or phases producing internal stress at the interface, etc. In such cases the simulation is carried out based on superposition principle. In this superposition principle, the problem is broken down in to an infinite medium with stresses only due to dislocations and a finite size domain having interfaces/free surfaces with displacement or stress boundary conditions due to dislocations far away and externally applied traction. The second part of the problem is also known as boundary value problem (i.e. finite size domain with external and internal traction specified) is solved using standard finite element method. In the present study, only first kind of boundary condition is used.

The stress field σ_{ij} at a point (x1, y1, z1) due to a dislocation segment *AB* with Burgers vector **b**(b_x, b_y, b_z) is obtained by

$$\sigma_{ij}\left(\mathbf{r}\right)=\sigma_{ij}\left(\mathbf{r}-\mathbf{r}_A\right)-\sigma_{ij}\left(\mathbf{r}-\mathbf{r}_B\right) \tag{2.21}$$

Where **r** is the position vector of point (x1, y1, z1), $\mathbf{r_A}$ and $\mathbf{r_B}$ are the position vectors representing the dislocation segment ends. Devincre [201] has given the formulation to calculate the stress field due to a dislocation segment *AB* in Cartesian coordinates as follows

$$\sigma_{ij}^{AB}(\mathbf{r}) = \frac{\mu}{\pi Y^2}\left[\left[\mathbf{bYt}\right]_{ij} - \frac{1}{1-\nu}\left[\mathbf{bYt}\right]_{ij} - \frac{(\mathbf{b},\mathbf{Y},\mathbf{t})}{2(1-\nu)}\left(\delta_{ij} + \mathbf{t_i}\mathbf{t_j} + \phi_{ij}\right)\right]_B^A \tag{2.22a}$$

$$\phi_{ij} = \frac{2}{\mathbf{Y}^2}\left(\rho_i Y_j + \rho_j Y_i + \frac{L}{R} Y_i Y_j\right) \tag{2.22b}$$

$$L = \mathbf{R}\cdot\mathbf{t} \tag{2.22c}$$

$$\boldsymbol{\rho} = \mathbf{R} - L\mathbf{t} \tag{2.22d}$$

$$\mathbf{Y} = \mathbf{R} + R\mathbf{t} \tag{2.22e}$$

$$\left[\mathbf{bYt}\right]_{ij} = \frac{1}{2}\left[\left(\mathbf{b}\otimes\mathbf{Y}\right)_i \mathbf{t}_j + \left(\mathbf{b}\times\mathbf{Y}\right)_j \mathbf{t}_i\right] \tag{2.22f}$$

with (***b***, ***Y***, ***t***) the scalar triple product, δ_{ij} the Kronecker symbol, ***t*** the unit vector along the line direction of the segment, and ***R*** the vector from the point ***A*** or *B* of the segment to the point ***r***.

The lattice friction refers to the critical stress required to start a dislocation glide in an otherwise perfect crystal. This arises as a direct consequence of the periodic structure of the crystal lattice and acts as a resisting force for glide of the dislocation. In DD simulations, connected straight dislocation segments are used to approximate the continuous curved dislocations. In order to account for the elastic energy of continuous curved dislocations a correction factor is introduced as a line tension. The expression for line tension $T(\theta)$ is given by $\Gamma = T(\theta)/(bR)$, this creates a force along the center of a dislocation arc having a radius of curvature *R*. The general expression of the $T(\theta)$ is given by the energy $E(\theta)$ of the dislocation arc with θ the angle between the Burgers vector and the dislocation line direction:

$$T(\theta) = E(\theta) + \frac{d^2 E(\theta)}{d\theta^2} \tag{2.23}$$

Depending on the form of E, the line tension models are named as isotropic and anisotropic. Since the energy of a dislocation is dependent on the character (screw dislocation has lower energy than the edge dislocation), in order to account this variation of the energy with character of the segment, different analytical equations exist. The simplest form of the line tension would be obtained by assuming that edge, screw and mixed segments would have the same energy per unit length, i.e. $E = \alpha\mu b^2$ with α is a numerical constant. The line tension of an arc of dislocation then becomes $\Gamma = \alpha\mu b/R$ from the Eq.2.23. In this thesis, the isotropic line tension model is used.

The effective stress on each dislocation segment is evaluated at corresponding segment midpoint using the expression (2.24).

$$\tau_{eff}^{i} = \tau_{PK}^{i} + \Gamma^{i} \tag{2.24}$$

where τ_{eff}^{i} is effective stress, τ_{PK}^{i} is sum of external applied and internal stresses and Γ^{i} is line tension. The plastic strain in a simulated volume is determined by summing up the slipped area of each slip system (***g***). The slip increment $\Delta\gamma^{g}$ is computed as:

$$\Delta\gamma^{g} = \frac{|\mathbf{b}|\left(\sum_{i=1}^{N} L^{i} v^{i} \Delta t_{n}\right)^{g}}{V} \tag{2.25}$$

with V a reference volume, which is the total simulation cell in conventional DDD simulations, and $\left(\sum_{i=1}^{N} L^{i} v^{i} \Delta t_{n}\right)^{g}$ is the area swept by all mobile dislocations of the slip system **g** during a time increment $\Delta t_{n,}$ with

$$v^i = \begin{cases} 0, if\ \tau_F > \tau_{eff}^i \\ \dfrac{\left[\tau_{eff}^i - \tau_F sign\left(\tau_{eff}^i\right)\right] b^i}{B}, if\ \tau_F \le \tau_{eff}^i \end{cases} \quad (2.26)$$

Where B is drag coefficient and b^i is Burger's vector of the i^{th} segment.

For the so-called massive simulations (i.e. with high dislocation density), Periodic boundary conditions (PBC) are needed in order to ensure that dislocation fluxes are balanced at the boundaries of the simulation cell to avoid undesirable size effects due to finite dimensions and artificial dislocation losses. In the presence of PBC, it is found that the dislocations are self-annihilating after certain number of boundary crossing. This artifact was found to reduce the average distance between the dislocations, density of mobile dislocations, their storage rates that in turn affects the strain hardening properties. In order to avoid the artifacts due to self-annihilation of a portion of dislocation loops after certain number of boundary crossing Madec et al. [222, 223] suggested the use of orthorhombic simulation volume.

Boundary conditions that are more rigorous need to be implemented to treat more general cases, such as a crystal with free surfaces, a crystal containing particles of a second phase or poly-crystal containing grain boundaries. A peculiar behavior was observed when the dislocation interacts with free surface resulting in the annihilation of the dislocation due to image forces. These image forces are ghost forces due to modulus mismatch between the materials and free medium. These image forces were found to be inversely proportional to distance between dislocation and the free surface. In the same way, the dislocations feel an opposing force for motion form rigid boundaries. The other details of formulation of DDD code microMegas can be found in the literature [224, 225].

Both network and nodal dislocation discretization models are extensively used to study the collective dislocation behavior leading to strain hardening due to junction formation, dislocation obstacle interaction, Baushinger effect, temperature dependence of flow stress in single crystals, etc. Kubin et al. [204], Monnet et al. [205] and Sylvain et al. [206] carried out three dimensional DDD simulations in pure Fe to study the slip system interaction, forest hardening and hardening due to the presence of impenetrable obstacles (Cr rich precipitates), voids and loops. Fivel et al. [207] performed the fatigue loading on 316L stainless steel to explain the persistent slip band formation. It was suggested that the MD simulations can feed the DDD simulations at least in two ways; one, dislocation mobility and second, local rules for dislocation loop interaction. Chaussidon et al. [208] performed DDD simulation on 16MND5 steel to study the plastic deformation behavior at ductile brittle transition temperature. DDD simulations have also been carried out to study the effect of different loading parameters on the yield strength, to examine the role of dislocation multiplication and dislocation mobility on the plasticity in small samples under uni-axial compression. Roman et al. [209] carried out 3D DDD simulation of interactions between prismatic loops different sizes and mobile dislocations in pure iron. It was found that the loop with its center on the slip plane offers maximum resistance to moving dislocation in comparison to loops with offset centers from the slip plane. Sylvain et al. [228, 232] carried out the DDD simulations to find the slip system interaction, Orowan/forest strengthening mechanisms and bauschinger effect in α iron at room temperature and in aluminum respectively. It was found that the collinear dislocation interactions are stronger interaction in comparison to symmetrical, asymmetrical, edge and dipolar and coplanar interactions. Zhou et al. [211] studied the effect of sample size on the flow stress of the single crystal Ni samples using DDD simulations.

Even though a lot of work has been carried out at individual (nano and meso) scales, limited information is available on bridging the different length scales. Studies involving the properties that can be extracted from different length scales have been carried out by a few authors. In this way a hierarchical multi-scale modeling technique and linking of different length scale, to determine the mechanical properties of materials under irradiated and un-irradiated conditions have been evolved. Diaz de la Rubia et al. [212] used MD and DDD simulations to explain the plastic flow localization in irradiated Cu. The kink formation mechanism in FCC materials observed during atomistic simulation of interaction of dislocation with SFT has been used as one of the local rules in DDD simulations. Sylvain [213] in his work performed DD simulations to predict the irradiation hardening in reactor pressure vessel steel, where a scale transition law was used to link nano and meso-scales. Bulatov et al. [214] have shown that the formation of dislocation junctions (a lomer-cottrell lock) and the force required to destroy this junction obtained from MD simulations are the critical conditions which can be used as local rules in DD simulations. Wirth et al. [17] successfully coupled the spatial distribution of defects to three dimensional DDD simulations to investigate the corresponding mechanical behavior of irradiated Cu and Pd. Yoshiie et al. [132] used MD and MC results in DD simulation to assess the effect of irradiation on spallation neutron source materials and obtained stress strain curve for irradiated nickel. Robertson et al. [215] studied the tensile response of the single iron crystal in the presence of ODS particles and loops which are modeled as impenetrable and penetrable faceted obstacles respectively. No shearing of the obstacles or absorption of the loops was considered.

Recently, Groh et al. [216] showed the complete multi-scale approach to determine the stress strain curve for the single crystal aluminum under unirradiated condition explaining successful linking of nano-scale to meso-scale and meso-scale to micro-scale. Dongshen li et al. [217] studied the collective interaction of dislocation and loops in Fe to determine the critical shear stress required for the dislocations to overcome the small frank sessile loops. Based on the outcome of the DD simulation, phenomenological equation was derived to relate the irradiation dose with the critical shear stress in the presence of the irradiation induced defect clusters. The phenomenological law was used in the self consistent viscoplastic formulation to find the yield strength of the irradiated T91 material. The results were found to be in good agreement with the experimentally reported. Gururaj et al. [218] carried out 3D DDD simulations in ferrite matrix with and without irradiation defects. Also the effect of oxide dispersiods on the deformation behavior of the ferrite matrix was studied in the presence of irradiation induced loops. In order to reduce the computational load, the loops and ODS particles were modeled as soft single faceted and hard eight faceted features respectively. It was found that the plastic strain localization is more pronounced in irradiated oxide dispersion (OD) free materials than in the material with oxide dispersion which is also reported in the literature. It was found that the materials in the presence of OD particles suppress the irradiation hardening due to loops and the plastic deformation spreading was found to be more homogeneous in the grains. Arsenlis et al. [219] have carried out DDD simulations to study plastic deformation localization in Fe in the presence of irradiation induced frank loops. The density of frank loops was varied to find the dependence of resolved shear stress on loop density.

CHAPTER 3: EXPEIRMENATL TECHNIQUES

3.1 Introduction

In the present work one of the FM steels T91 has been used to study the mechanical properties and microstructural changes before and after irradiation. The T91 steel was received as a plate of dimensions 2400mmx1200mmx15mm. The material was taken from a rolled plate normalized at 1050 ^{0}C for 15min followed by water cooling. The quenched material was then tempered at 770 ^{0}C for 45 min followed by still air cooling. The chemical composition of the as-received material is given in Table 3.1.

Table 3.1: Nominal composition of T91 material under as-received conditions

Material	C	Mn	P	S	Si	Cu	Ni
T91	0.097	0.386	0.02	0.005	0.218	0.08	0.115
	Cr	Mo	Al	Nb	V	Ti	N
	8.873	0.871	0.009	0.077	0.195	0.003	0.044

The different experimental techniques used in the present work are as follows;

1] Irradiation experiments by Ar^{9+} ions to dose levels of 5, 10 and 20dpa

2] Grazing incidence X-ray diffraction measurements

3] Nanoindentaion, and

4] Transmission electron microscopy of irradiated and unirradiated T91 steel samples.

3.2 Irradiation experiment: sample preparation and experimental conditions

Thin samples of dimensions 20mm x 20mmx1mm were cut from the main plate using electric discharge machining. Subsequently, these specimens were mechanically polished up to 1000 grade emery paper to have a smooth surface and finally polished using diamond paste upto the mirror finish surface. Mechanically polished samples were electro polished in a solution of

95% methanol and 5% perchloric acid at a temperature of -60^{0}C by maintaining a voltage of 20V to remove the work hardened layer due to mechanical polishing. These samples were mounted on a steel flange and then irradiated with 315 KeV Ar^{9+} ions from ECR, Variable Energy Cyclotron, Kolkata, India to different irradiation doses (fluence of 1 x 10^{15}, 2 x 10^{15} and 6 x 10^{15} ions/cm^2). During irradiation, the temperature of the sample did not rise above 313 K which was continuously measured by a thermocouple connected in the closest proximity of the samples.

Damage of materials due to irradiation is presented in terms of displacements per atom (dpa) [28, 241], which represents on an average, how many times an atom is displaced from its lattice site in a given volume of material without accounting the recombination and replacement collisions. Details of the dpa calculations for irradiation by different types of particles can be found in Ref [28].

The ion irradiation damage in the units of displacements per atom (dpa) is calculated by using Stopping and Ranging of Ions in Matter (SRIM-2008) program [221]. The damage profile of the Ar^{9+} ions is as shown in Figure 3.1. SRIM program is based on the binary collision approximation at 0 K temperatures in amorphous material without accounting the recombination process. The equation used for dpa calculation is as follows,

$$dpa = \frac{Total\ number\ of\ atoms\ displaced\ in\ a\ unit\ volume\ of\ material}{Number\ of\ atoms\ present\ in\ the\ unit\ volume} \tag{3.1}$$

or

$$dpa = \frac{Number\ of\ atoms\ displaced\ by\ an Ar^{9+} ion \times fluence}{Number\ of\ atoms\ in\ the\ irradiated\ volume} \tag{3.2}$$

Number of atoms displaced by an ion is obtained from SRIM calculations, for Ar^{9+} ions it is ~4300 atoms. Fluence is the product of flux and time where, flux is number of ions per second

per unit area. For the present study the fluence values considered are 2 x 10^{15}, 4 x 10^{15} and 8 x 10^{15} ions/cm^2. Number of atoms in the irradiated volume is the product of beam cross section area, beam penetration depth and atom density of the material and are determined to be 169μm^2, 250 nm and 8.024x10^{28} atoms per m^3. Substitution of above values in Eq. 3.2 results in ~5, ~10 and ~20 dpa corresponding to fluence of 2 x 10^{15}, 4 x 10^{15} and 8 x 10^{15} ions/cm^2 respectively. At low temperature irradiation saturation of mechanical properties are observed 5-10 dpa depending on the temperature. In order to study the saturation behavior of the T91 material, doses mentioned above were used.

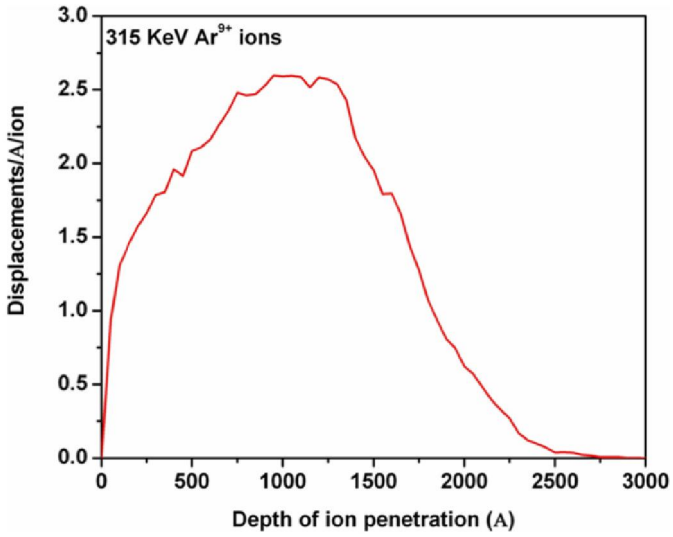

Figure 3.1: Schematic diagram showing the irradiation damage profile with respect to depth of penetration of Ar^{9+} ions in Iron-chromium alloy.

3.3 GIXRD sample preparation and experimental conditions

Subsequent to irradiation, samples were firstly subjected to X-ray diffraction experiments. GIXRD patterns were collected from PAN analytical Expert pro MRD for unirradiated as well as irradiated samples at grazing angle 1^0 and 2^0 using CuK_α radiation. Selection of these angles was based on the depths of penetration of CuK_α in T91 which were

found to be around 72.8 and 145.6 nm for grazing incident angles (ω) 1° and 2° respectively. These GIXRD patterns, therefore, provide microstructural information from two different layers. The range of 2θ was selected from 30^o to 120^o and a step scan of 0.02 degree was used. The time per step was selected as 3 second per step. Instrumental broadening correction was made using a standard defect free Si sample. In each case, a corrected β (integral breadth) was obtained using the software Winplotr [222] by using the refining parameters u, v, w, η obtained by Caglioti plot from defect free Si sample.

3.4 Nanoindentation: sample preparation and experimental conditions

Subsequent to GIXRD measurements, nanoindentation was carried out using Hysitron nanoindenter in the depth-controlled mode on the irradiated as well as unirradiated samples in the direction of beam as shown in Figure 3.2. Maximum load during indentation experiment was 2000 μN. The indents were spaced at a distance of 25 microns and at least 10 indents per depth were taken to get the statistically meaningful results.

Prior to carrying out nanoindentation on irradiated samples, unirradiated samples of T91 steel were used to optimize the parameters for nanoindentation. To standardize the load and the depth of penetration, series of experiments were carried out. Three indents were taken as a function depth (Figure 3.3) and average indentation hardness was evaluated. It was observed that at smaller depth of indentation (~100 nm) there was substantial scatter in the value of hardness which beyond 100 nm converged to nearly 2.75 GPa with increase in the depth of indentation (Figure 3.3). Based on this experiment, the optimized depth of indentation was established as 100 nm with corresponding hardness of 3 GPa and using formula $1/E_r=(1-$

$v_m)/E_m+(1-v_i)/E_i$; where E_r, E_m and E_i are reduced sample and indenter modulus, v_m and v_i are Poison's ratio of sample and indenter, Young's modulus of the steel was estimated as 220GPa.

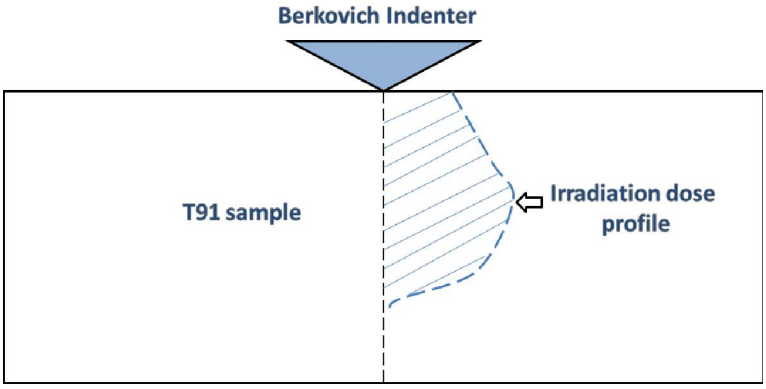

Figure 3.2: Schematic diagram showing the indenter and samples geometry before indentation.

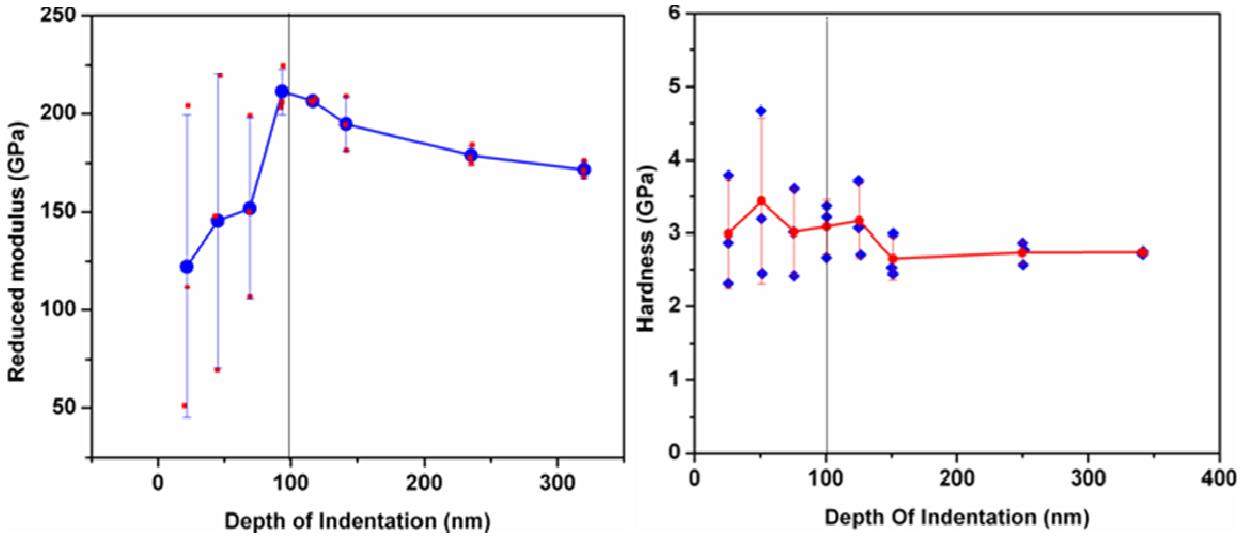

Figure 3.3: The variation of reduced modulus (a) and nanohardness (b) with respect to depth of indentation.

3.5 TEM sample preparation and experimental conditions

After conducting nanoindentation experiments, the samples were mechanically back thinned up to a thickness of 70-100μm. Discs of 3 mm diameters were punched out from back thinned samples. These discs were single jet thinned in Struers Tenupol-5 twin jet machine by using an electrolyte containing 5% perchloric acid and 95% methanol. The applied voltage was

kept at 20 V (DC) and the temperature of the bath was maintained at -60 ^{0}C throughout the thinning process.

CHAPTER 4: NANOINDNETATION AND MICROSTRUCTURE CHARACTERIZATION

4.1 Introduction

In the present study irradiation was imparted on the T91 ferritic/martensitic steel using Ar^{+9} ions. In the present chapter results of the experimental data generated using nanoindentation and microstructure characterization using TEM and GIXRD techniques of irradiated samples has been summarized. Major objectives of this chapter are:

(i) To determine the change in nanohardness of the material due to irradiation at different dose levels using nanoindentation technique.

(ii) Identifying the irradiation induced microstructural features responsible for the change in the nanohardness directly using TEM and GIXRD.

(iii) Correlating the variation in the nanohardness values thus obtained with the yield strength of the material using empirical equation reported in the literature

4.2 Transmission electron microscopy

4.2.1 Microstructural examination of unirradiated samples

TEM examination was performed on unirradiated specimens of the T91 steel to characterize the grain size, morphology of the precipitates, etc. Figure 4.1 shows the presence of several precipitates in the microstructure of T91 steel. Detailed microstructural observations revealed that the matrix comprised a dual phase morphology containing α-ferrite and martensite phases [223]. Chemical analysis of several precipitates showed that high concentration of Cr and Fe in these precipitates which indicated it could be the sigma phase (Table 4.1). In literature, however, most of the precipitates in this steel have been reported as carbide precipitates. In order to identify the precipitate phase unambiguously, systematic tilting experiments were done and

series of selected area electron diffraction (SAED) patterns were taken (Figure 4.2). These SAED patterns were indexed corresponding to the zone axes [001], [011], $[\bar{1}23]$, $[\bar{1}11]$ and [013] of the fcc lattice. Indexing of these SAED patterns confirmed that the precipitates were face centered cubic phases with a lattice constant of approximately 1.1 nm, which is within 5% of the reported value of the $M_{23}C_6$ phase [224]. Based on these informations these precipitates were identified as $(Cr,Fe)_{23}C_6$ phase. The two phases of the steel could also be identified by the difference in the dislocation density. High dislocation density was observed in the martensite regions whereas ferritic regions were relatively free from dislocations. The microstructural investigations also showed typical lath morphology of the martensite phase (Figure 4.3). Majority of the precipitates was found residing at ferrite and martensite lath boundaries. In addition, a fraction of these precipitates was also found within grain interiors. Typical size of the precipitates within grains was <100 nm whereas precipitates at the martensite and ferrite GBs were 100-500 nm in size. The tangled dislocation network and dislocation cells were also found in the unirradiated material (Figure 4.3).

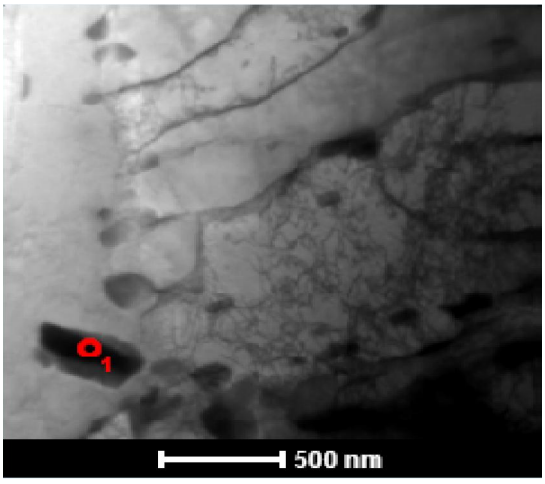

Figure 4.1: Microstructure of matrix and precipitate used for composition analysis by EDS.

Table 4.1: Nominal composition of matrix and a precipitate (shown in Figure 4.1) of T91 FM steel microstructure

Region	Composition in Wt%				
	Fe	Cr	Si	Mo	Mn
Matrix	88.4	8.9	0.11	1.15	1.42
Precipitate	61.6	30.62	-	3.37	4.39

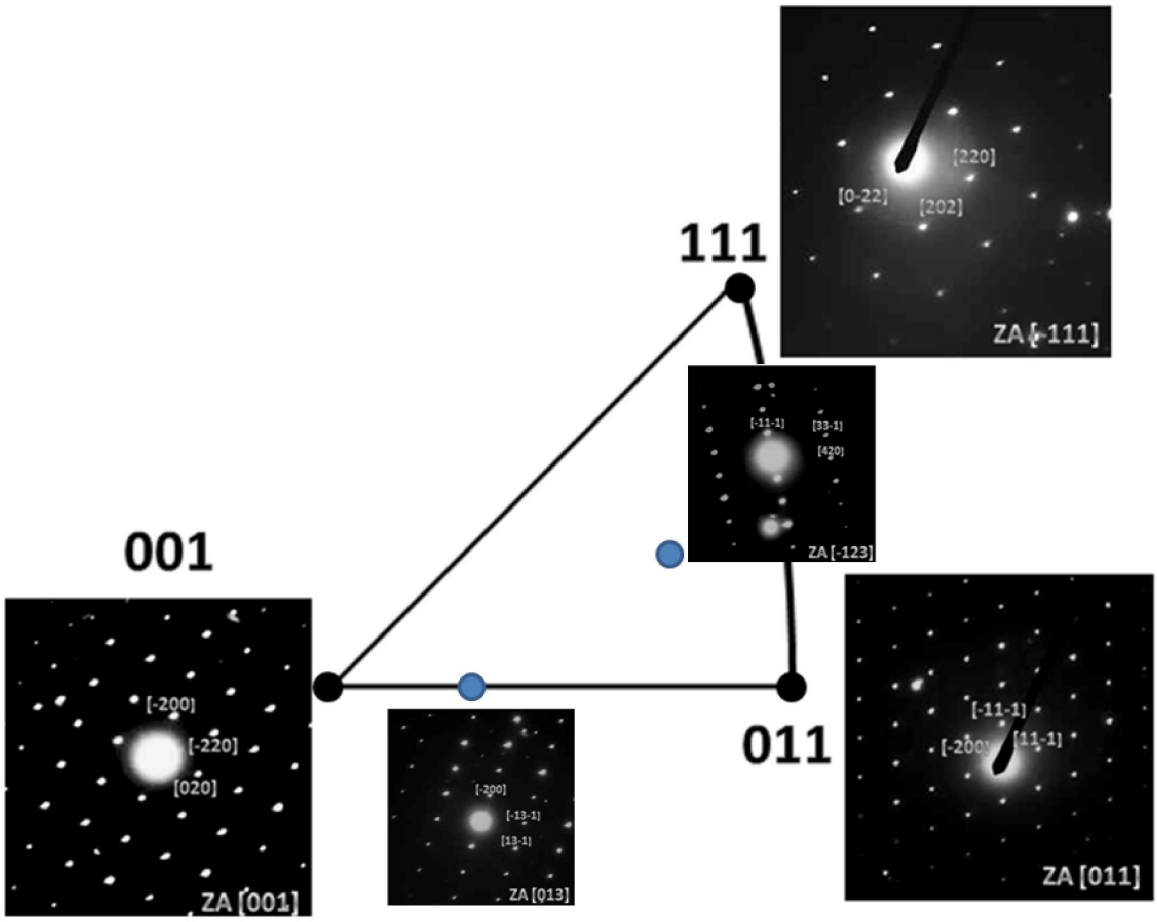

Figure 4.2: SAED patterns of a precipitate with zone axis as poles of the standard triangle of stereographic projection.

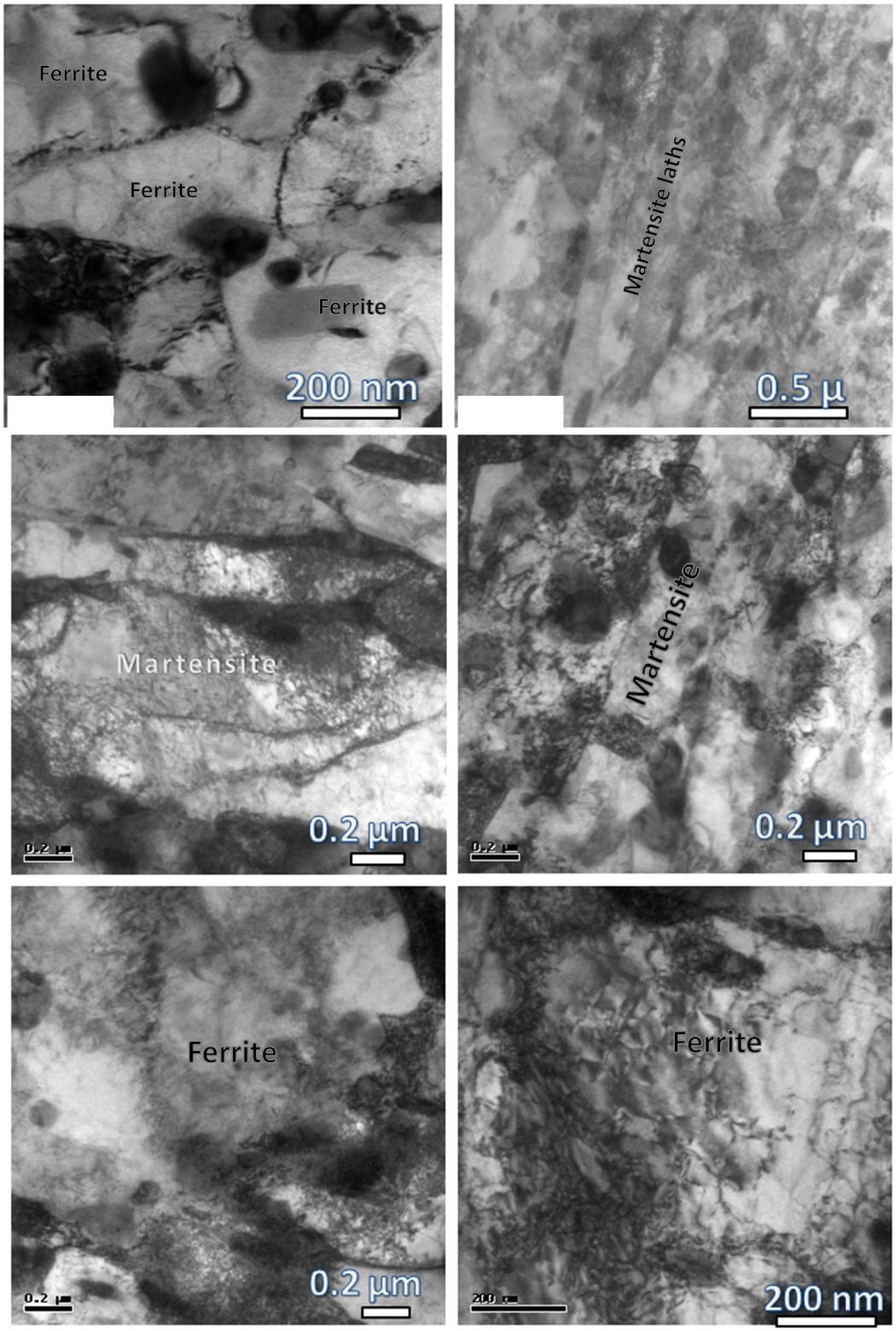

Figure 4.3: General microstructure image of unirradiated T91 sample showing the martensite lath structure with ferrite grains.

4.2.2 Microstructural examination of irradiated samples

A comparison between unirradiated and irradiated samples showed significant changes in the matrix microstructure. Irradiated microstructures consisted of the irradiation induced defects in terms of point defect clusters, dislocation loops and cavities/bubbles along with the pre-existing dislocation network and precipitates. Figure 4.4(a), (b), (c) and (d) show the comparison of the general microstructure of the unirradiated and irradiated samples to a dose 5, 10 and 20 dpa respectively. It was observed that the pre-existing precipitates had undergone partial dissolution upon irradiation due to ballistic collisions of heavy ions (Figure 4.5). For example, precipitates in the unirradiated samples have well defined ellipsoidal shape morphology with smooth edges (e.g; Figure 4.4a). After irradiation, a diffused layer around the pre-existing precipitates was noticed, as shown in Figure 4.5. In addition, precipitates in irradiated samples also showed facets with sharp edge corners (Figure 4.6). These observations remain consistent with all the irradiated samples investigated under TEM indicating dissolution of precipitates is a dominating phenomenon under irradiation. Formations of irradiation induced dislocation loops in the ferrite phase were also noticed in the irradiated samples. The TEM micrographs taken under various bright field and weak beam dark field conditions showed presence of various irradiation induced defects. Figures 4.7 to 4.9 show the typical micrographs of the dislocation loop structures in the samples irradiated with 5, 10 and 20 dpa. The loop size in the 10 dpa sample was found to vary between 10-15 nm and in 20 dpa sample it was found around ~20 nm. Also the cavities/bubbles were found in the samples irradiated with 10 and 20 dpa (Figure 4.9 and 4.10). The cavities/bubbles appeared as a white dot in the micrographs taken under bright field imaging conditions. The cavities/bubbles were heterogeneously distributed in the matrix. The approximate diameter of the bubbles was found to be 1.0-2.0 nm.

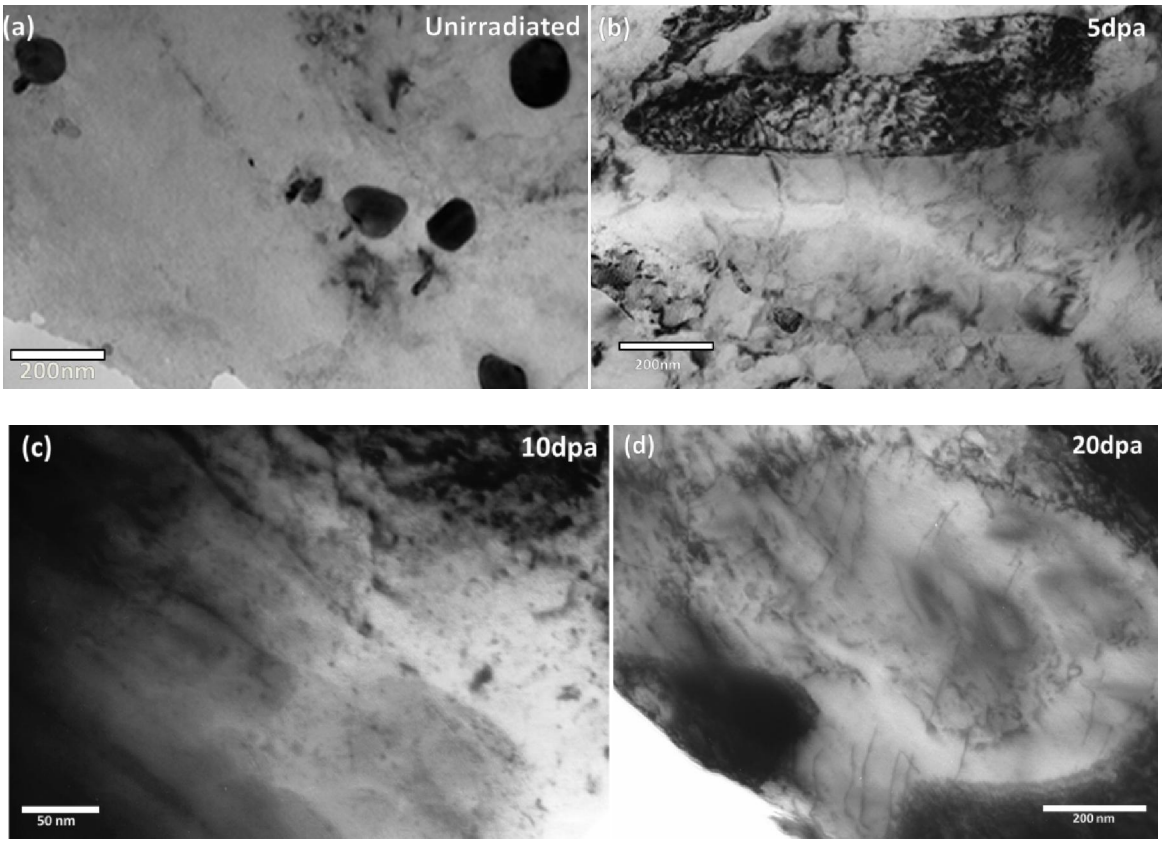

Figure 4.4: General microstructure of T91 samples of a) unirradiated and irradiated to b) 5, c) 10 and d) 20 dpa. Irradiated microstructure showing the black dots and loop like structures.

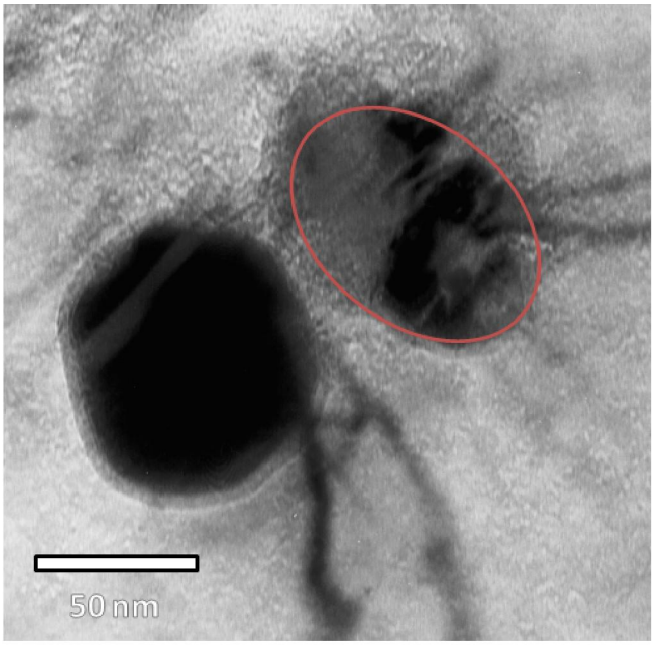

Figure 4.5: Dissolution or amorphization of a precipitate in a sample irradiated to 10 dpa. Highlighted precipitate show diffused edges due to dissolution or amorphization.

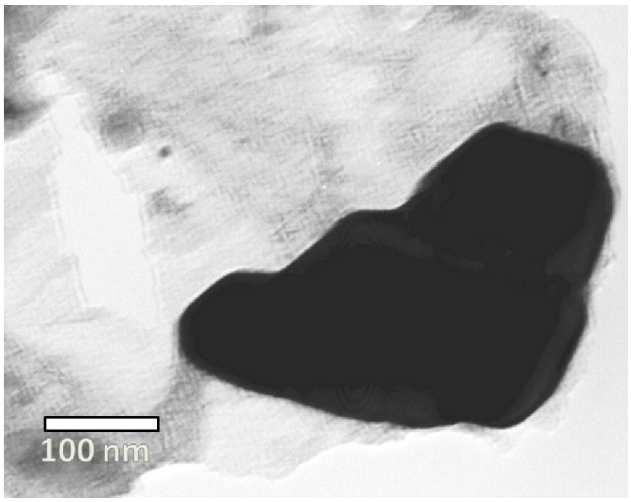

Figure 4.6: Precipitate facets in a sample irradiated to 10 dpa.

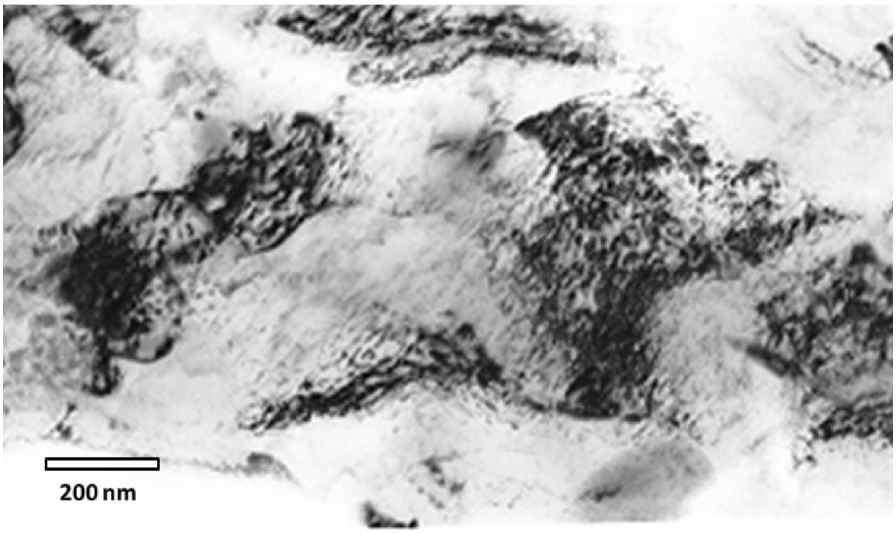

Figure 4.7: Irradiation damage of the matrix of a sample with a dose of 5 dpa.

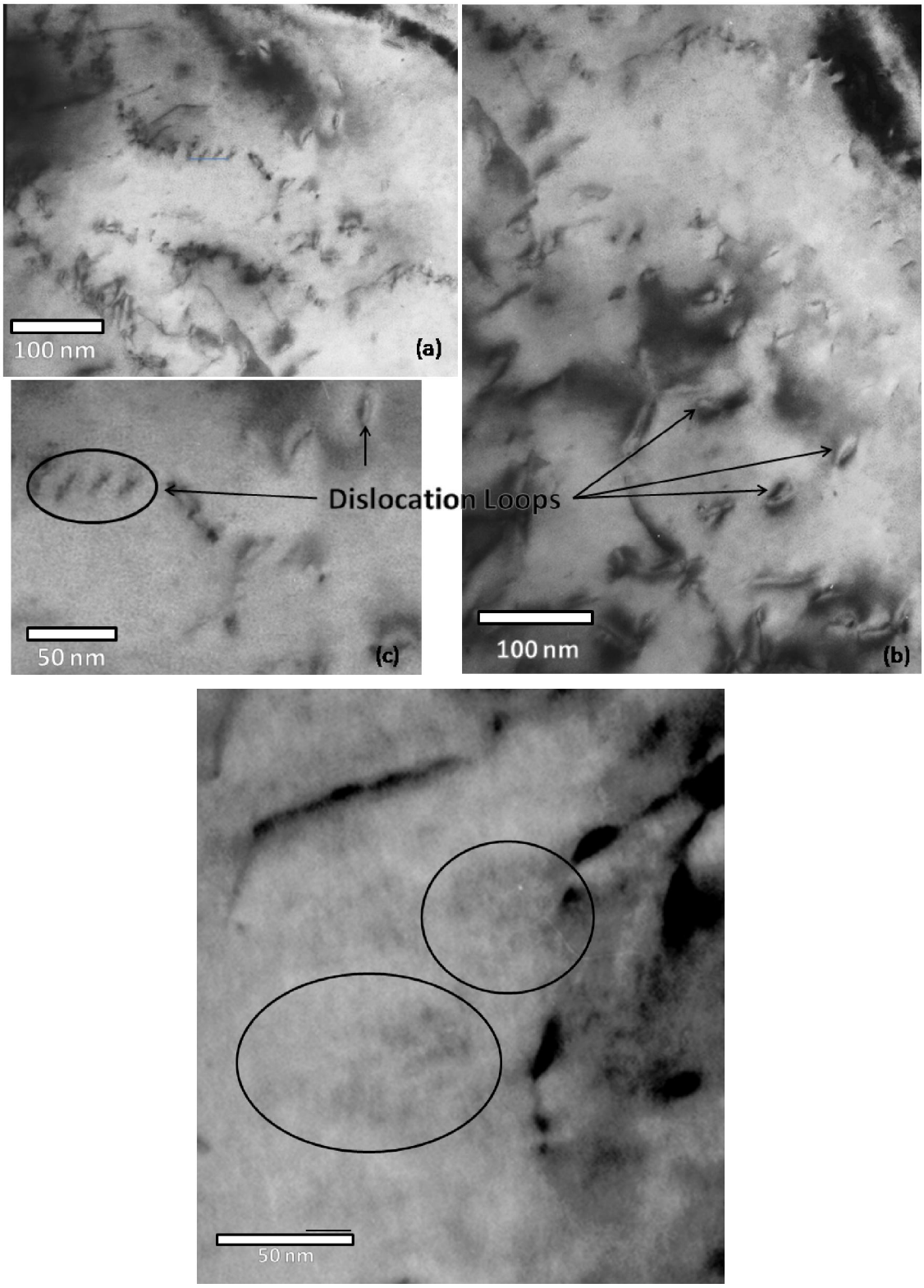

Figure 4.8: Microstructure in a sample irradiated to a dose level of 10 dpa showing the presence of dislocation loop like structures as indicated by arrows. Along zone axis [111] with **g**(4**g**) where **g**=[110] with **g**(2**g**) where **g**= [100].

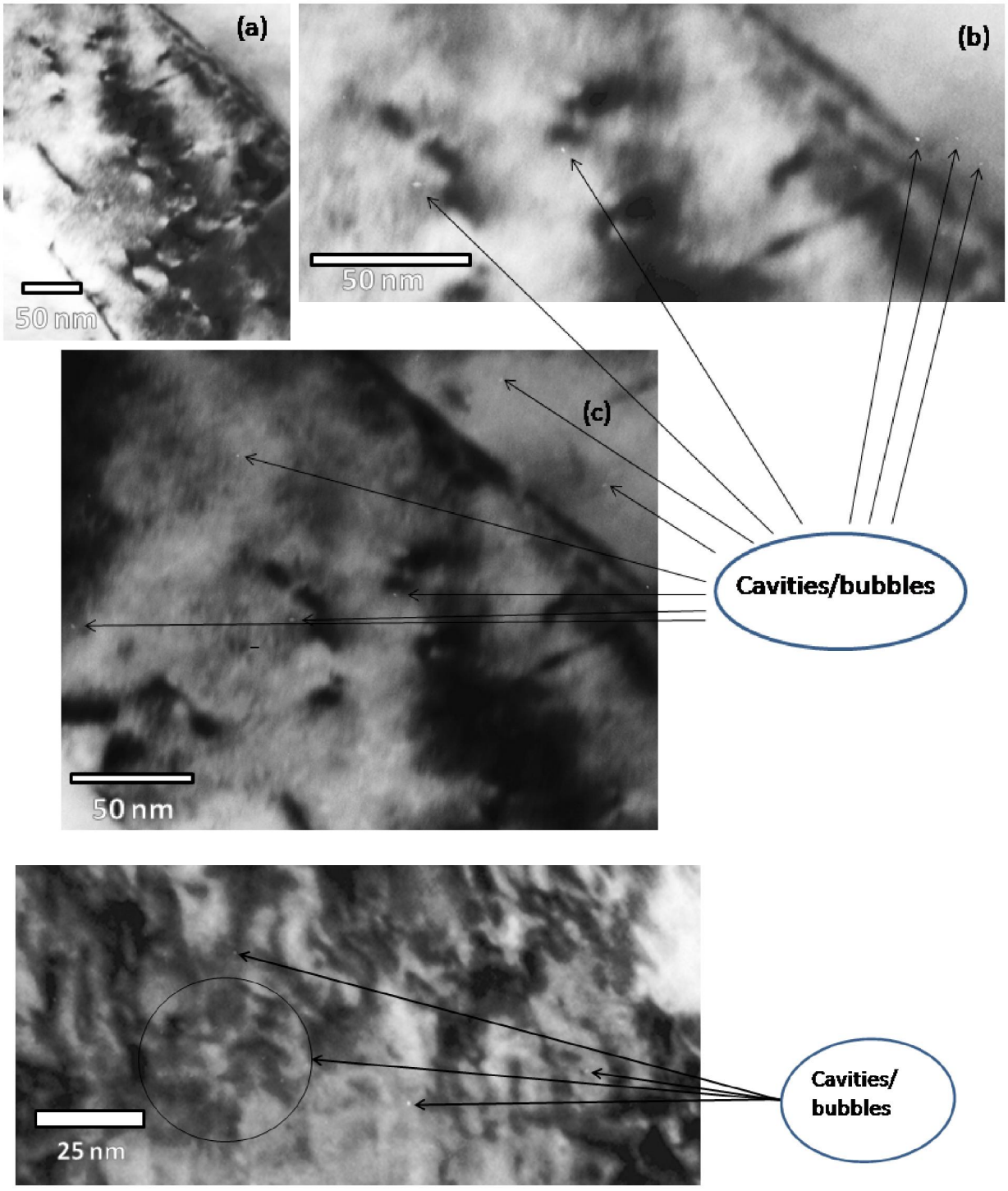

Figure 4.9: Microstructure of a sample with dose of 10 dpa showing the presence of cavities/bubbles as white dots indicated by arrow.

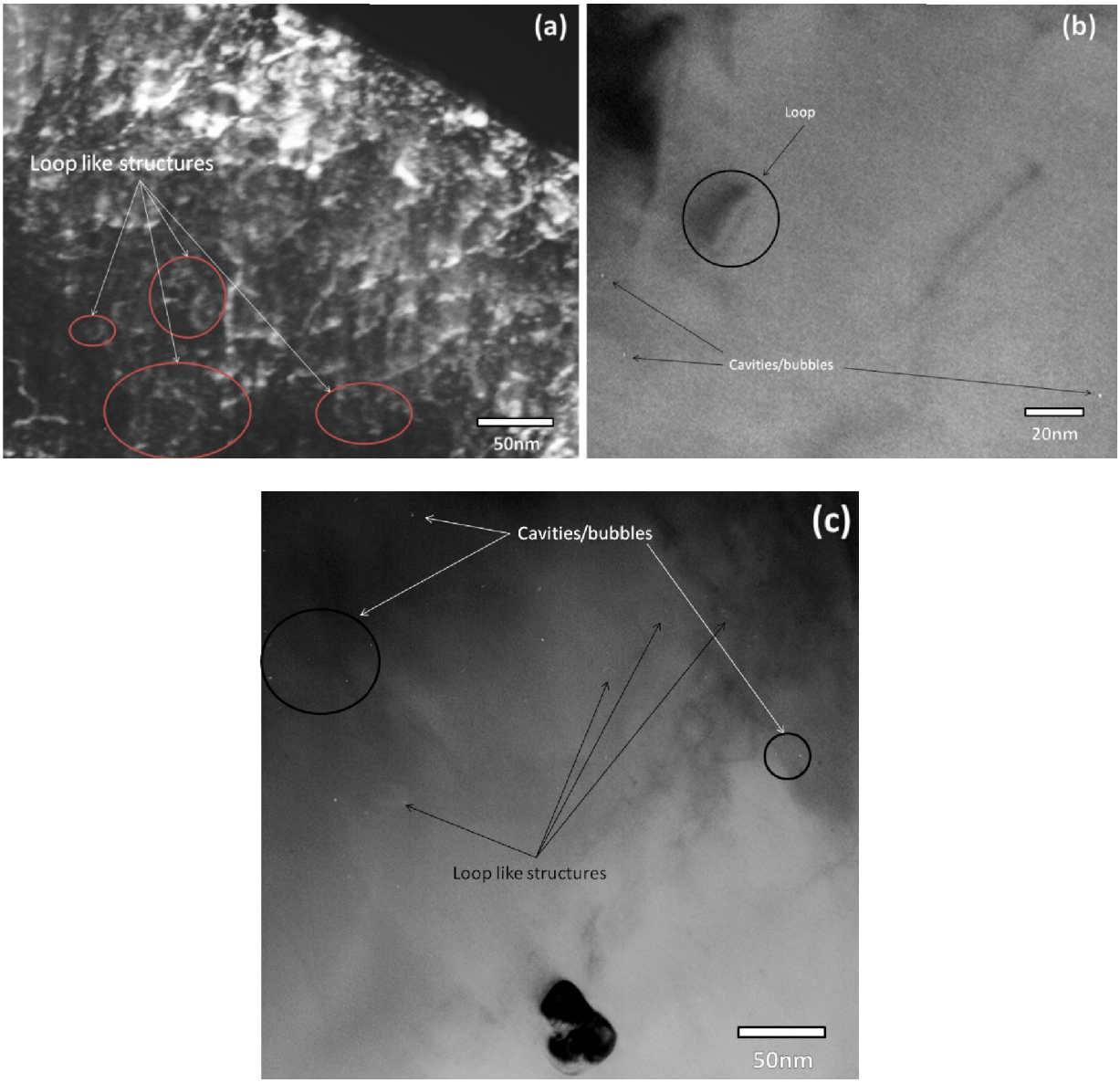

Figure 4.10: a) Weak beam dark field image showing the microstructure of dislocation loop like structures as highlighted by ellipses and other irradiation induced defect clusters, b) and c) presence of bubbles and loop like structures in a sample irradiated to a dose level of 20dpa.

4.3 Grazing incidence X-ray diffraction

The GIXRD profiles for the irradiated T91 samples as a function of dose are shown in Figure 4.11 (a) & (b) for 1 and 2 degree. No analysis could be done on unirradiated samples of

T91 as the broadening of the peaks was insignificant before irradiation and was comparable with instrumental broadening.

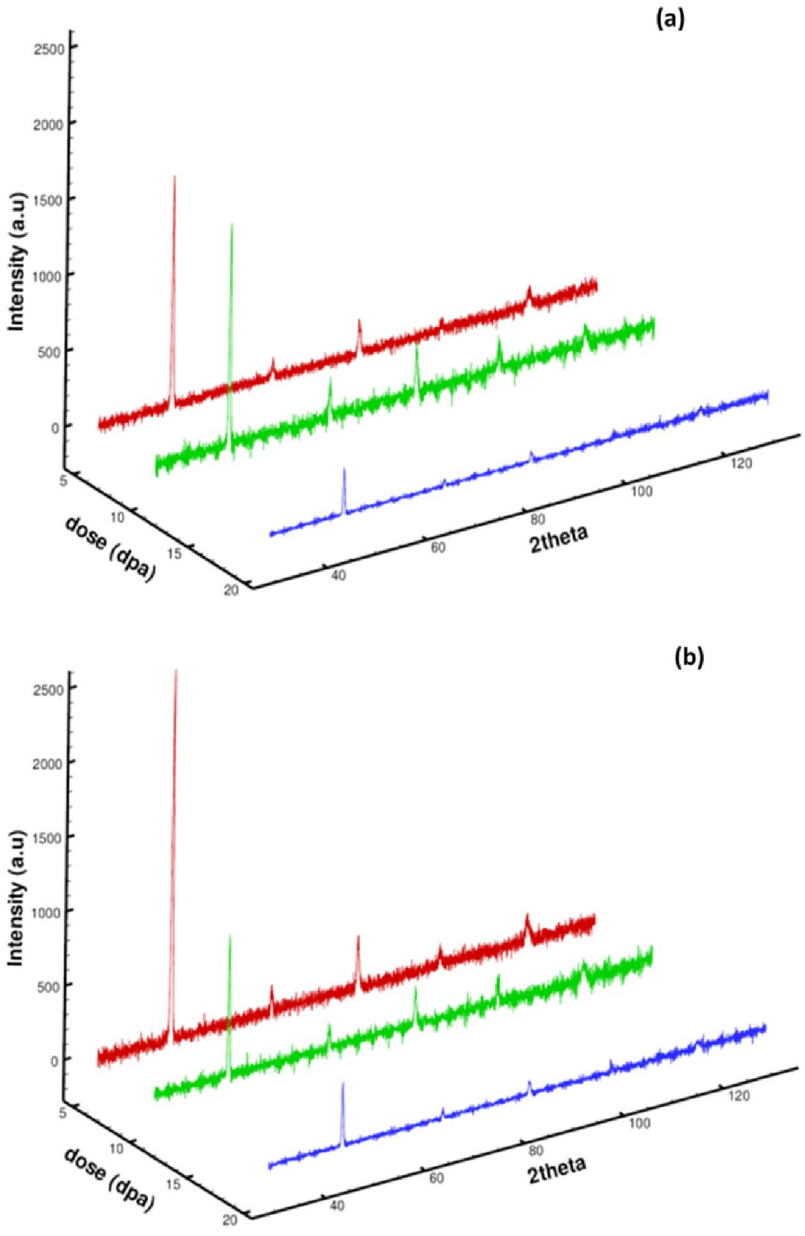

Figure 4.11: GIXRD line profiles of samples irradiated to 5, 10 and 20dpa at an GI angle of 1^0 & 2^0.

Single peak analysis using a simplified breadth method was done on the broadened peaks of the irradiated samples and for this purpose, a Voigt function, which is a convolution of a

Cauchy and a Gaussian function, has been used [225]. Using Voigt function, breadth of Cauchy and Gaussian part can be obtained. For a Voigt function, the shape factor φ (2ω/β, where ω is the Full Width at Half Maxima) varies between the limits $0.63 \leq \varphi \leq 0.94$; where $\varphi = 0.63$ is the Cauchy limit and $\varphi = 0.94$ is the Gaussian limit. In the absence of higher orders of a particular family of reflection the size-strain analysis based on a Voigt function requires the assumption of profile shapes for size and strain broadened profiles. It is generally assumed that the Cauchy component of the Voigt profile is solely due to small crystallite size and the Gaussian component is due to the microstrain.

The relation between D_v, ε, β_c and β_G is given by [108]:

$$D_v = \frac{\lambda}{\beta_c \cos\theta} \tag{4.2}$$

and

$$\varepsilon = \frac{\beta_G}{\tan\theta} \tag{4.3}$$

where, D_v is the volume weighted domain size, is the upper micro-strain. Using simplified breadth method, the irradiated samples were analyzed as a function of dose at the two different depths. The analysis was carried out for two high intensity peaks i.e. (110) and (211) planes for 10 dpa and 20 dpa samples. For 5 dpa samples, the analysis could not be done on (211) peak as the intensity of the peak was low and the shape factor of the peak had fallen beyond the permitted value. The volume weighted domain size (D_v) as a function of dose is shown at different planes in Figure 4.12. It is clearly seen from the Figure 4.12, D_v has decreased systematically with increasing dose of irradiation for both (110) plane and (211) plane. Moreover, it is also observed that there is a monotonic decrease of D_v with depth of penetration. No significant changes were observed in the microstrain values with dose. The values were

found to be around $7x10^{-3}$ for (110) planes and $4x10^{-3}$ for (211) planes at all doses. As these changes fall within error bar, it was inferred that the strain in the matrix phase got saturated prior to the dose of 5 dpa.

In the modified Rietveld analysis, the diffraction profiles have been modelled by pseudo-Voigt (pV) functions using the program LS1 [226]. The initial values of the lattice parameters were obtained from a least square fit of the powder diffraction peaks. The program includes the simultaneous refinement of structural and microstructural disorder of the polycrystalline material. It is based on the Rietveld method combined with the Fourier analysis of the broadened peaks. Crystallite size and the microstrain were regarded as fitting parameters. Instrumental broadening correction was done using a standard defect free Si sample. The lattice parameters, surface weighted average domain size and microstrain were used as fitting parameters simultaneously to obtain the best fit in order to calculate the average values of the fitting parameters.

Figure 4.13 represents a typical whole powder pattern fit using LS1 for the XRD profile of the irradiated T91 sample at a dose of 10 dpa and the extracted results from the plots are shown in Figure 4.14(a) and (b). From the analysis shown in Figure 4.14 (a), it was observed that the surface weighted domain size has decreased with dose of irradiation at a depth of penetration of 73nm as well as at higher depth of penetration i.e at 145 nm. On the other hand, the microstrain values did not change significantly with dose but were found to decrease slightly with depth of penetration (Figure 4.14 (b)).

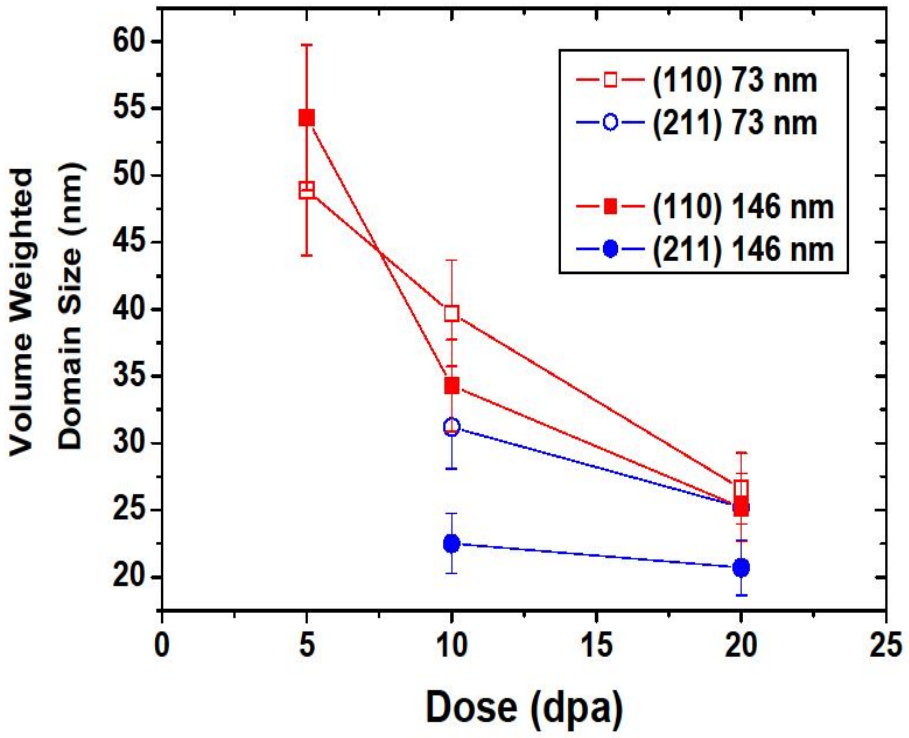

Figure 4.12: Volume weighted domain size as a function of irradiation dose in T91 steel. Decrease in the domain size indicating the increase in defect density as a function of irradiation dose.

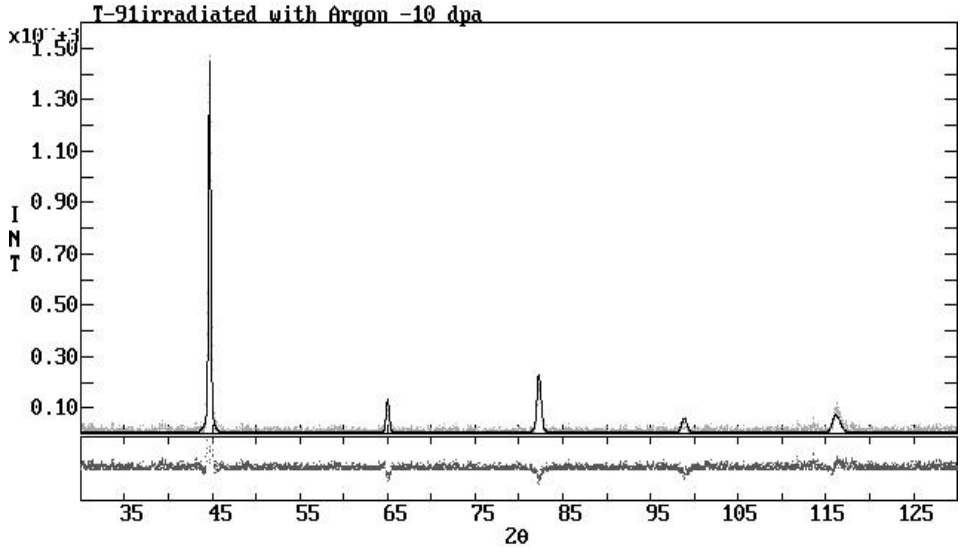

Figure 4.13: Typical whole powder pattern fit for the samples irradiated at 10 dpa.

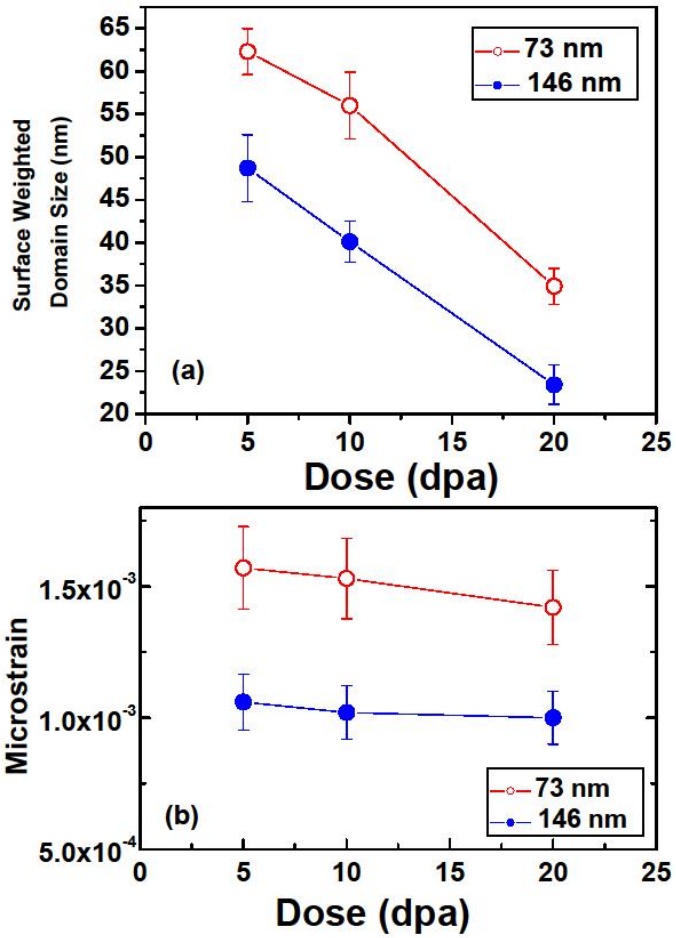

Figure 4.14: a) Surface weighted domain size and b) microstrain as a function of irradiation dose in T91 steel

4.4 Nanoindentation

In order to understand the effect of irradiation induced defects on mechanical properties, Nanoindentation was carried out. The load displacement (LD) curves for the irradiated samples along with unirradiated samples are summarized in Figure 4.15. Increase in hardness with increasing dose could clearly be noticed from the figure. Nanoindentation curves, many a times, showed plateau regions where the depth of indentation continuously increased under constant load. Behavior of material in this region is commonly known as 'pop-in' behavior which represents unhindered propagation of dislocation in the material. The reason for pop-in behavior

has been related to homogeneous dislocation nucleation [227] or activation of well-spaced dislocation sources [228]. Such behavior is highlighted in a magnified view of the portion of LD curve as an inset in Figure 4.15. In the case of unirradiated specimens where the ferrite phase was under the annealed condition presence of pop-in behavior was clearly noticed. In the irradiated material, on the other hand, the pop-in behavior was not observed. Reason for such behavior could be due to the presence of irradiation-induced defects, which hindered the smooth propagation of dislocation motion (Figure 4.15).

Loading part of load vs. depth of indentation curves of irradiated and unirradiated T91samples were fitted with quadratic functions shown in Figure 4.16(a). The difference in the rate of change of load with depth - stiffness (S=dp/dx) - increases with the depth of indentation clearly indicating increase in strain hardening with irradiation dose (Figure 4.16b). However, rate of change of stiffness decreases as function of irradiation dose at peak depth (Figure 4.16b) showing a tendency for saturation behavior. Interaction of dislocations with irradiation induced defects increase the required resolved shear stress by mobile dislocations. The resolved shear stress being proportional to applied load increases the applied load with irradiation. This implies that the peak load at maximum depth of indentation increases with irradiation dose. Increase in peak load with irradiation dose is also observed in Fe-9%Cr alloy irradiated with Fe^{3+} ions.

The variation in hardness with respect to the unirradiated hardness as a function of irradiation dose is shown in Figure 4.17. Irradiated samples have shown a systematic increase in hardness with increasing dose. The typical increase in hardness with respect to unirradiated material was found to be of ~1 GPa, ~1.1 GPa and ~1.4 GPa for samples irradiated with a dose of 5, 10 and 20 dpa respectively. The rate of increase of hardness with dpa is least in the case of

sample irradiated to 10 dpa, whereas it was maximum for sample irradiated to 5 dpa as shown in Figure 4.17. This increase in hardness with irradiation dose and the saturation behavior is in agreement with those reported in literature [103, 104, 108]. This saturation behavior of the hardness value has been attributed to the saturation of irradiation-induced defects in the microstructure. The best fit of the data could be represented in the form of a simple power law $\Delta H=A\ (dpa)^n$ (Figure 4.17) [103, 106]. Inset in Figure 4.17 shows the plot of log (ΔH_{nano}) vs. log (dpa) and log ($\Delta\sigma_{YS}$) vs. log (dpa). The intercept of the linear fit to the data with log ($\Delta\sigma_{YS}$) axis shows the proportionality constant for power law of hardening and slope (*n*) of the fit indicates the rate of change of $\Delta\sigma_{YS}$ as a function of irradiation dose. Linear fits to the hardness and YS had shown a slope (*n*) of 0.242 and 0.235 respectively. These values of *n* matches closely with the one reported in the literature (0.25) for the variation in yield strength as a function of dose [25,106]. Corresponding Y-axes intercepts (i.e. LogK) are found to be -0.41494 and 5.37568 respectively. Comparison of slope (*n*) had shown hardness values are nearly parallel to the experimentally reported YS values as shown in Figure 4.17 (inset). The figure also shows the shifted hardness values (blue color data points) which exactly fall on the linear fit to the experimentally observed shift in YS values of Mod 9Cr-1Mo FM steel irradiated and tested at room temperature [51]. Thus a correlation $\Delta\sigma_{YS} = K\ \Delta H_{nano}$ has been proposed, where K value is approximately 0.324.

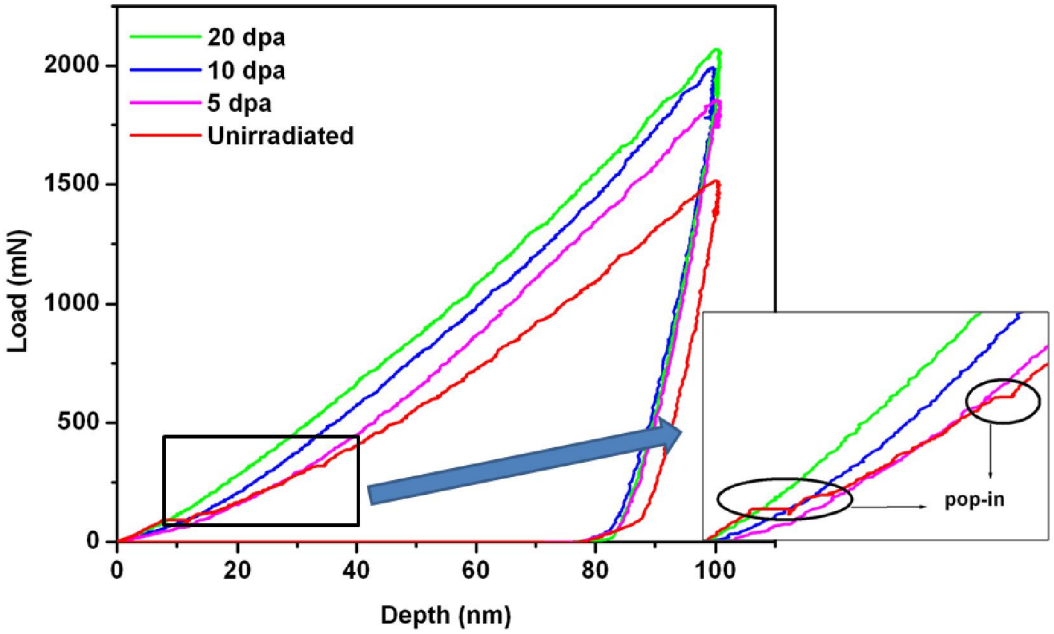

Figure 4.15: Load vs. depth of indentation curves for irradiated and unirradiated samples with pop-in.

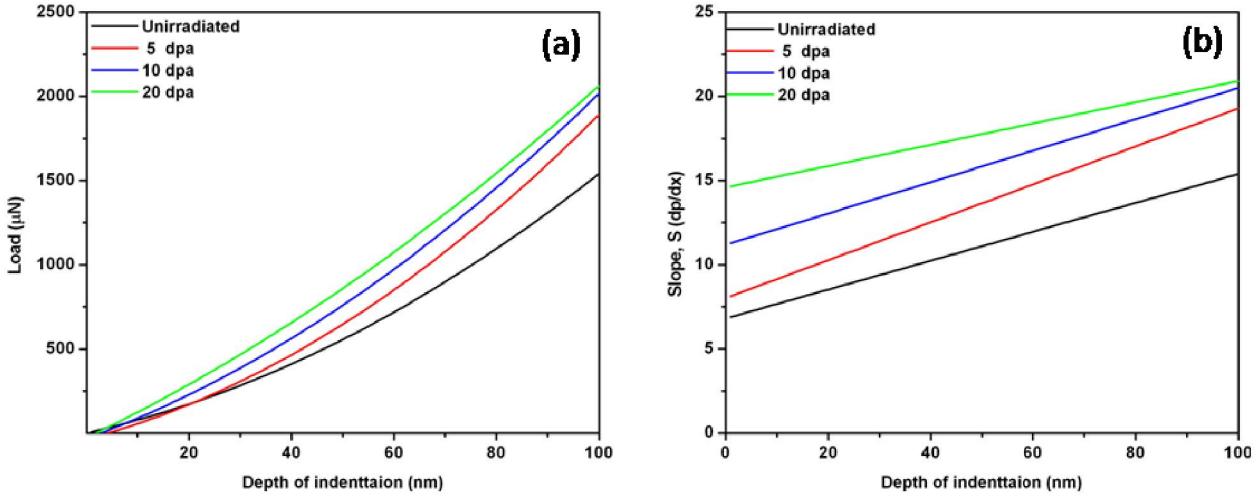

Figure 4.16: a) Load vs. depth of indentation curves with quadratic fit to loading part, b) stiffness as a function of depth on indentation.

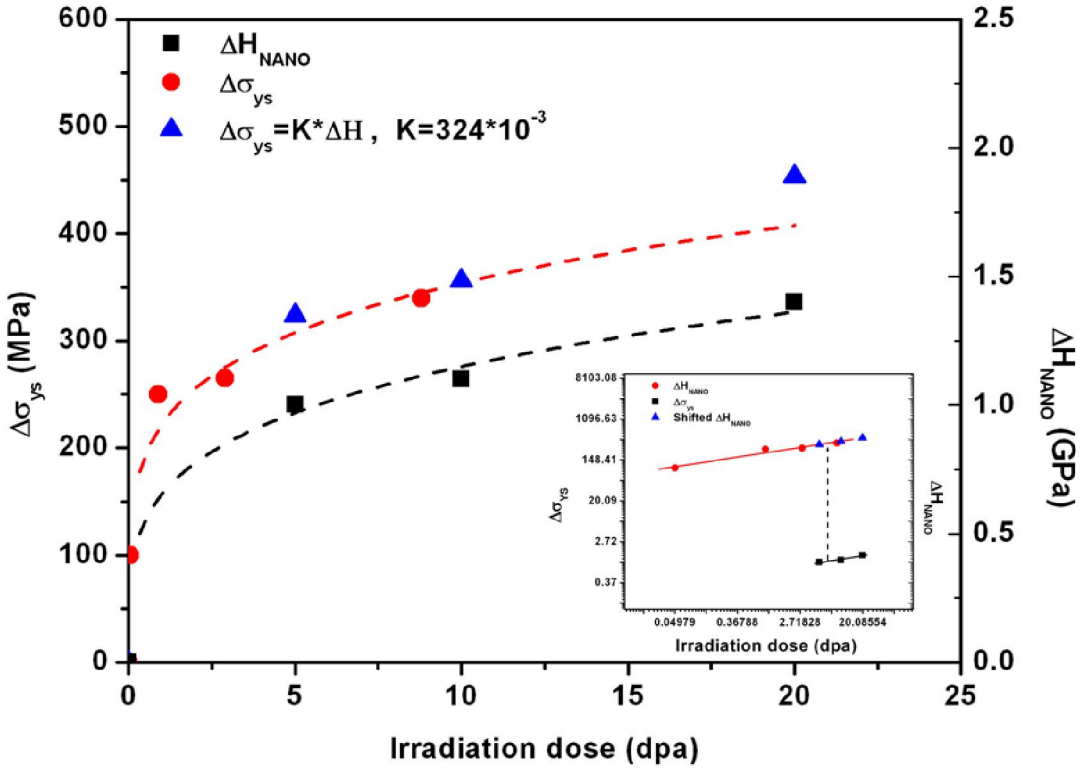

Figure 4.17: Change in hardness (GPa) and change in yield strength versus irradiation dose.(inset figure log ($\Delta\sigma_{YS}$) vs. log (dpa) for change in experimental change in YS (MPa) [51] and log (ΔH_{nano}) vs. log (dpa) for change in hardness determined present work).

Similarly, Rice and Stoller [93] correlated the change in yield strength to change in nanohardness as given in Eq.4.1 similar to the equation proposed in the present study. The equation is based on the relation between yield strength with Vickers hardness and Vickers hardness with nanohardness.

$$\Delta\sigma_{YS} = K \times \Delta H_{nano} \tag{4.1}$$

where the ΔH_{NANO} is the change in nanohardness and $\Delta\sigma_{YS}$ is the change in YS, K is slope of the linear fit between ΔH_{NANO} and $\Delta\sigma_{YS}$, and it was found to be 0.274. The details of the correlations are as given in the reference [93].

The estimated change in yield stress of T91 material due to irradiation of 5, 10 and 20 dpa by the correlation proposed in the present study is as shown in Figure 4.17. The qualitative and

quantitative assessment of the change in yield strength of the irradiated samples using correlation as given in Eq.4.1 was found to be in agreement with reported irradiation hardening behavior of the FM steels.

4.5 Discussions

Irradiation of materials with high energy Ar ions (> 1MeV) results in a higher depth of penetration and narrower region of deposition. Irradiation with low energy Ar ions (< 80KeV), on the other hand, results in sputtering phenomenon which preferentially removes atoms from the material surface. Irradiation with intermediate energy range (~200-800 KeV), however, provides a broad region of deposition of Ar ions. The deposition region of Ar ions of 315 KeV in T91 steel was found to be ~200 nm with peak damage region located at nearly 100 nm depth from the surface (Figure 3.1 in Chapter 3). Therefore, irradiation by the intermediate energy ions provides sufficient volume of irradiated material from where information about the local microstructure details using TEM/GIXRD tools and macroscopic properties using nanoindentation can be extracted. Implanting Ar^{9+} ions into a metal could knock out atoms in crystal lattice from its equilibrium position and cause collision cascades, inducing vacancies and interstitial atoms. The aggregation, formation and disappearance of these point defects induce larger size defects such as black spot damage and the secondary defects such as network dislocation and dislocation loop. During initial stages of irradiation, rate of formation of vacancies and interstitial atoms are higher. With the formation of secondary defects, which act as sink for vacancies and interstitial atoms, the rate of formation of these defects reduces and finally a steady state condition is reached. During neutron irradiation of T91 up to 7 dpa presence of the small dots was noticed [20]. Upon extending neutron irradiation up to 10 dpa formation of bubbles and other defects has been noticed. Similarly, a comparative study of irradiation by

proton and neutron has shown that the pattern of defect generation is nearly same in both the cases [28].

Two GI angles near peak damage region were chosen in such a way that the averaged effect of irradiation on the microstructural parameters associated with XRD-LP such as domain size and microstrain can be determined. The GIXRD-LPA (Figure 4.12 and 4.14a) results have shown decrease in domain size as a function of irradiation dose. This decrease in the domain size observed in of GIXRD-LPA can be attributed to irradiation-induced defects observed in TEM investigation. The reduction in the domain size with dose as obtained from LPA confirms the formation of irradiation defects partitioning the microstructure into smaller coherent domains. The domain sizes determined by LPA are comparable to the domain sizes indirectly estimated by TEM. For example, for the volume density of loops (~10^{22} m^{-3}) a typical separation between the two loops would be given by ~$1/\sqrt[3]{\rho}$(~46nm) where ρ is volume density of loops. On the other hand, the microstrain was expected to be higher with the generation of defect clusters. In our analysis, it did not show any significant change with dose of irradiation but were slightly less in more defect concentrated region. The increased defect concentration near the peak damage may have relaxed the overall strain in the matrix due to microstructural effects. The microstructural investigation results are as tabulated in the Table 4.2.

A typical experimental LD curve (Figure 4.15) of unirradiated material had shown the presence of pop-in due to the dislocation avalanches during plastic deformation. This type of pop-in is also observed by other authors during nanoindentation of different materials are due to homogeneous dislocation emission phenomena and activation of well spaced dislocation sources [249, 251, 252]. This pop-in behavior is not observed in LD curves of irradiated materials. This

is due to the obstruction of nucleated and propagating dislocations by irradiation-induced defects frequently in comparison to unirradiated material where the defects are not present. From figure 4.15 it can also be observed that the peak load at maximum depth of indentation increases with irradiation dose which is also reported by Shin et al. [92].

The hardness values determined from nanoindentation have shown saturation behavior similar to YS with increase in irradiation dose and it can be fitted with power law of the form ΔH_{nano} or $\Delta\sigma_{YS} = K_1(\text{dpa})^n$, where K_1 and n are fitting constants (Figure 4.17). Comparison of exponent n for $\Delta\sigma_{YS}$ values from literature [51] (~0.24) and ΔH_{nano} values from present work (~0.24) had shown good agreement with each other (Figure 4.17). The shifting of ΔH_{nano} towards $\Delta\sigma_{YS}$ as shown in inset of Figure 4.17 aligned the ΔH_{nano} data with that of $\Delta\sigma_{YS}$ obtained from literature[51]. Thus a correlation $\Delta\sigma_{YS} = K_2\Delta H_{nano}$ had been proposed, where K_2 value is approximately 0.324 as compared to 0.274 reported in the literature [93] for similar family of steels. In order to cross examine that the variation in hardness indeed shows changes in yield strength by irradiation induced defects, Taylor equation [230] can be used. Based on the density and the size of defects (loops and bubbles) observed during microstructural investigation (listed in Table 4.2) change in YS was estimated using the following equation.

$$\Delta\sigma = M\Delta\tau \tag{4.2}$$

where $\Delta\sigma$ represents change in axial stress, $\Delta\tau$ change in shear stress and M Taylors' factor, which is approximately equal to 3.06. $\Delta\tau$ can be expanded as follows in presence of defects,

$$\Delta\tau = \alpha_l \mu b\sqrt{\rho_l d_l} + \alpha_c \mu b\sqrt{\rho_c d_c} \tag{4.3}$$

where μ is shear modulus, b Burgers vector, α_l, ρ_l, d_l and α_c, ρ_c, d_c are defect strength coefficients, density and diameter of loops and cavities/bubbles respectively. In the present work

$\alpha_l = 0.4$, $\alpha_c = 0.5$, $\mu = 82 \times 10^9 GPa$, $b = 2.5 \times 10^{-10} m$ [61]. Irradiation induced defect densities were approximated to be of the order of $\rho_l \approx \rho_c \approx 10^{22} m^{-3}$, defect diameters $d_l \approx 200 \times 10^{-10} m$ and $d_c \approx 20 \times 10^{-10} m$.

Based on density and the size of defects (loops and bubbles) (Table 4.2) change in YS was estimated by Taylor formula is ~440 MPa, whereas increase in room temperature YS of conventional tensile samples irradiated at low temperatures (< 300^0C) was reported to be ~500 MPa for a dose of 20 dpa [231]. The estimated $\Delta\sigma_{YS}$ values are as tabulated in Table 4.3. The variation in YS is within 20% and can be attributed to the statistical variation as well as on other experimental and microstructure parameters.

Table 4.2: Summary of results obtained from TEM, GIXRD and nanoindentation experiments.

Dose	**Loops (nm)**	**Cavities (nm)**	**Micro-strain $1^0/2^0$**	**Domain size (nm)**		**ΔH (GPa)**
				Surface $1^0/2^0$	**Vol $1^0/2^0$**	
Unirr	-	-	-	-	-	0
5	-	-	1.6/1.1	62.5/50	52.5/-	1.0
10	~15.0	<2.0	1.5/1.05	56/40	37.5/27.5	1.1
20	~20.0	<2.0	1.4/1.0	35/23	27.5/22.5	1.4

Table 4.3: Comparison of estimated YS from the correlation $\Delta\sigma_{YS} = K\ \Delta H_{nano}$ and the power law fit to experimental YS values.

Dose	**YS (MPa) (from Fit to Literature data)**	**YS (MPa) (from $\Delta\sigma_{YS} = 327\ \Delta H_{nano}$)**
5	**~315**	**~327**
10	**~371**	**~360**
20	**~437**	**~457**

4.6 Closure

In the present chapter different characterization techniques were used and the results obtained are presented.

- The nanoindentation studies were carried out to determine the change in hardness of the T91 material due to irradiation. It was found that the irradiation increases the hardness of the material. An empirical relation has been developed to correlate the change in hardness with that of change in yield strength. The correlation estimated reasonable change in yield strength due to irradiation. Also the results show that the saturation behavior of hardness and thus yield strength due to low temperature irradiation.

- The TEM characterization of unirradiated material has shown the presence of precipitates along the ferrite and martensite lath boundaries. The precipitates were found to be $M_{23}C_6$ type. The precipitates were sparsely distributed in the ferrite matrix. All the irradiated sample microstructure showed the presence of loops, cavities/bubbles and defect cluster like structures. The size and density of the defects determined from the TEM are used in MMM methods to study the mechanical behavior of the FM steels after irradiation.

- The GIXRD line profile analysis showed that the micro domain size decreases with increase in irradiation dose. The microstrain should increase with irradiation dose due to increase in defect accumulation but no significant difference between the 5 and 20 dpa samples was observed.

CHAPTER 5: MOLECULAR DYNAMICS SIMULATIONS

5.1 Introduction

MD simulation covers a length of interatomic distance and a time scale of thermal vibration of atoms. MD simulation allows the understanding of atomic level phenomena occurring at different external and internal mechanical and thermal loading conditions of the materials under consideration. This technique has been extensively used for the estimation of material properties of thin films and nano structures. Even though a lot of work is carried out to improve the scalability, performance and physical dimensions used for the simulations, its use is mainly restricted to small domains containing ~10^8 atoms in comparison to atoms of the order of ~10^{23} observed in bulk material components. These computations need dedicated and sophisticated computational facility and resources for data handling and storage with increased time and resources for handling larger domains. This requirement of computational capability limits the sizes of the domain for addressing the given problem. In addition, only discrete individual defect-defect interaction phenomenon occurring at the atomic scale can be studied instead of their collective behavior [232]. Even in the presence of the significant limitations, this technique, in particular, became an indispensible tool for understanding the deformation mechanisms occurring at the atomic scale. This helps in improved understanding of materials and their microstructural behavior under severe irradiation and high temperature conditions. The MD simulations are mainly used for the study of irradiation cascading phenomenon, interaction of dislocation with crystalline defects (voids/precipitates/bubbles/loops/SFTs/GBs), GB sliding behavior and its energetics. Many authors studied the irradiation cascading phenomenon, dislocation defect interaction and GB sliding behavior in pure systems but less information is

available on binary and tertiary systems in particular the Fe-Cr-He systems as described in the section - due to the absence of suitable multi component interatomic potentials.

In this view, the present chapter describes the computational details and results obtained from the MD simulations of the behavior of dislocations in the bcc material (in particular iron and iron-chromium alloys). In order to study the effect of irradiation induced microstructures such as voids or bubbles, at atomic scale MD simulations are carried out. Even though the irradiation induced loops were observed no effort has been made to simulate the interaction of dislocation with loops due to the following reason; the loops found in the irradiated microstructure were of the order of 10-20 nm which needs bigger atomistic domain size with atom counts more than $2x10^6$. In the available computational facility and time, it is difficult to handle such domain for longer simulation times.

The dislocation mobility mainly depends on material composition/impurity, temperature, loading/strain rate and on the defects present in the material. In the following sections, only the effect of composition (10% Cr)/impurity (He), temperature (1, 10, 50, 100, 300, 600 K) and defects (void/bubble) is discussed for a given loading/strain rate. Two different sets of Fe-Cr-He interaction potentials were used in the present study.

5.2 Computational details:

All the simulations were carried out using the public domain molecular dynamics (MD) code, Large Atomic/Molecular Massive Parallel Simulator (LAMMPS) [233] developed by the Plimpton et al. [234] at Sandia National Laboratory. For visualization, the Open Visualization Tool (OVITO)[235], Dislocation Extraction Algorithm (DXA) [236] developed by Stukowski [237], Stukowski et al. [238] respectively and Parallel Viewer (PARAVIEW) [239] are used.

5.2.1 Inter-atomic Potentials:

The various inter atomic potentials used in the present study are listed in the Table 5.1. The potential listed in table are grouped as Potential-1 and Potential-2. Detailed formulations of the potential described in the respective literatures are also given in Table 5.1. The potential-1 is used initially due to the unavailability of suitable ternary potential required i.e. Fe-Cr-He. For the later simulations, the recently developed ternary potential-2 by Caro et al. [240] was used. Only results from the selected cases were compared for the two potentials.

Table 5.1: Two different set of potentials used in the present work for Fe-Cr-He interaction.

Interaction	Potential-1	Potential-2
Fe-Fe	Mendelev et al. [148]	Ackland et al. [241]
Cr-Cr	Wallenius et al. [242]	Olsson et al. [243]
He-He	Aziz et al. [244]	Beck et al. [245]
Fe-Cr	Stukowski et al. [118]	Caro et al. [240]
Fe-He	Seletskaia et al.[246]	Juslin et al. [247]
Cr-He	Terentyev et al. [248]	Terentyev et al. [248]

Unless otherwise specified simulation results in the present study correspond to Potential-1.

5.2.2 Dislocation mobility and dislocation Defect (Void and bubble and loop) Interaction in the matrix:

One of the active slip systems pertaining to the $\langle 111\rangle\{110\}$family was taken for simulation of edge dislocation (ED) motion in α iron having bcc lattice structure. The directions of bcc lattice $\langle 111\rangle, \langle 110\rangle$ and $\langle 112\rangle$ were oriented along x, y, and z direction. The dislocation was introduced in the crystal using the guidelines given by Osetsky et al. [249] which is shown as follows;

- Create two-half crystals with N and N-1 planes as shown in Figure 5.1.
- Strain the half crystal with N planes by an amount -b/2 and that with N-1 planes by an amount +b/2

- Join the two-half crystals along the slip plane and relax the structure to get the dislocation at the center of the domain as shown in Figure 5.1.

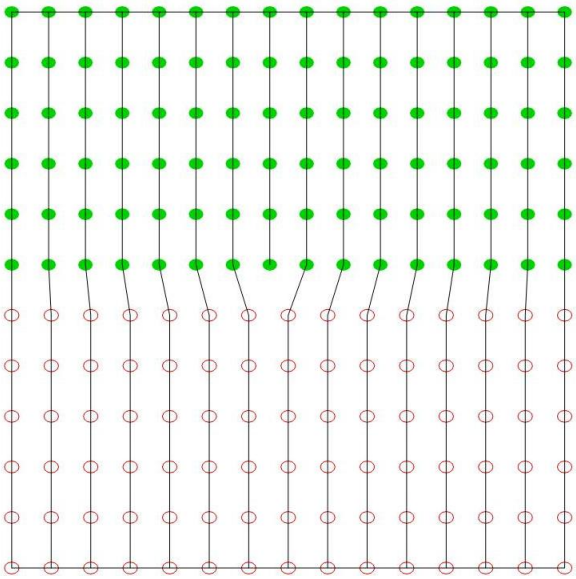

Figure 5.1: Schematic diagram showing the upper half crystal (filled circles) with N (=16) and lower half crystal (open circles) with N-1(=15) planes.

The simulation domain was divided in to three regions namely, upper, middle and lower. Atoms in the lower region were kept fixed to avoid the rigid body motion. The atoms in the middle region were allowed to evolve according to the Newton's equation of motion under the action of external forces. The load was applied by specifying shear stress or shear strain on the upper layer atoms of the crystal. In the present simulations, deformation of the crystal was carried out by specifying incremental shear strain on the upper layer of the domain which results in the dislocation motion. The minimization was carried out at intermediate strain to ensure the minimum potential energy configuration of the system. The internal resisting force (Fx) acting on the upper layer of atoms along the x direction in response to externally applied shear was used to obtain the shear stress $\tau = Fx / A$, where A is the area of the slip plane in the minimum energy

configuration. All the shearing simulations were carried out using the strain rate of 10^9 per second.

5.2.3 Dislocation-defect (bubbles) interaction at grain boundary:

The domain consisted of two crystals named as A and B as shown in Figure 5.2 (a). The twist grain boundary (TGB) is normal to the axis of twist [110]. The grains A and B were rotated about the [110] axis by an angle of $+2^o$ and -2^o respectively to create the hexagonal screw dislocation network as shown in Figure 5.2 (b).

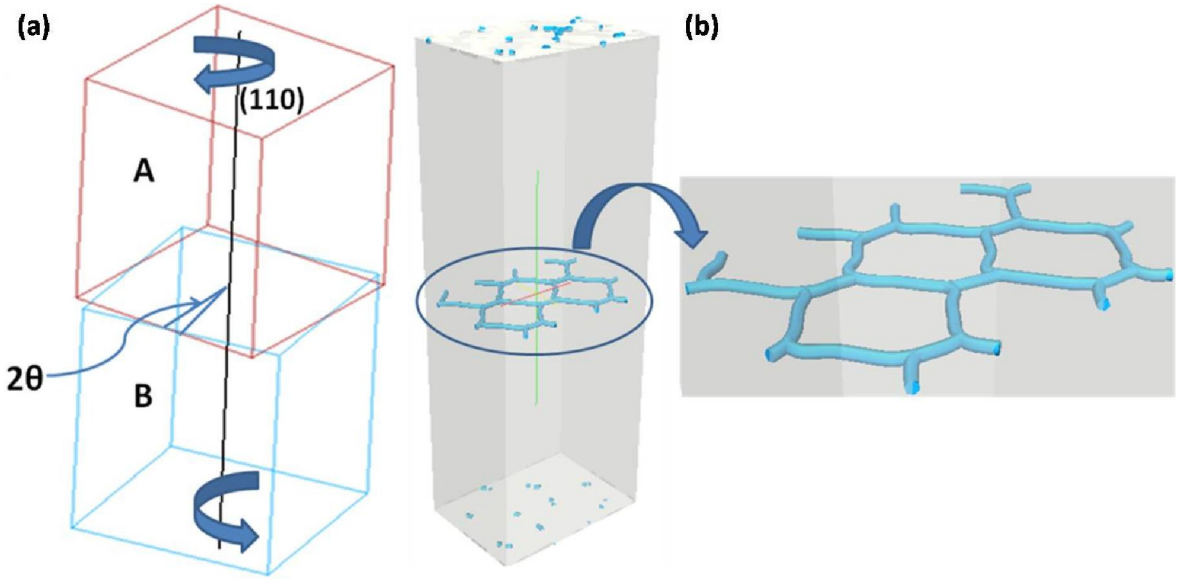

Figure 5.2: (a) Schematic diagram showing the two crystals rotated about $< 110 >$ direction to form the twist GB and (b) Hexagonal dislocation structure formed by low angle ($\theta = \pm 2$) twist GB.

The domain size considered here was 11.4x8.0x32.3 nm^3. The minimum energy configuration was achieved by conjugate gradient energy minimization method before thermal equilibration and straining the crystal. The thermal equilibration was carried out at 1K for 10 ps. The bottom and top regions were made by grouping 3-4 layers of atoms, which were used to rigidly fix and to apply the incremental strain respectively. All the shearing simulations were carried out using

the strain rate of 10^9 per second. The stress strain response was recorded as specified in the above paragraph. We employed centro symmetric parameter for visualizing grain boundary dislocation structure.

5.3 RESULTS AND DISCUSSION

In this section, results obtained from the MD simulation under three following situations are presented,

i) The edge dislocation mobility in Fe, Fe-10% Cr and Fe-10% Cr with different helium content in substitutional/interstitial positions and with different temperatures. The helium concentrations considered were 0.1, 0.5 and 1.0%. The temperatures considered were 1, 10, 50, 100, 300 and 600K. For 300 and 600K cases simulations were carried out only for selected cases.

ii) The edge dislocation interaction with void and helium bubbles of different diameter. The diameters considered were 0.8 nm, 1.2 nm and 1.6 nm.

iii) Friction stress for low angle twist grain boundary misfit dislocation network with and without helium bubbles.

The dislocation motion in an otherwise defect-free crystal occurs at a stress value, commonly known as friction stress, defined by the maximal stress; i.e., the average of peak values in shear stress-strain (τ-γ) plot. The resistance for the dislocation motion due to an obstacle is defined as CRSS, which is the maximum stress, required to overcome the obstacle.

5.3.1 Dislocation mobility in Fe, Fe-Cr and Fe-Cr-He systems

A typical τ-γ plot generated for pure Fe by carrying out MD simulation is shown in Figure 5.3 and the Figure 5.4 shows the initial configuration of the edge dislocation in pure Fe crystal. The linear region A (marked in the Figure 5.3) shows the elastic behavior of pure Fe.

This linear portion is followed by a region B where plastic deformation of the Fe-crystal occurs by the mobility of the dislocation. The periodic drop in the values of stress, as shown in Figure 5.3, is due to dislocation core movement by a distance of b/3 along x-direction [249], where b is magnitude of Burger's vector. The periodic maximum and minimum values of stress on the curve are due to breaking and making of the bonds between atoms near the dislocation core. The flow stress required to move the dislocation on its slip plane was found to be 81 MPa.

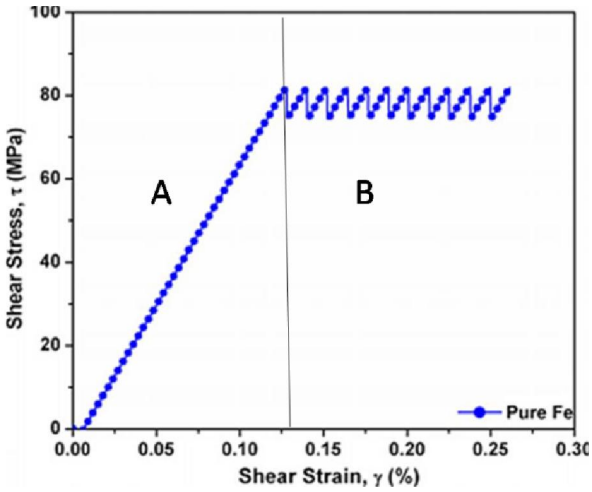

Figure 5.3: Shear stress strain curve corresponding to edge dislocation motion in pure Fe system (region A and B corresponding to elastic and plastic deformation).

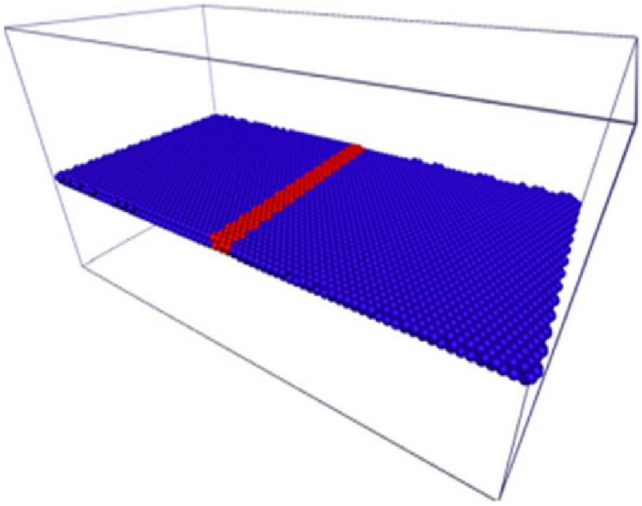

Figure 5.4: Initial edge dislocation configuration in pure Fe system (red and blue color atoms corresponding to dislocation core region and perfect lattice).

For the case of the Fe-10% Cr alloy simulations were carried out assuming Cr atoms are randomly distributed in the Fe matrix. Initially, the Fe-10% Cr system at 10 K was studied for potential-1. Cr atoms were distributed using different random number seeds to check the effect of random distribution of Cr on the shear stress strain plot, as shown in Figure 5.5. Figure 5.6 shows the initial configuration of the edge dislocation in the Fe-10% Cr crystal. Similar deformation behavior was observed in the shear stress-strain curves for all the Cr distribution cases using different random seeds (Figure 5.5). Average maximal stress of 130 MPa was obtained for all the cases. This average value of stress is shown by a dotted line in the Figure 5.5.

Using the potential-2, simulations were carried out at 1, 10, 50, 100, 300 and 600 K. The shear stress strain (τ-γ) plots for different temperatures are shown in Figure 5.7. These simulations have revealed that the friction stress or the resolved shear stress increased due to the addition of Cr which forms a substitutional solid solution with Fe. Cr atoms being slightly bigger in size as a substitutional solute atom in the Fe lattice generates a symmetric lattice strain field around itself. This lattice strain field interacts with the dislocation strain field leading to an increase in the resistance to ED motion. This increase in resistance manifests itself as an amplified stress peaks in a τ-γ plot. In addition, these stress peaks become less regular in shape in the case of Fe-Cr alloy, which is due to the pinning and releasing of the dislocation by clusters of two or more Cr atoms. The solute hardening behavior in pure metals is found to be due to short range interaction of solute atoms [154, 162, 184-189]. A pair of solute atoms in nearest neighbor configuration or a cluster of solute atoms lying on the adjacent planes above and below the geometric slip plane acts as a strong obstacle to gliding dislocation.

The maximal shear stress for Fe-10%Cr at 10 K for potential-2 is 30 MPa lesser than the maximal shear stress obtained by potential-1. In comparison to the results obtained by Hafez et al. [152], for 9% Cr in Fe at 100 and 300 K, maximum stresses in the present study are approximately lower by 60-70 MPa. These differences may be attributed to the combined effect of different potentials used, strain rate, domain size, random distribution of Cr and the strain range chosen for averaging. Figure 5.8 shows temperature dependence of friction stress in Fe-10% Cr. Temperature reduces the stress required for the plastic deformation of the materials i.e. stress required for the dislocation motion. The maximal stress saturates at a value of 50 MPa above 300 K temperature. The temperature independent minimum stress required for dislocation motion is known as athermal component of the friction stress.

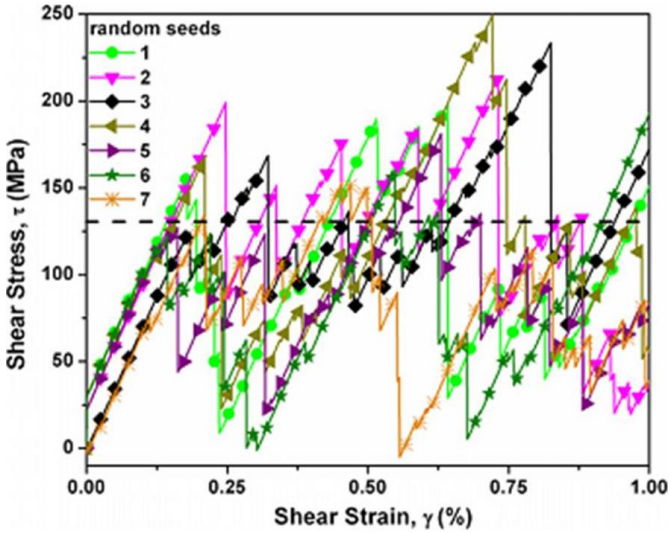

Figure 5.5: Shear stress strain curve corresponding to edge dislocation motion in Fe-10%Cr system with different random seed (different color curves corresponds to different random number seeds used for Cr distribution).

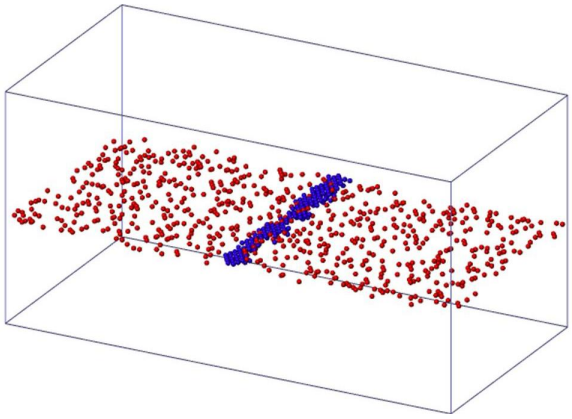

Figure 5.6: Initial edge dislocation configuration in Fe-10%Cr system (blue color atoms corresponds to Fe atoms near core region and red color atoms corresponding to Cr atoms present on the slip plane).

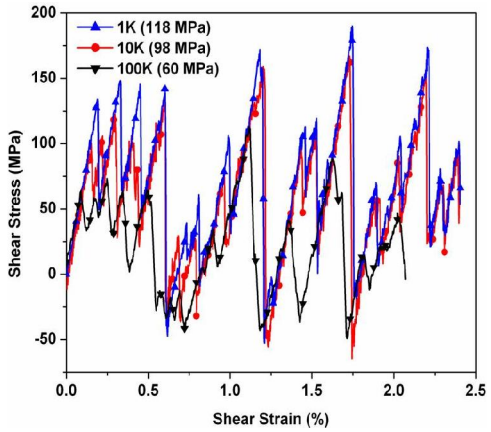

Figure 5.7: Shear stress strain curves corresponding to edge dislocation motion in Fe-10%Cr system at different temperatures.

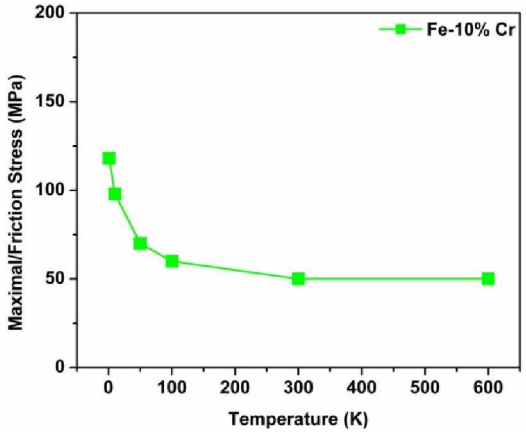

Figure 5.8: Temperature dependence of maximal/friction stress in Fe-10%Cr system (saturation of friction stress to lower stress values as temperature increase).

Similar to the case of binary Fe-10%Cr alloy, Fe-10%Cr alloys with He, Cr and x% He (where x stands for 0.1, 0.5 and 1.0%) atoms were distributed randomly with different random number seeds. Initially, the alloy matrix Fe-10%Cr with 1% He was studied using the potential-1. Cr and 1%He atoms were distributed using different random number seeds to check the effect of distribution on the shear stress strain plot, as shown in Figure 5.9. Similar deformation behavior was observed in the shear stress-strain curves for all the Cr and He distribution cases using different random seeds (Figure 5.9). Average maximal stress of 230 MPa was obtained for all the cases. A dotted line in the Figure 5.9 shows this average value of maximum stress and the Figure 5.10 shows the initial dislocation configuration in Fe-10%Cr-1% He system. Using the potential-2, the simulations were carried out at 1, 10, 50, 100, 300 and 600 K. Typical τ-γ plots for a single random number seed at different temperatures are shown in Figure 5.11 for 1% substitutional He. Only selected cases are plotted for the purpose of clarity. In the presence of He, the peak stress values are further amplified and the stress required to move the dislocation increases significantly. This increase in the stress required for dislocation motion manifests as hardening of Fe-Cr alloy due to irradiation induced He. The hardening due to 0.1% He in the present simulations is found to be significant in Fe-Cr system in comparison to 0.1% He in pure Fe. Figures 5.12 and 5.13 show the friction stress as a function of temperature and He concentration respectively. From Figure 5.12 it could be observed that as the temperature decreases the stress required for the dislocation motion increases. The temperature dependence of maximal/friction stress (Figure 5.12) is in qualitative agreement with the experimental observation of decrease in flow stress with increase in temperature. The rate of change of friction stress tends to decrease as He content is increased from 0.5 to 1.0% (Figure 5.13).

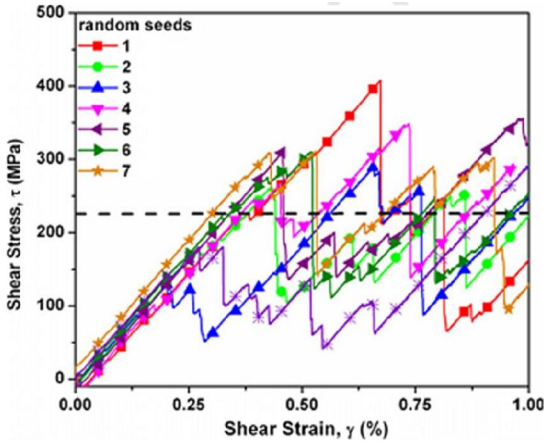

Figure 5.9: Shear stress strain curve corresponding to edge dislocation motion in Fe-10%Cr-1%He system with different random seed.

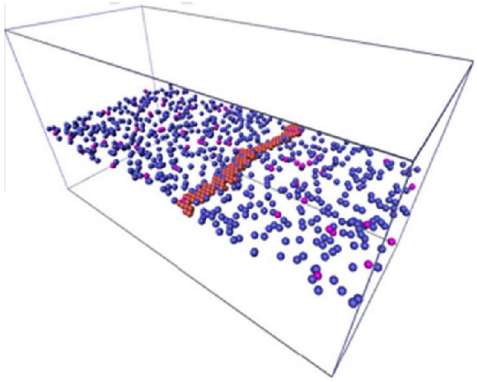

Figure 5.10: Initial edge dislocation configuration in Fe-10%Cr-1%He system (red color atoms corresponds to Fe atoms near dislocation core region and blue/magenta color atoms corresponding to Cr/He atoms present on the slip plane).

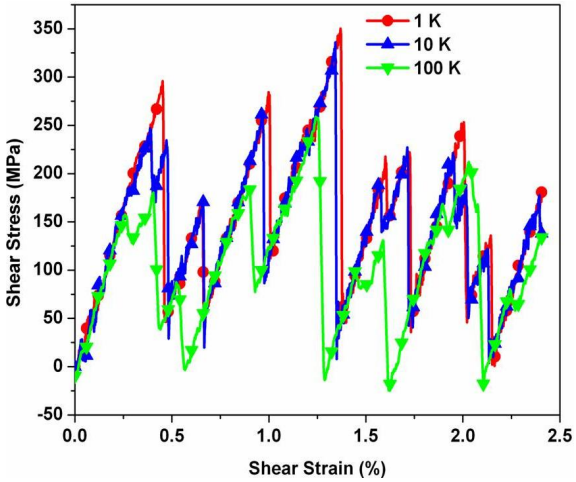

Figure 5.11: Shear stress strain curve corresponding to edge dislocation motion in Fe-10%Cr system with different temperatures.

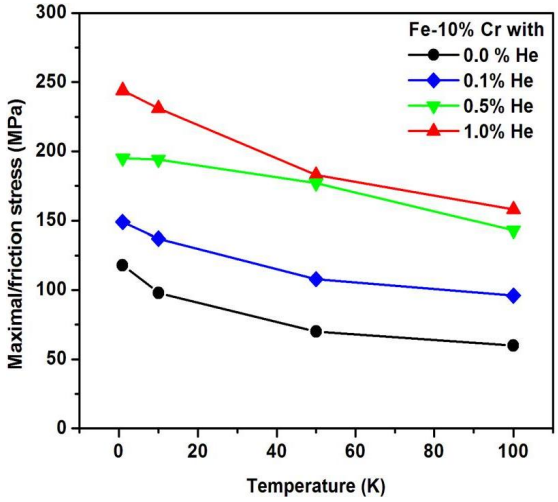

Figure 5.12: Dependence of maximal/friction stress of an edge dislocation on temperature in Fe-10% Cr system with 0.1, 0.5 and 1.0% He in substitutional position.

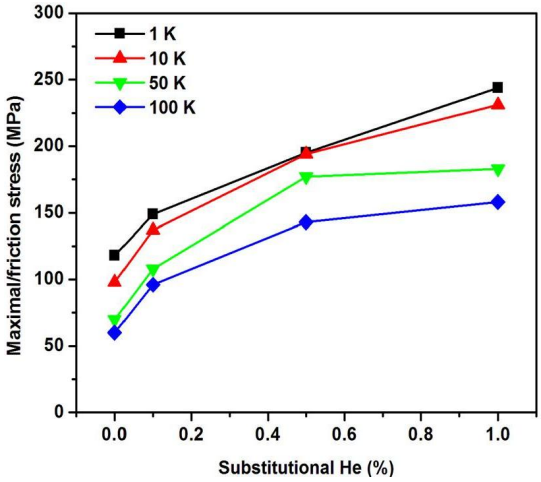

Figure 5.13: Dependence of maximal/friction stress of an edge dislocation on substitutional He content in Fe-10% Cr system at different temperatures.

For the case of interstitial He at 1K a typical τ-γ plot for single random number seed is as shown in Figure 5.14. In the presence of x% He in interstitial positions, the peak stress values are further amplified in comparison to He present as substitutional impurity. The variation of maximal shear stress/friction stress with respect to temperature and He content as interstitial is as shown in Figure 5.15 and 5.16 respectively. The results show that Fe-10%Cr with 0.1%

interstitial He requires higher stresses than the stresses required for dislocation motion in the 1.0% substitutional He in Fe-10%Cr. The friction stress vs. temperature plot shows a smooth decrease in stress values as the temperature increases for 0.1% He. The maximum He atoms are present as isolated He atoms in the case of 0.1%He. As the He content increased to 0.5 and 1.0%, it was observed that at higher temperature the maximal stress/friction stress started to increase. The visualization of atomic configuration has shown that when He atoms start to interact with each other and form clusters of He atoms, the cluster of He atoms acts as stronger obstacles than the isolated He atom (shown in Figure 5.17a-b). It may be noted that unlike in the case of substitutional He as well as dilute interstitial He alloys an increase in maximal/friction stress with temperature was observed in the case of 0.5 and 1.0% He (Figure 5.16).

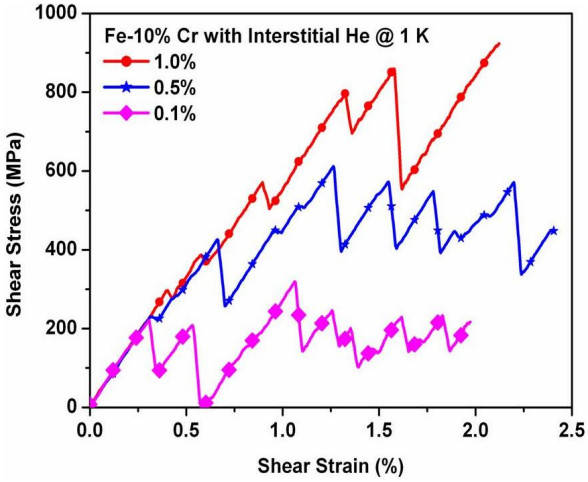

Figure 5.14: Shear stress strain curves for edge dislocation motion in Fe-10%Cr with 0.1%, 0.5% and 0.5%He in interstitial position at 1K.

It is a well-established fact that the interaction of asymmetric stress fields produced by interstitial He atoms with the dislocation results in the stronger pinning effect than the symmetric stress fields of substitutional one. It is also a known fact that the He atoms move toward the slip plane during deformation. In the present study increase in He concentration on the slip plane at the expense of He on the neighbor planes was observed. Figure 5.18, for example, shows the

normalized He content as a function of distance from the geometric slip plane for the case of 0.5% He. It clearly shows that, He atoms are attracted towards the tensile stress region of the dislocation. This is in accordance with the observation made by Wang et al. [157] that the interstitial He atoms have a strong positive binding energy in the tensile stress region. The Figure 5.18 also shows that the increase in temperature increases the number of He atoms moving towards the slip plane. The curvilinear shape of the dislocation in Fe-10%Cr and 1% He is as shown in Figure 5.19.

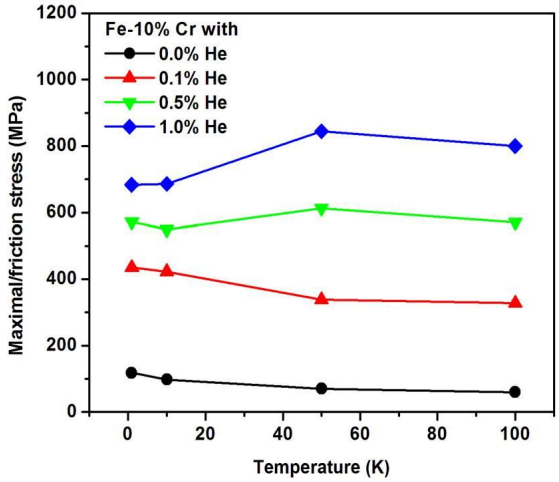

Figure 5.15: Dependence of maximal/friction stress of an edge dislocation on temperature in Fe-10% Cr system with 0.1, 0.5 and 1.0% He in interstitial position.

The Figure 5.20 shows the comparison of maximal friction stress for Fe-10%Cr and Fe-10%Cr with 1% He in substitutional (He_{sub}) and Interstitial (He_{int}) positions. At higher temperatures (~600 K) the substitutional atoms are found to form clusters due to increased mobility and diffusivity. These He clusters act as stronger obstacles to dislocation motion resulting in increased maximal stress as shown in Figure 5.20. Unlike in pure Fe, the dislocation line has been found to be curvilinear in later two cases. It is also found that the dislocation motion was jerky in nature.

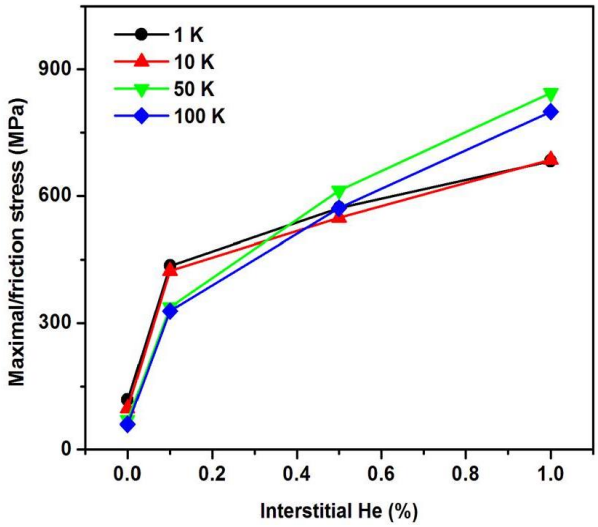

Figure 5.16: Dependence of maximal/friction stress of an edge dislocation on interstitial He content in Fe-10% Cr system at different temperatures.

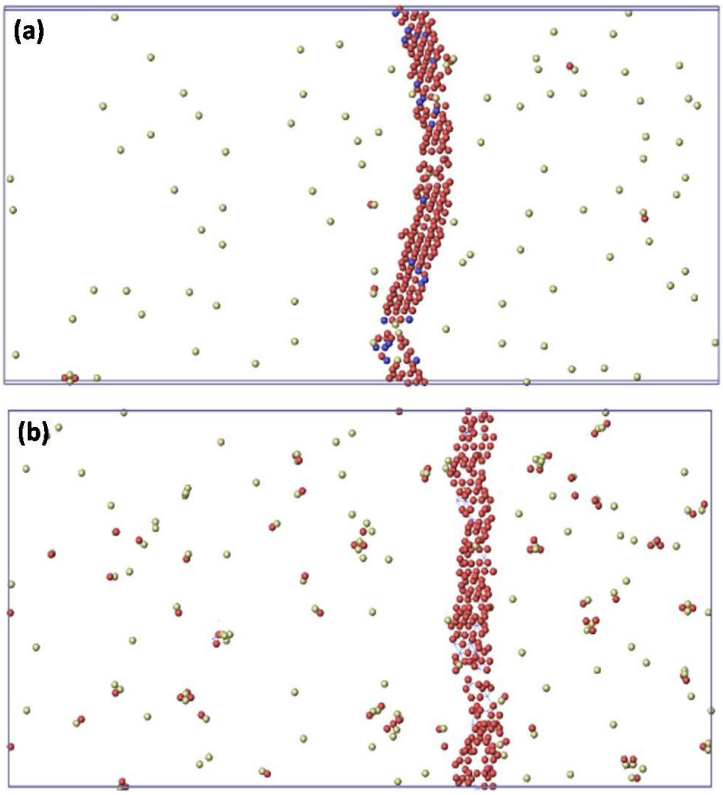

Figure 5.17: Isolated interstitial atoms at (a) 1K and (b) 100K in Fe-10%Cr with 0.5% interstitial atoms (red color dots-Fe atoms at dislocation core region, blue color dots-Cr atoms and yellow color dots-interstitial He atoms).

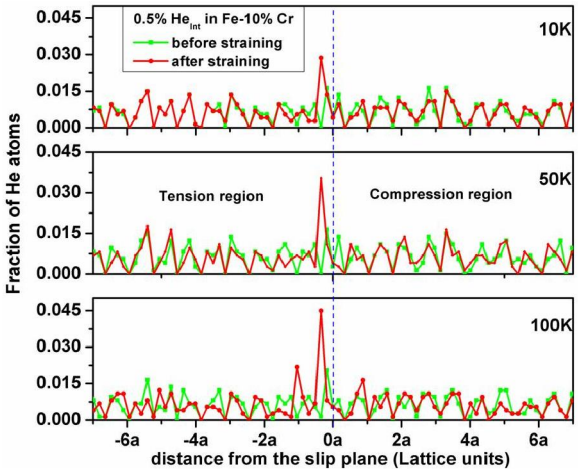

Figure 5.18: Fraction of He atoms present on {110} slip plane at a distance in Fe-10%cr sample as a function of temperature for 0.5% interstiatial He atoms (He atoms are more attracted toward the tensile region of dislocation core than that of compression region).

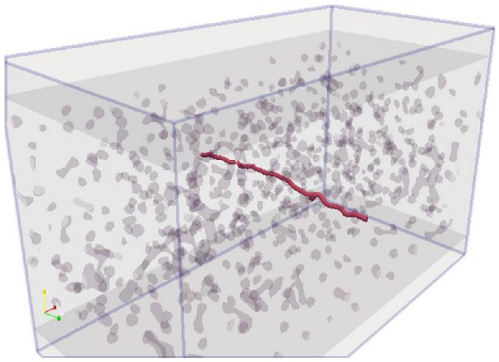

Figure 5.19: Curvilinear shape of the edge dislocation (red color curve) and interstial He (beed like structure) in Fe-10%Cr as extracted using DXA tool.

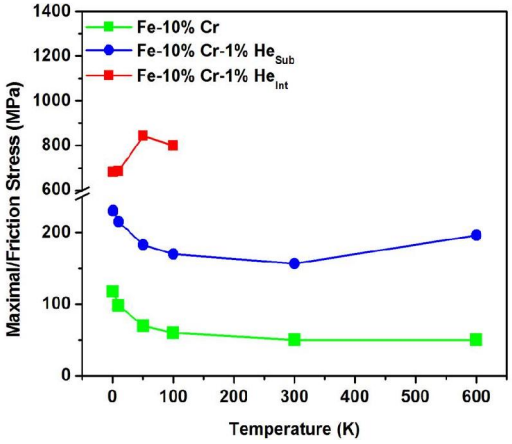

Figure 5.20: Comparison of variation of maximal/friction stress for an edge dislocation in Fe-10%cr with 1% substitutional and interstitial helium with respect to temperature.

5.3.2 Interaction of dislocation with defects

5.3.2.1 Interaction of dislocation with voids

The MD simulations of interaction of edge dislocation with voids were carried out to determine the CRSS. Figure 5.21 shows a τ-γ plot for the interaction of edge dislocation with voids of different diameters present in pure Fe. Four distinct regions of dislocation void interactions can be delineated from this plot, region A represents gliding of dislocation in an otherwise perfect crystal. Region B represents attractive interaction of dislocation with the void. As a void attracts the dislocation, the stress on dislocation becomes negative (attractive) resulting in the creation of a step of length b on the entry surface. The increase in applied strain results in the bowing of the dislocation and finally edge dislocation is released from the void at maximum stress value i.e. CRSS (region C). The release of the edge dislocation occurs with the formation of a step of size b on the void surface in all the simulations resulting in the shearing of the void as described in ref. 150, where b is magnitude of Burger's vector. Figure 5.22 shows the plot of CRSS vs. void diameter in pure Fe where it shows that the CRSS increases linearly within the range of void diameters considered. The initial configuration of the dislocation with a void in pure Fe is shown in Figure 5.23(a). At a critical stress value, the unpinning of the edge dislocation (ED) from void is accompanied with the screw segment formation for 1.2 nm and 1.6 nm void diameters. The screw segment formation for the void of 1.6 nm diameter is shown in Figure 5.23(b). In the case of 0.8 nm void diameter no screw segment formation was observed. The release of the dislocation was accompanied by the formation of a jog on the dislocation by the climb process, as shown in the Figure 5.24. It was also observed that the dislocation carries a vacancy as shown in Figure 5.24 (f).

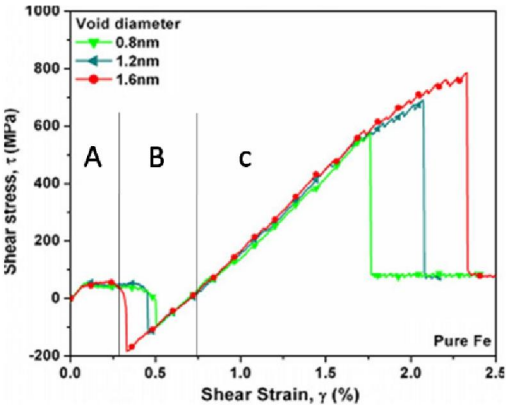

Figure 5.21: Shear stress strain curve for edge dislocation interacting with irradiation induced/produced voids of diameter 0.8, 1.2 and 1.6 nm in pure Fe (region A-initial dislocation motion, region B-attraction of dislocation by void and region C-increase in stress due to piining of ED by void and sudden drop in stress due to unpinning from void).

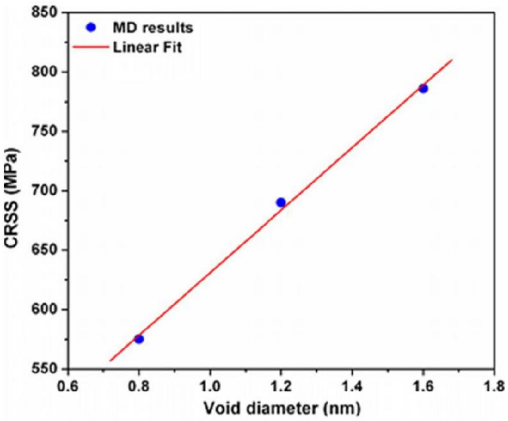

Figure 5.22: Dependence of critical resolved shear strength of edged dislocation on void diameter in pure Fe.

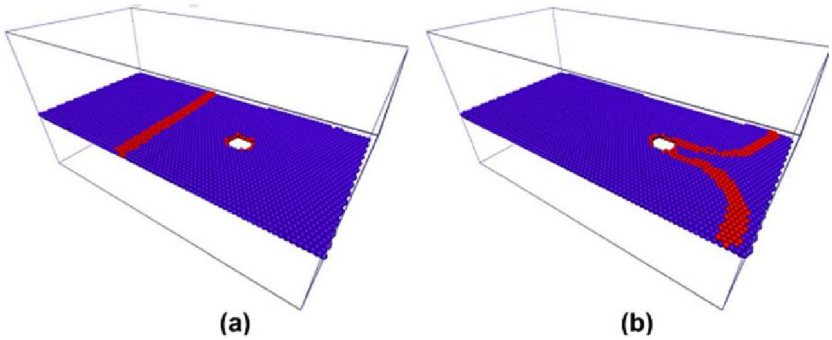

Figure 5.23: (a) Initial and (b) bowed out dislocation configuration of edge dislocation in pure Fe (red color and blue color corresponds to dislocation core region and perfect lattice atoms).

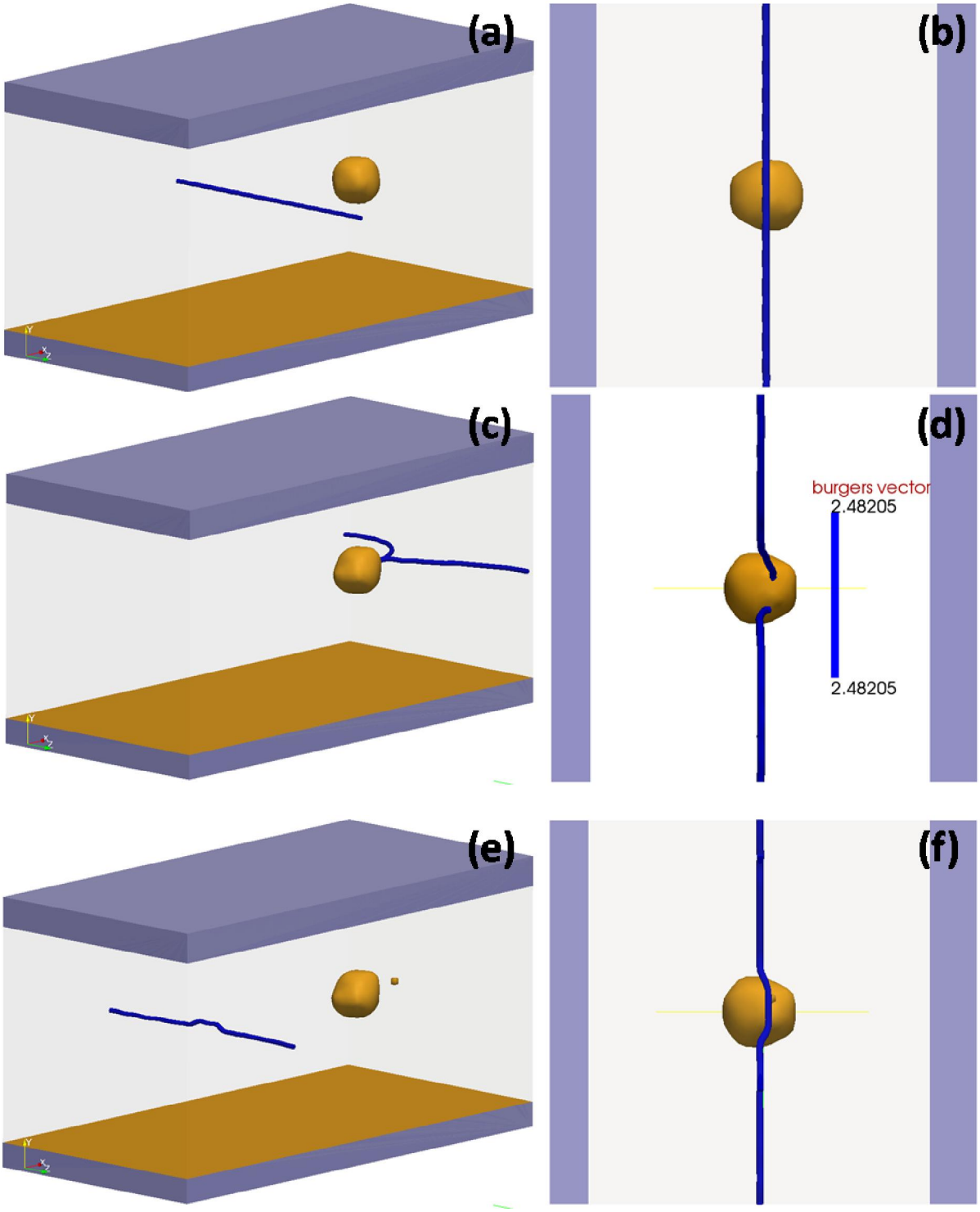

Figure 5.24: The snapshots showing the jog formation on edge dislocation while releasing from the void. (a) (b) initial, (c) (d) before release and (d) (e) after release (blue color line-dislocation, yellow color sphere-void, yellow color small sphere vacancy).

The increase in resistance to dislocation motion was manifested as decrease in radius of curvature of the dislocation segments between the periodic arrays of voids. The jog formation due to the climb of an edge dislocation interacting with a void is also reported by Osetsky et al. [134]. Recently Dutta et al. [149] tried to describe the climb of the dislocation during the release from the voids and found that the structural energy gradient itself is responsible for the void induced dislocation climb and jog formation.

Interactions of ED with voids have also been studied in the Fe-10%Cr system. The τ-γ plot for Fe-10%Cr is shown in Figure 5.25. The presence of Cr atoms seems to decrease the CRSS for smaller size voids and has a softening effect on the strength of the void. This has been checked for various distributions of Cr atoms and this observation has been found to be consistent. Out of the three cases (i.e. 0.8, 1.2 and 1.6nm) reported in the present study, there is a softening effect of Cr atoms for 0.8 nm diameter void. The dislocation configuration before release from the 0.8 nm and 1.6 nm diameter voids are as shown in Figure 5.26 (a) and (b) respectively. For the case of 0.8 nm void diameter, it was observed, from Figure 5.26 (a), that the curvature of the dislocation due to pinning in Fe-10%Cr is lesser than that of Pure Fe. Softening effect due to the presence of Cr atoms for lower diameter voids is unclear. A transition behavior has been observed for a void of 1.2 nm diameter. CRSS was noticeably higher for a void of 1.6 nm diameter as compared to smaller size voids. The dislocation line is more curvilinear and radius of curvature is slightly higher than that of pure Fe, as shown in Figure 5.26 (c).

The effect of irradiation induced He in FM steels on the interaction of ED with a void is considered by randomly placing the substitutional He atoms in Fe-10%Cr matrix. The τ-γ plot for Fe-10%Cr-1%He is shown in Figure 5.27. The CRSS values are found to be 687 MPa, 750

MPa and 950MPa for 0.8 nm, 1.2 nm and 1.6 nm diameters of voids respectively (Table 5.2). In comparison to pure Fe and binary Fe-10%Cr, a significant increase in CRSS is observed due to the presence of 1%He in Fe-10%Cr. Initial dislocation-void configuration and bowed dislocation due to pinning by a void of 1.6nm diameter in Fe-10%Cr-1%He is shown in Figure 5.28(a) and (b) respectively.

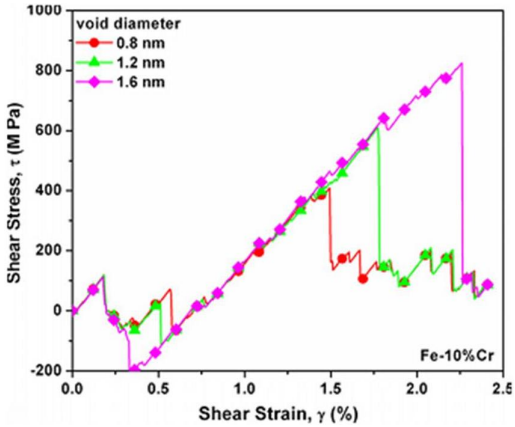

Figure 5.25: Shear stress strain curve for edge dislocation interacting with irradiation induced/produced voids of diameter 0.8, 1.2 and 1.6 nm in Fe-10%Cr.

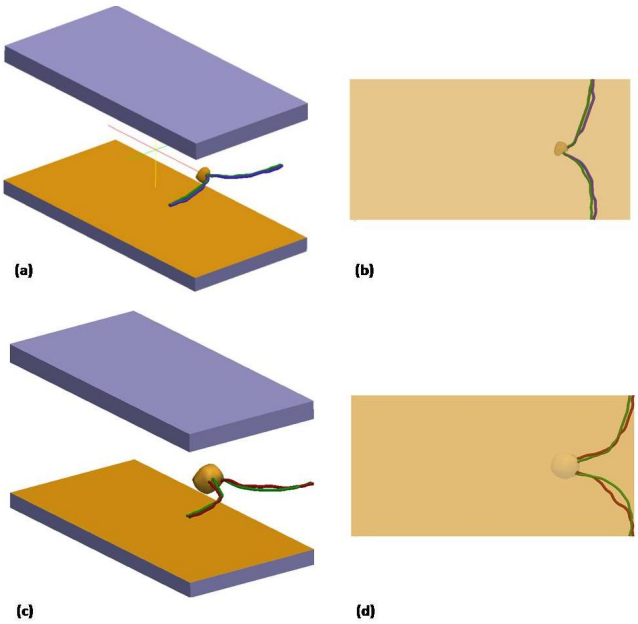

Figure 5.26: Dislocation configuration before release from the void of diameter (a) (b) 0.8nm in Fe (blue), Fe-10%Cr (green) and (c) (d) 1.6nm in Fe (green), Fe-10%Cr (brown).

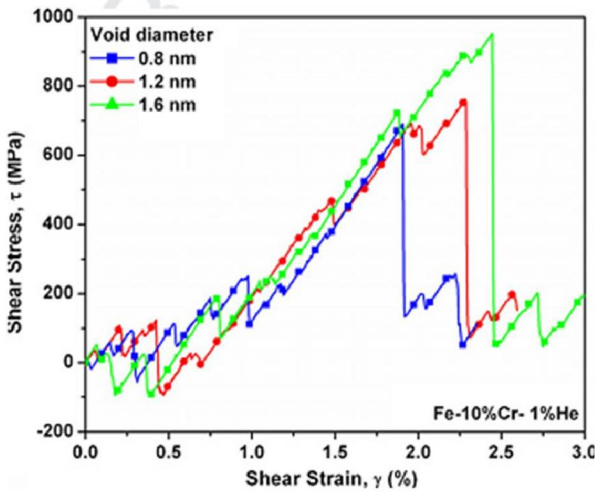

Figure 5.27: Shear stress strain curve for edge dislocation interacting with irradiation induced/produced voids of diameter 0.8, 1.2 and 1.6 nm in Fe-10%Cr-1%He.

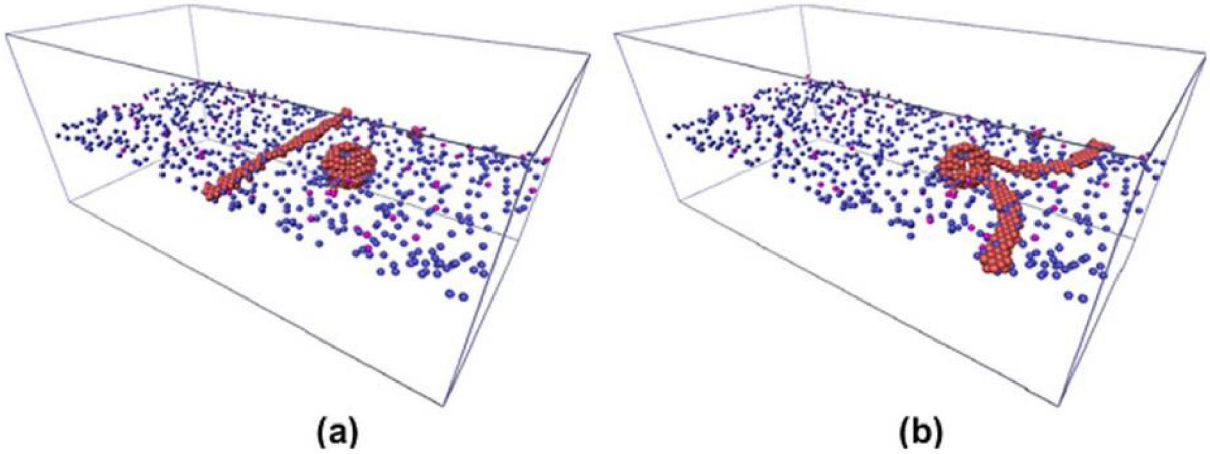

Figure 5.28: (a) Initial and (b) bowed out dislocation configuration of edge dislocation interacting with a void of 1.6 nm diameters in Fe-10%Cr-1%He (red, blue and magenta color corresponds to dislocation core region Fe, Cr and substitutional He atoms on dislocation slip plane).

5.3.2.2 Interaction of dislocation with He bubble

The bubbles of size 0.8 nm, 1.2 nm and 1.6 nm are inserted by replacing Fe lattice atoms with He atoms in a spherical volume of given diameter, which results in bubbles of type 1He-1V pair. The τ-γ plots for edge dislocation interacting with helium bubbles in pure Fe is as shown in

Figure 5.29. It is seen that He bubbles of 1He-1V type are weaker obstacles in comparison to the voids of the same size as highlighted by Hafez et al. [45, 172]. The dislocation bubble interaction behavior is similar to that of the dislocation void interaction as described in section 5.3.2.1. Figure 5.30 (a) and (b) shows the initial and bowed out dislocation configurations generated in the present simulations. In the case of a bubble of 1.6 nm diameter, formation of screw segment is observed while releasing of ED by bubble as shown in Figure 5.30(b).

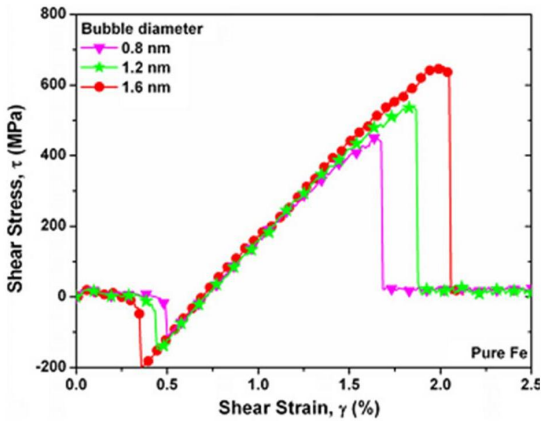

Figure 5.29: Shear stress strain curve for edge dislocation interacting with irradiation induced/produced bubbles of diameter 0.8, 1.2 and 1.6 nm in pure Fe.

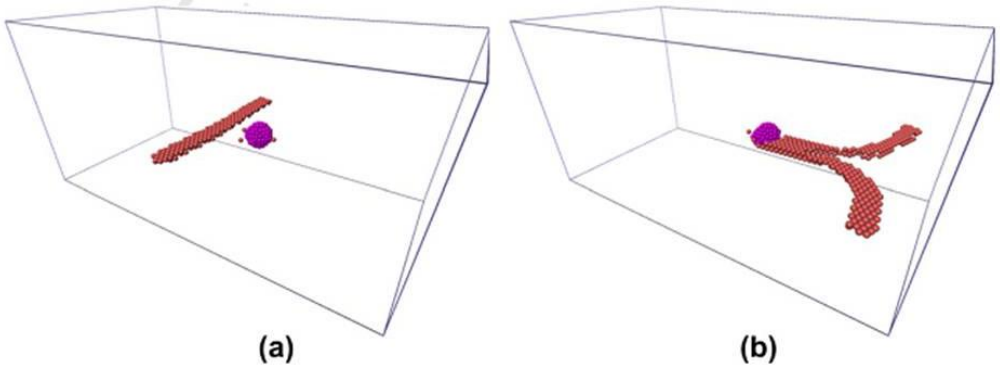

Figure 5.30: (a) Initial and (b) bowed out dislocation configuration of edge dislocation interacting with a bubble of 1.6 nm diameter in pure Fe.

Similar exercise has been carried out for the interaction of edge dislocations with helium bubbles in Fe-10%Cr system. The τ-γ curves are shown in the Figure 5.31. The simulation shows

that the CRSS for an edge dislocation interacting with He bubble (1He-1V) is comparable to that of a void. The CRSS for 1.6 nm diameter bubble is same as that of void in Fe-10%Cr, but for 0.8 and 1.2 nm bubbles, it is 157 and 129 MPa greater than that of void. The interactions of dislocation with He bubble as obtained by present computation are shown in Figure 5.32(a) and (b). It is observed that the dislocation curvature due to pinning by bubble in Fe and Fe-10%Cr are nearly same. The Figure 5.33 shows the comparison of CRSS in Fe and Fe-10% Cr. The figure shows that the CRSS varies linearly with the bubble diameter up to 1.6 nm in both the cases. Table 5.2 summarizes the CRSS required for edge dislocations to overcome the defects (i.e. voids and bubbles) of diameter 0.8, 1.2 nm and 1.6 nm in the above considered crystals.

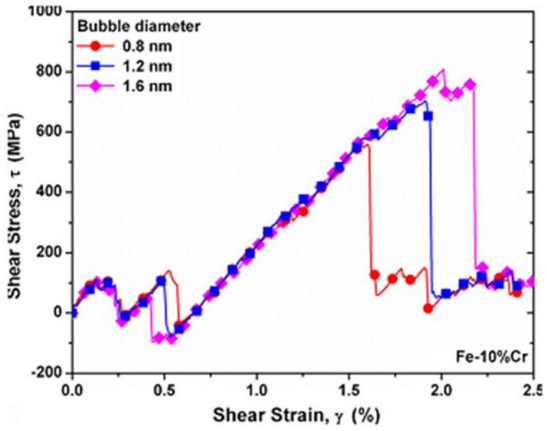

Figure 5.31: Shear stress strain curve for edge dislocation interacting with irradiation induced/produced bubbles of diameter 0.8, 1.2 and 1.6 nm in pure Fe-10%Cr.

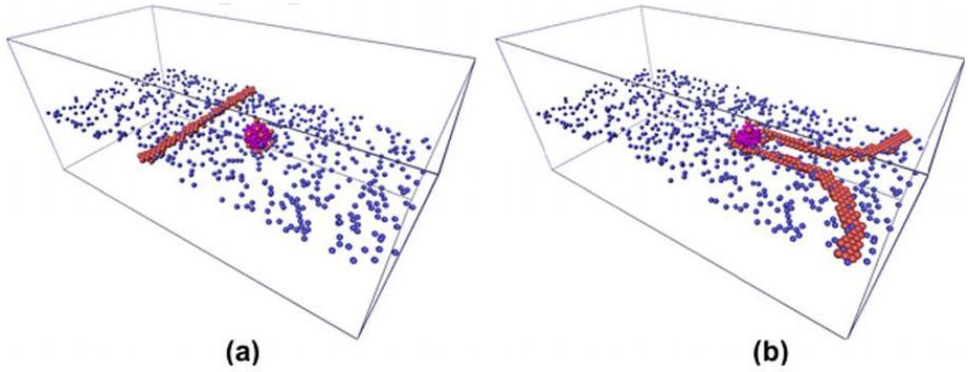

Figure 5.32: (a) Initial and (b) bowed out dislocation configuration of edge dislocation interacting with a bubble of 1.6 nm diameter in Fe-10%Cr.

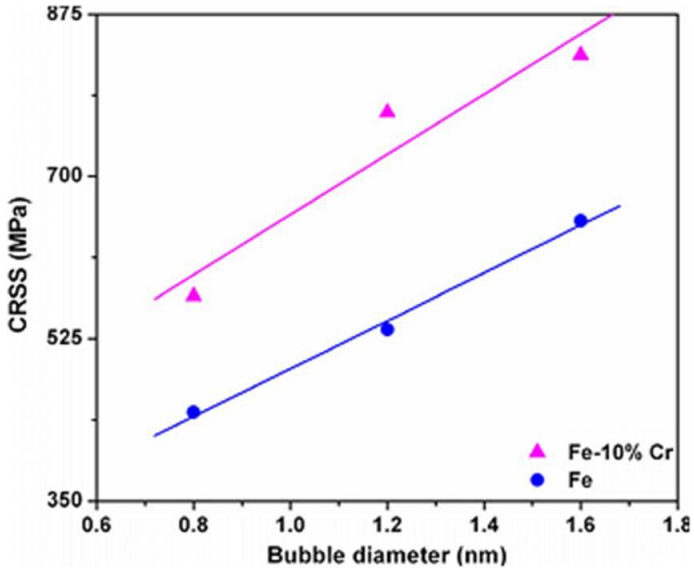

Figure 5.33: Dependence of critical resolved shear strength of edged dislocation on bubble diameter in pure Fe and Fe-10%Cr.

Table 5.2: CRSS for voids and bubbles of different diameters.

System	CRSS (MPa)					
	Void diameter in nm			Bubble diameter in nm		
	0.8	1.2	1.6	0.8	1.2	1.6
Pure Fe	575	690	784	450	538	652
Fe-10%Cr	408	607	822	565	736	820
Fe-10%Cr-1%He	687	750	950	-	-	-

5.3.3 Dislocation-defect (bubbles) interaction at grain boundary

In the following section, the effect of loading direction, strain rate and helium bubble of different diameter on the mobility of misfit dislocation network at low angle twist grain boundary in pure Fe crystals are discussed. The Potential-2 was used in all the cases studied in this section.

5.3.3.1 Effect of loading direction

Intra-grain and interface dislocations play important roles in plastic deformation of poly-crystalline materials. The shear stress-strain curves for the samples with and without He are

shown in Figures 5.34 and 5.36 respectively. These curves show an initial elastic part followed by plastic deformation where the network starts to move by overcoming the GB friction stress. Loading directions and strain rates were systematically varied to observe their effect in the material response. The shear stress-strain response of the pristine sample (without He bubbles) in different shear loading direction has been studied. The incremental shear load is applied on Z-plane along X-direction and Z-plane along Y-direction on the upper region of crystal. It was found that the stress required for shearing along the Y - direction was less than in the X-direction. The difference observed in shear stress between the two loading directions is ~60-80 MPa in average. In both the cases an initial stress peak was observed followed by a saturation region, as shown in Figure 5.34. In the case of shearing along X-direction the stress peak (~150MPa) is higher and clearly distinguishable in comparison to the stress peak during shear along Y-direction (~80MPa). The stress peak is found to be blunter in the case of Y-direction loading. The difference between the stress peak and the saturation value of X and Y directions were found to be ~40 MPa and ~20 MPa respectively. This behavior may be attributed to the <100> screw dislocation segments. The shear deformation of the GB has shown less resistance for loading along <011> direction (i.e. normal to <100> junction segment), in comparison to <100> direction (i.e. line direction of junction segment). This implies that these segments may provide directionality to the plastic deformation. The GB dislocation network configuration is shown in Figure 5.35 (a) and (b) for initial and strained configuration. In the figure the τ_{zx} and τ_{zy} show the loading direction, vector ***d*** shows the direction of dislocation network motion. It is found that the dislocation network moves with the formation of kinks on the <111> screw dislocation segments, as shown in Figure 5.35. This also observed by Bulatov et al. [174] during

the low temperature deformation of molybdenum crystal. From the results of the above case study, the Y-direction was chosen as the loading direction for all the succeeding simulations.

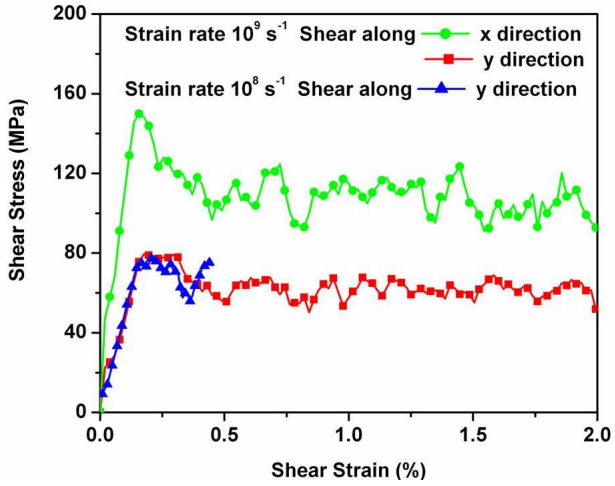

Figure 5.34: Shear stress strain curve for shear deformation twist grain boundary in pure Fe with different loading direction and strain rate.

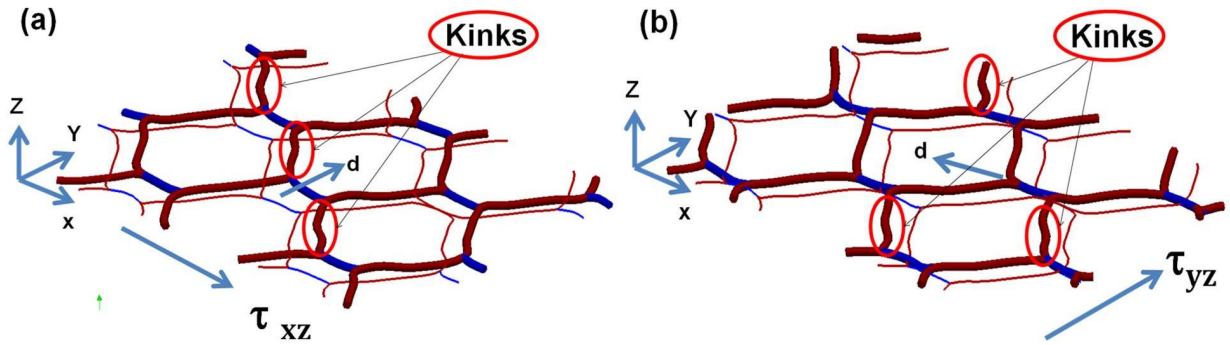

Figure 5.35: Snap shots showing the twist grain boundary dislocation network configuration during shear deformation (a) X-direction loading and (b) Y-direction loading.

5.3.3.2 Effect of strain rate

The effect of the strain rate on the stress-strain curve was also studied. For this purpose two strain rates, 10^9 s^{-1} and 10^8 s^{-1} have been selected. Only selected samples, one without He bubbles and another containing He bubble of size ~1.1 nm diameter were studied. No significant difference between the two stress strain curves is observed (see Figures 5.36). In the case of ~1.1 nm bubble, a small decrease in initial flow stress (~90 MPa) is observed for the 10^{-8} s^{-1} strain

rate. The decrease is small (< 5%) in comparison to maximal stress of 2400 MPa (see Figure 5.36), which shows the weak strain rate dependence in the investigated strain rate range i.e. $1*10^8$ to $1*10^9$ per second.

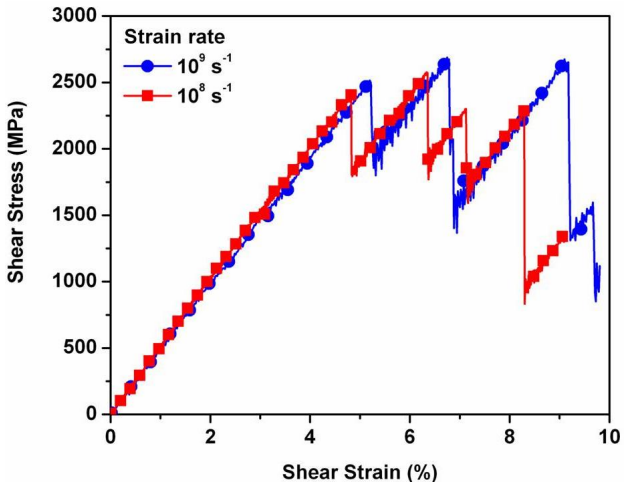

Figure 5.36: Shear stress strain curve for shear deformation of twist grain boundary in pure Fe with interface He bubble of diameter 1.1 nm.

5.3.3.3 Effect of helium bubble

Figure 5.37 shows the effect of different He content at the interface on stress strain response. The presence of He results in an increase in the stress required to move the dislocation network. Initially, the maximal shear stress was found to increase monotonically with interface He bubble diameter but started to drop for bubbles having diameters larger than ~1.9 nm, as shown in Figure 5.38. The nearest dislocation intersection nodes were approximately at a distance of 3.8 nm. The bubble diameter at which the stress started to drop was about 0.5 times the node distance. Figure 5.39 shows the dislocation and bubble configuration at the interface. In the sample having bubbles of diameters of 2.3 nm, the percolation of bubbles was observed and only a part of the dislocation network was visible as shown in Figure 5.39 (e) . The bubbles with 2.8 nm diameters were interconnected, no dislocation network was visible and for a He bubble

4.0 nm diameter, a layer of He atoms formed at the interface. Under the applied stress, these bubbles came in contact with each other before they were completely sheared by the dislocation network in the presence of 1.9 nm bubbles. The smaller He bubbles could be sheared easier than the bigger ones. Moreover, larger bubbles were carried by the dislocation network to long distances (in an average 1.0-2.0 nm) before they could be sheared. In the deformation process of the samples with high He content, point defects (isolated He atom and vacancies) were emitted by the interface, as shown in Figure 5.40. Once they were sheared, smaller bubbles formed, leading to an increase in the bubble density, as shown in Figure 5.40. In the case of bubbles with 4.0 nm diameter, the shear stress dropped below the pristine sample (see Figure 5.37). The glide mobility of the dislocations containing the He bubbles reduced significantly. The following reasons may be responsible for the reduced dislocation network mobility,

1. The presence of the He bubbles at the dislocation intersection avoids the formation of <100> dislocation segments.
2. The dislocations act as pre-existing parallel dislocations pinned by He bubbles and interconnected by other inclined screw dislocation segments.

The reduction in the mobility of dislocations and grain boundary sliding has a pronounced effect on the high temperature deformation behavior of the ferritic/martensitic steels. The presence of small bubbles (with diameter < 0.5 times inter node distance of dislocation network) can act as strong GB sliding inhibitor. The GB engineered materials under irradiation condition may show higher deformation resistance than the conventional one.

Table 5.3: Approximate He bubble diameter corresponding to given He content.

He content*	0.0005	0.001	0.002	0.003	0.004	0.005	0.01	0.022	0.0497	0.072	0.102
Diameter (nm)	0.3	0.6	0.7	0.8	1.0	1.1	1.35	1.9	2.3	2.8	4.0

*(#He atoms/# Total atoms)

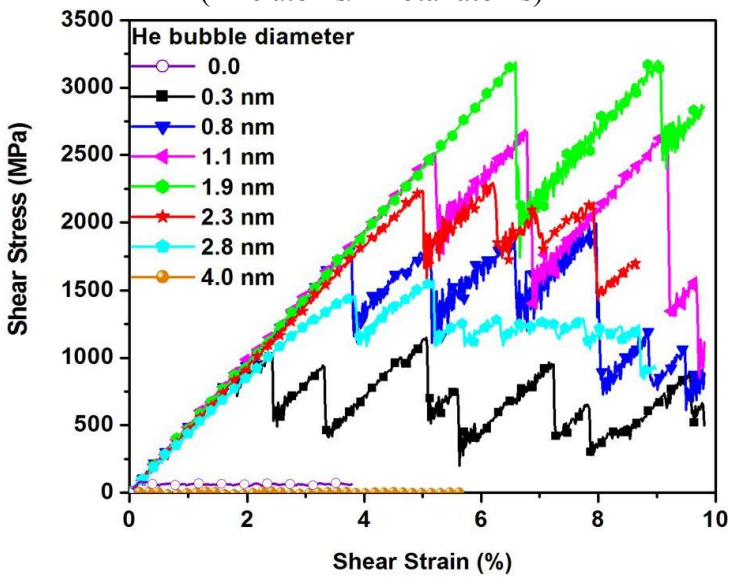

Figure 5.37: Shear stress strain curve for shear deformation of twist grain boundary in pure Fe with interface He bubbles of different diameter as given in Table 3.3.

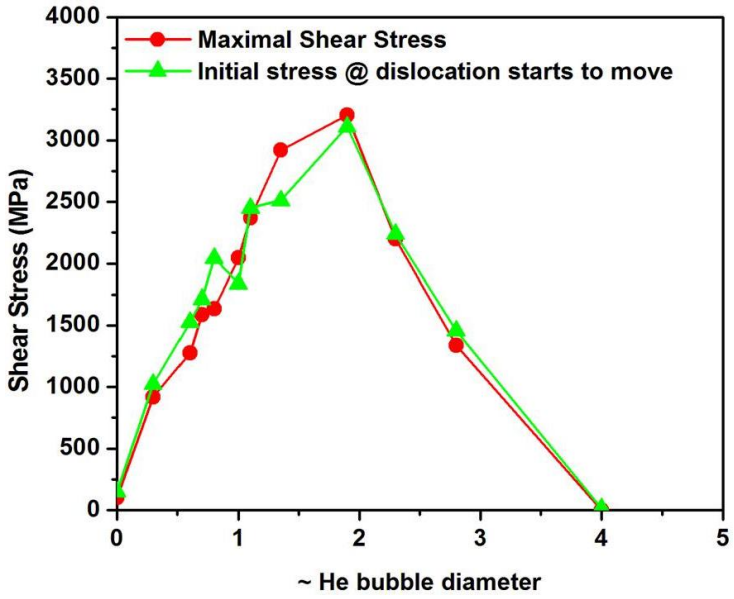

Figure 5.38: Dependence of maximal shear stress of twist grain boundary dislocation network on interface He bubble diameter.

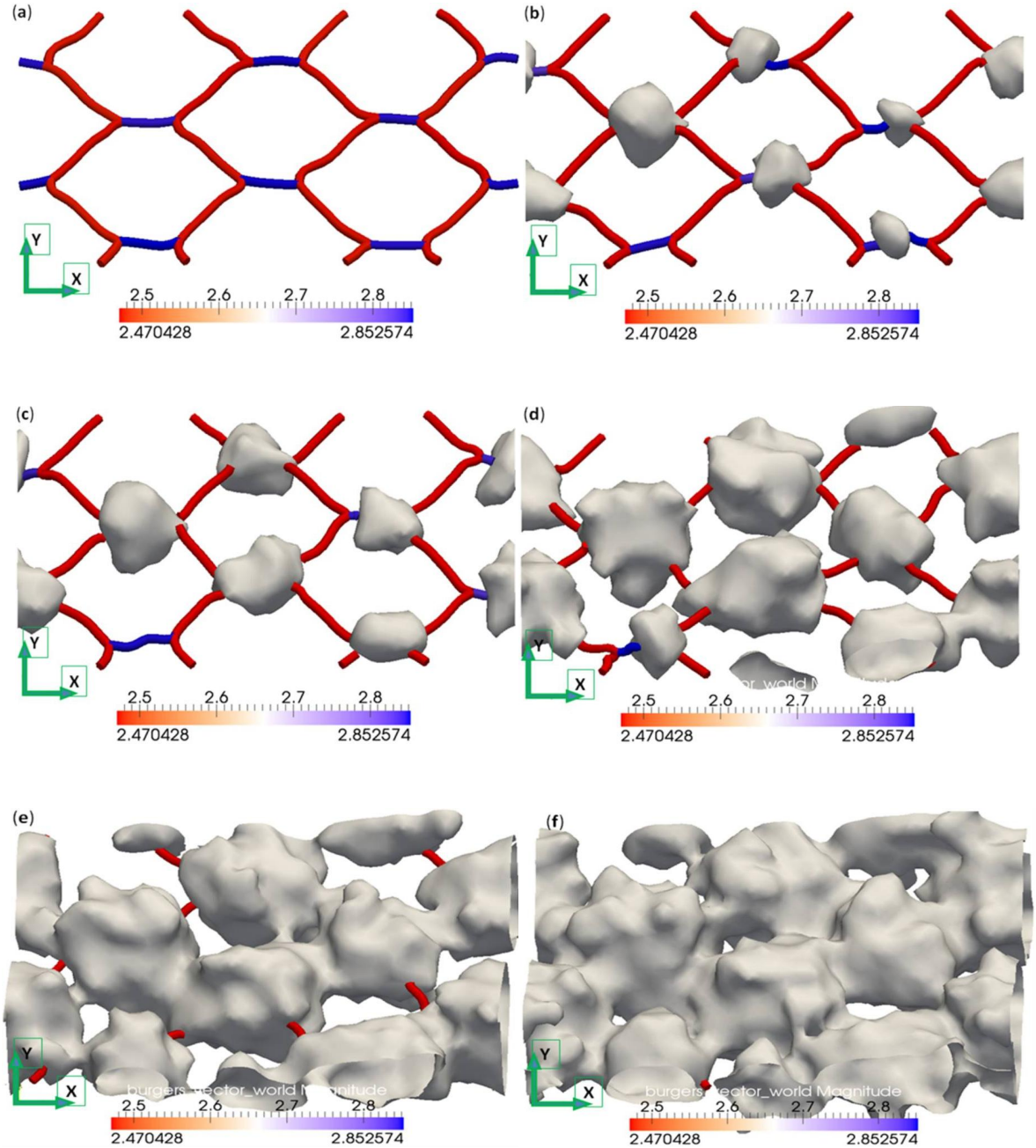

Figure 5.39: Low angle twist GB Dislocation structure in the presence of different He content a) 0.0 b) 0.003 c) 0.005 d) 0.022 e) 0.0497 f) 0.072. (See table 1) (Note: The red color corresponds to screw segment with Burger's vector magnitude of ~0.247 nm and blue color for <100> type screw segments Burger's vector magnitude of ~0.285 nm).

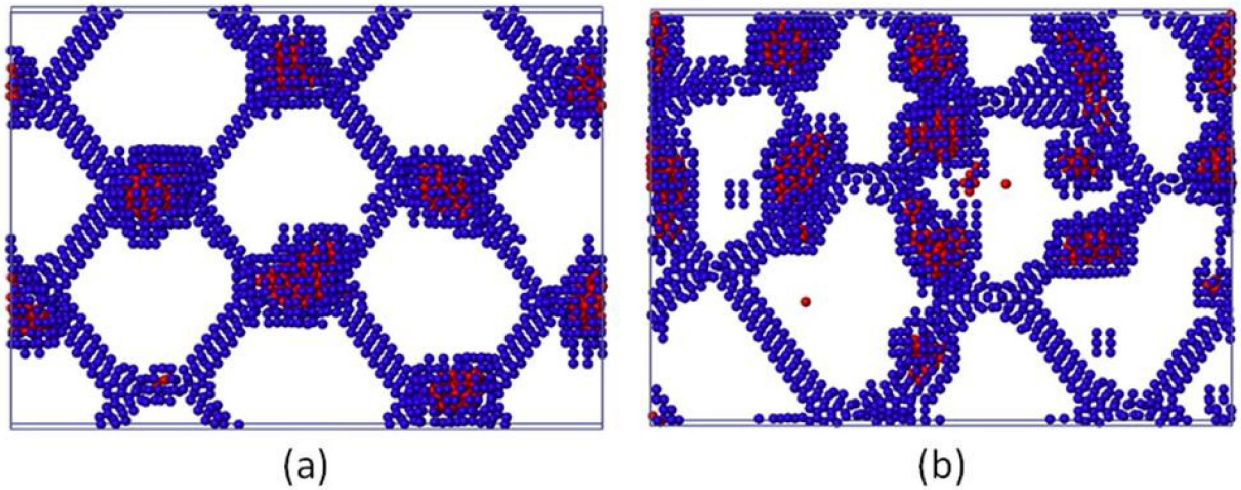

Figure 5.40: Dislocation network and He bubbles configuration (a) before and (b) after shear deformation.

As it was mentioned above, when the He bubble diameter becomes > 0.5 times the inter-node distance of interface dislocation network, the shear stress start to drop. The structural materials of the next generation nuclear reactors are expected to operate at temperatures above 500 ^{0}C. In the presence of transmutation induced He, softening behavior may occur at even smaller bubble diameter at these high temperatures due to thermal activation of dislocations and increased fluidity and diffusivity of the He atoms.

5.4 Closure

The main results obtained from the MD simulation of dislocation defect interaction and GBs sliding in the presence of helium bubbles are highlighted as follows,

- The MD simulations are carried out to study the mobility of ED in Fe, Fe-10%Cr and Fe-10%Cr with substitutional and Interstitial He. The results shows that the maximal/friction stress for ED increase due to addition of Cr in Fe in comparison to pure Fe. In the presence of substitutional atoms, the maximal/friction stress is slightly higher in Fe-10%Cr as compared to He in pure Fe. The substitutional He has less effect on ED mobility than that of interstitial He. In case of interstitial He, the maximal/friction stress for 0.1% case, is 2 to 3 times greater than the 1.0% substitutional case. At a given temperature, as the He content is increased, saturation of maximal/friction stress is observed in all cases substitutional He and 0.1% interstitial He, but not visible in case of 0.5 and 1.0% interstitial He. At higher concentration of He the interstitial He are readily found to form clusters which acts as strong pinning points. This supports the hardening behavior of ferritic/martensitic steels due to high density nanometric bubbles which are difficult to see in transmission electron microscope. The results are in qualitative agreement with the low temperature hardening of irradiated and He implanted ferritic/martensitic steels.
- In dislocation void interaction, it is found that the CRSS increases linearly with increase in void diameter from 0.8 nm to 1.6 nm in all the systems considered. The CRSS required for edge dislocation to overcome the void of diameter 1.6 nm in Fe-10%Cr is slightly higher (35-40MPa) than that of pure Fe. However, the same for Fe-10%Cr-1% He is significantly (150-160MPa) higher. The CRSS for interaction of edge dislocation with He bubble (1He-1V) in

pure Fe is lower than that of voids. In case of Fe-10%Cr it is observed that the bubbles are stronger obstacles than voids.

- MD simulations of shear deformation of low angle (110) twist GB in Fe with and without He bubbles have been carried out. It has been found that the presence of the $a_o/2$ <100> screw segments provides directionality to the grain boundary sliding, i.e. the shear stress required for the GB sliding is less along the direction perpendicular to the $a_o/2$ <100> screw segment in comparison to direction parallel to them. The bubbles formed at the junctions strongly pin the dislocation network reducing the mobility of GB dislocation network. At smaller diameter, the He bubbles are found to move with the network without shearing. The larger bubbles are found to be sheared by the network of dislocations, leading to smaller bubbles. Much of the sheared bubbles are found on <111> screw segments. Point defect (vacancies and He atoms) emission from the interface is observed for samples with larger bubble diameters. The shear stress required for the GB shearing increases monotonically up to a bubble diameter of 1.9 nm, which is 0.5 times the inter node distance, beyond which it drops. It is estimated that at higher temperature, the bubble diameter at which the drop occurs will be smaller.

The output variables/parameters from atomistic simulations relevant to higher length scale simulations are friction stress, critical resolved shear stress to overcome defects such as voids/bubbles and grain boundary sliding resistance in the presence and absence of irradiation induced defects i.e. void/bubbles.

CHAPTER 6: MOLECULAR DYNAMICS SIMULATIONS OF NANOINDENTATION

6.1 Introduction

MD simulations of nanoindentation tests were carried out to study the effect of irradiation induced defects by systematically introducing them in pure Fe and Fe-10%Cr systems. For this purpose defects like vacancies and dislocation loops were firstly introduced in the otherwise perfect lattice and subsequently subjected to indentation. Based on the depth of indent new set of dislocations were generated which started interacting with prior introduced defects. The interaction of defects with nucleated and propagating dislocations, different load versus depth of indentation have been generated. These simulation results are described in the following sections.

6.2 Computational details

Molecular dynamics simulation of nanoindentation was carried out on Fe and Fe-10%Cr systems consisting of ~$1.5x10^5$ and ~$1.0x10^6$ atoms. The recent ternary inter-atomic potential for Fe-Cr-He by Caro et al. [240] (Potential-2 of Chapter 5) was used in this study. The indenter was loaded on the top region of the sample (Figure 6.1). The simulations were carried out at 1 K and the selected cases were carried out at 300 K. Prior to indentation, sample was energetically minimized and then equilibrated at 1 K. The sample was oriented in standard <100>, <010> and <001> directions along X, Y and Z-axis. The indenter axis was aligned with Z-axis and was allowed to move in the negative Z-direction to indent on the top surface of the sample. The initial indenter sample configuration is as shown in Figure 6.1.

An attempt has been made to simulate the effect of irradiation induced defects (vacancies and loops) on nanoindentation load vs. depth of indentation curve in Fe and Fe-10%Cr alloy. In

order to examine the effect of the radiation firstly size of domains were optimized to 15.4x13.8x8.4 nm along X, Y and Z-directions and were kept identical for simulations of perfect samples as well as for irradiated samples. For the purpose of indentation, domains were divided into two regions; bottom and top. The bottom region was rigidly fixed to avoid any rigid body motion of the domain along the negative z direction while indenting. Two indenter shapes are considered for the simulations, one is spherical and other is Berkovich indenter. The spherical indenter is modeled as rigid indenter where the atoms within the radius of the indenter are moved outwards normal to the spherical surface. The Berkovich indenter was modeled explicitly using an arrangement of atoms in the form of diamond cubic structure. In the simulations with Berkovich indenter, interactions among the indenter atoms are ignored and it was assumed that there is no relative motion among the indenter atoms. The indenter was moved with a velocity of 10Å/ps with a time step size of 1 femto-second corresponding to a displacement increment of 0.001 nm. All the simulations were done using the public domain code LAAMPS [233] and the visualization atomic and dislocation structure are done using OVITO [235] and DXA [236] tools.

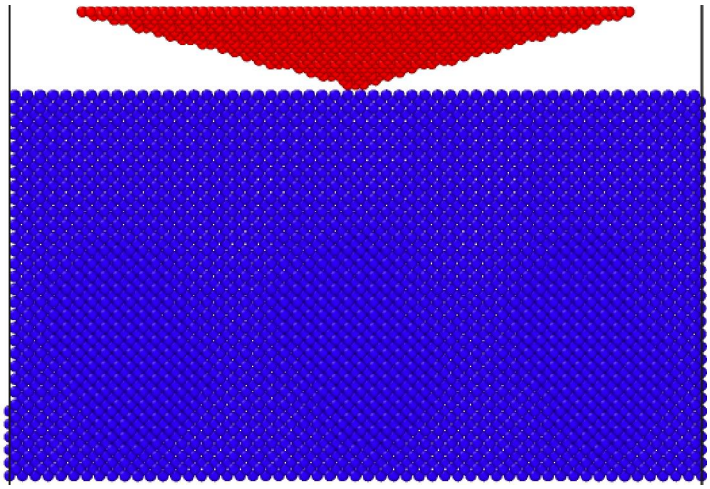

Figure 6.1: Initial Indenter and sample configuration in pure Fe case (Blue color-Fe sample atoms, red color-Indenter atoms).

6.3 MD simulation results

6.3.1 Effect of solute addition on load vs. depth of indentation curve

The dislocation structure generated during nanoindentation is shown in Figure 6.2 (a) and (b) for Fe and Fe-10%Cr systems respectively. The corresponding load versus depth of indentation (L-D) curves of simulated nanoindentation is shown in Figure 6.3 (a). From figure it could be noticed that in the initial part of loading both the curves are identical. The reason for such a behavior is due to the fact that both the samples are perfect in nature with Fe as the base material. The effect of alloying elements randomly distributed within the Fe sample at substitutional positions is not realized in terms of variation in the elastic properties of Fe. However, the effect of alloying is mainly realized in terms of dislocation activity as shown in Figure 6.3 (b). The dislocation nucleation load increases in the case of Fe-10%Cr system. Typical load at which a dislocation nucleated was found to be between 260-298 nN for Fe and 324-362 nN in the case of Fe-10%Cr system. Figure 6.3 (b) shows dislocation density as a function of depth of indentation (DI) in Fe and Fe-10%Cr systems. From the figure it is clear that the nucleation of dislocation is delayed due to the presence of Cr in Fe. Density of dislocation was found to be slightly higher in Fe-10%Cr in comparison to Fe at the maximum DI. In the case of Fe-10%Cr it has been also found that the dislocation recovery was slower in comparison to the pure Fe during unloading.

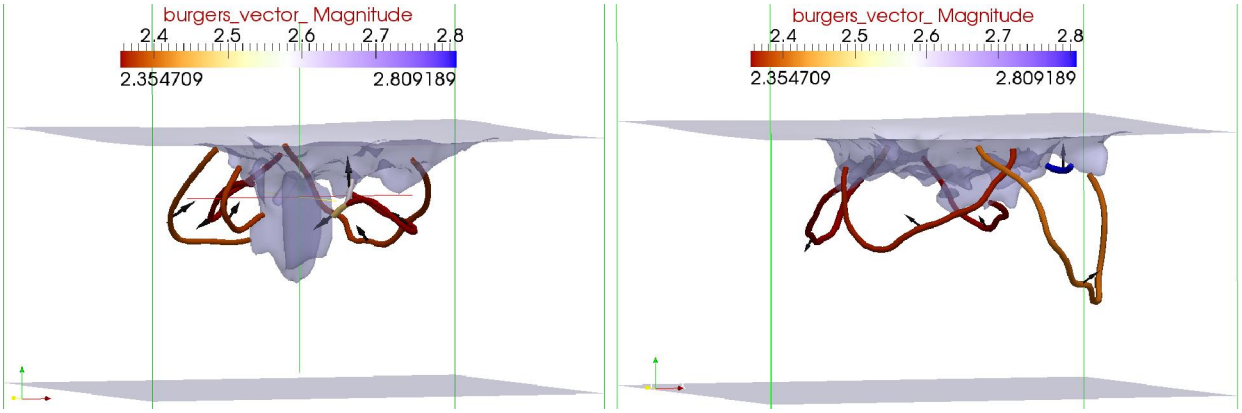

Figure 6.2: Final dislocation configuration at maximum depth of indentation in a) Fe and b) Fe-10%Cr system (arrows indicating the Burger's vector direction).

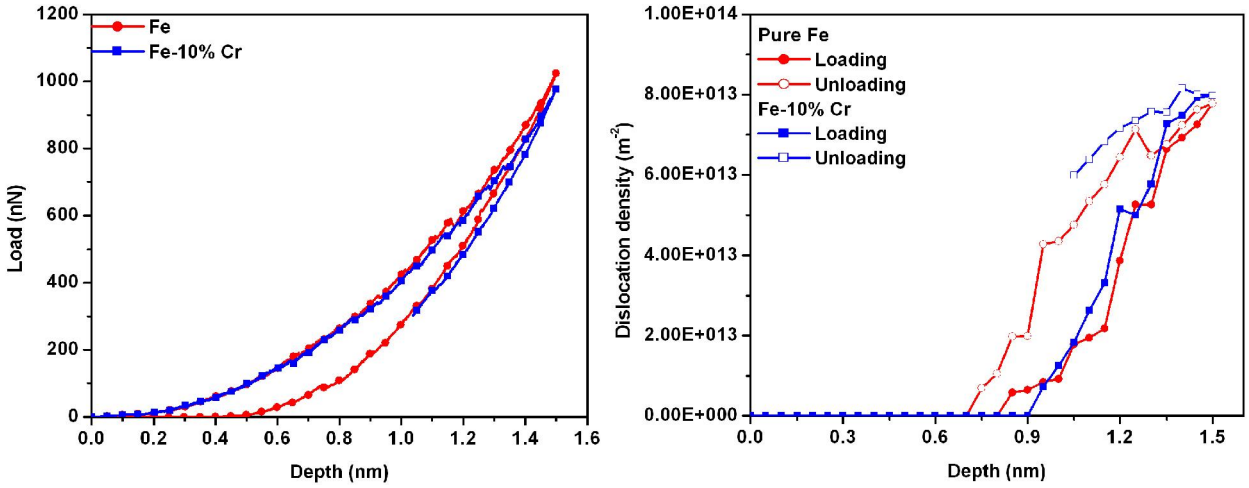

Figure 6.3: a) Load vs. depth of indentation curves and b) dislocation evolution in perfect Fe and Fe-10%Cr system.

6.3.2 Effect of irradiation induced defects on L-D curves

Figure 6.4 (a) and (b) shows Fe and Fe-10%Cr system configuration at maximum DI with randomly distributed 1% vacancies in the matrix. The L-D curves obtained are shown in Figure 6.5(a) for both the systems. In both the cases the load for the nucleation of a dislocation decreased in comparison to perfect systems. It was found to be in between 220-256 nN for Fe and 286-308 nN for Fe-10%Cr systems respectively. Several significant drops in the load were observed with increase in DI above 0.85 nm and 0.9 nm subsequent to the formation of first

dislocation in both the systems. These drops in the load could be attributed to the sudden release of dislocations from the vacancies present on the active slip planes or unzipping of the triple point junctions formed during dislocation nucleation and growth. Figure 6.5 (b) shows the dislocation density as a function of DI in both the systems. From the figure it can be observed that during unloading the presence of Cr in Fe-10%Cr system helps in retaining a small fraction of dislocations generated during the indentation which is not observed in the Fe system.

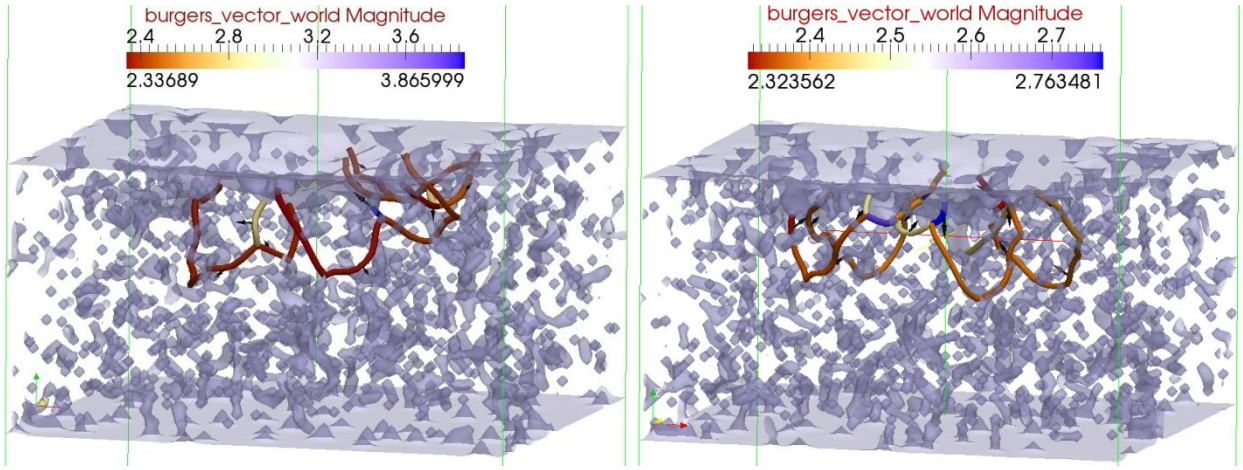

Figure 6.4: Final dislocation configuration at maximum depth of indentation in a) Fe and b) Fe-10%Cr system with 1% vacancies (arrows indicating the Burger's vector direction).

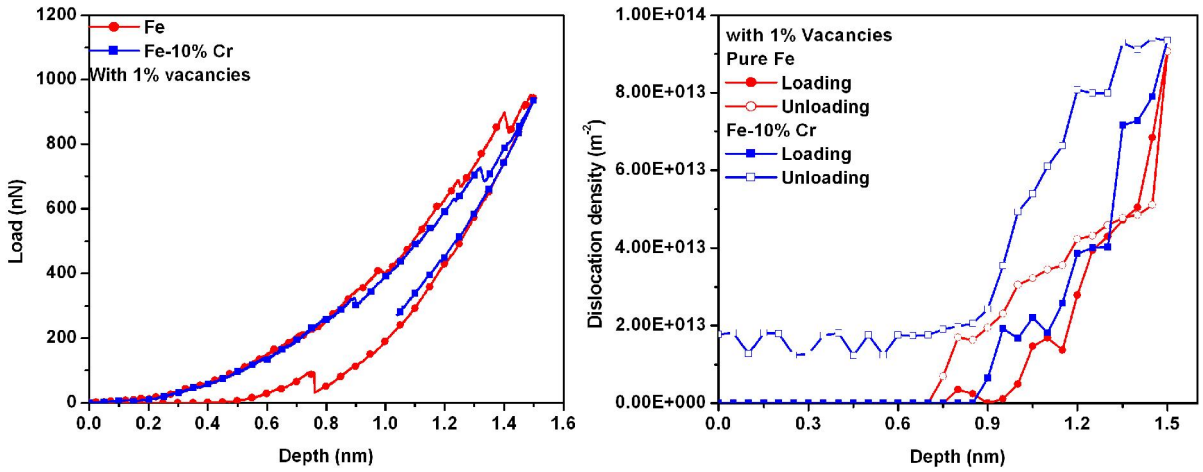

Figure 6.5: a) Load vs. depth of indentation curves and b) dislocation evolution in Fe and Fe-10%Cr system with 1% vacancies.

In the case of dislocation loops, two cases were taken up to understand the role of irradiation induced defects in Fe and Fe-10%Cr systems. As a first case, systems with ½ [111] type loops only were considered. Figures 6.6 & 6.7 show the initial and final configurations of both the systems. Figures 6.8 (a) & (b) show the corresponding L-D curves and dislocation density as a function of DI. As a second case, systems with randomly chosen loops from the family of ½ <111> Burger's vector were considered. In the second case during initial thermal relaxation steps it was observed that the segments from nearest ½<111> loop started interacting with each other and started forming <100> segments. This observation supports the formation <100> type loops reported in irradiated samples [250]. Figure 6.9 & 6.10 shows the initial and final configurations of both the systems. Figure 6.11 (a) & (b) shows corresponding L-D curves and dislocation density evolution with respect to DI in both systems. In both cases the loops were uniformly distributed on the plane normal to the indentation direction at ½ and 5/6 of the domain length. The typical diameter of a loop was taken as 2.0 nm which has been noticed in post irradiation microstructure characterization using TEM. In both the cases the dislocation nucleation load was found to be lower than the perfect domains and domain with 1% vacancies. However, in Fe-10%Cr with one type of loop, the value of nucleation load was higher than all other cases, as given Table 6.1. Major load drops in the L-D curves were found to be due to the interaction of a freshly nucleated dislocation with preexisting dislocations and started growing in the system. Reduction in dislocation density was observed with increase in DI as shown in Figure 6.8(b) & 6.11(b).

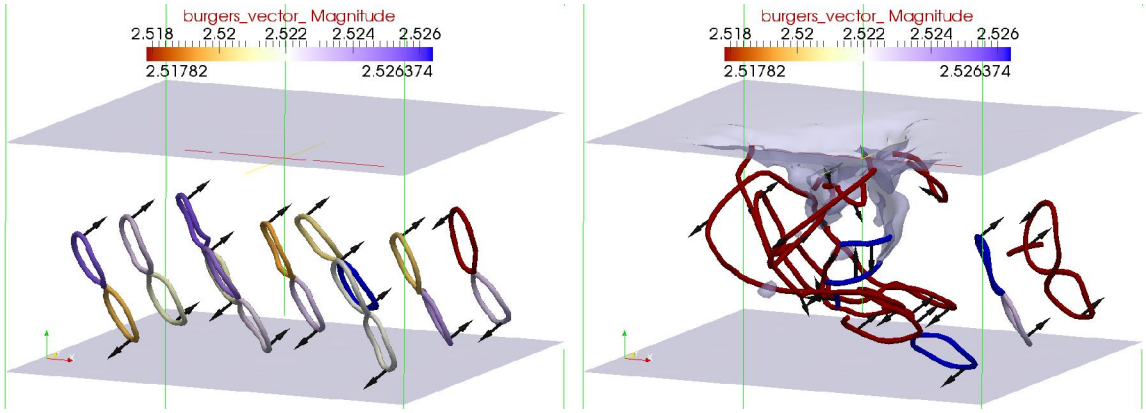

Figure 6.6: Initial and Final dislocation configuration of Fe (S1) system with uniformly distribute ½ <111> type loops (arrows indicating the Burger's vector direction).

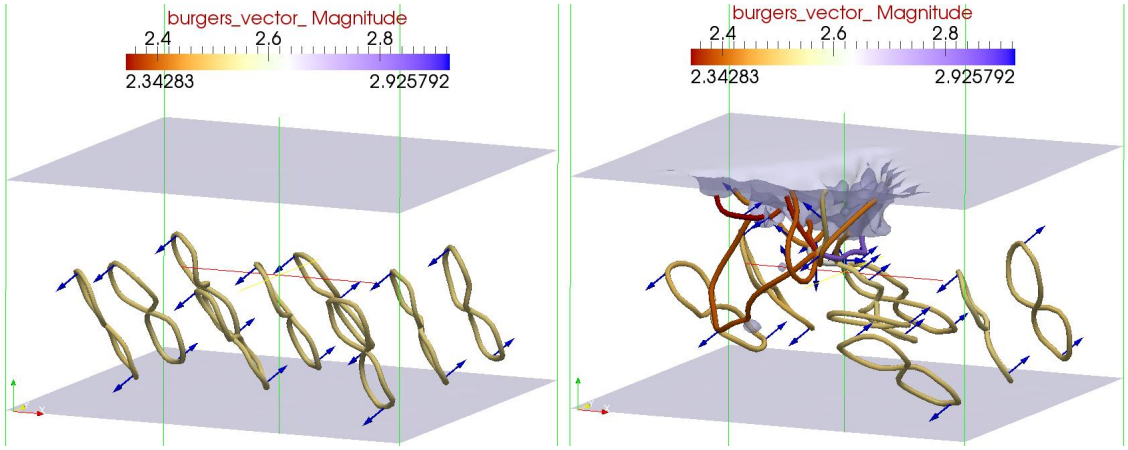

Figure 6.7: Initial and Final dislocation configuration of Fe-10%Cr (S2) system with uniformly distribute ½ <111> type loops (arrows indicating the Burger's vector direction).

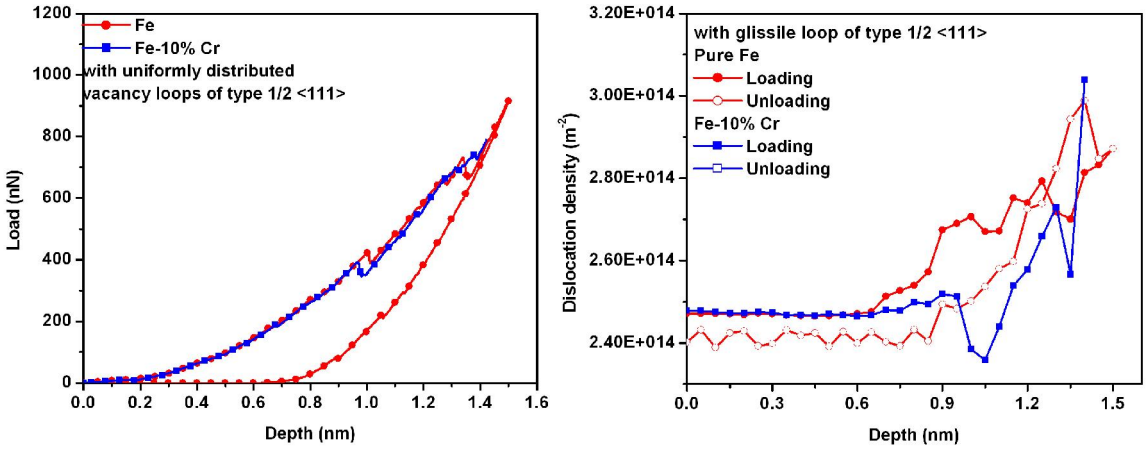

Figure 6.8: a) Load vs. depth of indentation curves and b) dislocation evolution in Fe and Fe-10%Cr system with vacancy loops of type ½<111>.

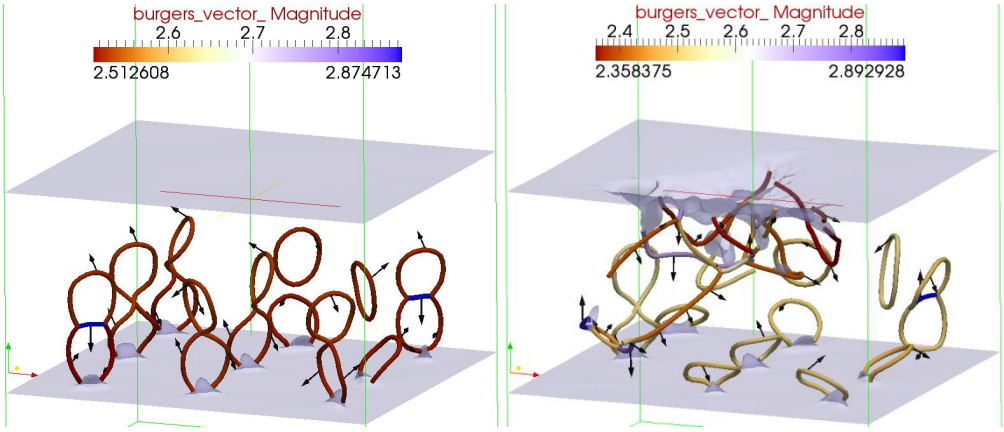

Figure 6.9: a) Initial and b) Final dislocation configuration of Fe (S1) system with uniformly distributed ½ [111] type loops (arrows indicating the Burger's vector direction).

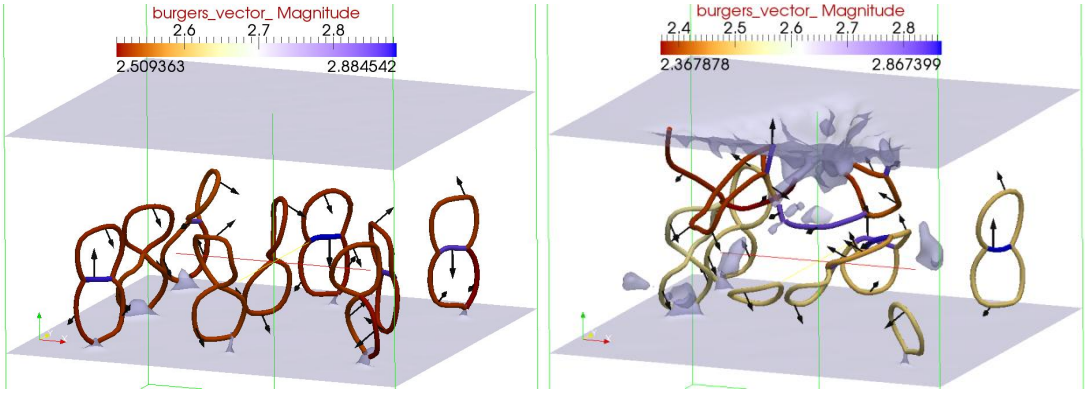

Figure 6.10: a) Initial and b) Final dislocation configuration of Fe-10%Cr (S2) system with uniformly distributed ½ [111] type loops (arrows indicating the Burger's vector direction).

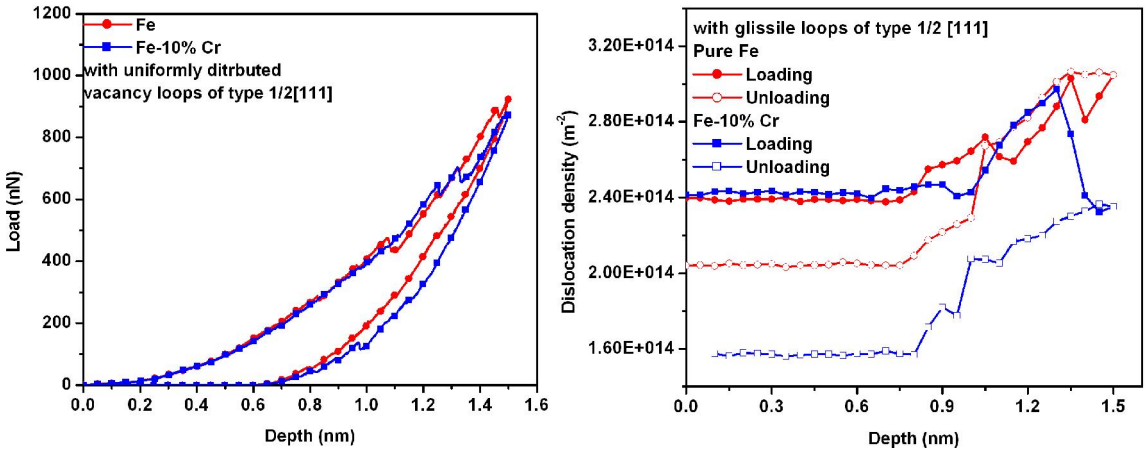

Figure 6.11: a) Load vs. depth of indentation curves and b) dislocation evolution in Fe and Fe-10%Cr system with vacancy loops with one of the type from $\frac{1}{2}[111]$ family.

Table 6.1: Dislocation nucleation load range in Fe and Fe-Cr system with and without defects.

	Fe	**Fe-10%Cr**
Pure	260-298	324-362
With 1% Vacancies	220-256	286-308
With Loops (1/2[111](110))	176-201	392
With Loops (1/2<111>{110})	202-240	143-170

The simulated load displacements curves obtained in all the cases exhibited similarity with the one obtained from the experiments. All L-D curves show an increase in the load with an increase in the depth of indentation due to increased area of indentation. From the atomistic visualization it was observed that dislocations nucleated under the indention region near one of the indenter face. The end points of dislocations were always pinned either at the indenter or at sample contact surface. As the load increases, the dislocation end points move towards the edges of the indenter and free surface of the sample. It was found that in the presence of the defects, the area under the loading and unloading curve was increased due to the partial recovery of dislocations. The dislocations nucleated and grew under indenter interacted with the loops resulting in the junction formation. Dislocation loop emission, which was observed during the indention of Fe with spherical indenter, was not observed in the present case. In general, it has been observed that the nucleation of dislocations in the case of Berkovich indenter is heterogeneous in nature. This heterogeneous nucleation leads to heterogeneous distribution of dislocation on different slip planes which may significantly affect the nanohardness if the indentation depth is too small. The main parameters which may affect the dislocation density evolution at small scale simulations are indenter shape, domain size and loading direction/rate. This shows the loop emission is a function of the indenter shape used for the indentation.

6.3.3 *Dislocation structure analysis*

Detailed analysis of dislocation structure was carried out on selected cases to find out the slip plane of each dislocation segment and the nature of dislocations in terms of edge, screw or mixed dislocation. Slip plane normal vector of a dislocation segment was determined by the cross product of vectors representing the segment line direction and burgers vector of the dislocation. This method of slip plane determination does not work in the case of screw dislocations. In such cases the slip plane was determined by taking account of the slip planes of the immediate neighboring dislocation segments. This exercise of determining of slip planes of dislocations revealed that dislocations were active on (110), (112), (123) and (100) slip planes. Figure 6.12 shows the activated slip systems and length of dislocation segments on each slip plane as a function of depth of indentation for pure Fe and Fe-10%Cr. From the figure it can be observed that the dislocations are mainly distributed on the (110), (112) and (123) slip planes and only a minor fraction of dislocations was also observed on (100) slip planes. This minor fraction on 100 slip plane represents sessile <100> dislocation segments generated due to the interaction of different ½<111> family dislocations. This shows that in bcc iron dislocations present in all possible slip planes with Burger's vector 1/2<111>.

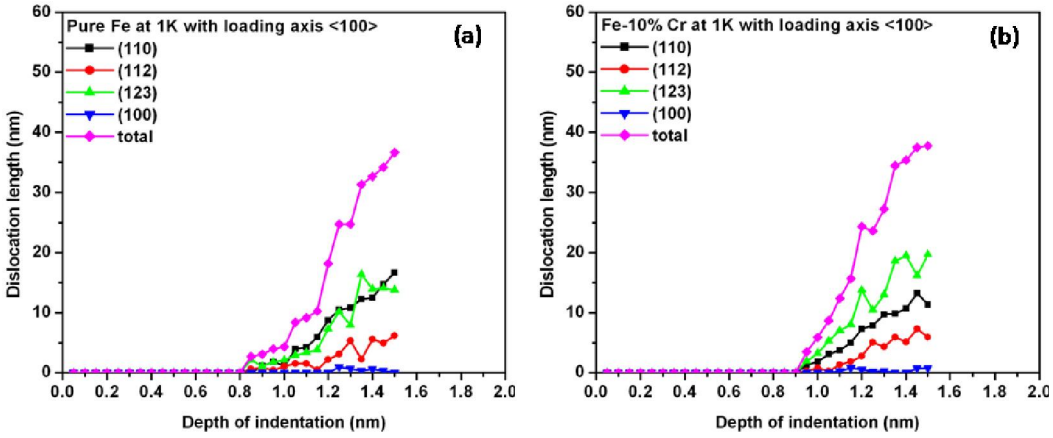

Figure 6.12: Dislocation evolution during nanoindentation in a) pure Fe and b) Fe-10%Cr system (smaller domain size with ~150000 atoms) at 1K.

In all the cases investigated in the present study, a significant fraction of dislocations was found confined mainly on (110) and (123) slip planes. The (112) family of slip planes was found to contain lower dislocation density in comparison to dislocation density observed in (110) or (123) slip planes. This observation highlights the importance of other slip systems while studying dislocation evolution during deformation. Figure 6.13 shows the dislocation line character distribution in smaller domain with Berkovich indenter.

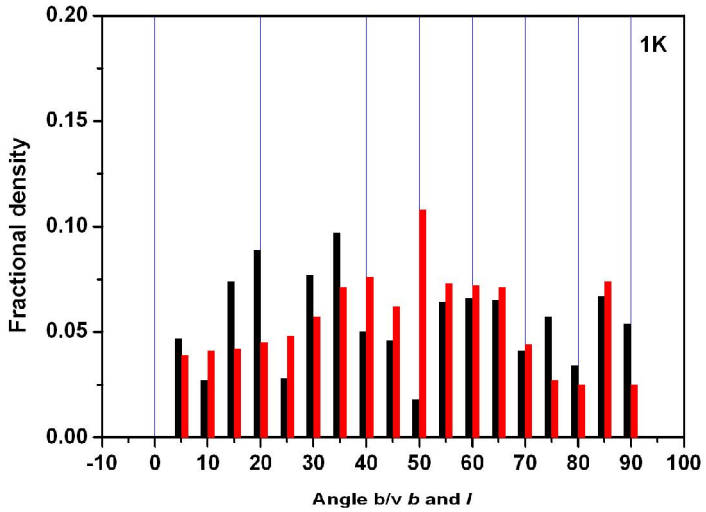

Figure 6.13: Dislocation line character distribution in pure Fe, Fe-10%Cr system at 1K for Berkovich indenter.

6.3.3.1 Effect of indenter shape on dislocation activity

In order to study the effect of indenter shape, nanoindentation simulations using spherical indenter were carried out on Fe and Fe-10%Cr system without any irradiation induced defects in the matrix. During indentation nucleation of dislocation loops was observed along all the four body diagonal directions <111>, <11-1>, <1-11> and <-111>. Evolution of dislocation density at 1K is shown in Figure 6.14 and 6.15 have behavior similar to that of Berkovich indenter case i.e. dominating slip planes found to be (110) and (123) in both the cases. Therefore, the effect of

shape of indenter was found negligible and was ignored in subsequent simulations. Figure 6.15 shows the dislocation line character distribution in smaller domain with spherical indenter. In the case of spherical indenter an increase in the fractional density was observed (Figures 6.15) when the character of dislocation changed from mixed either to edge (towards 90^0) or to screw character (towards 0^0).

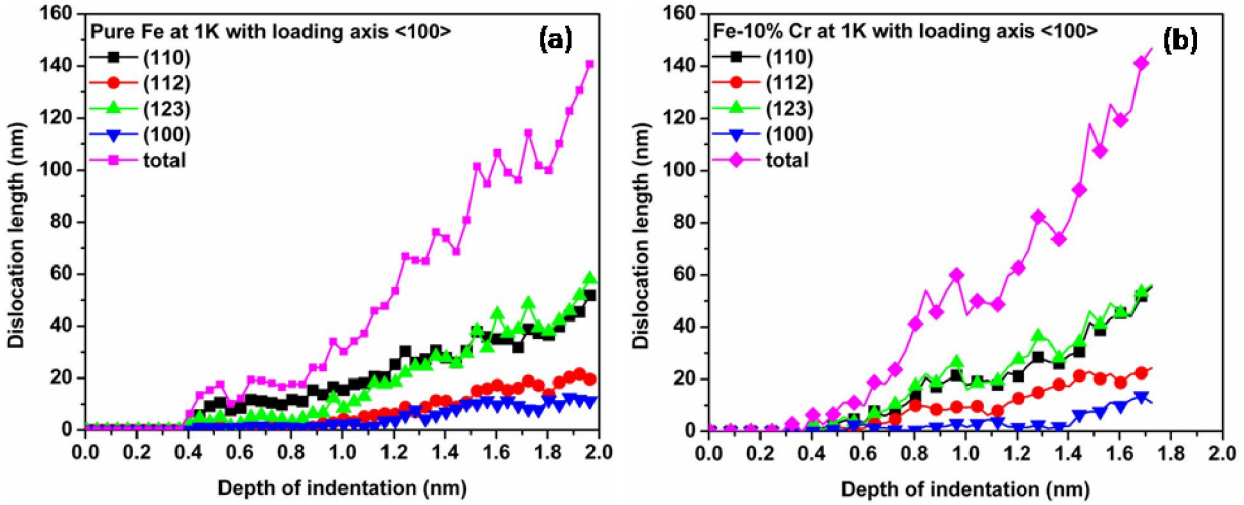

Figure 6.14: Dislocation evolution during nanoindentation in a) pure Fe and b) Fe-10%Cr system at 1K.

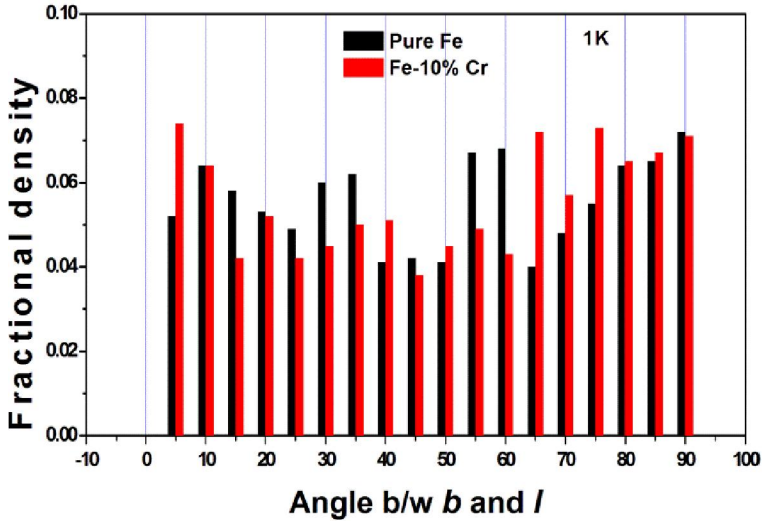

Figure 6.15: Dislocation line character distribution in pure Fe, Fe-10%Cr system at 1K for spherical indenter.

6.3.3.2 Effect of temperature on dislocation activity

The simulations carried out at 300 K for pure Fe and Fe-10%Cr system with Berkovich and Spherical indenter has shown that even at room temperature (123) slip planes were dominating in comparison to any other slip planes (Figure 6.16 & 6.17). In addition, it was observed that the dislocation density in the Fe-10%Cr system was slightly higher than that in pure Fe as the depth of indentation increases. This effect could be attributed to increase in localized stored energy of the system by the addition of Cr atoms during plastic deformation, which may help in the initiation of dislocation activity even at lower indentation loads. Figure 6.18 shows the dislocation line character distribution in smaller domain with Berkovich indenter. It shows that there is no preferential presence of screw characters at low as well as room temperature deformations during nanoindentation.

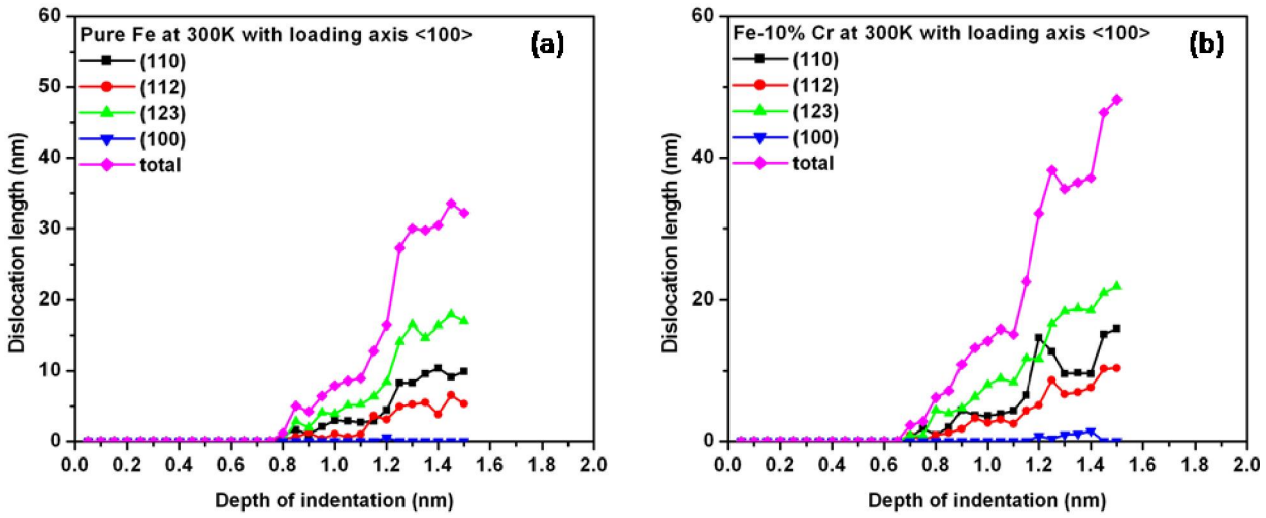

Figure 6.16: Dislocation evolution during nanoindentation in a) pure Fe and b) Fe-10%Cr system (smaller domain size with ~0.15x10^6 atoms) at 300K.

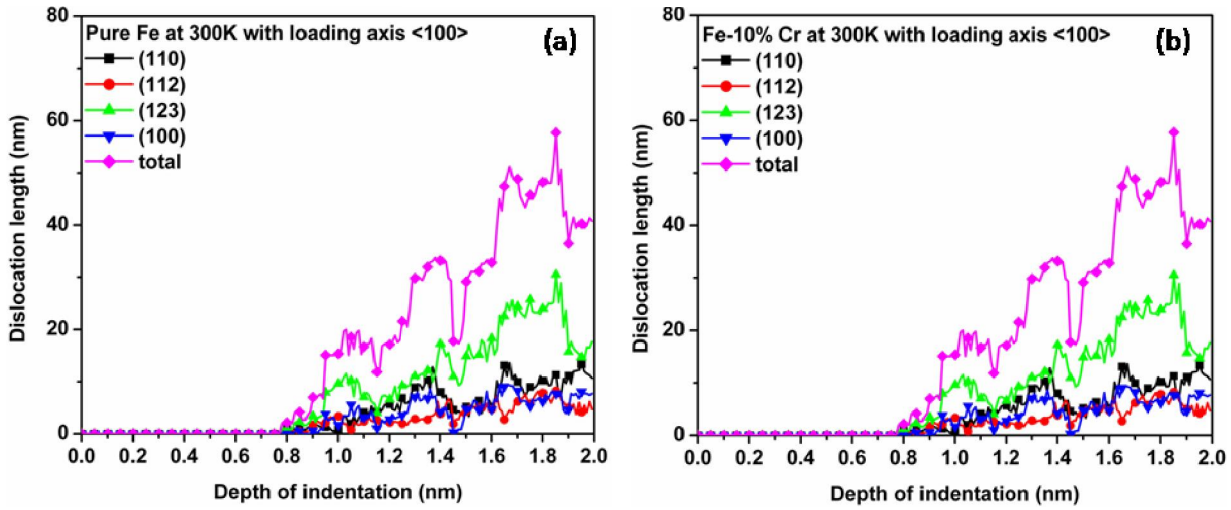

Figure 6.17: Dislocation evolution during nanoindentation in a) pure Fe and b) Fe-10%Cr system at 300K.

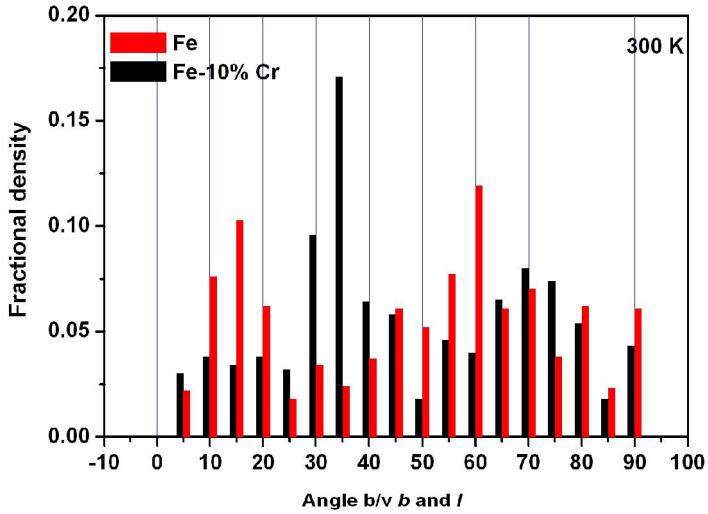

Figure 6.18: Dislocation line character distribution in pure Fe, Fe-10%Cr system (smaller domain size with ~0.15x10^6 atoms) at 300K.

6.3.3.3 Effect of loading direction on dislocation activity

In case of spherical indenter, the indentation was also carried out with loading direction along <111>. Figure 6.19a shows dislocation length versus depth of indentation for sample indented along <111>. In the case of spherical indenter with loading axis along <111> (Figure 6.19a) it was observed that the dislocation length on {110} and [51] slip planes are comparable

but {123} slip planes still remained dominating. Figure 6.19b shows the dislocation line character distribution in smaller domain with Spherical indenter. An increase in the fractional density of screw and Edge character was found at low temperature deformations during nanoindentation. Both Fe and Fe-10%Cr system have shown same line character distribution behavior.

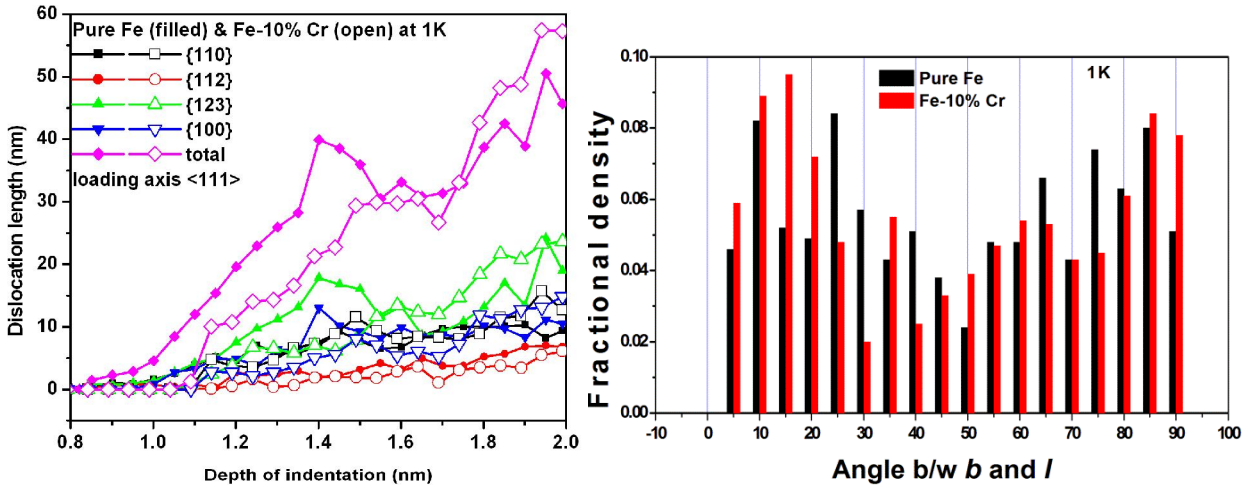

Figure 6.19: a) Dislocation evolution during nanoindentation along <111> and, b) Dislocation line character distribution in pure Fe, Fe-10%Cr system at 1K.

6.3.3.4 Effect of Domain size on dislocation activity

In order to study the effect of domain size, a larger domain containing ~$1.0*10^6$ atoms was considered for carrying out simulations of indentation on Fe and Fe-10%Cr system. The L-D curve for Fe and Fe-10%Cr system are shown in Figure 6.20 (a) along with a typical dislocation structure in Fe-10%Cr is shown in Figure 6.20 (b). The dislocation evolution on different slip planes is shown in Figure 6.21 (a) & (b) for Fe and Fe-10%Cr system respectively. The dislocation evolution patterns were similar to the one observed in smaller domains. Therefore, the effect of domain size on dislocation evolution on different slip planes is negligible. This study was also extended to study the effect of loading rate on dislocation evolution. The loading rate in Fe-10%Cr system was one order less than that in Fe system. Both the system have similar

trends in dislocation evolution and comparable with that of smaller domains. From this result loading rate effect can also be neglected on dislocation evolution on different slip planes for Berkovich indenter. Figure 6.22 shows the dislocation line character distribution in bigger (~1.0*10^6 atoms) domain with Berkovich indenter. In the case of larger domain size (Figure 6.22) for pure iron nearly uniform distribution of dislocation line character was observed. However, in case of Fe-10%Cr dislocation structures have shown that major fraction of dislocations have either pure edge or pure screw character.

In this study, the role of Cr atoms in impeding the dislocation motion is also highlighted. Dislocation structure has shown that the cluster of Cr atoms near the dislocation core impede the dislocation motion. For example, a region marked by ellipse in Figure 6.20 (b) shows a pinned dislocation. In the absence of the Cr atoms, the dislocation can attain a smooth shape as highlighted by dotted line in the Figure 6.20 (b). Due to the pinning of dislocations by Cr atoms, a portion of the dislocation segment was bent and a small portion of dislocation extended inside the samples where the concentration of Cr atoms was relatively lower as shown Figure 6.20 (b).

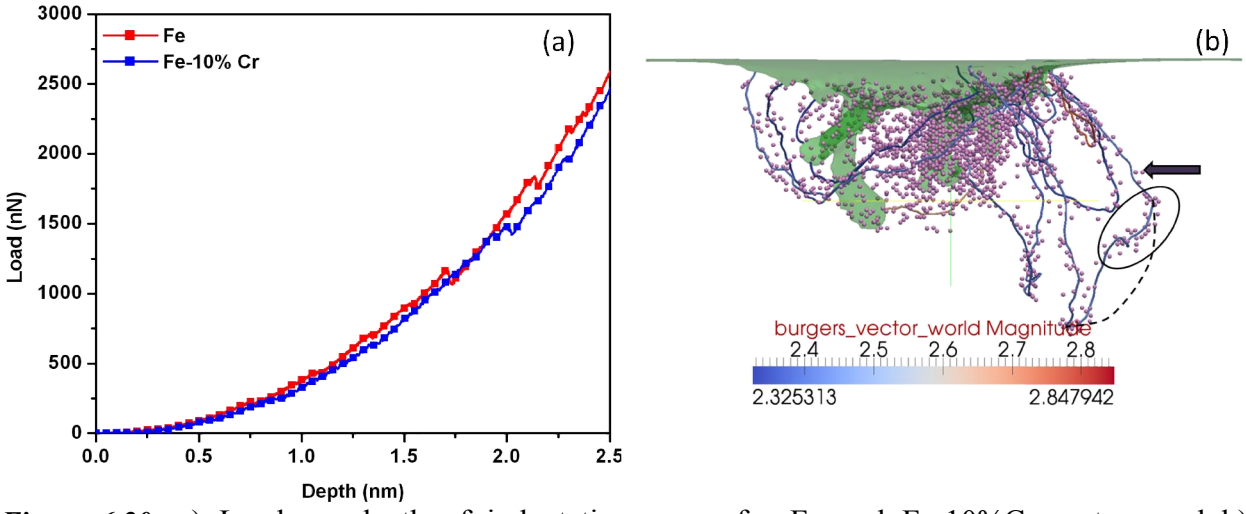

Figure 6.20: a) Load vs. depth of indentation curve for Fe and Fe-10%Cr system and b) Dislocation microstructure and Cr atoms arrangement near dislocations during nanoindentation in Fe-10%Cr system (bigger domain size ~1.0*10^6 atoms).

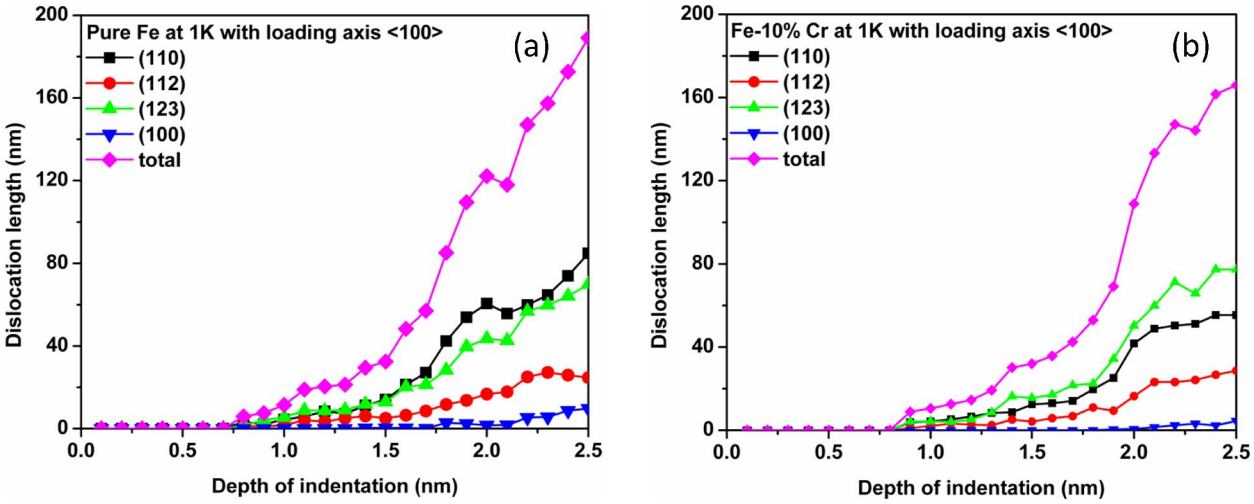

Figure 6.21: Dislocation evolution during nanoindentation in a) pure Fe and b) Fe-10%Cr system (bigger domain size ~1.0*10^6 atoms).

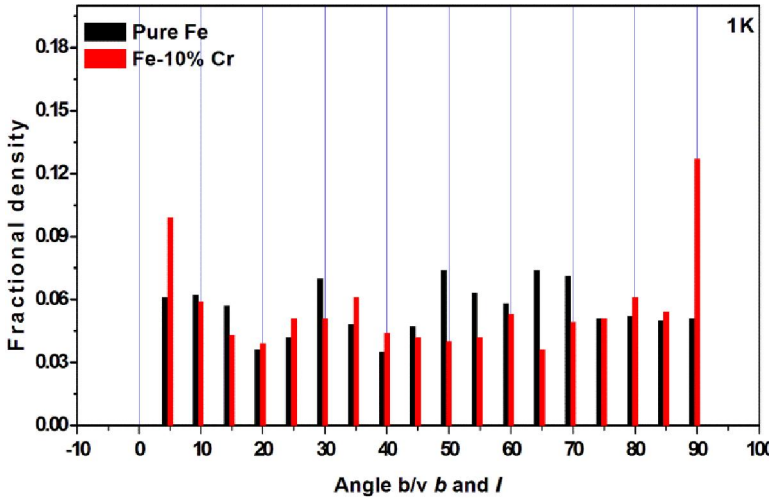

Figure 6.22: Dislocation line character distribution in pure Fe, Fe-10%Cr system at 1K for Berkovich indenter (bigger domain size ~1.0*10^6 atoms).

This study has shown that the nucleation of dislocation occurred heterogeneously due to the pyramid shape of the indenter with tip radius of two to three atomic diameters. Even though the indenter was placed symmetrically along the y-plane, asymmetric dislocation structure was observed in the all the cases. Dislocations nucleated and grew under indenter load and were found to form triple point junctions. The mixed symmetrical and asymmetrical junctions of

dislocations were also formed during indentation. The resulting junction segments were found to be with burgers vector of [100]. The presence of alloying element (Cr) in Fe was found to affect the dislocation nucleation and propagation. From Figure 6.2 it can be observed that the dislocation structure at maximum depth of indentation is significantly different in Fe-Cr system from the dislocation structure of the pure Fe. The region of spread of the dislocation is larger in the case of Fe-Cr as compared to region of spread in case of pure Fe.

The plastic region was approximately contained in a hemispherical region 3-4 times in size of the depth of indentation from a point formed by the intersection of indenter axis and the free surface of the sample. In the case of domain containing loops, the propagation of dislocation was found to be biased by the presence of loops which depending on the nature of its stress field may attract or repel the nucleated dislocation segment. This interaction of loops with nucleated dislocations assists in the heterogeneous distribution of dislocations near the indentation area resulting in the non uniform strain gradient. Many a times this non-uniform strain gradient manifests itself in terms of variation in hardness, which in literature is addressed as an indentation size effect [251].

6.4 Discussion

To capture the dislocation nucleation and their interaction with other nucleated/propagating dislocations or with irradiation induced defects while indenting the materials are difficult to observe using existing characterization techniques and are not available easily. Therefore, in the present work, MD simulations are carried out to study the effect of systematically introduced irradiation defects on load versus depth of indentation curve in pure iron and Fe-10%Cr system. The FM T91 steel is a dual phase steel having ferrite and martensite

distributed in the microstructure. In the present MD simulations martensite phase has been neglected and study is confined to the ferrite phase. This can be justified as, martensite has tangled dislocation network and it is difficult to identify the presence of irradiation-induced defects in martensite. Also, the tangle dislocation network acts as a sink for the point defect clusters and reduces the irradiation induced defect formation in the martensite phase. Therefore, the ferrite matrix having relatively dislocation free structure is suitable for the MD simulations to study the irradiation-induced defects. The systematic study has shown that the presence of randomly distributed defects such as vacancies and dislocation loops affect the load versus depth of indentation curves. In addition, the presence of Cr delayed dislocation nucleation by increasing the load in comparison to pure Fe. Dislocation nucleation was found to be heterogeneous due to the pyramid shape of the indenter with tip radius of two to three atomic diameters. Even though the indenter is placed symmetrically along the y-plane, asymmetric dislocation structure evolved. In the beginning of indentation a small number of atoms immediately below the indenter were found to be displaced elastically without the formation of any crystalline defects. In process of accommodating the elastically displaced material in the neighborhood nucleation of dislocation starts. The nucleated and growing dislocations under indenter load were found to form triple point junctions. The mixed symmetrical and asymmetrical junctions of dislocations were also formed during this time. The resulting junction segments were found to be with [100] burgers vectors. In the case of domain with loops the heterogeneously nucleated dislocation segments absorbed some of loops near the indenter edge region. The presence of alloying element (Cr) in Fe is found to affect the dislocation nucleation and propagation. It was observed that the dislocation structure at maximum depth of indentation is significantly different for Fe-Cr system from that of pure Fe. Also the region of dislocation

spread is more in case of Fe-Cr than in Fe. Due to the difficulty in determining the contact area no hardness has been estimated. In perfect crystals, load at maximum depth is higher in comparison to defective crystals as shown by MD simulations (Figure 6.3). This finding is in agreement with crystal plasticity simulation of nanoindentation on aluminium by Engels et al. [252].

In materials with bcc crystal structure a long standing ambiguity is present on the number of slip systems active during the plastic deformation. It is not clear that whether the deformation is due to localized slip on {110} or {112} or {123} planes, or due to the cooperative composite micro slip on different non-parallel {110} slip planes [253]. Taylor [254] concluded that for iron crystals, the mean plane of gross slip is the plane of maximum resolved shear stress in <111> direction. However, till date there are no techniques and results exist supporting the fact that the gross deformation is due to appropriate participation of two non parallel {110} slip systems which have maximum resolved shear stress. In order to find the active slip systems in bcc iron, many of the computer simulations has been carried out by assuming a relative activity of one or more slip systems to validate the results obtained from experimental studies of deformation and texture evolution [277- 279]. Simulation studies reported in the literature had shown that the activation of one or more slip systems can lead to given texture pattern depending on the texture evolution model used and stress state (i.e. tri-axial or bi-axial). Since the texture evolution models do not consider the dislocations explicitly, it is difficult to evaluate the relative dislocation density evolution on different slip plane families during deformation. In order to overcome this limitation MD simulations of nanoindentations were carried out, where the dislocation nucleation and evolution can be traced during deformation. In the present study,

analysis of dislocation structure generated during MD simulation of indentation had shown dislocation activity is present in all the slip planes i.e. (110), (112) and (123) (Figure 6.21). MD simulations also have shown that, effect of indenter shape, size of the domain, loading rate and temperature have negligible effect on the slip plane activity.

In general, deformation studies have been simulated using uniaxial load condition because of which activities of slip systems strongly depend on the orientation with respect to the loading direction. A more comprehensive approach would be to consider a triaxial state of stress which is relatively less sensitive to orientation. Under such a condition, activities of all possible slip systems in bcc will have nearly equal chance to contribute in deformation. In the present study during nanoindentation triaxial stress conditions were dominating which showed that {110} and {123}slip planes were dominant ones and appreciable dislocation activity also spreads on {112} planes. This study also shed light on the fact that the forest hardening observed FM steels may have a significant contribution from {123} slip systems and therefore should be considered in the higher length scale simulations.

6.5 Closure

The following conclusions can be drawn from the MD simulation of nanoindentation;

- The MD simulation of nanoindentation was carried out on FM steels base materials, Fe and Fe-10%Cr. The effects of irradiation induced defects like vacancies and loops on load displacement curves has been investigated and are in good agreement with experimental observed load displacement curves.
- The comparison of the experimental and simulated load versus depth of indentation curves showed reasonable agreement with each other due to the self similar geometry of the Berkovich indenter at any depth of indentation.
- The deformation behavior and slip system activity analysis in selected cases showed that all the possible slip planes of bcc iron ({110}, {112} and {123}) found in the literature were active during the indentation. The dislocation character analysis showed no preferential presence of screw or edge character in Fe and Fe-10%Cr system during nanoindentation at temperatures ≤ 300K.
- The relative activity of dislocations in different slip plane families can be used as input to higher length scale simulations such as dislocation dynamics and finite element based crystal plasticity formulation. In these higher length and time scale methods, hardening is a function of dislocation evolution on different slip plane families considered in the material models.

CHAPTER 7: DISCRETE DISLOCATION DYNAMICS (DDD) SIMULATIONS

7.1 Introduction

The DDD simulation is also known as meso scale simulation in the MMM methodology, which allows the investigation of the collective behavior of microstructural features which affects the macro scale material properties. In this scale, the line defects which are also called as carriers of plasticity are discretized into small straight line segments depending on the formulation as described in the section 2.3.2. As given in section 3.4 the output/results of the MD simulations were used as phenomenological local rules for the dislocation defect interaction in the DDD simulations. In particular, till date the MD simulation results, such as dislocation drag coefficient, critical resolved shear stress for dislocation to overcome an isolated defect under consideration, stress required to overcome the lattice friction (or resistance) and dislocation-dislocation interaction mechanisms were used in the DDD methodology. The formulation of local rules from MD results allows simulation of the interaction of ensemble (or group) of dislocations with the ensemble of (point, planar or volumetric) defects which are modeled explicitly or considered as implicit in the resistance for the dislocation motion. The simulations carried out till date consider single crystals of size from microns to few tens of microns containing single frank read source to dislocation density of the order of 10^{14} m^{-2}. The computational resource (time and data storage space) required for the simulation increases with the increase of the dislocation segment nodes which increases with the increase in plastic deformation or strain.

In the present study, linking of atomistic with meso scale is achieved by passing the information gained from atomistic simulations (e.g. friction stress and resistance of defects for

moving dislocations) to the dislocation dynamics simulations. The DD simulations were carried out to estimate flow stress for a) Fe, Fe-10% Cr and Fe-10%Cr-1%He alloy systems and, b) Fe, Fe-10%Cr alloy system in the presence of irradiation induced defects with selected case studies. The crystal defects such as second phase particles and irradiation induced voids, bubbles and precipitates are known to act as pinning points or barriers for dislocation motion. Dislocations need more external applied stress to overcome these barriers. The particles may be sheared by dislocations or bypassed by the formation of Orowan loops. The Orowan loop formation is observed in dislocation interacting with impenetrable obstacles, e.g. carbide particles. In the present DD simulations only obstacles which can be sheared (i.e. voids and bubbles) were considered for analysis.

The presence of effect of Cr and He in Fe was taken into account by the threshold friction stresses (τ_f) as derived from MD simulations. As a first approximation, it is assumed that the friction stress obtained for edge dislocation is applicable for all dislocation characters, i.e. edge screw and mixed. The irradiation induced obstacles are randomly distributed in Fe and Fe-10%Cr crystal and overlapping of these obstacles are avoided in all the cases. The stress required to shear the obstacle is dependent on the size and type of the obstacles. The shear resistance or stress needed for the dislocation segments to overcome obstacles is also taken from MD simulations. Table 7.1 lists the shear resistance values for different cases considered.

7.2 Computational details

For DD simulation, the domain was assumed as isotropic and elastic, with a shear modulus of 83.6GPa, the poisons ratio of 0.33 and the Burger's vector of 0.248nm which corresponds to pure iron [206]. The volume of domain considered for the simulation was

selected as $7\times8\times9$ μm^3 with periodic boundary conditions. The x, y, z directions correspond to [100], [010] and [001]crystallographic directions of the bcc crystal respectively. Initial microstructure was generated by straining the crystal having 48 sources for nucleation of dislocations with random (edge, screw or mixed) character. An equal number of sources in each slip system of slip family ⟨111⟩{110} were considered which are known to be active in iron at low temperatures. Initial microstructure consisted of a dislocation density of 9×10^{11} m^{-2}. A drag coefficient of 10^{-4} Pa.s was used in the simulations [206]. The tensile loading was applied by specifying strain rate of 100 s^{-1} along [001] direction. A discretization length of 0.25μm and a time step size of 3.5×10^{-11} s was used in all the simulations. The cross-slip behavior of screw dislocations were not considered in the present simulations.

For studying the effect of irradiation induced defects, obstacle density (either voids or bubbles) of 2×10^{21} m^{-3} was used. The voids and bubbles were considered as obstacles of diameter 'd' with spherical volume having friction stress shear as given by Monnet [256]. To bridge the length scales, the computed CRSS values from MD simulations of dislocation-defect interactions was used to find the friction stress (τ_f) as input to DD simulations. For this bridging, the scaling law described by Sylvain [213] was used to calculate τ_f from τ_{CRSS} as given in equation (4.1):

$$\tau_f = \tau_{CRSS} \frac{l}{d} \tag{7.1}$$

where, l is the average distance between two obstacles and d is the average diameter of obstacles. Various results obtained from these DD simulations are presented in the following sections

7.3 Results and discussion

7.3.1 Flow stress for Fe, Fe-10%Cr and Fe-10%Cr-1%He samples

Figure 7.1 shows the simulated tensile stress (σ-ε) strain curve for *Fe, Fe-10%Cr and Fe-10%Cr-1%He* samples in the absence of irradiation induced defects. From the figure it can be observed that the addition of Cr increases the value of the flow stress from 120 MPa to 250 MPa which was further enhanced to 500 MPa in the presence of 1%He. It is observed that in the initial linear region no significant dislocation activity was observed but as load increases plastic deformation starts i.e. dislocation starts to move.

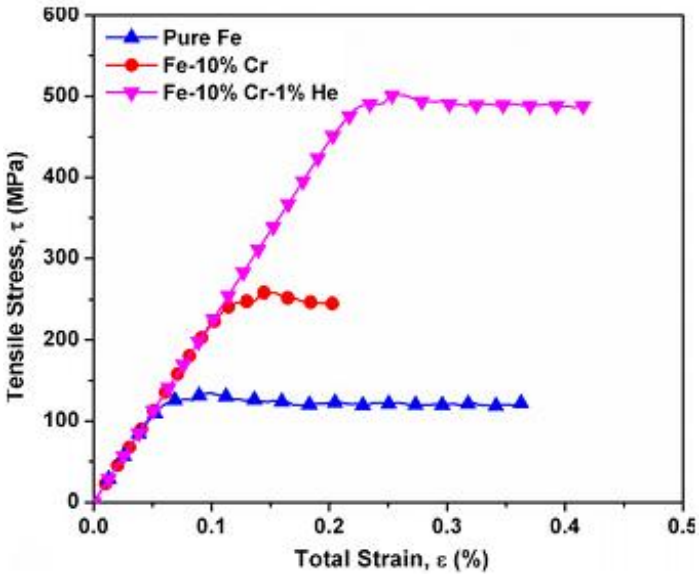

Figure 7.1: Tensile stress strain curves for Fe, Fe-10%Cr and Fe-10%Cr-1%He crystals estimated using DD simulations.

7.3.2 Flow stress for Fe, Fe-10%Cr with irradiation induced voids

The DD simulations were performed to determine the flow stress variation in Fe and Fe-10%Cr in the presence of different sized voids. The simulation conditions were kept identical as that were defined in the previous section. The σ-ε plot for Fe and Fe-10% Cr with different void diameters is as shown in Figure 7.2 and 7.3 respectively. The simulations were stopped as the σ-ε

plot started to indicate the plateau region. It could be observed from this figure that with increase in diameter of the void for a given obstacle density the flow stress of the material increases. An approximate increase in flow stress of 20 MPa for 0.8 nm, 35 MPa for 1.2 nm and 50 MPa for 1.6 nm diameter void was observed in both the systems. A schematic diagram of a dislocation interacting with an obstacle obtained from DD simulation is shown in Figure 7.4. The DD simulation does not mimic the initial attraction of dislocation by voids as observed in MD. From the figure it can be observed that the dislocation pinning and release by the obstacle is similar to as observed from the MD simulations.

Table 7.1: Critical stress for voids and bubbles used in DD.

Defect	Size (nm)	Shear resistance (GPa)	
		Fe	Fe-10%Cr
Void	0.8	5.8	4.1
	1.2	4.4	3.8
	1.6	3.5	3.7
Bubble	0.8	4.5	-
	1.2	3.4	-
	1.6	2.9	-

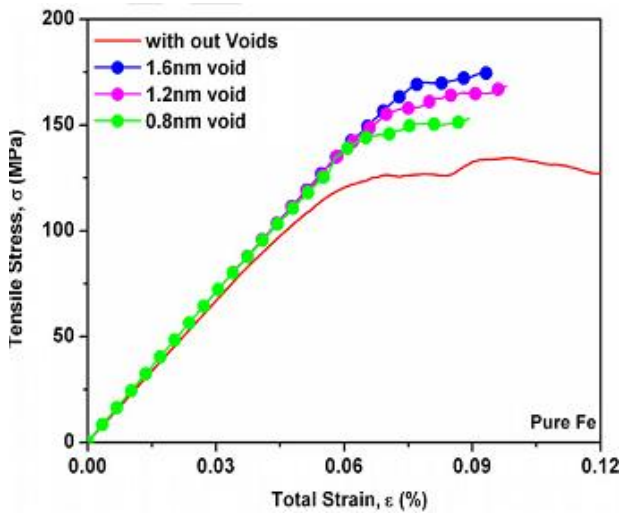

Figure 7.2: Tensile stress strain curve for Fe crystal with voids of different diameter (density of void 2×10^{21} m^{-3}).

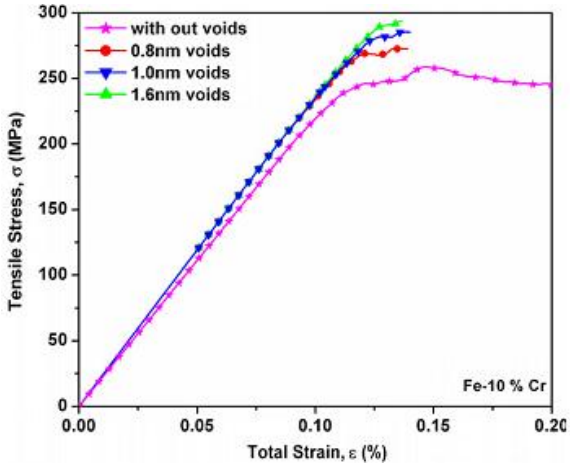

Figure 7.3: Tensile stress strain curve for Fe-10%Cr crystal with voids of different diameter (density of void 2×10^{21} m^{-3}).

7.3.3 Flow stress for Fe with irradiation induced bubbles

In this case, DD simulations were performed to determine the flow stress variation in pure Fe with different sizes of helium bubbles due to irradiation. The simulation conditions were as described in previous section. The σ-ε plot for Fe with different bubble diameters is as shown in Figure 7.5. A similar hardening behavior was observed in case of voids as obtained in the present case too. An approximate increase in the flow stress of 10MPa for 0.8nm, 25MPa for 1.2nm and 35MPa for 1.6nm diameter bubbles was observed. In all simulations, the obstacles were lying on the slip planes and were sheared by the dislocations. Assuming a constant bubble density, the increase in bubble size was related to irradiation dose using the estimated He production rate of 15 appm/dpa [11]. The helium production rate of 15appm/dpa corresponds to a volume fraction of '*f*' per dpa, then a given diameter of bubble of volume 'Ω' with a given density 'ρ' corresponds to a dose of Ω×ρ/f. For example, a spherical bubble with 0.8 nm diameter $\rho=2\times10^{21}$ m^{-3} and $f=15\times10^{-6}$ results in 0.035 dpa. Similarly, the bubbles with 1.2nm and 1.6 nm correspond to an irradiation dose of 0.12 and 0.28 dpa respectively. The flow stress vs.

dpa plot is shown in Figure 7.6. The figure shows that the rate of change of flow stress is higher in the initial region up to 0.125 dpa beyond which it shows a tendency for saturation in pure Fe.

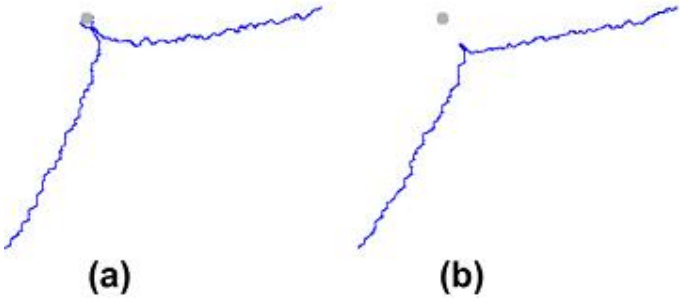

Figure 7.4: Schematic diagram showing the dislocation void/bubble interaction (dislocation configuration (a) before release (b) after release from the obstacle).

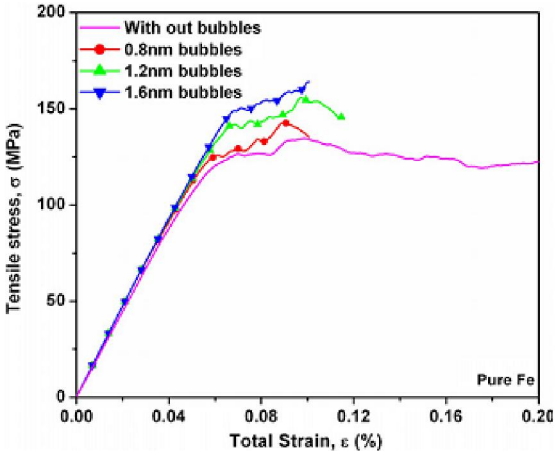

Figure 7.5: Tensile stress strain curve for Fe crystal with helium bubbles of different diameter (density of bubble 2×10^{21} m^{-3}).

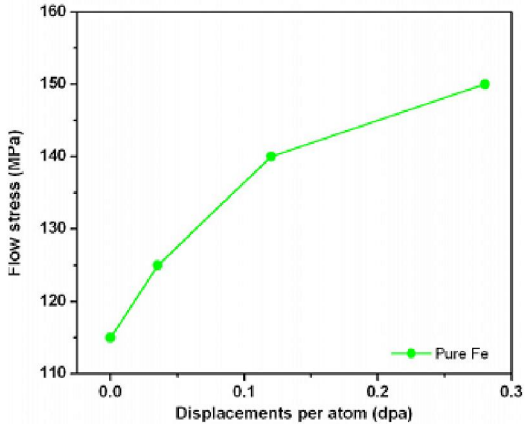

Figure 7.6: Flow stress variation with respect to dpa in pure Fe.

7.3.4 *Comparison of experimental results and multi-scale approach*

An effort was made to predict the experimental values of yield stress as reported by Dai et al. [257] for the T91 tensile samples irradiated at different temperature and tested at 523 K using multi-scale approach. The samples were irradiated by Dai et al. [257] to different doses as tabulated in Table 7.2 and shown in Figure 7.7. The irradiated microstructure has shown black dots in TEM imaging which were assumed as point defect clusters. The defects were responsible for the increase in the yield stress of the material. The density and average diameter of the defects as a function of dose was found by using the correlation given by Deo et al. [258]. It is given that the defect density and diameters vary as square root of dose for the investigated dose range. The following procedure was adopted in determining the yield stress of the unirradiated and irradiated T91material.

Table 7.2: Experimental data of T91 material as taken from Dai et al. [257].

Dose (dpa)	Irradiation Temperature (c)	Test Temperature (c)	He (appm)	Yield strength (MPa)	ΔYS (MPa)
0	-	250	0	484	0
3	95	250	180	702	218
5.9	194	250	390	754	270
7.6	216	250	565	843	359
9.8	300	250	815	900	416

Initially the parametric study was carried out by varying the friction stress for unirradiated material such that the flow stress obtained from the DD simulation matches with the experimental one. Due to complex nature of the interaction of dislocations with different solute atoms, grain boundaries and other microstructural features, it is assumed that the friction stress adjusted accounts for the solute friction, presence of grain boundary and other micro-structural

features. This friction stress was found to be 125 MPa. This friction stress was kept constant throughout the remaining simulation work.

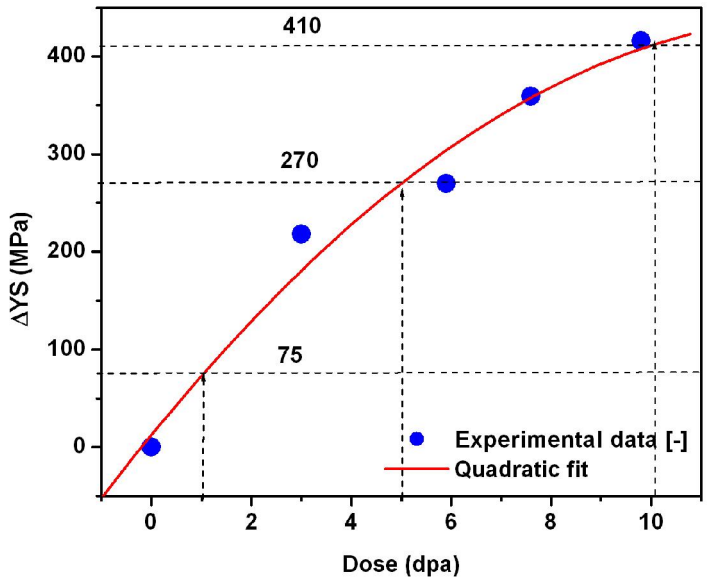

Figure 7.7: Change in yield strength with respect to dose in T91 materials (The experimental values are taken from Dai et al. [257]).

Table 7.3: List of estimated defect size, defect density, CRSS using equations 7.2a-c and average domain size used in MD simulation.

Dose (dpa)	**Density (m^{-3})**	**Cluster diameter D (m)**	**DBH CRSS (MPa)**	**MD domain size (m)**	**Approximate Cluster equivalent void diameter d (m)**
1	5.0×10^{22}	3.7×10^{-9}	~111	27.14×10^{-9}	1.3×10^{-9}
5	1.18×10^{23}	8.27×10^{-9}	~250	20.76×10^{-9}	2.27×10^{-9}
10	1.58×10^{23}	11.7×10^{-9}	~352	18.5×10^{-9}	3.0×10^{-9}

The defect density and diameter were found from the Eq.7.2a and b respectively. Since the defects were assumed to be point defect clusters (in the absence of information that, what fraction of the atoms and point defects were present in the cluster), the equivalent void diameters having the strength as determined from the dispersed barrier hardening (DBH) model, as shown

in Table 7.3, were calculated. In the DBH model it is assumed that the defect clusters are shearable and having a strength coefficient (α) of in between 0.4-0.5 as found in [61].

$$\rho = A\sqrt{dpa} \quad (m^{-3}) \qquad where\ A = 5.0 \times 10^{22}\ (m^{-3}.dpa^{-1/2}) \tag{7.2a}$$

$$d = B\sqrt{dpa} \quad (nm) \qquad where\ B = 3.7 \times 10^{-9}\ (nm.dpa^{-1/2}) \tag{7.2b}$$

$$CRSS = \alpha\mu b\sqrt{\rho d}\ (MPa) \quad where\ \alpha = 0.4\ , \mu = 82GPa, b = 0.248 \times 10^{-9}m \tag{7.2c}$$

Where ρ is defect density, D is defect cluster diameter. CRSS is critical resolved shear stress required for dislocation to overcome the obstacle of given diameter. μ is shear modulus and b is Burger's vector magnitude.

The equivalent void diameters with the defect density as obtained from equation 7.2a, the MD simulation domain was determined. Table 7.4 gives the simulated domain size as determined from the inverse of the cube root of defect density. The MD simulation was carried out using the three domain sizes with X, Y and Z dimensions as given in table 7.4. From the literature, it was found that the domain size along the burger vector direction and along the slip plane normal direction has little or no effect on the CRSS obtained, therefore, in all the simulations the X and Y direction of the simulation cell was kept at a length of 40.0 nm and 20.0 nm respectively. The defect density defined the Z-direction length. A strain rate of 1.0×10^9 s^{-1} was used in the present calculation.

Table 7.4: Domain size chosen for the MD simulations for different dose.

Dose (dpa)	X-direction	Y-direction	Z-direction
1	40.0×10^{-9}	20.0×10^{-9}	27.14×10^{-9}
5	40.0×10^{-9}	20.0×10^{-9}	20.76×10^{-9}
10	40.0×10^{-9}	20.0×10^{-9}	18.5×10^{-9}

Figure 7.8 shows the shear stress strain plot for different void diameters for the case of 1dpa. Figure 7.9 shows the variation of CRSS with respect to void diameter as obtained from

MD simulations for a dose 1dpa at 523 K. The variation of CRSS with respect to void diameters for 5 and 10 dpa along with 1 dpa is shown in Figure 7.10. The equivalent diameter was found by searching for the void diameter corresponding to CRSS of DBH model between the diameters for which the CRSS is obtained from MD simulation. The equivalent void diameter was always found to be less than the defect cluster diameter, since voids are stronger obstacles than the defect clusters. The square root dependence of defect diameter and equivalent void diameter is shown in Figure 7.11.

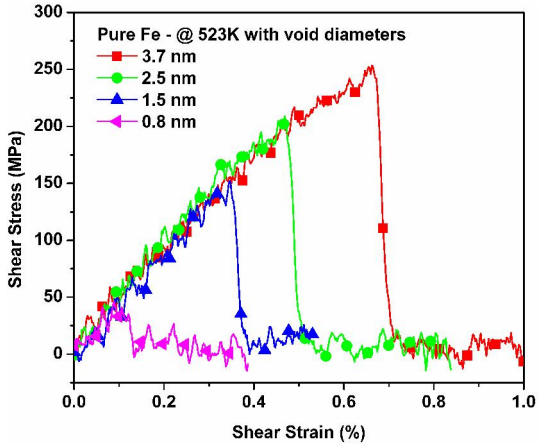

Figure 7.8: Shear stress strain curve for edge dislocation interacting with voids of different diameter in pure Fe at 523K (Molecular dynamics simulations).

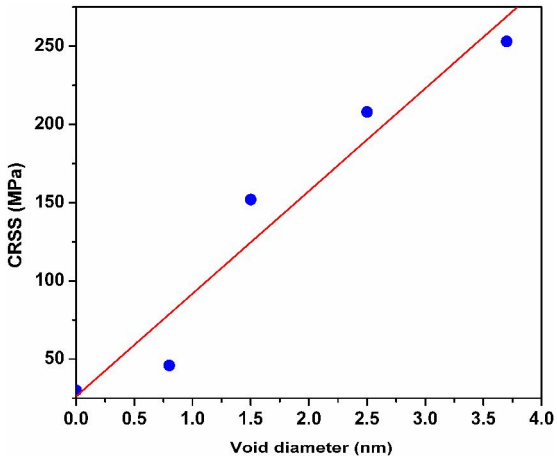

Figure 7.9: CRSS as a function of void diameter in pure Fe at 523K (Molecular dynamics simulations).

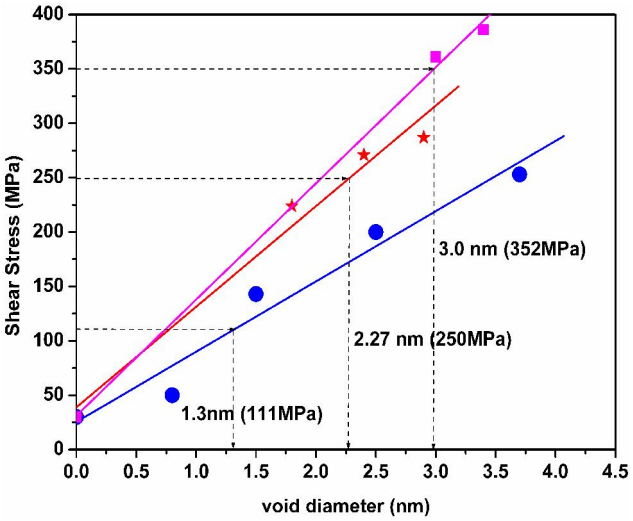

Figure 7.10: CRSS as a function of void diameter in pure Fe at 523K for different dose (Molecular dynamics simulations).

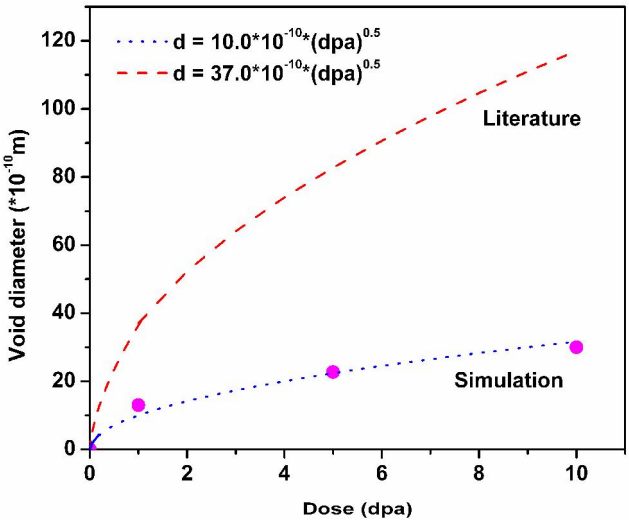

Figure 7.11: Comparison of void diameter dependence on dose between reported by Deo et al. [61] and as obtained from MD simulation in the present study.

The equivalent diameter, defect density and CRSS were used as input to DD simulations. The initial dislocation density considered was 2.2×10^{14} m^{-2}, which corresponds to nominal dislocation density observed in the ferritic/martensitic steels. A strain rate of 10^3 s^{-1} was used. In addition, the drag coefficient at 523 K was used which was obtained from the Queyreau et al. [259]. The drag coefficient for all the dislocation characters was approximated to be same as

$3.4*10^{-4}$ Pa-s. The approximation was made based on the assumption that the dislocations spend their most of the time by pinning at the obstacles and negligible time as freely gliding dislocations. The CRSS values obtained from DBH is converted into DD compatible stress values using the scale transition law as given in Eq. 7.1.

In DD simulation, the domain size was chosen as 1x1x1 μm^3, based on the assumption that, to represent the statistical distribution of obstacles the domain size must be equal to or greater than ten times the average distance ($\lambda \approx 3.0$ nm-100.0 nm) between the smallest features to capture i.e. dislocation bowing between the two obstacles. The discretization length of the segments was chosen to be $\lambda/5$. The domain size and discretization length were chosen to reduce the computational time without compromising the accuracy. The voids of equivalent size and density corresponding to 1 and 5 dpa were randomly distributed in the domain without overlapping of the defects. The flow stress curves obtained for the case of 1 and 5 dpa are as show in Figure 7.12. The simulations were stopped as the stress strain curves showed a tendency for saturation. The corresponding saturation stress is shown as a dotted line in Figure 7.12. The σ-ε curves show no appreciable difference between the unirradiated and sample corresponding to a dose of 1dpa. For the case of 5 dpa, it shows an increase of ~85MPa as opposed to ~270MPa obtained from experimental data. The DD simulations significantly underestimate the yield stress values in comparison to experimental results. The significant underestimation of flow stress from multi-scale approach was attributed to different strain rates used in MD and DD simulations as well as in the shearable obstacles treatment in DD simulations. The experiments were usually carried out in the quasi-static manner (i.e. low strain rate of the order of 10^{-4} s^{-1}) which is not possible in the current computational facility available. The lowest strain rate simulated to date

corresponds to 10^6-10^7 per second [249]. Due to such a large variation in the strain rates under experimental and simulated conditions, no direct quantitative comparison can be done. However, the nature of the flow stress curve as a function of irradiation dose can be qualitatively predicted. A suitable material model has to be developed at micro scale such that, the macro scale real experiments and micro scale virtual experiments can be compared. A more detailed study need to be carried out to understand the effect of different parameters on the stress strain curves obtained from the DD simulations. The main parameters that may affect the simulation results are drag coefficient of different dislocation characters, strain rate, domain size, discretization length, Initial dislocation density/distribution and obstacle density/distribution/strength. The study of effect of strain rate, domain size, discretization length, initial dislocation density/distribution and obstacle density/distribution/strength are inherent length scale limitation and computational facility available.

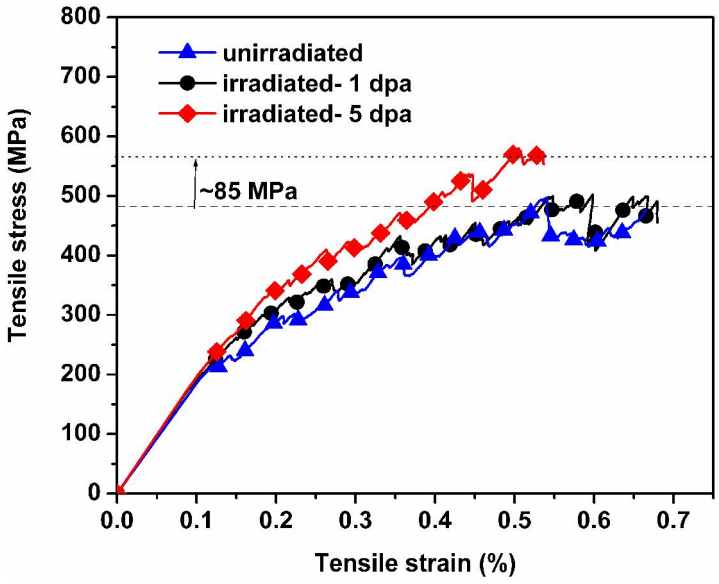

Figure 7.12: Simulated tensile stress strain curve for un-irradiated and irradiated (1dpa and 5 dpa) T91 samples.

7.4 Closure

The DDD simulations are carried out using the MD results matrix friction stress and CRSS required for the dislocation to overcome the obstacles and the drag coefficient of the dislocation as obtained from the literature. From the simulations it was found that, with increase in obstacle diameter keeping density constant, flow stress of the material increases. Also, in case of distributed He bubbles it was shown that the flow stress of the material increases with dose, where the He bubble fraction was correlated with the dose using the estimated He production rate of 10-15 He appm/dpa in fusion reactors. An attempt has been made to estimate the flow stress of T91 material irradiated to 1 and 5 dpa using the experimental microstructure details as obtained from literature in MD to find the equivalent void diameters and CRSS. These parameters are used in DDD simulations by adjusting the matrix friction stress to unirradiated materials flow stress to determine the flow stress of the irradiated material. Other microstructural features such as solute hardening, GBs and precipitates are considered by a single term matrix friction stress. The flow stress values of the T91 material for a dose of 1 and 5 dpa at 523 K was underestimated by the MMM methodology comprising MD and DD techniques. This is attributed to the strain rate used in simulations, absence of grain boundaries, other precipitate structures present in the material and scale difference between experiments and simulations.

CHAPTER 8: CONCLUSIONS AND FUTURE PERSPECTIVE

In the present work, changes in the microstructure and mechanical properties of the T91 steel due to irradiation had been investigated by imparting radiation defects using 315KeV Ar^{+9} ions. These radiation defects were characterized by using complementary characterization techniques, like GIXRD-LPA and TEM. Change in the mechanical property due to irradiation defects have been determined using nanoindentation technique. In addition, multiscale material modeling technique comprising molecular dynamics and dislocation dynamic simulations were used to study the dislocation-defect interaction and its effect on the macroscopic property of the pure Fe and the Fe-10%Cr alloy systems. The effect of interaction of dislocations with solute (Cr) atoms, impurity (He) atoms and irradiation-induced defects (voids/bubbles) were also studied using MD simulations. The output of TEM in terms of the size and density of dislocation loops and voids were used in the MD and DD simulations. The results of MD simulations in terms of strength of defects and friction stresses were used as input to DD simulations. In addition, MD simulations on GB sliding and nanoindentation were carried out at atomistic scale to study the effect of irradiation induced defects on the shear deformation resistance and load versus depth of indentation curves respectively.

The main conclusions from the present study could be summarized as follows,

- Microstructural characterization of irradiated samples showed the presence of dislocation loops and voids/Ar bubbles along with pre-existing secondary carbides particles. The T91 samples irradiated to 10 and 20 dpa at temperature < 60^0C resulted in an Ar ion concentration of 1000 and 3000 appm. This high concentration of Ar and high irradiation dose was responsible for the formation of Ar bubbles. Sizes of the cavities/bubbles were found to be less than 2.0 nm.

Microstructural characterization using grazing incidence X-ray diffraction showed decrease in the coherent domain size due to the alignment of dislocations. This investigation provided qualitative information about the increase in the density of defects produced during irradiation.

- The nanoindentation testing of irradiated T91 material samples at low temperature (< 60^0C) showed an initial sharp increase in the hardness up to 10 dpa and also the saturation behavior. This saturation behavior is in agreement with the saturation behavior of YS observed in FM steels upon irradiation at low temperatures to a dose level above 10 dpa. The increase in the hardness of the considered T91 steel was due to the microstructural features such as preexisting dislocation network and precipitates, loops, cavities or bubbles as observed in TEM and their interaction during deformation.

- Changes in the hardness of the T91 material determined from nanoindentation have been correlated to the change in YS of the material upon irradiation using linear correlation of the form $\Delta H_{NANO}=K\Delta\sigma_{YS}$, where K represents the proportionality constant to be determined by conducting systematic nanoindentation and tensile test experiments. The K value determined in the present study (i.e. ~$324x10^{-3}$) and the one reported by Rice and Stoller [93] (~$274x10^{-3}$) are found to be in agreement with each other. This shows the applicability of such correlations in estimating the YS of the materials under irradiation conditions.

- MD simulations of dislocation motion in pure Fe and Fe-10%Cr revealed that pure Fe offers less resistance to the plastic deformation which increases significantly by chromium addition. In the presence of He, flow stress for dislocation motion in Fe-10%Cr increased further. The increase in friction stress is higher in case of interstitial He than in the case of substitutional He. MD simulations on dislocation motions in the present study also showed that interstitial He

atoms were attracted towards the slip plane as the dislocations glided and thereby He content increased on the slip plane.

- Interaction of dislocations with irradiation induced defects (voids/bubbles) in pure Fe and Fe-10%Cr increased the required stress for dislocation motion. It was found that voids were stronger obstacles than the bubbles of type 1Va-1He. In the alloy (Fe-10% Cr) system, it was found that smaller (< ~0.8 nm) voids offered lesser resistance in comparison to the pure system. The reason for this behavior was the complex interaction between the stress fields of solutes and dislocations around voids. The maximum stress required by a dislocation to overcome a periodic array of defects increased significantly for the case of substitutional He in Fe-10% Cr system in comparison to Fe-10% Cr system. The investigated range of the diameter of obstacles showed a linear increase in the critical resolved shear stress as a function of defect diameter.

- MD simulations of low angle twist GBs showed that in the presence of transmutation induced helium, the strength of twist GBs enhanced due to the formation of He bubbles. The variation of GB sliding resistance as a function of bubbles diameter can be used as a phenomenological local rule for higher length scale simulations such as dislocation dynamics or crystal plasticity models.

- MD simulation of nanoindentation at 1K and 300 K showed the existence of dislocation activities on the {110}, {112} and {123} families of slip planes. MD simulations of nanoindentation by systematic introduction of irradiation-induced defects (loops and vacancies) had shown that the presence of defects in a perfect crystal reduces the critical load for dislocation nucleation. In the case of nanoindentation in the presence of dislocation loops, it was found that the loops with Burger's vector of ½<111> and ½<1-1-1> interacted to form sessile <100> dislocation segments. In addition, the growing dislocation segments below the indenter

interacted to form different dislocation junction segments, which play an important role in the strain hardening of the materials. Similar to GB sliding behavior the number of active slip plane families, as found from the MD simulations, can be used in the higher length scale models.

- Discrete dislocation dynamics simulations were carried out by using the results of MD simulations. These DD simulations showed that the collective behavior of dislocations and defects are in qualitative agreement with the experimental results as reported in literature. The values of the flow stress of irradiated T91 steel obtained using multiscale approach were smaller than the values obtained experimentally. This underestimation of flow stress is due to treating polycrystallinity, solute hardening and other irradiation-induced defects as a single friction stress factor.

- From the present investigation of the mechanical properties of the irradiated T91 material, it can be concluded that the complementary approaches (experiments and MMM simulation) provide an indispensible tool to understand and to estimate the mechanical property variation from the information obtained from different length and time scales.

Finally the coordinated experimental and simulation studies carried out are found to help in understanding the mechanical properties of unirradiated/irradiated materials and different phenomena occurring at different length scales. There is a lot of scope to improvise the current simulation methodologies by considering different microstructural features in dislocation dynamics simulations and in higher length scales, physics based material models of crystal plasticity. The present study suggests that the dislocation behavior on the slip plane {123} has to be investigated along with {110} and {112} slip planes. Due to computational difficulty, screw dislocations are lesser studied defects as compared to edge dislocations, therefore, extra attention

is needed in understanding the behavior of screw dislocations in all the slip systems activities, at least, in the α iron, which is the base material for the ferittic-martensitic steels. In order to predict the flow strength of the material by dislocation dynamics simulations, it is necessary to incorporate grain boundaries, other active slip planes observed in alpha Fe, along with other phenomenological rules (e.g;. dislocation nucleation, GB shear resistance, strength of the secondary particles, etc.,) and computational ability to handle the simulation domains of the order of millimeters. Also, the interaction of dislocations with different defects needs to be studied by molecular dynamics simulations to formulate physics based or phenomenological rules which can be used in the higher length scale simulations.

There is a need to identify/categorize the different atomistic/mesoscale phenomena based on their participation/importance in the deformation process using experimental and simulation techniques. These atomistic/mesoscale processes or phenomena have to be included directly or as phenomenological local rules in the higher length and time scale models to predict the realistic deformation behavior of the unirradiated/irradiated materials.

REFERENCES

[1] V. Bhatnagar, M. Deffrennes, M. Hugon, P. Manolatos, K. Ptackova, G. Van Goethem, S. Webster, Nuclear Engineering and Design 241 (2011) 3376.

[2] E.E. Bloom, S.J. Zinkle, F.W. Wiffen, Journal of Nuclear Materials 329–333, P (2004) 12.

[3] C. Fazio, A. Alamo, A. Almazouzi, S. De Grandis, D. Gomez-Briceno, J. Henry, L. Malerba, M. Rieth, Journal of Nuclear Materials 392 (2009) 316.

[4] C. Fazio, D.G. Briceno, M. Rieth, A. Gessi, J. Henry, L. Malerba, Nuclear Engineering and Design 241 (2011) 3514.

[5] K.L. Murty, I. Charit, Journal of Nuclear Materials 383 (2008) 189.

[6] P. Yvon, F. Carré, Journal of Nuclear Materials 385 (2009) 217.

[7] S.J. Zinkle, J.T. Busby, Materials Today 12 (2009) 12.

[8] P. Jung, Journal of Nuclear Materials 301 (2002) 15.

[9] R.L. Klueh, K. Ehrlich, F. Abe, Journal of Nuclear Materials 191–194, P (1992) 116.

[10] R.J. Kurtz, A. Alamo, E. Lucon, Q. Huang, S. Jitsukawa, A. Kimura, R.L. Klueh, G.R. Odette, C. Petersen, M.A. Sokolov, P. Spätig, J.W. Rensman, Journal of Nuclear Materials 386–388 (2009) 411.

[11] R. Schäublin, J. Henry, Y. Dai, Comptes Rendus Physique 9 (2008) 389.

[12] G.E. Lucas, Journal of Nuclear Materials 117 (1983) 327.

[13] G.E. Lucas, G.R. Odette, M. Sokolov, P. Spätig, T. Yamamoto, P. Jung, Journal of Nuclear Materials 307–311, P (2002) 1600.

[14] G.E. Lucas, G.R. Odette, H. Matsui, A. Möslang, P. Spätig, J. Rensman, T. Yamamoto, Journal of Nuclear Materials (2007) 1549.

[15] E. Wakai, H. Ohtsuka, S. Matsukawa, K. Furuya, H. Tanigawa, K. Oka, S. Ohnuki, T. Yamamoto, F. Takada, S. Jitsukawa, Fusion Engineering and Design 81 (2006) 1077.

[16] G.R. Odette, M. He, D. Gragg, D. Klingensmith, G.E. Lucas, Journal of Nuclear Materials 307–311, P (2002) 1643.

[17] B.D. Wirth, M.J. Caturla, T. Diaz de la Rubia, T. Khraishi, H. Zbib, Nuclear Instruments and Methods in Physics Research Section B: Beam Interactions with Materials and Atoms 180 (2001) 23.

[18] D.J. Bacon, Y.N. Osetsky, Materials Science and Engineering: A 365 (2004) 46.

[19] M. Samaras, M. Victoria, W. Hoffelner, Journal of Nuclear Materials 392 (2009) 286.

[20] Z. Tong, Y. Dai, Journal of Nuclear Materials 398 (2010) 43.

[21] L. Peng, Y. Dai, Journal of Nuclear Materials 417 (2011) 996.

[22] Klueh, Elevated Temperature-ferritic/martensitic Steels and Their Application to Future Nuclear Reactors, ORNL, 2004.

[23] E.E. Bloom, Journal of Nuclear Materials 258–263, P (1998) 7.

[24] T. Muroga, M. Gasparotto, S.J. Zinkle, Fusion Engineering and Design 61–62 (2002) 13.

[25] T. Yamamoto, G.R. Odette, H. Kishimoto, J.-W. Rensman, P. Miao, Journal of Nuclear Materials 356 (2006) 27.

[26] R. Tewari, G. Sanyal, B. Viswanath, P. Mukharjee, P. Barat, A.P. Srivastava, S. Saha, K. Muraleedharan, G.K. Dey, Radiation Effects and Defects in Solids 168 (2013) 29.

[27] Raghvendra Tewari, Zr-Al Based Intermetallics: Processing, Microstructure Evolution and Indentation Creep, PhD thesis, IIT-B, Mumbai, 2000.

[28] G.S. Was, Fundamentals of Radiation Materials science-Metals and Alloys, Springer, 2007.

[29] P.D.G. Gilbert M. R. Derlet P. M. Dudarev S L, Journal of Physics: Condensed Matter 20 (2008).

[30] C. Domain, C.S. Becquart, L. Malerba, Journal of Nuclear Materials 335 (2004) 121.

[31] Y. Dai, W. Wagner, Journal of Nuclear Materials 389 (2009) 288.

[32] Y. Dai, S.A. Maloy, G.S. Bauer, W.F. Sommer, Journal of Nuclear Materials 283–287, P (2000) 513.

[33] H. Ogiwara, A. Kohyama, H. Tanigawa, H. Sakasegawa, Fusion Engineering and Design 81 (2006) 1091.

[34] http://www.fusion.ucla.edu/FNST/Renew_Presentations/Tuesday/5.4-Stoller.pdf.

[35] F.A. Garner, M.B. Toloczko, B.H. Sencer, Journal of Nuclear Materials 276 (2000) 123.

[36] A. Hasegawa, M. Ejiri, S. Nogami, M. Ishiga, R. Kasada, A. Kimura, K. Abe, S. Jitsukawa, Journal of Nuclear Materials 386-388 (2009) 241.

[37] E. Wakai, M. Ando, T. Sawai, K. Kikuchi, K. Furuya, M. Sato, K. Oka, S. Ohnuki, H. Tomita, T. Tomita, Y. Kato, F. Takada, Journal of Nuclear Materials 356 (2006) 95.

[38] Greenwood A.J.E. Foreman G W, D.E. Rimmer, Journal of Nuclear Materials 1 (1959).

[39] J.H. Evans, A. van Veen, L.M. Caspers, Scripta Metallurgica 15 (1981) 323.

[40] H. Trinkaus, W.G. Wolfer, Journal of Nuclear Materials 122 (1984).

[41] S.M. Hafez Haghighat, R. Schäublin, Philosophical Magazine 90 (2010) 1075.

[42] D.N. Braski, H. Schroeder, H. Ullmaier, Journal of Nuclear Materials 83 (1979) 265.

[43] Z. Jiao, V. Shankar, G.S. Was, Journal of Nuclear Materials 419 (2011) 52.

[44] H. Tanigawa, R.L. Klueh, N. Hashimoto, M.A. Sokolov, Journal of Nuclear Materials 386–388 (2009) 231.

[45] H. Ogiwara, A. Kohyama, H. Tanigawa, H. Sakasegawa, Journal of Nuclear Materials 367–370, P (2007) 428.

[46] R. Schaeublin, D. Gelles, M. Victoria, Journal of Nuclear Materials 307–311, P (2002) 197.

[47] V.K. Shamardin, V.N. Golovanov, T.M. Bulanova, A. V Povstianko, A.E. Fedoseev, Y.D. Goncharenko, Z.E. Ostrovsky, Journal of Nuclear Materials 271–272 (1999) 155.

[48] M. Victoria, N. Baluc, C. Bailat, Y. Dai, M.I. Luppo, R. Scha□ublin, B.N. Singh, Journal of Nuclear Materials 276 (2000) 114.

[49] Y. Dai, X. Jia, S.A. Maloy, Journal of Nuclear Materials 343 (2005) 241.

[50] J. Marian, B. Wirth, J. Perlado, Physical Review Letters 88 (2002) 255507.

[51] S.A. Maloy, M.R. James, G. Willcutt, W.F. Sommer, M. Sokolov, L.L. Snead, M.L. Hamilton, F. Garner, Journal of Nuclear Materials 296 (2001) 119.

[52] K. Farrell, T.S. Byun, N. Hashimoto, Journal of Nuclear Materials 335 (2004) 471.

[53] B. van der Schaaf, C. Petersen, Y. De Carlan, J.W. Rensman, E. Gaganidze, X. Averty, Journal of Nuclear Materials 386–388 (2009) 236.

[54] P. Spätig, R. Schäublin, S. Gyger, M. Victoria, Journal of Nuclear Materials 258–263, P (1998) 1345.

[55] R. Chaouadi, T. Hirai, J. Linke, G. Pintsuk, Journal of Nuclear Materials 386–388 (2009) 544.

[56] R.J. Kurtz, G.R. Odette, T. Yamamoto, D.S. Gelles, P. Miao, B.M. Oliver, Journal of Nuclear Materials 367–370, P (2007) 417.

[57] A. Seeger, S. Mader, J. Diehl, H. Rebstock, Philosophical Magazine 2 (1957).

[58] F. Kroupa, P.B. Hirsch, Discuss. Faraday Soc. 38 (1964) 49.

[59] S.J. Zinkle, Y. Matsukawa, Journal of Nuclear Materials 329–333 (2004).

[60] S.J. Zinkle, Radiation Effects and Defects in Solids 148 (1999) 447.

[61] C. Deo, C. Tomé, R. Lebensohn, S. Maloy, Journal of Nuclear Materials 377 (2008) 136.

[62] J. Henry, M.H. Mathon, P. Jung, Journal of Nuclear Materials 318 (2003) 249.

[63] F.A. Garner, M.L. Hamilton, N.F. Panayotou, G.D. Johnson, Journal of Nuclear Materials 104 (1981) 803.

[64] A. Kohyama, A. Hishinuma, D.S. Gelles, R.L. Klueh, W. Dietz, K. Ehrlich, Journal of Nuclear Materials 233–237, P (1996) 138.

[65] R.L. Klueh, J.-J. Kai, D.J. Alexander, Journal of Nuclear Materials 225 (1995) 175.

[66] M.A. Sokolov, H. Tanigawa, G.R. Odette, K. Shiba, R.L. Klueh, Journal of Nuclear Materials 367–370, P (2007) 68.

[67] E. Gaganidze, H.C. Schneider, B. Dafferner, J. Aktaa, Journal of Nuclear Materials 367–370, P (2007) 81.

[68] R.L. Klueh, D.J. Alexander, Journal of Nuclear Materials 187 (1992) 60.

[69] T. Yamamoto, G.R. Odette, P. Miao, D.J. Edwards, R.J. Kurtz, Journal of Nuclear Materials 386–388 (2009) 338.

[70] R.S. Nelson, D.J. Mazey, J.A. Hudson, Journal of Nuclear Materials 37 (1970) 1.

[71] W.C. Oliver, G.M. Pharr, Journal of Materials Research 7 (1992) 1564.

[72] I.N. Sneddon, International Journal of Engineering Science 3 (1965).

[73] K.L. Johnson, Contact Mechanics, Cambridge University Press, Cambridge, 1985.

[74] M.F. Doerner, W.D. Nix, Journal of Materials Research 1 (1986) 9.

[75] T.Y. Tsui, G.M. Pharr, W.C. Oliver, Journal of Materials Research 11 (1996).

[76] A. Bolshakov, G.M. Pharr, Journal of Materials Research 13.

[77] A.K. Bhattacharya, W.D. Nix, International Journal of Solids and Structures 24 (1988) 881.

[78] M. Dao, N. Chollacoop, K.J. Van Vliet, T.A. Venkatesh, S. Suresh, Acta Materialia 49 (2001) 3899.

[79] J.L. Bucaille, S. Stauss, E. Felder, J. Michler, Acta Materialia 51 (2003) 1663.

[80] N. Chollacoop, M. Dao, S. Suresh, Acta Materialia 51 (2003) 3713.

[81] M. Zhao, X. Chen, J. Yan, A.M. Karlsson, Acta Materialia 54 (2006) 2823.

[82] J.M. Antunes, J. V Fernandes, L.F. Menezes, B.M. Chaparro, Acta Materialia 55 (2007) 69.

[83] J. Yan, A.M. Karlsson, X. Chen, International Journal of Solids and Structures 44 (2007) 3720.

[84] X. Chen, J. Yan, A.M. Karlsson, Materials Science and Engineering: A 416 (2006) 139.

[85] C. Heinrich, A.M. Waas, A.S. Wineman, International Journal of Solids and Structures 46 (2009) 364.

[86] P. Hosemann, C. Vieh, R.R. Greco, S. Kabra, J.A. Valdez, M.J. Cappiello, S.A. Maloy, Journal of Nuclear Materials 389 (2009) 239.

[87] R. Kasada, Y. Takayama, K. Yabuuchi, A. Kimura, Fusion Engineering and Design 86 (2011) 2658.

[88] C. Heintze, C. Recknagel, F. Bergner, M. Hernández-Mayoral, A. Kolitsch, Nuclear Instruments and Methods in Physics Research Section B: Beam Interactions with Materials and Atoms 267 (2009) 1505.

[89] K. Yabuuchi, H. Yano, R. Kasada, H. Kishimoto, A. Kimura, Journal of Nuclear Materials 417 (2011) 988.

[90] A.K. Yoshiyuki Takayama Kiyohiro Yabuuchi Dai Hamaguchi, Masami Ando, Hiroyasu Tanigawa, Ryuta Kasada, Materials Science Forum 654-656 (2010).

[91] Y. Xin, X. Ju, J. Qiu, L. Guo, J. Chen, Z. Yang, P. Zhang, X. Cao, B. Wang, Fusion Engineering and Design 87 (2012) 432.

[92] C. Shin, H. Jin, M.-W. Kim, Journal of Nuclear Materials 392 (2009) 476.

[93] P.M. Rice, R.E. Stoller, in:, Mat. Res. Soc. Symp. Proc, 2000.

[94] H.-H. Jin, C. Shin, D.H. Kim, K.H. Oh, J.H. Kwon, Nuclear Instruments and Methods in Physics Research Section B: Beam Interactions with Materials and Atoms 266 (2008) 4845.

[95] R. Schäublin, M. Victoria, Journal of Nuclear Materials 283–287, P (2000) 339.

[96] X. Jia, Y. Dai, Journal of Nuclear Materials 318 (2003) 207.

[97] G. Yu, X. Li, J. Yu, Y. Wu, H. Kinoshita, H. Takahashi, M. Victoria, Journal of Nuclear Materials 329–333, P (2004) 1003.

[98] G. Gupta, Z. Jiao, A.N. Ham, J.T. Busby, G.S. Was, Journal of Nuclear Materials 351 (2006) 162.

[99] Z. Jiao, N. Ham, G.S. Was, Journal of Nuclear Materials 367–370, P (2007) 440.

[100] B.H. Sencer, F.A. Garner, D.S. Gelles, G.M. Bond, S.A. Maloy, Journal of Nuclear Materials 307–311, P (2002) 266.

[101] E. Wakai, N. Hashimoto, Y. Miwa, J.P. Robertson, R.L. Klueh, K. Shiba, S. Jistukawa, Journal of Nuclear Materials 283–287, P (2000) 799.

[102] Th H de Keijser, E.J. Mittemeijer, J.I. Langford, A.B.P. Vogels, J. Appl. Cryst. 15 (1982).

[103] H.C. Van de hulst, J.J.M. Reesinck, Journal of Astrophysics 106 (1947).

[104] Langford J. I., Journal of Applied Crystallography (1978).

[105] S.P. Lutterotti L., J. Appl. Crystallogr. 23 (1990).

[106] A. Sarkar, P. Mukherjee, P. Barat, Materials Science and Engineering A 485 (2008).

[107] P. Mukherjee, M. Bhattacharya, P. Barat, A. Sarkar, N. Gayathri, Journal of Nuclear Materials 395 (2009).

[108] P. Mukherjee, A. Sarkar, P. Barat, S.K. Bandyopadhyay, P. Sen, S.K. Chattopadhyay, P. Chatterjee, S.K. Chatterjee, M.K. Mitra, Acta Materialia 52 (2004) 5687.

[109] P.S. Chowdhury, N. Gayathri, P. Mukherjee, M. Bhattacharya, A. Chatterjee, A. Dutta, P. Barat, Materials Science and Engineering A 528 (2011) 967.

[110] A. Sarkar, P. Mukherjee, P. Barat, Journal of Nuclear Materials 372 (2008).

[111] P. Mukherjee, A. Sarkar, P. Barat, Materials Characterization 55 (2005).

[112] B.M. Mukherjee P. Sarkar A. Gayathri N.,, Barat P, Nuclear Materials (2011).

[113] M.S. Daw, M.I. Baskes, Physical Review B 29 (1984) 6443.

[114] E.B. Tadmor, R.E. Miller, Modeling Materials: Continuum, Atomistic and Multiscale Techniques, Cambridge University Press, 2012.

[115] M.W. Finnis, J.E. Sinclair, Philosophical Magazine A 50 (1984) 45.

[116] B.S. Daan Frenkel, Understanding Molecular Simulation, Second, Academic press, 2002.

[117] A. Caro, D.A. Crowson, M. Caro, Physical Review Letters 95 (2005) 75702.

[118] A. Stukowski, B. Sadigh, P. Erhart, A. Caro, Modelling and Simulation in Materials Science and Engineering 17 (2009) 075005.

[119] D.J. Bacon, A.F. Calder, F. Gao, Journal of Nuclear Materials 251 (1997) 1.

[120] D.J. Bacon, A.F. Calder, J.M. Harder, S.J. Wooding, Journal of Nuclear Materials 205 (1993) 52.

[121] D.J. Bacon, H.F. Deng, F. Gao, Journal of Nuclear Materials 205 (1993) 84.

[122] D.J. Bacon, T. Diaz de la Rubia, Journal of Nuclear Materials 216 (1994) 275.

[123] D.J. Bacon, F. Gao, Y.N. Osetsky, Nuclear Instruments and Methods in Physics Research Section B: Beam Interactions with Materials and Atoms 153 (1999) 87.

[124] D.J. Bacon, F. Gao, Y.N. Osetsky, Journal of Nuclear Materials 276 (2000) 1.

[125] D.J. Bacon, Y.N. Osetsky, R. Stoller, R.E. Voskoboinikov, Journal of Nuclear Materials 323 (2003) 152.

[126] R.E. Stoller, L.R. Greenwood, Journal of Nuclear Materials 271-272 (1999) 57.

[127] J. Pu, L. Yang, F. Gao, H.L. Heinisch, R.J. Kurtz, X.T. Zu, Nuclear Instruments and Methods in Physics Research Section B: Beam Interactions with Materials and Atoms 266 (2008) 3993.

[128] L. Yang, X.T. Zu, H.Y. Xiao, F. Gao, K.Z. Liu, H.L. Heinisch, R.J. Kurtz, S.Z. Yang, Materials Science and Engineering: A 427 (2006) 343.

[129] L. Yang, X.T. Zu, H.Y. Xiao, F. Gao, H.L. Heinisch, R.J. Kurtz, Z.G. Wang, K.Z. Liu, Nuclear Instruments and Methods in Physics Research Section B: Beam Interactions with Materials and Atoms 255 (2007) 63.

[130] N. Juslin, K. Nordlund, Nuclear Instruments and Methods in Physics Research Section B: Beam Interactions with Materials and Atoms 267 (2009) 3420.

[131] J.-H. Kwon, G.-G. Lee, C.-S. Shin, Nuclear Engineering and Technology 41 (2009) 11.

[132] T. Yoshiie, T. Ito, H. Iwase, Y. Kaneko, M. Kawai, I. Kishida, S. Kunieda, K. Sato, S. Shimakawa, F. Shimizu, S. Hashimoto, N. Hashimoto, T. Fukahori, Y. Watanabe, Q. Xu, S. Ishino, Nuclear Instruments and Methods in Physics Research Section B: Beam Interactions with Materials and Atoms 269 (2011) 1740.

[133] Y.N. Osetsky, D.J. Bacon, Journal of Nuclear Materials 323 (2003) 268.

[134] Y.N. Osetsky, D.J. Bacon, V. Mohles, Philosophical Magazine 83 (2003) 3623.

[135] S.M. Hafez Haghighat, M.C. Fivel, J. Fikar, R. Schaeublin, Journal of Nuclear Materials 386–388 (2009) 102.

[136] H.-J. Lee, B.D. Wirth, Journal of Nuclear Materials 386–388 (2009) 115.

[137] D. Terentyev, D.J. Bacon, N.O. Yu, Journal of Physics: Condensed Matter 20 (2008) 445007.

[138] D. Terentyev, G. Bonny, L. Malerba, Journal of Nuclear Materials 386–388 (2009) 257.

[139] D.J. Bacon, Y.N. Osetsky, Z. Rong, Philosophical Magazine 86 (2006) 3921.

[140] Y.N. Osetsky, D.J. Bacon, F. Gao, A. Serra, B.N. Singh, Journal of Nuclear Materials 283–287, P (2000) 784.

[141] S. Patinet, L. Proville, Philosophical Magazine 91 (2011) 1581.

[142] Z. Rong, V. Mohles, D.J. Bacon *, Y.N. Osetsky, Philosophical Magazine 85 (2005) 171.

[143] Y.N. Osetsky, D.J. Bacon, Philosophical Magazine 90 (2010) 945.

[144] D.J. Bacon, Y.N. Osetsky, Materials Science and Engineering: A 400–401 (2005) 353.

[145] S.M. Hafez Haghighat, J. Fikar, R. Schäublin, Journal of Nuclear Materials 382 (2008) 147.

[146] Y.N. Osetsky, D.J. Bacon, Materials Science and Engineering: A 400–401 (2005) 374.

[147] G.J. Ackland, D.J. Bacon, a. F. Calder, T. Harry, Philosophical Magazine A 75 (1997) 713.

[148] M.I. Mendelev, S. Han, D.J. Srolovitz, G.J. Ackland, D.Y. Sun, M. Asta, Philosophical Magazine 83 (2003) 3977.

[149] G.C. Das A. Dutta N. Gayathri P. Barat, M Bhattacharya, Acta Materialia 60 (2012).

[150] K. Christopher, K. Peter, S. Siegfried, Modelling and Simulation in Materials Science and Engineering 13 (2005) 35.

[151] D. Terentyev, P. Olsson, L. Malerba, a. V. Barashev, Journal of Nuclear Materials 362 (2007) 167.

[152] S.M. Hafez Haghighat, D. Terentyev, R. Schäublin, Journal of Nuclear Materials 417 (2011) 1094.

[153] R. Schäublin, Y.L. Chiu, Journal of Nuclear Materials 362 (2007) 152.

[154] S.M.H. Haghighat, G. Lucas, R. Schäublin, IOP Conference Series: Materials Science and Engineering 3 (2009) 12013.

[155] H.L. Heinisch, F. Gao, R.J. Kurtz, E.A. Le, Journal of Nuclear Materials 351 (2006) 141.

[156] L. Yang, X.T. Zu, Z.G. Wang, F. Gao, X.Y. Wang, H.L. Heinisch, R.J. Kurtz, Nuclear Instruments and Methods in Physics Research Section B: Beam Interactions with Materials and Atoms 265 (2007) 541.

[157] Y.X. Wang, Q. Xu, T. Yoshiie, Z.Y. Pan, Journal of Nuclear Materials 376 (2008) 133.

[158] D. Rodney, G. Martin, Physical Review Letters 82 (1999) 3272.

[159] Y.N. Osetsky, A. Serra, V. Priego, Journal of Nuclear Materials 276 (2000) 202.

[160] T. Nogaret, C. Robertson, D. Rodney, Philosophical Magazine 87 (2007) 945.

[161] D. Terentyev, L. Malerba, Journal of Nuclear Materials 377 (2008) 141.

[162] Y.N. Osetsky, D. Rodney, D.J. Bacon, Philosophical Magazine 86 (2006) 2295.

[163] Y.N. Osetsky, A. Serra, M. Victoria, S.I. Golubov, V. Priego, Philosophical Magazine A 79 (1999) 2259.

[164] H.J. Lee, B.D. Wirth, Philosophical Magazine 89 (2009) 821.

[165] S. Patinet, L. Proville, Physical Review B 78 (2008) 104109.

[166] D.L. Olmsted, L.G. Hector Jr, W.A. Curtin, Journal of the Mechanics and Physics of Solids 54 (2006) 1763.

[167] K. Tapasa, D.J. Bacon, Y.N. Osetsky, Materials Science and Engineering: A 400–401 (2005) 109.

[168] K. Tapasa, D.J. Bacon, N.O. Yu, Modelling and Simulation in Materials Science and Engineering 14 (2006) 1153.

[169] S. Schmauder, C. Kohler, Computational Materials Science 50 (2011) 1238.

[170] M. Winning, A.D. Rollett, Acta Materialia 53 (2005) 2901.

[171] Y. Mishin, M. Asta, J. Li, Acta Materialia 58 (2010) 1117.

[172] J.B. Yang, Y. Nagai, M. Hasegawa, Y.N. Osetsky, Philosophical Magazine 90 (2010) 991.

[173] M.J.F. Sansoz F., Acta Materialia 53 (2005).

[174] V. V Bulatov, W. Cai, Physical Review Letters 89 (2002) 115501.

[175] X.M. Liu, X.C. You, Z.L. Liu, J.F. Nie, Z. Zhuang, Journal of Physics D: Applied Physics 42 (2009) 35404.

[176] D. Terentyev, X. He, Computational Materials Science 50 (2011) 925.

[177] J. Hetherly, E. Martinez, M. Nastasi, A. Caro, Journal of Nuclear Materials 419 (2011) 201.

[178] M.J. Demkowicz, A. Misra, A. Caro, Current Opinion in Solid State and Materials Science 16 (2012) 101.

[179] Z. Di, X.-M. Bai, Q. Wei, J. Won, R.G. Hoagland, Y. Wang, A. Misra, B.P. Uberuaga, M. Nastasi, Physical Review B 84 (2011) 52101.

[180] B.N. Singh, T. Leffers, W. V Green, M. Victoria, Journal of Nuclear Materials 125 (1984) 287.

[181] J. Hetherly, E. Martinez, Z.F. Di, M. Nastasi, A. Caro, Scripta Materialia 66 (2012) 17.

[182] A. Hasnaoui, P.M. Derlet, H. Van Swygenhoven, Acta Materialia 52 (2004) 2251.

[183] L.S.K. Salehinia I. Bahr D. F., Acta Materialia 61 (2013).

[184] P.S.J. Cynthia L. Kelchner Hamilton J. C., Physical Review B 58 (1998).

[185] D.F. Arun K. Nair peter Gaudreau Ronald D. Kriz, Edward Parker, International Journal of Plasticity 24 (2008).

[186] B.G. Lin Yuan Debin Shan Zhenhai Xu, Applied Surface Science (2012).

[187] H.J.C. Zimmerman J. A. Klein P. A. Foiles S. M., Kelchner C L, Physical Review Letters 87 (2001).

[188] R.A.I.E.P.M. Leiva, Acta Materialia 54 (2006).

[189] R.P. Vivek B. Shenoy Ellad B. Tadmor, Journal of the Mechanics and Physics of Solids 48 (2000).

[190] S.S. Wenshan Yu, Computational Materials Science 46 (2009).

[191] H.J. Begaua C. Hartmaiera A., Journal of the Mechanics and Physics of Solids 60 (2012).

[192] Y.-S.L. Chung-Ting Wang Jason Shian-Ching Jang Ping-Feng Yang, Sheng-Rui Jian, Applied Surface Science 255 (2008).

[193] R.S. David Christopher Asta Richter, Nanotechnology 12 (2001).

[194] C.-L. Liu, T.-H. Fang, J.-F. Lin, Materials Science and Engineering: A 452-453 (2007) 135.

[195] E. Martínez, J. Marian, A. Arsenlis, M. Victoria, J.M. Perlado, Journal of the Mechanics and Physics of Solids 56 (2008) 869.

[196] M.V. Hyung-Jun Chang David Rodney Marc Fivel, Comptes Rendus Physique 11 (2010).

[197] http://zig.onera.fr/mm_home_page/

[198] http://www.numodis.fr/tridis/

[199] http://paradis.stanford.edu/

[200] http://www.cmms.wsu.edu/Research/Research.html

[201] B. Devincre, Solid State Communications 93 (1995) 875.

[202] B.D. R. Madec L. P.Kubin, On the Use of Periodic Boundary Conditions in Dislocation Dynamics Simulations, 2004.

[203] Aur´ elien VATTRE, Strength of Single Crystal Superalloys: from Dislocation Mechanisms to Continuum Micromechanics,2009, Mines de Paris.

[204] L.P. Kubin, G. Canova, M. Condat, B. Devincre, V. Pontikis, Y. Br'echet, Solid-State Phys. 23&24 (1992) 455.

[205] G. Monnet, S. Naamane, B. Devincre, Acta Materialia 59 (2011) 451.

[206] S. Queyreau, G. Monnet, B. Devincre, International Journal of Plasticity 25 (2009) 361.

[207] M.C. Fivel, Comptes Rendus Physique 9 (2008) 427.

[208] C. Julien, R. Christian, F. Marc, M. Bernard, Modelling and Simulation in Materials Science and Engineering 18 (2010) 25003.

[209] R. Novokshanov, S. Roberts, Journal of Nuclear Materials 386–388 (2009) 64.

[210] S. Queyreau, G. Monnet, B. Devincre, Acta Materialia 58 (2010) 5586.

[211] C. Zhou, S.B. Biner, R. LeSar, Acta Materialia 58 (2010) 1565.

[212] T. Diaz de la Rubia, H.M. Zbib, T.A. Khraishi, B.D. Wirth, M. Victoria, M.J. Caturla, Nature 406 (2000) 871.

[213] Q. Sylvain, ETUDE DES MÉCANISMES D'ECROUISSAGE SOUS IRRADIATION DE LA FERRITE PAR SIMULATIONS DE DYNAMIQUE DE DISLOCATIONS, Univ. Pierre et Marie Curie Paris, 2008.

[214] V. V Bulatov, L.L. Hsiung, M. Tang, A. Arsenlis, M.C. Bartelt, W. Cai, J.N. Florando, M. Hiratani, M. Rhee, G. Hommes, T.G. Pierce, T.D. de la Rubia, Nature 440 (2006) 1174.

[215] C. Robertson, K. Gururaj, Journal of Nuclear Materials 415 (2011) 167.

[216] S. Groh, E.B. Marin, M.F. Horstemeyer, H.M. Zbib, International Journal of Plasticity 25 (2009) 1456.

[217] D. Li, H. Zbib, H. Garmestani, X. Sun, M. Khaleel, Computational Materials Science 50 (2011) 2496.

[218] K. Gururaj, C. Robertson, Energy Procedia 7 (2011) 279.

[219] C.R. Arsenlis A. Hommes G. Marian J., Rhee M, Acta Materialia 60 (2012).

[220] B.M. Liz Kautz, Fusion Reactor Materials, 2010.

[221] http://www.srim.org/

[222] http://www.cdifx.univ-rennes1.fr/winplotr/winplotr.htm

[223] F.D.J. Jin S. X. Yang Z. Liu C. S., Tang R., Liu F. H., Qiao Y. X., Zhang H. D., Guo L P, Materials Characterization 62 (2011).

[224] Yakel H. L., Acta Crystallography Section B: Structural Science 43 (1987).

[225] L.H. Balzar D., J. Appl. Crystallogr. 26 (1993).

[226] S.P. Lutterotti L., J. Appl. Crystallogr. 23 (1990).

[227] A. Barnoush, Acta Materialia 60 (2012) 1268.

[228] M.J. Cordill, N.R. Moody, M. Gerberich, International Journal of Plasticity 25 (2009) 281.

[229] N.H. Vehoff H Barnoush A Hempelmann R Z., Yang B, Physical Chemistry 222 (2008).

[230] G.. Taylor, Proceedings of the Royal Society at London A 145 (1934) 388.

[231] B.T.S. Farrell K., Journal of Nuclear Materials 318 (2003).

[232] Y.. Osetsky, D.. Bacon, Nuclear Instruments and Methods in Physics Research Section B: Beam Interactions with Materials and Atoms 202 (2003) 31.

[233] http://lammps.sandia.gov/

[234] S. Plimpton, Journal of Computational Physics 117 (1995) 1.

[235] http://ovito.org/

[236] http://ovito.org/dxa/

[237] S. Alexander, Modelling and Simulation in Materials Science and Engineering 18 (2010) 15012.

[238] S. Alexander, A. Karsten, Modelling and Simulation in Materials Science and Engineering 18 (2010) 85001.

[239] http://www.paraview.org/paraview/resources/software.php

[240] A. Caro, J. Hetherly, A. Stukowski, M. Caro, E. Martinez, S. Srivilliputhur, L. Zepeda-Ruiz, M. Nastasi, Journal of Nuclear Materials 418 (2011) 261.

[241] G.J. Ackland, M.I. Mendelev, D.J. Srolovitz, S. Han, A. V Barashev, Journal of Physics: Condensed Matter 16 (2004) S2629.

[242] J. Wallenius, I.A. Abrikosov, R. Chakarova, C. Lagerstedt, L. Malerba, P. Olsson, V. Pontikis, N. Sandberg, D. Terentyev, Journal of Nuclear Materials 329–333, P (2004) 1175.

[243] P. Olsson, J. Wallenius, C. Domain, K. Nordlund, L. Malerba, Physical Review B 72 (2005) 214119.

[244] R.A. Aziz, A.R. Janzen, M.R. Moldover, Physical Review Letters 74 (1995) 1586.

[245] D.E. Beck, Molecular Physics 14 (1968) 311.

[246] T. Seletskaia, Y.N. Osetskiy, R.E. Stoller, G.M. Stocks, Journal of Nuclear Materials 367–370, P (2007) 355.

[247] N. Juslin, K. Nordlund, Journal of Nuclear Materials 382 (2008) 143.

[248] D. Terentyev, N. Juslin, K. Nordlund, N. Sandberg, Journal of Applied Physics 105 (2009) 103509.

[249] N.O. Yu, D.J. Bacon, Modelling and Simulation in Materials Science and Engineering 11 (2003) 427.

[250] B.D.W. and J.M.P. 88 Jaime Marian 25(2002), 255507., Phy. Rev. Lett. 88 (2002).

[251] G.G. Nix W. D., Journal of the Mechanics and Physics of Solids 46 (1998).

[252] A.M. Philipp Engels Alexander Hartmaier, Int. J. Plast. 38 (2012).

[253] H.K. S., Finite Plastic Deformation of Crystalline Solids, Cambridge University Press, 1992.

[254] W.F. Hosford, Mechanical Behavior of Materials, 2nd editio, Cambridge university press.

[255] M.A.B. M. J. Serenelli J. W. Signorelli, Int. J. Mech. Sci. 52 (2010).

[256] G. Monnet, Philosophical Magazine 86 (2006) 5927.

[257] Y. Dai, X.J. Jia, K. Farrell, Journal of Nuclear Materials 318 (2003) 192.

[258] C.S. Deo, M.A. Okuniewski, S.G. Srivilliputhur, S.A. Maloy, M.I. Baskes, M.R. James, J.F. Stubbins, Journal of Nuclear Materials 361 (2007) 141.

[259] S. Queyreau, J. Marian, M.R. Gilbert, B.D. Wirth, 004100 (2011) 1.

SYMBOLS

A	constant
α	Obstacle strength
B	constant
b	Burgers vector magnitude
b	Burgers vector
^{0}C	Degree centigrade
d	Diameter
ΔH	Change in hardness
ΔH_{NANO}	Change in hardness determined from nanoindentation
$\Delta\sigma_{YS}$	Change in yield stress
$\Delta\tau$	Change in shear stress
E	Young's modulus
γ	Shear strain
K	Kelvin
l	Length
L^i	Length of segment
λ	Average distance
μ	Shear modulus
m	Slip vector
M	Taylor factor
n	Slip plane normal vector
nN	Nano Newton
ν	Poisons ratio
ν^i	Velocity
ρ	Density
σ	Tensile stress
σ–ε	Tensile stress vs. tensile strain
T_m	Melting temperature

T	Temperature
T_{irr}	Irradiation temperature
T_{test}	Testing temperature
τ	Shear stress
τ–γ	Shear stress vs. shear strain
V	Volume
He_{int}	Helium in interstitial position
He_{sub}	Helium in substitutional position
Fe	Iron
Cr	Chromium
Ti	Titanium
Cu	Copper
B	Boron
Ni	Nickel
S	Sulphar
He	Helium

ABREVATIONS

appm	Atomic parts per million
CG	Conjugate gradient method
CD-EAM	Concentration dependent Embedded Atom Model
CRSS	Critical Resolved Shear Stress
dpa	Displacements per atom
DBH	Dispersed Barrier Hardening
DXA	Dislocation Extraction Algorithm
DBTT	Ductile to brittle Transition Temperature
DD	Dislocation Dynamics
DDD	Discrete Dislocation Dynamics
DI	Depth of Indentation
ED	Edge Dislocation
EAM	Embedded Atom Model
FKH	Fridel-Kroupa-Hirsch
FM	Ferritic Martensitic
GB/GBs	Grain Boundary/ Grain Boundaries
GIXRD	Grazing Incidence X-Ray Diffraction
GPa	Giga Pascal
ISE	Indentation Size Effect
KeV	Kilo electron Volt
LPA	Line Profile Analysis
L-D	Load versus Depth of indentation
LAMMPS	Large Atomic/Molecular Massive Parallel Simulator
mM	microMegas
MMM	Multiscale Material Modeling
MD	Molecular Dynamics
MC	Metropolis Monte-Carlo method
MPa	Mega Pascal
MeV	Million electron Volt

OVITO	Open Visualization Tool
ODS	Oxide Dispersion Strengthened
PARADIS	PARAllel DISlocation dynamics
PKA	Primary Knock-on Atom
PARAVIEW	Parallel Viewer
R/LAFM	Reduced/Low Activation Ferritic Martensitic
SFT	Stalking Fault Tetrahedra
SKA	Secondary Knock-on Atom
SRIM	Stopping and Ranging of Ions in Matter
SAED	Selected Area Electron Diffraction
TKA	Tertiary Knock-on Atom
TEM	Transmission Electron Microscope
TGB	Twist Grain Boundary
UTS	Ultimate Tensile Strength
XRDLPA	X-Ray Diffraction Line Profile Analysis
YS	Yield Strength
3D	3 Dimensional

LIST OF PUBLICATIONS

1 "**Active slip systems in bcc iron during nanoindentation: A molecular dynamics study**", **N. Naveen Kumar**, R. Tewari, P.V.Durgaprasad, B.K.Dutta and G.K.Dey, **Computational Materials Science Computational Materials Science 77 (2013) 260–263.**

2 **"Plasticity at interfaces with Helium bubbles: Computer simulations of shear deformation of twist boundaries in α-Fe", N. Naveen Kumar**, E. Martinez, B. K. Dutta, G. K. Dey, A. Caro, **Physical Review B, 87(2013) 054106.**

3 **"Modeling of radiation hardening in ferritic/martensitic steel using multi-scale approach", N. Naveen Kumar**, P.V. Durgaprasad, B.K. Dutta, G.K. Dey, **Computational Materials Science 53 (2012) 258–267**.

4 **"Molecular dynamics simulations of interaction of edge dislocation and void in Fe and Fe-10%Cr system", N. Naveen Kumar** , P.V. Durgaprasad, B.K. Dutta, G.K. Dey , in **First international conference on Advances in Interaction and Multi-scale Mechanics**, Seogwipo KAL Hotel, Jeju, Korea, 30 May – 4 June 2010.

5 **"Study of interaction of edge dislocation with irradiation induced defects using molecular dynamics simulations in fe-10%cr model alloy"**, **N. Naveen Kumar**, P.V. Durgaprasad, B.K. Dutta, G.K. Dey, in Transactions, **21st International Conference on Structural Mechanics in Reactor Technology (SMiRT-21)**, 6-11 November, 2011, New Delhi, India.

6 **"Molecular dynamics simulation of edge dislocation motion in Fe-10%Cr model alloy with substitutional or interstitial He"**, **N. Naveen Kumar**, P.V. Durgaprasad, B.K. Dutta, G.K. Dey, **ICCMS-12**, Indian Institute of Technology, Hyderabad, 9-12 December, 2012.